Title
Understanding the Interiors of Vesta and Ceres Through Their Interactions with the Solar Wind

Author
Villarreal, Michaela Nicole

Publication Date
2018

Peer reviewed|Thesis/dissertation

UNIVERSITY OF CALIFORNIA

Los Angeles

Understanding the Interiors of Vesta and Ceres Through Their Interactions with the Solar Wind

A dissertation submitted in partial satisfaction of the requirements for the degree Doctor of Philosophy in Geophysics and Space Physics

by

Michaela Nicole Villarreal

2018

ABSTRACT OF THE DISSERTATION

Understanding the Interiors of Vesta and Ceres Through

Their Interactions with the Solar Wind

by

Michaela Nicole Villarreal

Doctor of Philosophy in Geophysics and Space Physics

University of California, Los Angeles, 2018

Professor Christopher T. Russell, Chair

The Gamma Ray and Neutron Detector (GRaND) onboard the Dawn spacecraft is sensitive to energetic protons, energetic electrons, and strong magnetic fields. This allows us to probe the local space environment while Dawn was in orbit about Vesta and Ceres. Understanding how these planets interact with the solar wind provides information about properties of the planetary surface and its interior. At Vesta, we searched for evidence of a past dynamo by attempting to indirectly detect remanent crustal fields. We scanned the GRaND data for solar wind electrons reflected by local crustal fields and by sensing effects of the magnetic field on the BGO spectrum. We did not find any evidence for reflected electrons or shifts in the BGO spectrum caused by magnetism associated with Vesta. Based on the sensitivity of the instrument, we conclude the upper bound for the magnetic dipole moment to be $\mu \leq 6{\times}10^{8}\ Tm^{3}$.

At Ceres, we have interpreted sudden bursts of energetic electrons detected by GRaND to be an electron foreshock produced by reflection and acceleration of solar wind electrons encountering a bow shock surface. This phenomenon occurred on a timescale of ~10 days, suggesting the bow shock to be a transient feature, most likely produced by a temporary exosphere. We show that a temporary exosphere at Ceres can be produced by solar energetic particle events which are capable of sputtering water ice from the surface.

The dissertation of Michaela Nicole Villarreal is approved.

Robert J. Strangeway

Vassilis Angelopoulos

Edward Donald Young

Christopher T. Russell, Committee Chair

University of California, Los Angeles

2018

This manuscript is dedicated to my grandparents.

Si se puede.

TABLE OF CONTENTS

List of Figures

List of Tables

ACKNOWLEDGEMENTS

I would like to thank my advisor, Christopher Russell, for including me as a Dawn Team Science Member and providing me with feedback and guidance through graduate school. I would also like to thank my committee members for providing their feedback on this dissertation.

Thank you Tom Prettyman and Yuki Yamashita for teaching me and guiding me on how to analyze the GRaND data and for providing valuable feedback on this work.

Thank you Yingdong Jia for running the MHD simulations used in Chapter 6.

Thank you Janet Luhmann and Leila Mays for providing the Enlil and SEPMOD simulations used in Chapter 7. Thank you also to Christina Lee who also provided input on related SEP events at Mars.

Thank you Steve Joy for providing the orbit and pointing data of the Dawn spacecraft, used in Chapters 4 and 7.

Thank you Philip Rousselot, Michael Küppers, and Mike A'Hearn for your insights and comments on the relation between the telescopic observations and solar energetic particle events (Chapters 7 and 8).

I would like to thank the Dawn Team, Margaret Landis, Norbert Schorgofer, Carol Raymond, Julie Castillo-Rogez, and the Russell Group for useful discussions and feedback on this work.

I would like to thank the Cota-Robles Fellowship, the NASA Space Grant Fellowship, the Harold & Mayla Sullwold Fellowship, the Wilbur B. Sherman Fellowship, and the Dawn grant for funding this work and giving me the opportunity to present my work at professional conferences.

Most importantly, I would like to thank my family and friends for providing their unconditional support through graduate school. For my parents, grandparents, and siblings, I am incredibly thankful for. Thank you to Ky Hughson, Emily Hawkins, Erin Leonard, Amanda Garcia, Ricky Hart, Raquel Nuno, Mojhgan Haghnegahdar, Cong Zhao, and Aaron Heick for keeping me sane throughout grad school.

Lastly, I would like to recognize my service animal Luna T. Villarreal who was by my side helping me work on every homework set, study session, presentation, abstract, code, data analysis, and the entirety of this work.

Chapter 6 includes work that the author of this dissertation undertook as a co-author, which is published as:
Jia, Y.D., M.N. Villarreal, C. T. Russell, Possible Ceres Bow Shock Surfaces Based on Fluid Models, J. Geophys. Res. Space Physics, 122, 4976-4987 (2017).

Chapter 7 includes work that the author of this dissertation undertook as first author, which is published as:

Villarreal, M.N., C. T. Russell, J.G. Luhmann, W. T. Thompson, T. H. Prettyman, M.F. A'Hearn, M. Küppers, L. O'Rourke, and C. A. Raymond, The Dependence of the Cerean Exosphere on Solar Energetic Particle Events, ApJL **838**, L8 (2017).

VITA

Education: 2016 Geophysics and Space Physics, M.S., UCLA

2011 Planetary Science, B.A., UC Berkeley

Memberships: American Geophysical Union

American Astronomical Society

Awards: 2013-2017 Cota-Robles Fellowship

2013-2017 NASA Space Grant Fellowship

2017 Harold & Mayla Sullwold Fellowship

2015 Wilbur B. Sherman Fellowship

Publications:

- Villarreal, M.N., C. T. Russell, J.G. Luhmann, W. T. Thompson, T. H. Prettyman, M.F. A'Hearn, M. Küppers, L. O'Rourke, and C. A. Raymond, The Dependence of the Cerean Exosphere on Solar Energetic Particle Events, ApJL **838**, L8 (2017).
- Villarreal, M.N., C. T. Russell, H. Y. Wei, Y. J. Ma, J. G. Luhmann, R. J. Strangeway, and T. L. Zhang, Characterizing the low-altitude magnetic belt at Venus: Complementary observations from the Pioneer Venus Orbiter and Venus Express, J. Geophys. Res. Space Physics, 12, 2232-2240 (2015).
- Jia, Y.D., M.N. Villarreal, C. T. Russell, Possible Ceres Bow Shock Surfaces Based on Fluid Models, J. Geophys. Res. Space Physics, 122, 4976-4987 (2017).

- Schorghofer, N., S. Byrne, M.E. Landis, E. Mazarico, T.H. Prettyman, B. E. Schmidt, M. N. Villarreal, J. Castillo-Rogez, C. A. Raymond, and C. T. Russell, The Putative Cerean Exosphere, ApJ 850 85 (2017).
- Russell, C. T., et al., Dawn arrives at Ceres: Exploration of a small volatile-rich world, Science 353 (6303), 1008-1010 (2016).
- Zhang, T. L., W. Baumjohann, C. T. Russell, M.N. Villarreal, J. G. Luhmann, and W. L. The, A statistical study of the low-altitude ionospheric magnetic fields over the north pole of Venus, J. Geophys. Res. Space Physics, 120, 6218-6229 (2015).
- Luhmann, J.G., Y.J. Ma, M.N. Villarreal, H. Y. Wei, T.L. Zhang, The Venus-solar wind interaction: Is it purely ionospheric?, Planetary and Space Science 119, 36-42 (2015).

Chapter 1

Introduction to Vesta, Ceres, and the Dawn Mission

1.1 Introduction

How dust grains in the solar nebula grow into large planets has long remained a mystery. Goldreich and Ward (1973) proposed that as dust particles settled to the ecliptic plane, gravitational instabilities caused the dust to cluster and form planetesimals up to radii of 5 km, followed by additional growth by collisions. Mizuno et al. (1978) argued that once these planetesimals reached a critical mass dictated by their location in the solar disk, they were able to hold onto large amounts of gas and grow into giant gas planets, also known as core accretion.

The largest intact remnants documenting the intermediate segment of solar system formation are Vesta and Ceres, two protoplanets located in the asteroid belt at 2.4 AU and 2.8 AU, respectively. They are the largest bodies in that region of the solar system and combined account for about half the total mass contained in the asteroid belt. Though these bodies are similar in size, they have quite contrasting properties. Vesta is dense, dry, and fully differentiated with an iron and nickel core while Ceres has a low density, is ice-rich, and appears to be only partially differentiated. In addition to the differences in their interiors, the geological features at their surfaces are also quite different, though they both have a similar surface gravity of ~ 0.25 m/s^2, indicating inherent differences in their chemical compositions. The Dawn mission journeyed to Vesta and Ceres to determine the conditions at the time of their formation and understand how

these bodies have evolved to be so different despite forming in the same region of the solar system.

1.2 The Dawn Mission

The Dawn spacecraft launched on September 27, 2007 from Cape Canaveral. It arrived first at Vesta, residing at the protoplanet from July 2011- August 2012. It then cruised to Ceres for 3 years, arriving at the dwarf planet in March 2015. The extended Dawn mission is expected to continue through summer 2018, after which the spacecraft will be placed permanently in a stable orbit about Ceres.

Figure 1.1 shows a schematic of the Dawn spacecraft. The Dawn payload consists of three instruments: a Framing Camera (FC), a Visible and Infrared (VIR) Spectrometer, and a Gamma Ray and Neutron Detector (GRaND). A second framing camera is also included on the payload for redundancy. A High Gain Antenna and three Low Gain Antennas are incorporated to communicate with Earth using the Deep Space Network. The spacecraft is powered by solar arrays each with dimensions 2.27 m x 8.30 m. Dawn carries three ion thrusters which use xenon to propel the spacecraft through interplanetary space.

The Dawn mission is an international collaboration with each instrument provided by a different agency. The Max Planck Institute for Solar System Research (MPS) joint with the German Aerospace Center (DLR) Institute of Planetary Research supplied the Framing Camera (FC), which consists of a clear filter and 7 band-pass filters ranging from visible to near infrared (Sierks et al., 2011). Framing Camera data are used to produce geological maps of the surface, digital terrain models, and surface mineralogy via its color filters. The Visible and Infrared (VIR) Spectrometer was provided by the Italian Space Agency (ASI) and measures the mineralogical

composition within the top millimeters of the surface (De Sanctis et al., 2011). The Los Alamos National Laboratory (LANL) built the Gamma Ray and Neutron Detector (GRaND) which senses the elemental abundance within the top meter of the surface (Prettyman et al., 2011). GRaND together with VIR investigated the geochemical evolution and current composition of each body. Information on the internal structure of the asteroids were obtained by gravity measurements using X-band Doppler tracking and optical landmark tracking (Konopliv et al, 2011). This technique resolved Vesta's gravitational field to harmonic degree 20 (Ermakov et al., 2014) and Ceres to harmonic degree 14 (Ermakov et al., 2017). The Jet Propulsion Laboratory (JPL) and the University of California, Los Angeles (UCLA), provided management of the spacecraft and its data.

Dawn observed the surfaces of Vesta and Ceres using four different orbital phases (Polanskey et al., 2013; Polanskey et al., 2016). Table 1 summarizes each orbit relative to the respective body's center while Dawn was in its prime mission phase. All orbits were designed to be circular, polar orbits. At Ceres, the spacecraft was first inserted into the Rotational Characterization (RC) orbit after approach. This orbit allowed for the determination of the spin pole axis and better accuracy of the rotation period. A dedicated RC orbit was not implemented at Vesta. Rather, the Approach phase in conjunction with the Survey orbit was used to determine the spin pole axis and rotation period (Russell et al., 2012, Supplemental Material). The remaining three orbits—Survey, the High Altitude Mapping Orbit (HAMO), and the Low Altitude Mapping Orbit (LAMO)—are used to map the surface at different spatial resolutions and coverages while also optimizing the performance of each instrument, as dictated by the Level 1 mission objectives (Russell and Raymond, 2011).

To create geologic maps of the surface, the Dawn mission established planetary coordinates and naming schemes for geologic features at both protoplanets. The Claudia coordinate system at Vesta is based relative to Claudia crater, a 625 m diameter crater located at (-1.6°, 356°) using a spin pole orientation of RA=309°, Dec=42° measured by Dawn. All of Vesta's craters are named after the Vestal Virgins and notable Roman women. At Ceres, the prime meridian is defined by Kait crater, a crater with diameter 0.4 km and location (0°, -2.1°), with spin pole orientation of RA=291°, Dec=67° updated by Dawn. The naming convention for geologic features on Ceres is derived from Harvest gods and festivals from around the world.

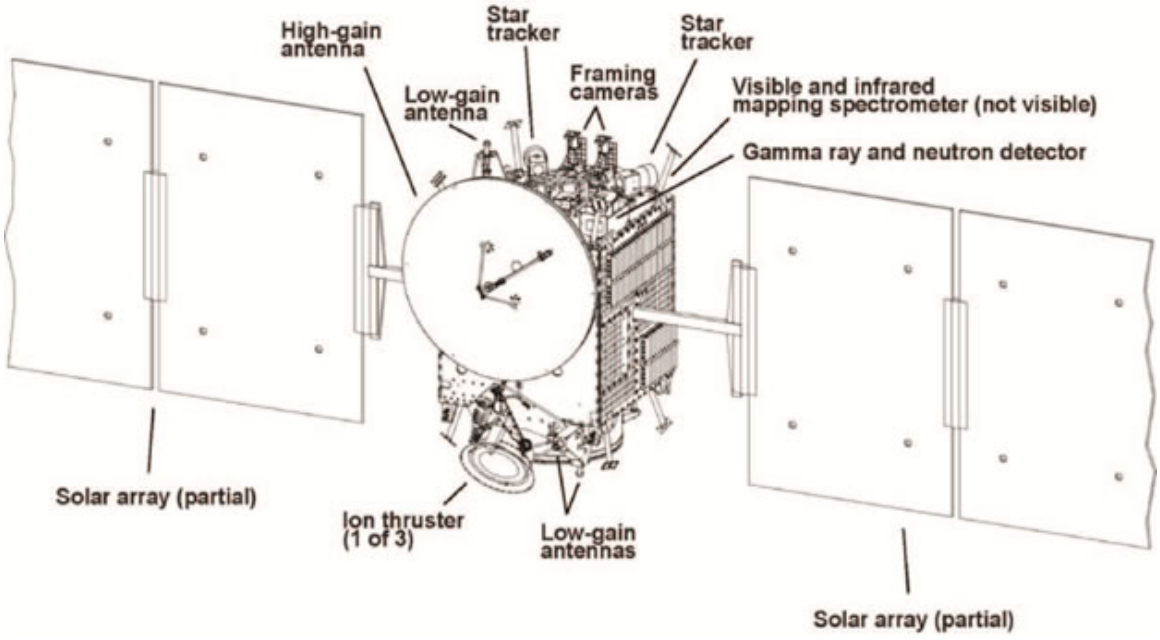

Figure 1.1 *The payload for the Dawn spacecraft includes 3 instruments (Framing Camera, VIR, and GRaND), solar arrays for power, ion thrusters, and low and high gain antennas for communication. Figure from https://dawn.jpl.nasa.gov/spacecraft/spacecraft.html.*

Orbital Phase	Vesta	Ceres
Rotational Characterization (RC)	N/A	14,000 km; 15.2 days
Survey	3000 km; 69 hrs	4,900 km; 75 hrs
High Altitude Mapping Orbit (HAMO)	950 km; 12.3 hrs	1,950 km; 19 hrs
Low Altitude Mapping Orbit (LAMO)	465 km; 4 hrs	850 km; 5.4 hrs

Table 1.1 *Summary of Dawn's orbital phases at Vesta and Ceres during its prime mission. The distances are measured from the body center and the time represents the length to complete one orbit at each phase.*

1.3 Vesta

Prior to Dawn's arrival at Vesta, information about the body was inferred from analysis of the Howardite, Eucrite, and Diogenite (HED) meteorites. Evidence for the HEDs originating from Vesta was first proposed by McCord et al. (1970), who highlighted the similarities in absorption bands at ~0.5 and 0.9 microns in the reflectance spectra of Vesta and the HED meteorites. Radioactive dating of the HED meteorites implied Vesta differentiated 1-3 Myr after the formation of Calcium Aluminum Inclusions (CAIs) (McSween et al., 2011). The mineralogy of the meteorites also implied Vesta to be extensively thermally altered, and thus highly differentiated (McSween et al., 2011). Upon Dawn's arrival, in-situ analysis of the surface mineralogy (DeSanctis et al., 2012) and its elemental abundance (Prettyman et al., 2012) confirmed Vesta to be the parent body of the HED meteorites.

Dawn's visit to Vesta in 2011 characterized it as a relatively dry body with its surface geology dominantly composed of impact craters (Figure 1.2). The craters are relatively bowl shaped, typical for a dry body. Rheasilvia, a large impact crater with a diameter ~500 km and a

central peak ~ 20 km high dominates the topography in the southern hemisphere. Peculiarly, the Rheasilvia crater is superimposed on an even older crater, Venenia, which is similar in size with a diameter of ~400 km (Schenk et al., 2012). The HED meteorites and the Vestoids, Vesta's dynamical family, are believed to have been dominantly excavated during the large impacts that created the Rheasilvia and Veneneia craters (Schenk et al., 2012). Despite being a dry body, curvilinear gullies observed in the Marcia, Calpurnia, and Cornelia craters provided evidence that water flowed in the walls of these craters indicating small, localized regions of ice below the surface (Scully et al., 2015).

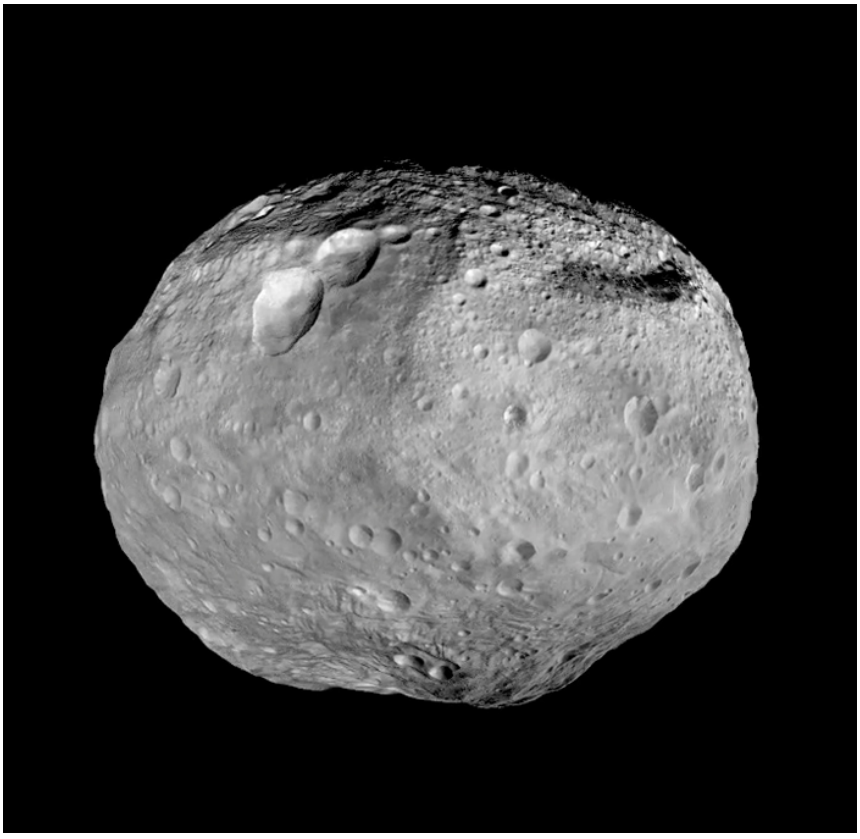

Figure 1.2 *Global mosaic of Vesta. The topography in the southern hemisphere is dominated by the Rheasilvia crater, which displays a large central peak. Image from https://dawn.jpl.nasa.gov/multimedia/full_view_vesta.html.*

In addition to its composition, Dawn refined the physical properties of the protoplanet. Vesta is an oblate spheroid with a rotation period ~5 hr (Russell et al., 2012). It was found to have a mean radius of ~262 km and a mass of ~2.6×10^{20} kg, resulting in a bulk density of 3,456 kg/m^3 (Russell et al., 2012). Using the HED meteorites to constrain the properties of the crust and mantle, estimates for the internal structure were derived. Vesta is believed to be differentiated into three layers: an iron core with a density ~7800 kg/m^3 and radius ~110 km, an olivine-rich mantle of density ~3200 kg/m^3 and radius ~225 km, and a eurcritic and diogenitic crust with density ~2900 kg/m^3 and radius ~260 km (Russell et al., 2012; Ermakov et al., 2014).

The identification of a metallic core raises the question of whether Vesta had a dynamo in its past and if a record of it exists through surface crustal fields. Several of the HED meteorites were found to have a natural remanent magnetization implying crustal fields at the surface. In their paper, Collinson & Morden (1994) analyzed the remanent magnetization of 9 HED meteorites and concluded that the parent body would have likely had a surface field of 5-50 μT at the time of magnetization. Based on cooling ages, Fu et al. (2012) determined that the magnetization of the HED meteorite Allan Hills ALHA81001 likely formed in the presence of a paleofield anywhere between 10-37 μT, while the Millbillillie meteorite is believed to have formed after Vesta's dynamo ceased, implying crustal fields between 5-10 μT. Although not associated with Vesta, Wang et al. (2015) and Weiss et al. (2008) found several Angrite meteorites to be magnetized, providing evidence for dynamos in other planetesimals early in the solar system. Since Dawn's payload does not include a magnetometer, the mission was unable to directly confirm this result. However, this thesis explores indirect methods that may be able to detect remanent fields at Vesta and induced fields at Ceres.

1.4 Ceres

Ceres is the largest object in the asteroid belt and the only dwarf planet in the inner solar system. Despite its large size, there are no known meteorites nor a dynamical family associated with the body. Therefore, all knowledge of Ceres preceding Dawn's arrival was acquired through remote sensing. Parker et al. (2002) resolved the disk of Ceres at the ultraviolet wavelengths with the Hubble Space Telescope. They determined Ceres to have equatorial radii, a=b, of 484.4 km and a polar radius, c, of 466.4 km. Based on previous mass estimates for Ceres, they arrived at a relatively low mean density of 1.9-2.6 g/cm^3. Carry et al. (2008) used adaptive optics to observe Ceres with the Keck II Observatory. They attained similar results for the dimensions of Ceres, with a=b=474.7 km and c=444.4 km and established Ceres to have a rotation period ~9 hrs. Additionally, albedo variations showed Ceres to exhibit two surface features: a dark region with a bright center located at (234°, +23°) and a dark feature located at (125°, +20°) in planetocentric longitude and latitude (Carry et al., 2008). These features correspond to the now-resolved Occator and Dantu regions, respectively.

The inferred low density of Ceres led to two models for its internal structure. Castillo-Rogez and McCord (2010) argued that the low density of Ceres could be explained by differentiation into a silicate core overlain by an icy mantle. In contrast, Zolotov (2009) proposed Ceres to be undifferentiated and attributed its low density to porosity within the body rather than ice. Assuming an icy Ceres, Bland et al. (2013) considered the effect of viscous relaxation on crater morphology. They predicted craters would persist at the poles where the ice is colder with few to no craters in the equatorial region where the ice is warmest and viscous relaxation is strongest.

Fanale and Salvail (1989) demonstrated that ice should not be stable on the surface of Ceres and suggested a water exosphere should be present. Subsequent observations of OH emission

and H_2O absorption over the next three decades indicated the water exosphere is time varying; the exosphere was detected only on half of the telescopic attempts (A'Hearn and Feldman, 1992; Rousselot et al., 2011; Küppers et al., 2014). While it was proposed the exosphere of Ceres was produced via sublimation (A'Hearn and Feldman, 1992), its sporadic presence led Küppers et al. (2014) to suggest localized plumes as its source. However, the source areas identified by Küppers et al. (2014)—the Dantu and Occator craters—have shown no evidence for water ice present today as seen by Dawn's VIR, although VIR has detected water ice elsewhere. Prior to the arrival of Dawn, there was still no consensus as to the production mechanism for the cerean exosphere.

In March 2015, Dawn arrived at Ceres providing the first in-situ measurements of the dwarf planet. In contrast to the expectation of Bland et al. (2013), Ceres was observed to be extensively cratered (Figure 1.3). The craters commonly have steep walls with flat floors, displaying an intermediate crater morphology between dry and icy bodies (Schenk et al., 2016). Polygonal craters are also prevalent on Ceres, indicating pre-existing fractures prior to the crater-forming impacts (Buczkowski et al., 2016). Ceres' surface is largely dark with an average bond albedo of ~0.03 (Li et al., 2016), but contains 92 bright spots interspersed throughout the surface which can reach bond albedos >0.5 and are typically found in geologically young craters (Palomba et al., 2017; Stein et al., 2017). A majority of the bright spots show a composition similar to that of the average Ceres surface mixed with Mg-Ca carbonates (Palomba et al., 2017). The most significant of these bright spots are the Cerealia Facula and Venalia Facula which reside in Occator crater (Figure 1.3), and consist of sodium carbonates, implying they were emplaced by a brine solution that flowed from the interior (De Sanctis et al., 2016).

Dawn measured Ceres to have a total mass of ~9.4 x 10^{20} kg with a mean radius of ~470 km, confirming it to have a low mean density of 2,162 kg/m^3 (Russell et al., 2016). Gravity measurements suggest Ceres to only be partially differentiated into a crust and mantle layer, though a rocky core cannot be excluded (Park et al., 2016). Viscous relaxation was observed to preferentially occur in large impact craters implying a strong crust with a viscous layer at depth (Ermakov et al., 2017). Imposing a two-layer model, Ermakov et al. (2017) estimates Ceres to have a crustal thickness of 41 km with a crustal density of ~1,300 kg/m^3 and a mantle with density ~2,400 kg/m^3.

Observations of Ceres show a wide array of evidence for water ice present at or near the surface. Craters at high latitudes exhibit fluidized flow features with morphologies consistent with being formed by ground ice (Schmidt et al., 2016). The distribution of these craters are in agreement with the observations made by the Gamma Ray and Neutron Detector which showed the hydrogen content within the top meter of the surface to increase above 40 degrees latitude (Prettyman et al., 2017). That study suggested an ice table exists within a meter of the surface which contains 10 wt.% water ice. Water ice also provided the best fit for absorption features seen by the VIR instrument for nine locations on the surface. The largest signals observed were located at the Oxo and Juling craters (Combe et al., 2016; Combe et al., 2017). VIR penetrates to a depth of a few millimeters, requiring the water to be very near the surface to be detected. Surface ice was also detected by identifying bright deposits in polar craters (Platz et al., 2016). These craters were found in locations that were predicted to be cold traps for water ice (Schorghofer et al., 2016). Dawn also attempted detect water in the form of a plume while in its RC orbit at an altitude of 13,520 km. Forward scattering observations of Ceres' limb were conducted in an attempt to detect lofted dust particles, which produced a null result (Russell et

al., 2016). However, Dawn was not designed for this type of experiment and would have required a substantial amount of lofted dust to be detected. While there is an abundance of evidence for ice near or on the cerean surface, how these features contribute to the production of the cerean exosphere is still unknown.

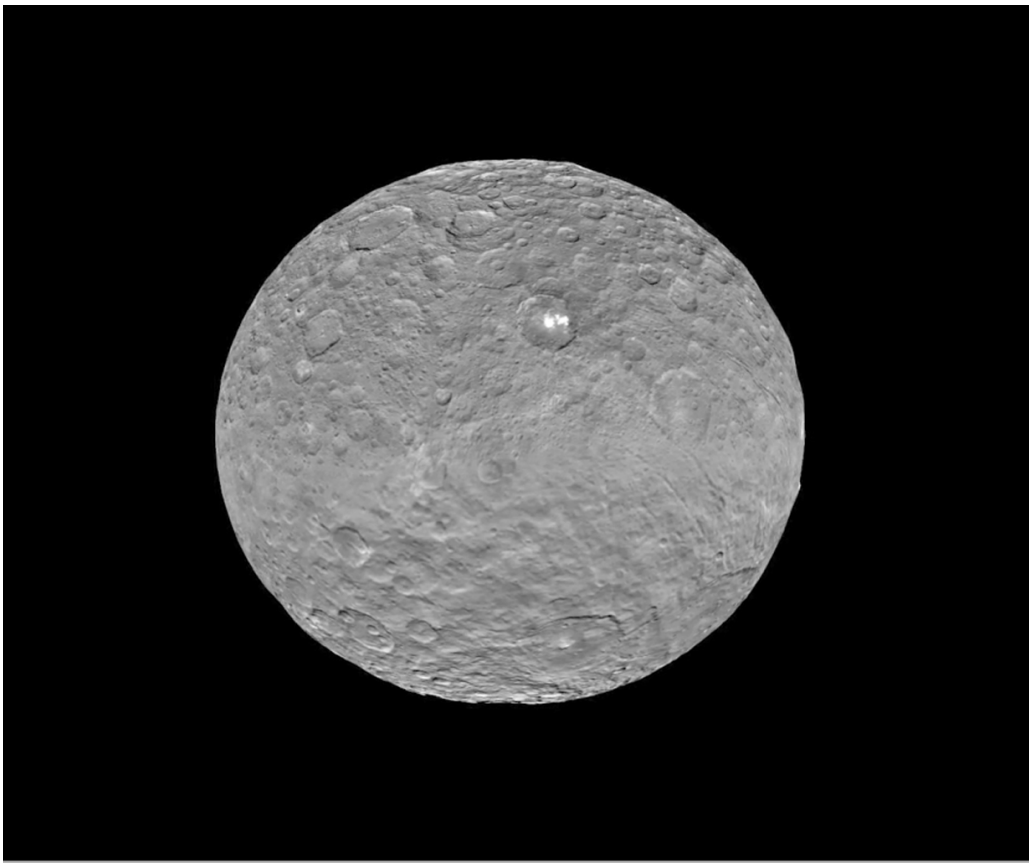

Figure 1.3 *Global view of Ceres. Ceres is extensively cratered with a low bond albedo. Its most significant bright spots are located in Occator crater (seen here in the northern hemisphere). Image from https://www.jpl.nasa.gov/spaceimages/images/largesize/PIA19619_hires.jpg.*

1.5 Understanding the Interiors of Vesta and Ceres Through Their Interaction with the Solar Wind

One avenue that has not yet been explored is understanding how the solar wind interacts with the surface environments of Vesta and Ceres and the information can be gained from this. Meteorites from Vesta suggest remanent magnetic crustal fields are present on the surface, which could be capable of reflecting incoming solar wind electrons similar to the moon (Howe et al., 1974; Lin, 1979; Mitchell et al., 2008), or if the surface field is large enough, produce a bow shock that is capable of reflecting energetic electrons at the bow shock surface (Wu, 1984; Leroy and Mangeney, 1984). A portion of the solar wind electrons will not be able to cross the shock and will be reflected, forming an electron foreshock upstream. In the case of Ceres, an exosphere created by the vapor production rates reported by telescopic observations could be large enough to create a bow shock through mass loading. Both scenarios produce regions of enhanced densities of energetic electrons to which the Gamma Ray and Neutron Detector is sensitive, providing a method to detect this phenomenon with Dawn. Additionally, the performance of GRaND's BGO detector is affected by the presence of strong magnetic fields which can be used to further identify and constrain the surface crustal fields at Vesta.

Large spikes in counts seen in the exterior scintillators of Dawn's Gamma Ray and Neutron Detector appeared during both encounters at Vesta and Ceres which do not appear to be energetic particles inherent in the solar wind and on initial inspection appear to have the characteristics of electron beams. There is a distinct difference in the nature of the spikes at the two bodies, suggesting they have different production mechanisms. At Vesta the spikes occurred as short, large amplitude, single events lasting ~10 minutes; at Ceres the spikes occurred in clusters and were longer in time with an average duration of ~20 minutes but weaker in

amplitude. The electron bursts at Ceres also appeared immediately following the onset of solar energetic particle events, signifying solar protons might be sputtering water molecules from the surface and producing the exosphere. In this dissertation, we explore if the spike signatures observed by GRaND can be explained by incoming solar wind particles reflected by remanent magnetic patches in the case of Vesta or by a bow shock at Ceres. We further investigate the crustal field of Vesta using the Gamma Ray and Neutron Detector as a proxy to detect magnetic fields.

This thesis has two primary objectives:

1) Place constraints on the surface magnetic field of Vesta and interpret what that may imply about the evolution of its internal structure and time of formation.
2) Investigate the release mechanism for the cerean exosphere and discern the subsurface-surface dynamics that replenish the exosphere.

1.5.1 Implications for the internal structure of Vesta

How the internal structures of planetesimals evolved and operated is still poorly understood. It is often assumed that planetesimals cooled quickly due to their small sizes, which presents a problem for dynamo theory. Models such as Sterenborg & Crowley (2013) estimate that a dynamo produced by a Vestan sized body with a surface field strength of 20 μT can last only up to million years. Similarly, calculations by Weiss et al. (2008) show that a planetesimal dynamo can last up to several tens of millions of years if the heat flux out of the core is super-adiabatic. Confirming a remanent magnetization at Vesta would not only provide strong evidence that a planetesimal could support a dynamo, but would also help infer the internal processes early in its evolution.

Vesta has remained intact and has additional meteoritic evidence to help constrain its composition and magnetization, making it a prime target to study. A remanent field detection at Vesta would provide information about its time of accretion since it would require the body to trap enough radiogenic heat to sustain a dynamo. Additionally, the relative duration of the dynamo could be inferred through stratigraphy if crustal field regions are found to be associated with geographical features. This will further help refine models of the thermal evolution of planetesimals.

1.5.2 Implications for the internal structure of Ceres

The electron bursts observed by Dawn's Gamma Ray and Neutron Detector while in orbit about Ceres display similar attributes as those reported in electron foreshocks at other planets. It is conceivable that the same process is occurring to produce the electron bursts at Ceres. This mechanism allows the electrons to travel to the spacecraft from large distances and can provide explanations for why they occur at a particular location, how the bursts are seen 10 radii away from the body, and how the large energies of the energetic electrons.

Ceres' lack of a metallic core implies that it should not be a magnetized body, and therefore the genesis of the bow shock has significant implications for its surface and/or internal processes. The best candidates that can act as an obstacle to the solar wind are mass loading due to a transient atmosphere or magnetic induction from a conductive layer at depth. Geochemical models of Ceres' interior indicate the body could harbor a saline, muddy layer that could act as a conductor (Castillo-Rogez et al., 2016). The observance of the electron bursts immediately after the passage of solar energetic particle events suggests that these protons may be liberating water at or near the surface. This can cause a non-negligible exosphere, which is capable of producing

a bow shock in the solar wind. Alternatively, if the planet has an electrically conducting layer, a bow shock can be generated through magnetic induction as the layer responds to the change in the interplanetary magnetic field. An enhancement in the IMF due to a solar event could trigger such a response.

This dissertation investigates whether solar wind sputtering or an internal conductive layer at depth can explain the electron bursts observed by GRaND. If the bursts are consistent with a salty, muddy layer at depth, the conductivity required will place constrains on the type of salts that may exist and their concentrations. Alternatively, if the bursts can be explained by solar wind sputtering, this has implications for the depth to which the protons sputter water ice and replenishment mechanisms from the subsurface.

1.6 References

A'Hearn, M. F. and P.D. Feldman, Water Vaporization on Ceres, Icarus 98, 54-60 (1992).

Bland, M. T. (2013). Predicted crater morphologies on Ceres: Probing internal structure and evolution. Icarus, 226(1), 510–521.

Buczkowski, D. L. et al., The geomorphology of Ceres, Science, Vol 252, Issue 6303, aaf4332 (2016).

Carry, B. et al., Near-infrared Mapping and Physical Properties of the Dwarf-planet Ceres, Astronomy & Astrophysics, 478, 235-244 (2008).

Castillo-Rogez, J. C. and T. B. McCord, Ceres' Evolution and Present State Constrained by Shape Data, Icarus 205, 443-459 (2010).

Castillo-Rogez, J. et al., Where is Ceres' Ice Shell?, Lunar and Planetary Science Conference abstract (2016).

Collinson, D. W. and S. J. Morden, Magnetic Properties of Howardite, Eucrite and Diogenite (HED) Meteorites: Ancient Magnetizing Fields and Meteoritic Evolution, Earth and Planetary Science Letters, 126, 421-434 (1994).

Combe, J. P. et al., Detection of local H_2O exposed at the surface of Ceres, Science, Vol 353, Issue 6303 (2016).

Combe, J. P. et al., Exposed H_2O-rich areas detected on Ceres with the Dawn Visible and Infrared Mapping Spectrometer, Icarus 000, 1-20 (2018).

De Sanctis, M. C. et al., The VIR Spectrometer, Space Sci Rev, 163, 329-369 (2011).

De Sanctis, M. C. et al., Spectroscopic Characterization of Mineralogy and Its Diversity Across Vesta, Science, Vol 336, 697-700 (2012).

De Sanctis, M. C. et al., Bright carbonate deposits as evidence of aqueous alteration on (1) Ceres, Nature, Vol 536, 54-57 (2016).

Ermakov, A. I. et al., Constraints on Vesta's Interior Structure using Gravity and Shape Models from the Dawn Mission, Icarus, Vol 240, 146-160 (2014).

Ermakov, A. I. et al., Constraints on Ceres' Internal Structure and Evolution From its Shape and Gravity Measured by the Dawn Spacecraft, Journal of Geophysical Research: Planets, 122, 2267-2293 (2017).

Fanale, F. P. and J. R. Salvail, The Water Regime of Asteroid (1) Ceres, Icarus 82, 97-110 (1989).

Fu, R. et al., An Ancient Core Dynamo in Asteroid Vesta (2012), Science 338, 238-241 (2012), DOI: 10.1126/science.122564.

Goldreich, P. and W. R. Ward, The Formation of Planetesimals, The Astrophysical Journal, Vol. 183, 1051-1061 (1973).

Howe, H. C. et al., Energetic Electron Scattering from the Lunar Remanent Magnetic Field, Geophysical Vesearch Letters, Vol 1, No. 3, 101-104 (1974).

Konopliv, A. S. et al., The Dawn Gravity Investigation at Vesta and Ceres, Space Sci Rev, 163, 461-486 (2011).

Küppers, M. et al., Localized sources of water vapour on the dwarf planet (1) Ceres, Nature, 505, 525-527 (2014).

Leroy, M. M. and A. Mangeney, A theory of energization of solar-wind electrons by the Earth's bow shock. Annales Geophys. 2, 449-456 (1984).

Li, J. Y. et al., Surface Albedo and Spectral Variability of Ceres, The Astrophysical Journal Letters, Vol 817, L22 (2016).

Lin, R. P., Constraints on the Origins of Lunar Magnetism From Electron Reflection Measurements of Surface Magnetic Fields.

McCord, T. B. et al., Asteroid Vesta: Spectral Reflectivity and Compositional Implications, Science, New Series, Vol. 168, No. 3938, 1445-1447 (1970).

McSween, H. Y. et al., HED Meteorites and Their Relationship to the Geology of Vesta and the Dawn Mission, Space Sci Rev, 163, 141-174 (2011).

Mitchell, D. L. et al., Global Mapping of Lunar Crustal Magnetic Fields by Lunar Prospector, Icarus 194, 401-409 (2008).

Mizuno, H. et al., Instability of a Gaseous Envelope Surrounding a Planetary Core and Formation of Giant Planets, Progress of Theoretical Physics, Vol. 60, No. 3 (1978).

Palomba, E. et al., Compositional Differences Among Bright Spots on the Ceres Surface, Icarus 000, 1-11 (2017).

Park, R. S. et al., A Partially differentiated interior for (1) Ceres deduced from its gravity field

and shape, Nature, 537, 515-517 (2016).

Parker, J. W. et al., Analysis of the First Disk-Resolved Images of Ceres from Ultraviolet Observations with the Hubble Space Telescope, The Astronomical Journal, Vol 123, 549-557 (2002).

Platz, T. et al., Surface water-ice deposits in the northern shadowed regions of Ceres, Nature Astronomy, Vol 1, 7 (2016).

Polanskey, C. A. et al., Efficacy of the Dawn Vesta Science Plan, Space Operations: Experience, Mission Systems, and Advanced Concepts, edited by M. Schmidhuber, C. Cruzen, J. Kehr, Vol. 242, 501-515 (2013)

Polanskey, C. A. et al., Dawn Ceres Mission: Science Operations Performance, SpaceOps Conferences (2016).

Prettyman, T.H. et al. (2011), Dawn's gamma ray and neutron detector, Space Sci. Rev. 163, 371-459, doi: 10.1007/s11214-011-9862-0.

Prettyman, T. H. et al., Elemental Mapping by Dawn Reveals Exogenic H in Vesta's Regolith, Science, Vol 338, 242-246 (2012).

Prettyman, T. H. et al., Extensive water ice within Ceres' aqueously altered regolith: Evidence from nuclear spectroscopy, Science, Vol 355, Issue 6320, 55-59 (2017).

Rousselot, P. et al., A Search for Water Vaporization on Ceres, The Astronomical Journal, Vol 142, 125 (2011).

Russell, C. T. and C. A. Raymond, The Dawn Mission to Vesta and Ceres, Space Sci Rev 163, 3 23 (2011).

Russell, C. T. et al., Dawn at Vesta: Testing the Protoplanetary Paradigm, Science, Vol 336, 684-686 (2012).

Russell, C. T. et al., Dawn arrives at Ceres: Exploration of a small, volatile-rich world, Science, Vol 353, 1008-1010 (2016).

Schenk, P. et al., The Geologically Recent Giant Impact Basins at Vesta's South Pole, Science, Vol 335, 694-697 (2012).

Schenk, P. et al., Impact Cratering on the Small Planets Ceres and Vesta: S-C Transitions, Central Pits and the Origin of Bright Spots, 47 Lunar and Planetary Science Conference, Abstract 2697 (2016).

Schmidt, B. E. et al., Geomorphological evidence for ground ice on dwarf planet Ceres, Nature Geoscience, 10, 338-343 (2016).

Schorghofer, N. et al., The permanently shadowed regions of dwarf planet Ceres, Geophysical Research Letters, Vol 43, 6783-6789 (2016).

Scully, J. E. C. et al., Geomorphological evidence for transient water flow on Vesta, Earth and Planetary Science Letters, 411, 151-163 (2015).

Sierks, H. et al., The Dawn Framing Camera, Space Sci Rev, 163, 263-327 (2011).

Stein, N. T. et al., The formation and evolution of bright spots on Ceres, Icarus (2017), https://doi.org/10.1016/j.icarus.2017.10.014.

Sterenborg, M. G. and J. W. Crowley, Thermal Evolution of Early Solar System Planetesimals and the Possibility of Sustained Dynamos, Physics of the Earth and Planetary Interiors, 214, 53-73 (2013).

Wang, H. et al, Onset of a Planetesimal Dynamo and the Lifetime of the Solar Nebular Magnetic Field, 46th Lunar and Planetary Science Conference, abstract 2516 (2015).

Wu, C. S., A Fast Fermi Process: Energetic Electrons Accelerated by a Nearly Perpendicular Bow Shock, Journal of Geophysical Research, Vol. 89, NO A10, 8857-886 (1984).

Weiss, B. P. et al, Magnetism on the Angrite Parent Body and the Early Differentiation of Planetesimals, Science, Vol 322, 713-716 (2008).

Zolotov, M. Y., On the Composition and Differentiation of Ceres, Icarus, Vol 204, 183-193 (2009).

Chapter 2

Dawn's Gamma Ray and Neutron Detector's Response to Energetic Particles and Magnetic Fields

2.1 Introduction

Dawn's prime mission objectives were to characterize the geology, geochemistry, and evolution of the protoplanets Vesta and Ceres, and therefore its payload did not include traditional instrumentation used in studying solar wind properties such as a magnetometer or a plasma analyzer. Despite this, Dawn is still capable of detecting energetic protons and energetic electrons encountering the spacecraft with its Gamma Ray and Neutron Detector (GRaND). Radiation is produced by particle interactions of electrons and protons above a threshold energy with spacecraft material, which is then detected by GRaND. In addition, a photomultiplier tube associated with the instrument's BGO scintillator is sensitive to strong magnetic fields, causing shifts in the spectrum and allowing the instrument to act as a proxy to detect the presence of magnetic fields.

2.2 Description of Dawn's Gamma Ray and Neutron Detector

Dawn's Gamma Ray and Neutron Detector (GRaND) is an omnidirectional instrument designed to measure the bulk surface composition of Vesta and Ceres to depths ~1 m. GRaND is located on the +Z face of the spacecraft (Figure 2.1), where $+X_{spacecraft}$ points in the direction of the high gain antenna, $+Z_{spacecraft}$ points in the direction the science instruments are mounted on, and $+Y_{spacecraft}$ points along the solar panel that completes the right hand set. During data

acquisition, the +Z axis of the spacecraft is pointed nadir and the spacecraft pivots about the Z-axis to keep the Y-axis orthogonal to the direction of the Sun. Rotating the solar panels around the Z-axis allows sunlight to continuously illuminate the solar panels. The sampling rate of the instrument is adjusted with different orbital phases, ranging from 210 s upon arrival to 140 s during the Low Altitude Mapping Orbit (LAMO).

The instrument is composed of a Bismuth Germanate (BGO) scintillator at its center surrounded by four exterior scintillators (Figure 2.2). Two of the exterior detectors are Phoswich scintillators which have a layer of Lithium Loaded Glass (LiG) on their +/- Z outward-facing sides above a layer of Boron Loaded Plastic and point in the +/- $Z_{spacecraft}$ directions. The remaining two scintillators are composed of Boron Loaded Plastic (BLP) which are L-shaped and point dominantly in the +/- $Y_{spacecraft}$ directions and share a portion of their surface areas along the $-X_{spacecraft}$ direction. These scintillators detect gamma rays and neutrons by the radiation produced when they interact and excite the scintillator material.

The central BGO scintillator is designed to detect gamma rays originating from radioactive decay and by cosmic ray interactions with the planetary surface. Incoming gamma rays interact with the BGO crystal via the photoelectric effect and Compton scattering which ionize the atoms within the crystal and produce secondary light. The secondary light interacts with the photocathode and causes photoelectrons to be emitted which are then multiplied by the photomultiplier tube (PMT) and read out as an output signal. The analog to digital converter (ADC) places counts in channels (energy bins) based on the strength of the output signal. The BGO scintillator measures gamma ray energies between 300 keV-10 MeV. There is also a Cadmium Zinc Telluride (CZT) semiconductor sensor located between the BGO and +Z Phoswich which better resolves longer wavelength gamma rays between 300 keV-3 MeV.

The exterior scintillators detect thermal, epithermal, and fast neutrons ejected from the planetary surface. Elastic scattering (fast neutrons) and neutron capture (thermal and epithermal neutrons) interactions with the boron-loaded plastic result in ionization of the medium that can be measured similarly to the BGO. For the +/- Z Phoswiches, the additional LiG fully absorbs thermal neutrons, shielding their BLP component from these particles. Gold foil is wrapped around the remainder of the perimeter of the +/- Z Phoswiches to ensure thermal neutrons are not penetrating the BLP material on their non-Z faces. Counting rates for thermal and epithermal neutrons can then be derived by subtractions of the LiG and BLP count rates of the scintillator. All exterior scintillators measure energies between 20 keV-2.55 MeV.

Differentiation between the types of impinging particles is also provided by the isolation and simultaneity of events within the different scintillators. These events are divided into the following categories (CAT). CAT1 is a single pulse detected in the LiG in one of the +/-Z Phoswiches, where events can be produced by either thermal or epithermal neutrons. CAT2 is a coincidence in events between the BGO and any single exterior scintillator; the BLP detects radiation from the primary particle interaction while a secondary interaction emits a gamma ray at 478 keV detectable by the BGO. CAT2 events for the +/- Z Phoswiches will only be produced by epithermal neutrons while CAT2 events for the +/- Y BLP scintillators can be produced by either thermal or epithermal neutrons. A CAT4 event corresponds to successive double pulses of light occurring in any single exterior scintillator caused by a sequence of interactions with fast neutrons. A CAT7 event refers to coincidence in events between any CZT sensor and the BGO; these events are used to identify gamma rays originating from the spacecraft and are subsequently removed from the data. Gamma rays from the spacecraft can be identified by the relative energies deposited in the CZT and BGO during a CAT7 event: cases where the energy is

greater in the BGO than the CZT are assumed to be coming from the spacecraft since a gamma ray coming from the nadir direction will lose energy when it interacts with a CZT sensor. CAT9 is designated for a single pulse occurring only in the BGO detector and can only be caused by gamma rays. A CAT10 event refers to an event detected only by a CZT sensor and provides better resolution of gamma rays at the lower end of the BGO spectrum. Categories 3, 5, 6, and 8 were removed after the category scheme was developed.

In addition to the detection of neutrons, the exterior scintillators also act as an anti-coincidence shield for galactic cosmic rays. Events that are coincident in three or more scintillators are assumed to be caused by the interactions with galactic cosmic rays and are therefore used as a proxy for their presence, referred to as the Triples count rate. Galactic cosmic rays are important as the bombardment of these particles into the planetary surface results in the release of neutrons and emission of gamma rays and therefore greatly affect the magnitude of the neutron and gamma ray counts detected. However, a portion of the gamma rays emitted from the surface will also be due to radioactive decay.

Analysis of the gamma ray data in conjunction with the neutron data provides a profile for the elemental abundance within the top meter of the surface. Elements within the planetary surface can be identified by the energy-specific gamma rays that are emitted corresponding to the discrete energy levels of a particular atom—these will appear as peaks in the BGO spectrum. The ratio of thermal and epithermal neutrons emitted per cosmic ray strongly varies with the mass of the atoms within the surface: neutrons lose more of their energy through elastic collisions with light atoms than heavy atoms (Prettyman, 2014). For example, a planetary surface with a large hydrogen content will exhibit a strong suppression in the flux of neutrons detected. A more detailed description of GRaND can be found in Prettyman et al. (2011).

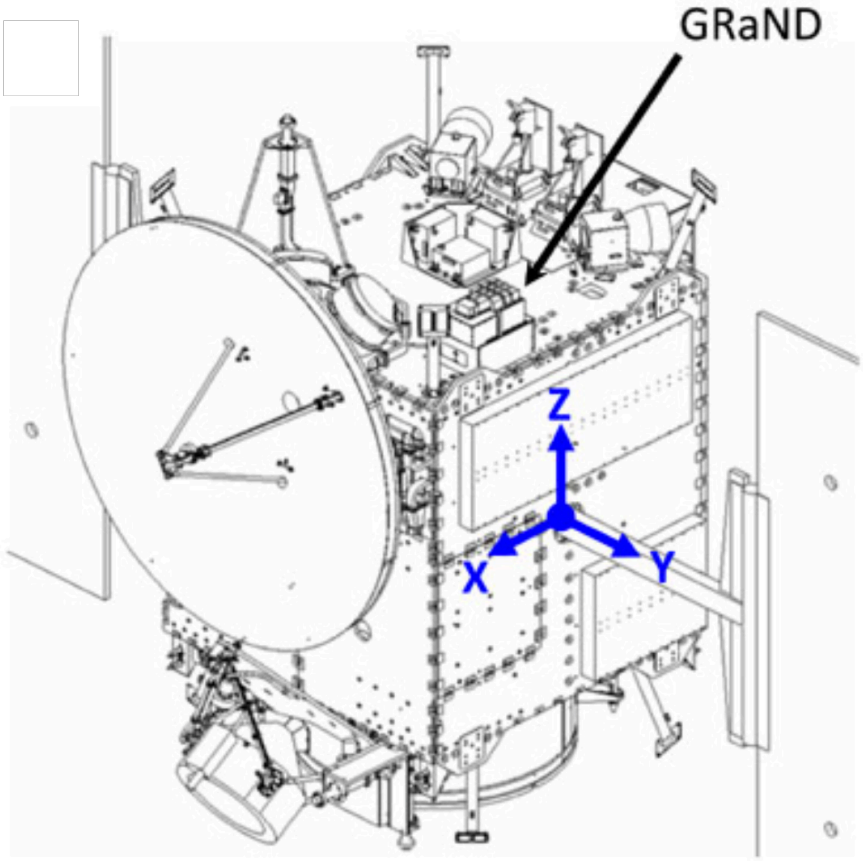

Figure 2.1 *Dawn's spacecraft coordinates: $+X_{spacecraft}$ points in the direction of the high gain antenna, $+Z_{spacecraft}$ points in the direction the science instruments are mounted on, and $+Y_{spacecraft}$ points along the solar panel that completes the right hand set. The GRaND instrument is located on the +Z face of the spacecraft. During data acquisition, the +Z axis is pointed nadir. Figure from Prettyman et al. (2011).*

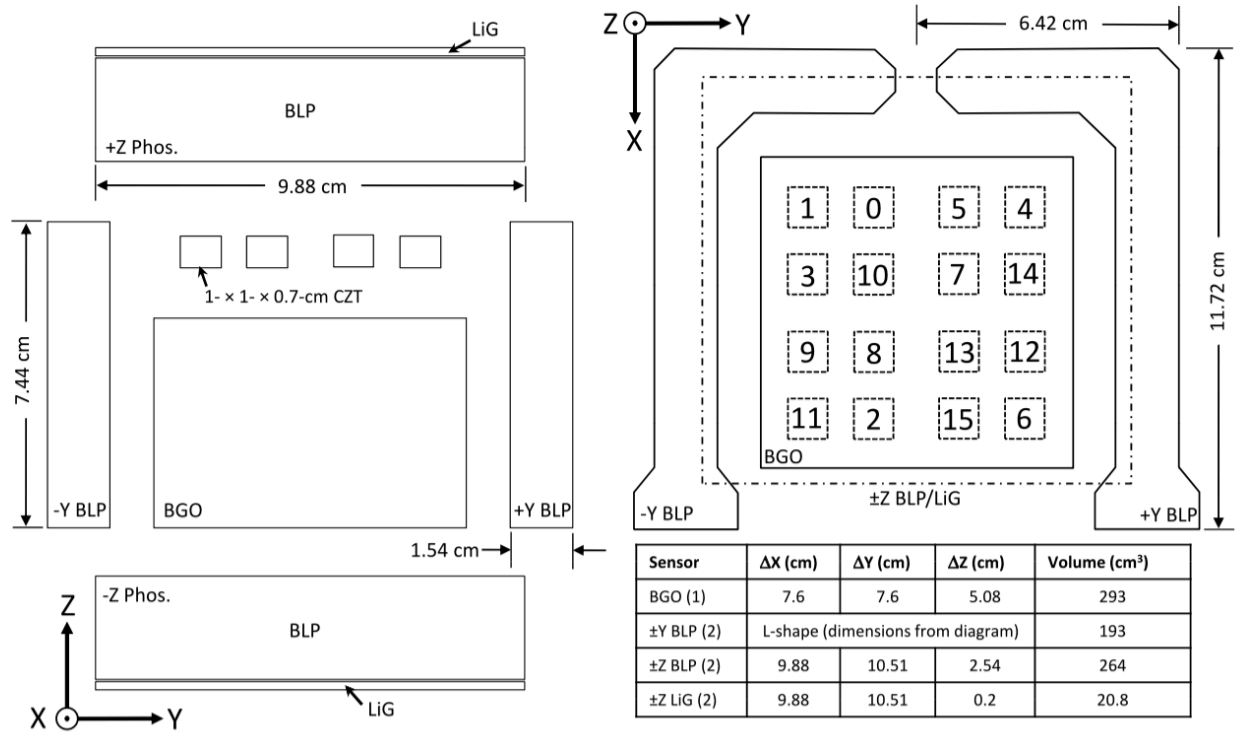

Sensor	ΔX (cm)	ΔY (cm)	ΔZ (cm)	Volume (cm³)
BGO (1)	7.6	7.6	5.08	293
±Y BLP (2)	L-shape (dimensions from diagram)			193
±Z BLP (2)	9.88	10.51	2.54	264
±Z LiG (2)	9.88	10.51	0.2	20.8

Figure 2.2 *The arrangement of Dawn's Gamma Ray and Neutron Detector (GRaND) shown in spacecraft coordinates. The +Z Phoswich points nadir during data acquisition while the –Z Phoswich is located on the face of GRaND mounted onto the spacecraft. The -/+ Y BLP scintillators are L-shaped and share a common face on the –X face of GRaND. Diagram from Prettyman et al. (2011).*

2.3 Identification of Energetic Particles

Both energetic protons and electrons that encounter GRaND leave a distinct signature, allowing for differentiation between the two particles. The type of particle interaction that occurs will depend both on the incident particle's mass and energy. The Gamma Ray and Neutron Detector is capable of sensing bremsstrahlung produced by electrons and gamma rays produced by inelastic collisions of energetic protons with spacecraft material.

2.3.1 Identification of Energetic Protons

Inelastic collisions of energetic protons with spacecraft material leave nuclei in an excited state. The nuclei then emit gamma rays which are detected by the central BGO or by the exterior scintillators through further particle interactions. Specifically, the proton particle interactions will cause an increase in counts in the 4.4 and 6.1 MeV elemental peaks (Carbon and Oxygen peaks respectively) of the BGO spectrum due to the composition of the spacecraft. The incoming protons must have energies greater than 4.4 and 6.1 MeV to produce gamma rays of these energies through inelastic scattering. Energetic protons may lose energy through other types of collisions before they inelastically scatter, and therefore modeling is needed to understand exactly what initial energy is needed. However, at this point in time the Dawn mission does not have the financial and time resources to conduct such modeling. Still, using 4.4 and 6.1 MeV as minimum energies should be sufficient.

All energetic protons observed thus far by GRaND have been associated with solar energetic particle events (SEPs). Energetic protons typically cause the largest enhancement in the CAT1 +Z Phoswich of GRaND, but they are simultaneously observed in all scintillators during a solar energetic particle event. Hence, SEP events are first identified by the large, days long

enhancement they cause in the total counts of the CAT1 +Z Phoswich (Figure 2.3). The elemental peak enhancements in the BGO spectrum are then used to validate the SEP events by confirming the expected radiation due to the proton interactions with the spacecraft.

Figure 2.4 shows the steps of the validation process. First a time window is identified for the proposed length of the SEP event. To verify the count increases to the carbon and oxygen elemental peaks, the proposed event needs to be compared relative to the background. A background window consisting of 500 consecutive data points is chosen immediately preceding the SEP window (or after if the data prior to the SEP event is not available). The top panel of Figure 2.4 shows the time series for the total counts of the BGO spectrum during an event that occurred June 18, 2015. The large jump in total counts is defined as the SEP window, shown in red, and a background window is specified, shown in black. The BGO spectra over these windows are averaged to eliminate noise and resolve the elemental peaks, shown in the middle panel. The averaged background spectrum is then subtracted from the averaged SEP spectrum to identify which channels, if any, experience increases in counts. Channel numbers of the BGO spectrum can be converted to energy by using the relation Energy(keV)=8.9*channel (Yamashita and Prettyman, 2015). The bottom panel of Figure 2.4 shows strong enhancements in counts near 4.4 MeV with minor enhancements near 6.1 and 6.9 MeV. This corresponds to the excited energy levels of C and O, indicating energetic protons are present. In cases where energetic protons are not present, there will be no discernable difference in the elemental peaks between the averaged background spectrum and the averaged spectrum for the defined SEP period.

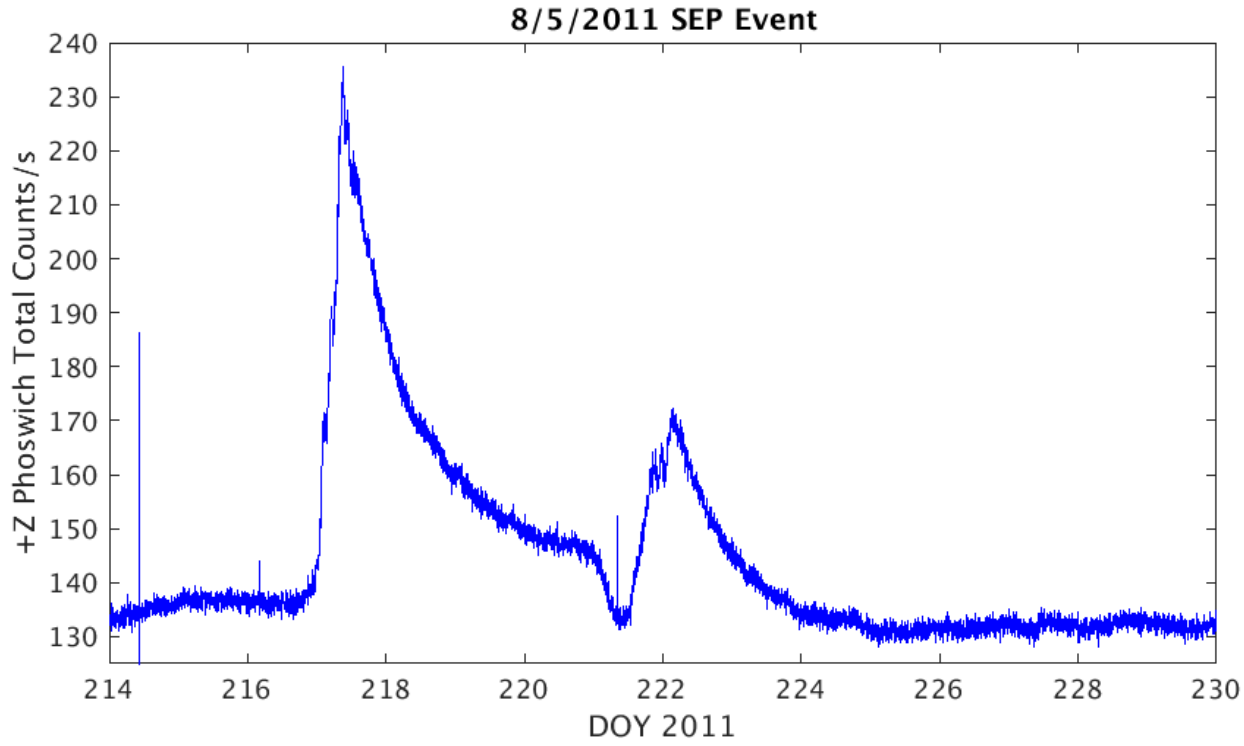

Figure 2.3 *Two consecutive SEP events observed by the +Z Phoswich. SEP events are identified as large jumps in the total counts of the +Z Phoswich, typically lasting days. The presence of energetic protons is then confirmed by the increases in the carbon and oxygen elemental peaks of the BGO spectrum.*

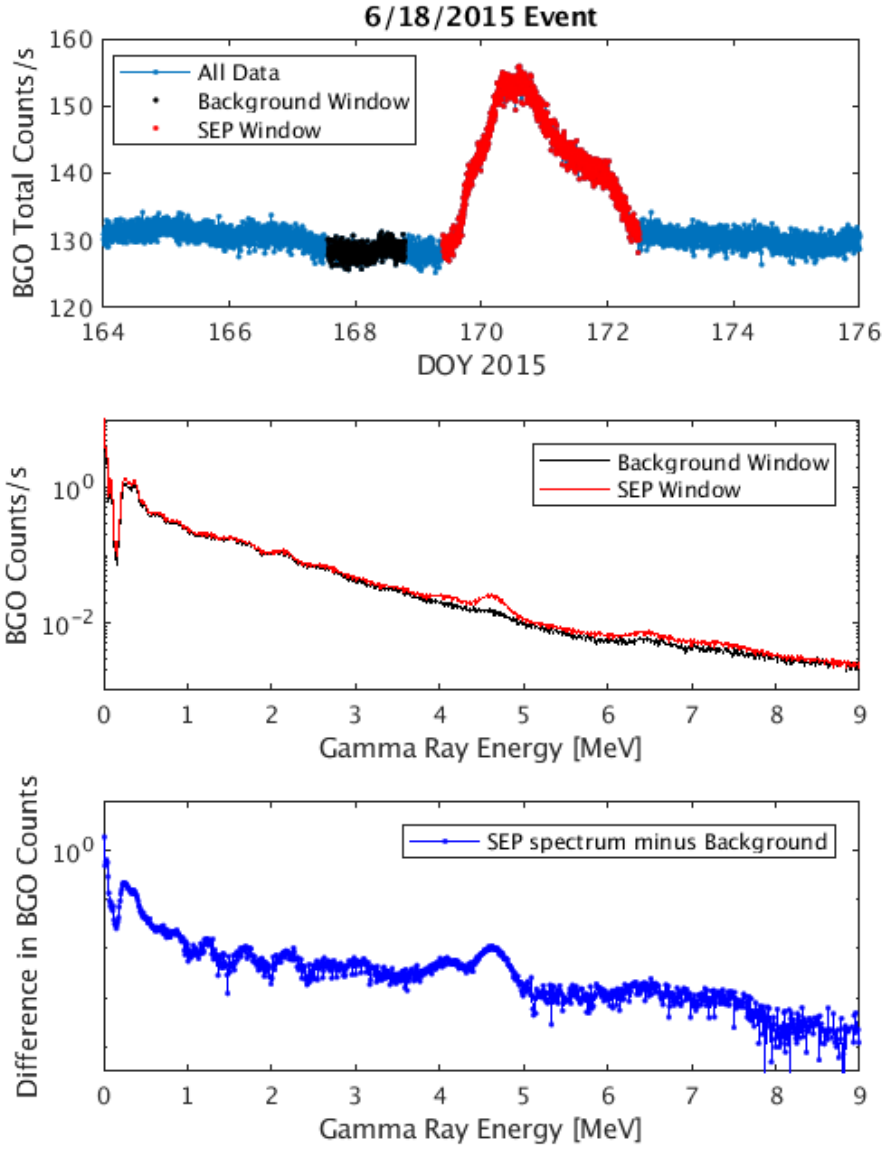

Figure 2.4 *Identification of energetic protons. Top: SEP (red) and background (black) windows are specified for comparison. Middle: The BGO spectra of the respective windows are averaged to resolve elemental peaks. Bottom: the averaged background BGO spectrum is subtracted from the SEP spectrum to identify enhancements in the C and O elemental peaks. In this example, clear enhancements in counts can be seen ~4.4 MeV corresponding to proton interactions with Carbon.*

Though the energies of the gamma rays produced by inelastic scattering are too high to directly be detected by the exterior scintillators, secondary Compton scattering of the gamma rays produces radiation at lower wavelengths which are then sensed by the exterior scintillators. The resulting wavelength will be dependent on the angle at which the photon is scattered and can be described by the equation:

$$E_f = \frac{E_i}{1+\frac{E_i}{m_e c^2}(1-\cos\theta)}$$

Where E_f is the final energy of the photon, E_i is the initial energy of the photon, $m_e c^2$=0.511 MeV is the rest mass of the energy of electrons. For a 4.4 MeV gamma ray emitted by a Carbon atom, scattering angles 0 to 180 degrees result in photons with energies 241 keV-4.4 MeV, well within the exterior scintillators detection range of 20 keV-2.55 MeV. Thus, the Compton scattering of a 4.4 MeV gamma ray alone can create enhancements across almost all of the energy channels of the exterior scintillators. Figure 2.5 shows an example of increases in counts across all the energy channels during a solar energetic particle event. The energy each +Z Phoswich channel corresponds to can be calculated by Energy(keV)=(2.41*channel)+42.5 (Prettyman et al., 2011). A method similar to that used for the BGO is employed to identify the channels the enhancements in counts reside. The increase at energies lower than 240 keV are likely caused by gamma rays produced by inelastic scattering of lower mass atoms found within the spacecraft.

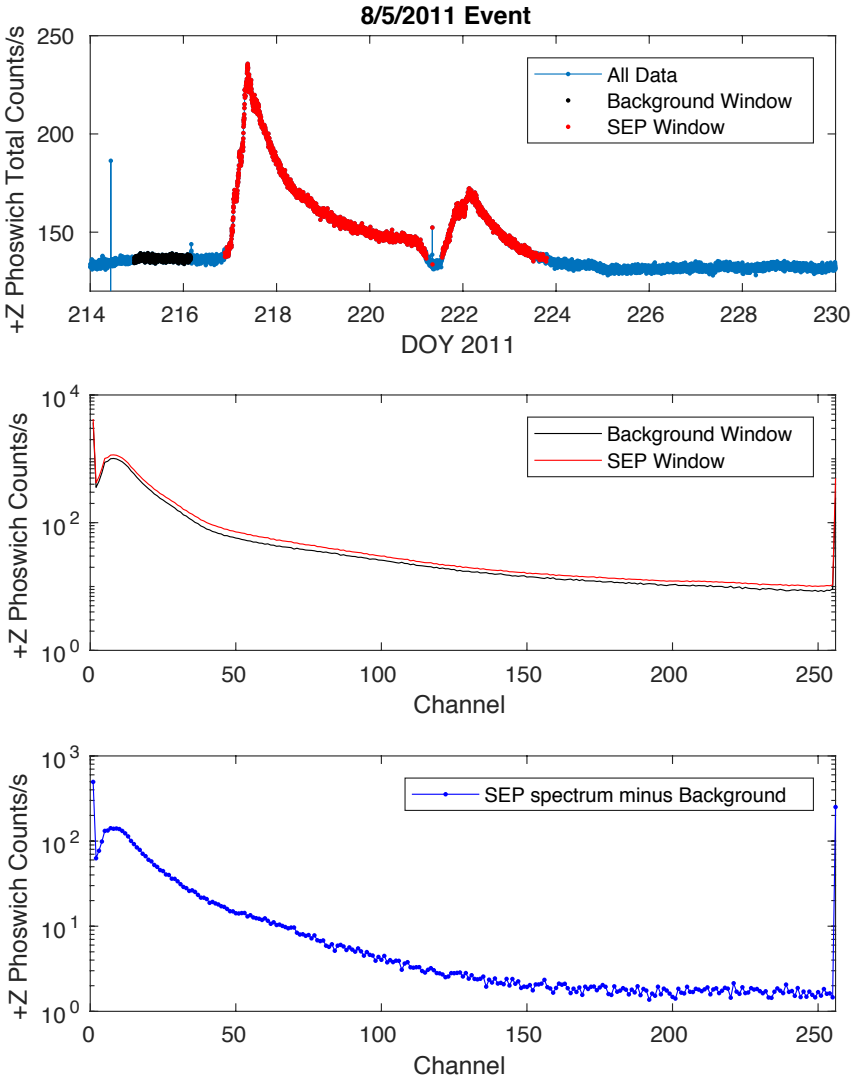

Figure 2.5 *SEP event detected by the +Z Phoswich. Top panel: The SEP window (red dots) and background window (black dots) are defined. Middle panel: The SEP (red) and background (black) windows are averaged to produce their spectra. Bottom panel: subtraction of the background window from the SEP window shows increases in counts across all energy channels. Inelastic scattering of spacecraft material produces gamma rays which can then undergo Compton scattering to produce wavelengths detectable in the exterior scintillators. This creates enhancements across all energy channels of the exterior scintillators.*

2.3.2 Identification of Energetic Electrons

Energetic electrons impacting the spacecraft are forced to decelerate, causing them to emit bremsstrahlung. The radiation is fully absorbed in the exterior scintillators for electron energies less than 2 MeV, but may reach the BGO for energies greater than 2 MeV (Russell et al., 2016, supplemental material). Since 2 MeV electrons are scarce, the presence of energetic electrons are typically characterized by an enhancement in counts in the exterior scintillators while the BGO observes no change. It is important to note that the –Z Phoswich detector is located on the face of the instrument mounted to the spacecraft, making it difficult for electrons to reach the detector. Therefore, the signal caused by electrons impinging on the –Z Phoswich is generally muted or below the noise level.

Effects on the spacecraft from energetic electrons produced by SEPs have not been established. This could be due to the flux of the electrons being too low or due to the protons overpowering the increase in counts in the exterior scintillators. Hence, energetic electrons can only be identified when not originating from SEP events. Energetic electrons observed by GRaND are characterized as short-lived jumps in the total counts of the exterior scintillators. This complicates their identification since the exterior scintillators also experience quick spikes in counts due to gamma ray bursts and instrument artifacts.

We identify energetic electrons using a method established by Lawrence et al. (2015), who identified the presence of energetic electrons at Mercury using the Gamma Ray and Neutron Spectrometer on MESSENGER. A background window immediately preceding or following the spike event is specified and an average spectrum over that window is produced. Subtraction of the background spectrum from the spectrum due to the spike indicates which energy bins the enhancements in counts reside. The range in energy of the electrons can be found by looking at

the pulse height spectrum for the +Z Phoswich: the channels the enhancements occur in will correspond to the electron energy of the impinging particles. Figure 2.6 Column C shows the pulse height spectrum when energetic electrons were present. Analysis of these spectra show that the enhancement in counts is restricted to channels 20 (91 keV) and below, corresponding to electron energies less than 100 keV, consistent with an energy range we would expect for electrons. With a threshold energy of 20 keV, this gives an energy range for the electrons of 20-100 keV. Since the BGO has a threshold energy of 300 keV, it does not detect the radiation produced by the electrons. Assuming all the kinetic energy from the electrons goes into producing bremsstrahlung, 20-100 keV electrons would produce X rays with wavelengths 0.0124 to 0.062 nm.

The data is further scrutinized to rule out gamma ray bursts and instrument artifacts as the sources for spikes in counts in the +Z Phoswich. Column A of Figure 2.6 exhibits a spike caused by an instrument artifact. These spikes are single-point enhancements in the total counts accompanied by a single-point decrease of equal value (not shown). Analysis of spikes due to artifacts show that they cause consistent increases in counts across all channels and do not show a fall-off with higher energies, inconsistent with the expected distribution of electrons and can be ruled out.

Gamma ray bursts, on the other hand, show a fall-off in the increase in counts with increasing energy and appear similar in signature to energetic electrons (Figure 2.6 column B). However, like the instrument artifacts, gamma ray bursts only last one sampling cycle and appear as single point enhancements. Gamma ray burst events are well documented and monitored. We refer to the gamma ray burst catalogues available (Gruber et al., 2014) to identify which events can be attributed to gamma ray bursts.

Comparisons of the gamma ray burst and the electron bursts signatures shown in Figure 2.6 have subtle differences. The energetic electrons have a narrower distribution in their energy range and show a sharp cutoff after channel 20 (91 keV). The increase in counts caused by the gamma ray burst is much broader and increases counts in channels up to ~channel 75. In addition, artifacts and gamma ray bursts are recorded as single-point enhancements in the total counts while energetic electrons are typically observed over several consecutive sampling cycles (Figure 2.6). Once instrument artifacts and gamma ray bursts are ruled out as sources, the remaining explanation for the spike in counts is bremsstrahlung radiation from electrons.

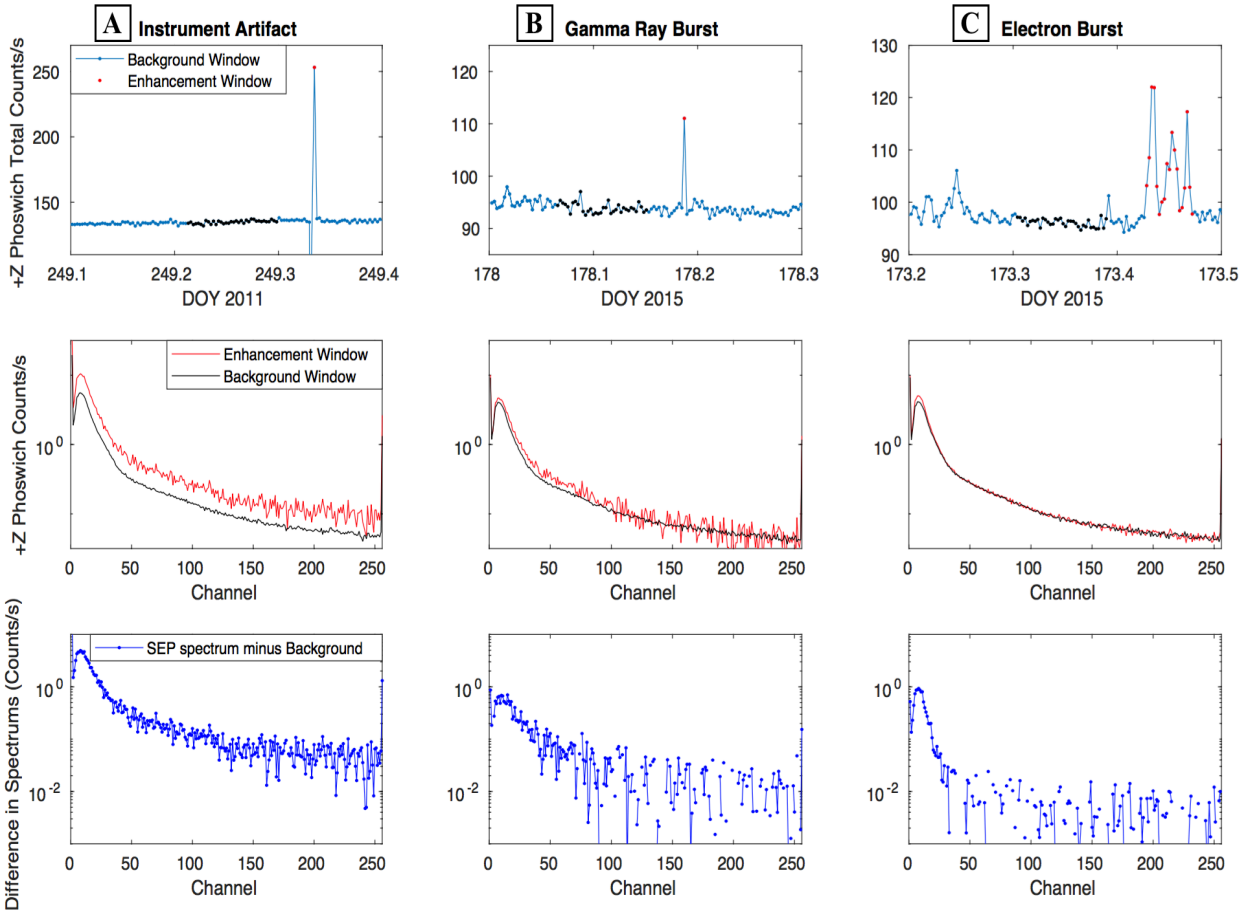

Figure 2.6 *Three panel plots for different types of count spikes. The first panel shows the total count rate of the +Z Phoswich scintillator with the background window denoted by the black dots and the enhancement region denoted by red dots. The second panel shows the average spectra for these respective windows. Subtraction of the background window (black spectrum) from the enhancement window (red spectrum) identifies which energy channels the increase in counts reside. This analysis is shown for a) instrument artifact, b) Gamma Ray Burst, c) Electron burst.*

2.4 GRaND's Sensitivity to Magnetic Fields

The photomultiplier tube attached to the BGO scintillator is unshielded allowing it to be influenced by strong magnetic fields. Due to the VxB force, a magnetic field can affect the output of a photomultiplier tube (PMT) by deflecting the photoelectrons as they travel from the photocathode to the first dynode. The amount of deflection, and thus its sensitivity, will strongly depend on the distance the electron has to travel from the photocathode to the first dynode. This distance is typically proportional to the diameter of the photomultiplier tube (Hamamatsu Photonics, 2010). At 2 inches, the diameter of GRaND's BGO PMT is larger than average making it more sensitive to magnetic fields than most spacecraft photomultiplier tubes. This can be used to detect strong magnetic fields near Dawn.

Figure 2.7 shows the change in the output of the photomultiplier tube in the presence of magnetic fields of differing strength and direction in spacecraft coordinates (photomultiplier tube data provided by Hamamatsu Photonics). Due to its arrangement, the output of the PMT varies with which axis of the tube the magnetic field is aligned. The BGO PMT is most sensitive to magnetic fields parallel to the $Y_{spacecraft}$ axis and is affected by magnetic fields on the order of microteslas.

If a magnetic field is parallel to the sensitive axis, it will cause the electrons to either focus toward or deflect away from the first dynode and affect the output of the PMT. The output amplitude of the PMT is then measured by the analog-to-digital converter, and counts are placed at either higher or lower energy bins than they should for the given gamma ray energy. The resulting gamma ray spectrum will have corresponding shifts in the prominent elemental peaks relative to their undisturbed locations. The amount of shift in the elemental peaks relative to their positions in the absence of a magnetic field can be calculated and the strength of the magnetic

field can be inferred.

Magnetic field sources such as the solar wind or spacecraft instruments will not affect the spectrum. The solar wind is too weak (~few nanoteslas) to substantially deflect the electrons in the photomultiplier tube and can be ignored. To ensure magnetic fields originating from the spacecraft instrument are constant, data can be selected when the spacecraft is only operating at its nominal settings. This will result in no net shift and the spacecraft magnetic fields can be ignored. Hence, shifts in the elemental peaks of the BGO can then only be caused by strong magnetic fields originating from the body Dawn is observing.

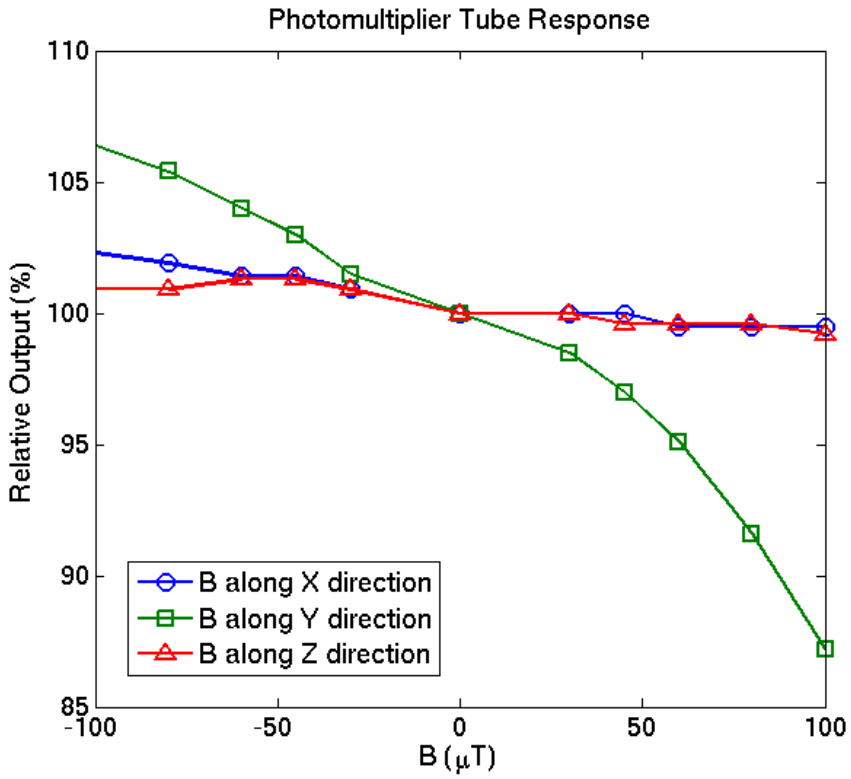

Figure 2.7 *Response of the photomultiplier tube to magnetic fields of various strengths and directions. The output of the photomultiplier tube is only greatly affected when the magnetic field is aligned with the spacecraft's Y-axis. Data provided by Hamamatsu Photonics.*

2.5 Summary

Though GRaND is configured to measure radiation produced by particle interactions from planetary gamma rays and neutrons, additional effects from energetic protons, electrons, and magnetic fields on the instrument can be used to infer their presence. Radiation produced by inelastic collisions of protons with the spacecraft affect all of GRaND's scintillators and encounters can be confirmed by identifying increases in the carbon and oxygen peaks of the BGO spectrum. A minimum proton energy of 4.4 MeV is needed to induce these inelastic collisions. Bremsstrahlung produced by energetic electrons only affect the exterior scintillators and do not cause enhancements in the total counts of the BGO. The threshold energy for detection by the exterior scintillators is 20 keV, requiring electrons to have energies above this. Increases in counts below channel 20 (91 keV) of the +Z Phoswich can be used to infer the presence of electrons. Strong magnetic fields can also be identified by recognizing shifts in the prominent elemental peaks of the BGO spectrum.

2.6 References

Gruber et al., The Fermi GBM Gamma Ray Burst Spectral Catalog: Four Years of Data, The Astrophysical Journal Supplement Sereies, Vol 211, 12 (2014).

Lawrence, D. J. et al., Comprehensive survey of energetic electron events in Mercury's magnetosphere with data from the MESSENGER Gamma-Ray and Neutron Spectrometer, JGR: Space Physics, 120, 2851-2876 (2015).

Photomultiplier Tubes: Photomultiplier Tubes and Related Products, Hamamatsu Photonics K. K., 2010.

Prettyman, T.H. et al., Dawn's gamma ray and neutron detector, *Space Sci. Rev.* **163**, 371-459

(2011).

Prettyman, T.H., Remote Sensing of Chemical Elements Using Nuclear Spectroscopy, in Encyclopedia of the Solar System, edited by T. Spohn, D. Breuer, T. V. Johnson, 1161-1183 (2014).

Russell, C. T. et al., Dawn arrives at Ceres: Exploration of a small, volatile-rich world, Science, Vol 353, 1008-1010 (2016).

Yamashita, N. and T. H. Prettyman, Dawn's Gamma Ray and Neutron Detector: BGO Data Processing, https://sbn.psi.edu/archive/dawn/grand/DWNC4GRD_1A/DOCUMENT/BGO_DATA_PROCESSING/GRD_L1B_BGO_DATA_PROCESSING_V4_1.PDF, (2015).

Chapter 3

Constraining the Surface Magnetic Field of Vesta Using Dawn's Gamma Ray and Neutron Detector

3.1 Introduction

Howardite, Eucrite, and Diogenite (HED) meteorites are ferromagnetic due to FeNi grains contained within the rock (Nagata, 1979). The local magnetic field at the time of formation is recorded by the electron spins of the ferromagnetic grains which align with the magnetic field as the rock is cooling and becomes frozen-in once the rock solidifies. The strength of this remanent magnetization will depend on the rock's magnetic susceptibility, χ. Experiments have shown Eucrites and Diogenites have similar average magnetic susceptibilities with log χ~3 while the average susceptibility for Howardites is slightly higher at log χ ~3.3, where χ is in units of 10^{-9} m^3/kg (Rochette et al., 2009).

As mentioned in Chapter 1, several HED meteorites were found to possess remanent crustal magnetization on the order of ten microteslas, implicating crustal fields exist on the surface of Vesta (Fu et al., 2012a; Fu et al., 2012b). Due to the absence of a magnetometer onboard Dawn's payload, the Dawn spacecraft is incapable of directly measuring Vesta's predicted crustal fields. However, Dawn's Gamma Ray and Neutron Detector is sensitive to both magnetic fields and energetic particles, potentially allowing us to sense Vesta's crustal fields via two indirect methods. The first is by analyzing shifts in the elemental peaks of the BGO spectrum which will vary in the presence of a magnetic field (as described in Chapter 2). The second is by observing by-products of the interaction of the crustal fields with the incoming solar

wind. Lunar spacecraft have utilized electron reflectometry to map the surface crustal fields at the moon (Howe et al., 1974; Lin, 1979; Mitchell et al., 2008). Incoming solar wind electrons encountering a region of a magnetized crustal field are magnetically mirrored and stream back toward the spacecraft and subsequently detected. Similarly, if the surface magnetic field is strong enough to produce a bow shock, energetic electrons that cannot conserve their magnetic moment across the shock will get reflected at the shock surface and form an electron foreshock (Wu, 1984; Leroy and Mangeney, 1984). If the orbit of the spacecraft intersects the electron foreshock they will be detected as bursts. In both cases, reflected energetic electrons encountering the spacecraft can be identified as increases in the total counts of the exterior scintillators.

3.2 Short Enhancements in Counts of the Exterior Scintillators at Vesta

3.2.1 Burst Properties

While Dawn was at Vesta, it saw numerous sudden, large spikes in counts in its exterior GRaND scintillators. Spikes were identified as enhancements at least four standard deviations above the background in the +Z Phoswich scintillator. The majority of these bursts were single-point enhancements that could be identified as either instrument artifacts or as gamma ray bursts using the methods described in Chapter 2. However, twelve of the bursts could not be explained in this way, listed in Table 1. Given that the bursts could not be explained by traditional explanations for sudden count rises, we inspected whether energetic electrons caused by the solar wind interaction with Vesta could explain them.

In contrast to instrument artifacts and gamma ray bursts, the spikes in counts persisted for several sampling cycles, with the jumps in total counts lasting ~5-20 minutes. The bursts occurred as isolated events with an average peak magnitude (after background subtraction) of

39.1 counts/s and a standard deviation of 28.4 counts/s. The spikes also appeared to show a preference for orbit location: they were detected during the Survey and HAMO 1 orbits, after which they disappeared until Dawn relocated back to the HAMO 2 orbit. Figure 3.1 shows the subspacecraft location at the instance of each burst in the Claudia coordinate system (Chapter 1). There appear to be four small clusters associated with the appearance of the bursts. The bursts in each cluster are not similar in magnitude and vary by more than a standard deviation.

Date	**Time (DOY)**
8/4/11	216.1632
8/9/11	221.3361
9/6/11	249.0757
9/6/11	249.9306
9/7/11	250.9431
9/8/11	251.6556
9/24/11	267.4021
11/2/11	306.9167
11/3/11	307.8514
6/2/12	154.1868
7/6/12	188.9632
7/10/12	192.5722

Table 3.1 *List of peculiar bursts observed in the +Z exterior scintillator while in orbit at Vesta.*

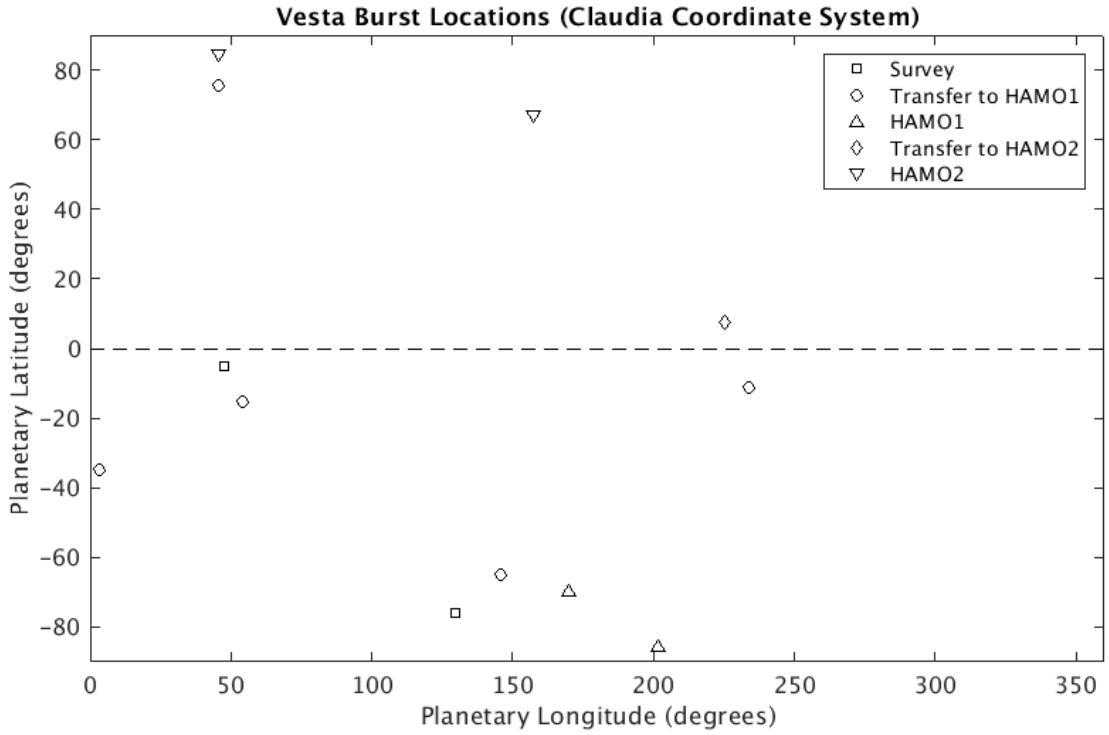

Figure 3.1 *The subspacecraft locations for each spike observed at Vesta in Claudia planetary coordinates. There appear to be four clusters in the locations at which the bursts appear.*

3.2.2 Inconsistency with Energetic Electrons

The +Z Phoswich detector points nadir during data acquisition and is optimum for detecting reflected electrons from crustal patches or a bow shock. We applied the method described in Chapter 2 to diagnose if these bursts could be attributed to energetic electrons (Figure 3.2). After subtracting the background windows from the burst windows, the spectra look similar to the electron signature with one caveat: the distribution in counts is broader than expected. We would expect the electron energy to be limited to 100 keV as this is the approximate cutoff for foreshock electrons at Earth and electrons detected through electron reflectometry become increasingly harder to detect for energies above 10 keV due to low fluxes. The increase in counts extends far beyond channel 20 (91 keV) and extends to as far as channel

50 (163 keV), showing a distribution intermediate between that characteristic for energetic electrons and a gamma ray burst.

Further analysis showed simultaneity of the +Z Phoswich bursts with bursts in the other exterior scintillators, and occasionally, even the central BGO scintillator (Figure 3.3). The appearance of the bursts in the BGO is inconsistent with energetic electrons. Electrons would require a minimum energy of 2 MeV to produce bremsstrahlung capable of reaching the BGO scintillator, thereby causing an increase in counts (Russell et al., 2016, supplementary material). This is a much higher energy than we would expect to be present in large enough fluxes to affect the BGO scintillator. In addition, scrutiny of the Ceres data revealed that bursts with the same characteristics but smaller in magnitude were also present, indicating these bursts are not Vesta specific. Ceres does not possess a metallic core and therefore incapable of producing a past dynamo nor crustal fields.

3.2.3 Identification of Solar X-Rays

Though these bursts have a signature very similar to energetic electrons, they cannot be explained by the particle interaction with the spacecraft and demand an alternative explanation. The GRaND instrument is a radiation detector sensitive to X-rays, and thus solar X-Rays produced by flares could theoretically interact with the instrument and cause short-term bursts. Vesta was near opposition with Earth during a majority of the burst events, allowing us to use the X-Ray Sensor (XRS) aboard GOES 15 to probe the solar activity in the region. GOES measures radiation in two wavelength bins: 0.1-0.8 nm and 0.05-0.4 nm. The latter energy bin overlaps with the threshold wavelength detectable by GRaND of 0.062 nm and therefore we use this energy bin for our analysis.

Figure 3.4 shows a comparison of the time series for GOES 15 and the +Z Phoswich during a burst event. Though the instruments differ in resolution, it can be seen that the peak magnitude of the burst at Vesta occurs ~10 minutes after the peak magnitude of the flare detection by GOES, consistent with the travel time of the speed of light from 1 AU to 2.4 AU. Each of the twelve burst events identified at Vesta have a corresponding solar flare detected at 1 AU which occurs ~10 minutes prior to the detection by Dawn. However, the corresponding solar X-ray events generally lasted about 20 minutes while the bursts at Vesta lasted ten minutes on average (Figure 3.4). We explain the reason for this later in the section.

Figure 3.5 shows a time series of the GOES 15 data for the 0.05-0.4 nm bin while Dawn was in orbit about Vesta. The top panel highlights the instances when the Vesta bursts were detected (red dots) and the bottom panel displays the separation in heliolongitude of Vesta and Earth with time. Early in the mission when Vesta and Earth were close to radial alignment, Vesta detected bursts immediately after the greatest intensity X-Rays were observed by GOES. During HAMO 2 in June and July 2012 the heliolongitude is too large to use GOES 15 as a proxy. However, for the 2012 events where GOES cannot be used as a proxy, an M-class flare is reported on July 6, 2012 and an X-class flare is reported for July 10th, 2012 in the SolarSoft solar flare catalogues (http://www.lmsal.com/solarsoft/latest_events_archive.html).

Figure 3.5 suggests there is an intensity threshold of ~$1x10^{-5}$ W/m^2 the solar X-rays must exceed to be detectable by GRaND. These intensities correspond to M-class and X-class solar flares. There are only two instances when GOES 15 recorded an irradiance greater than this value in 2011 without a corresponding GRaND detection. One event occurred during a period of corrupt GRaND data, and hence bursts could not reliably be identified. The other event had an

intensity near the threshold limit of GRaND and was likely not strong enough to cause counts above the background.

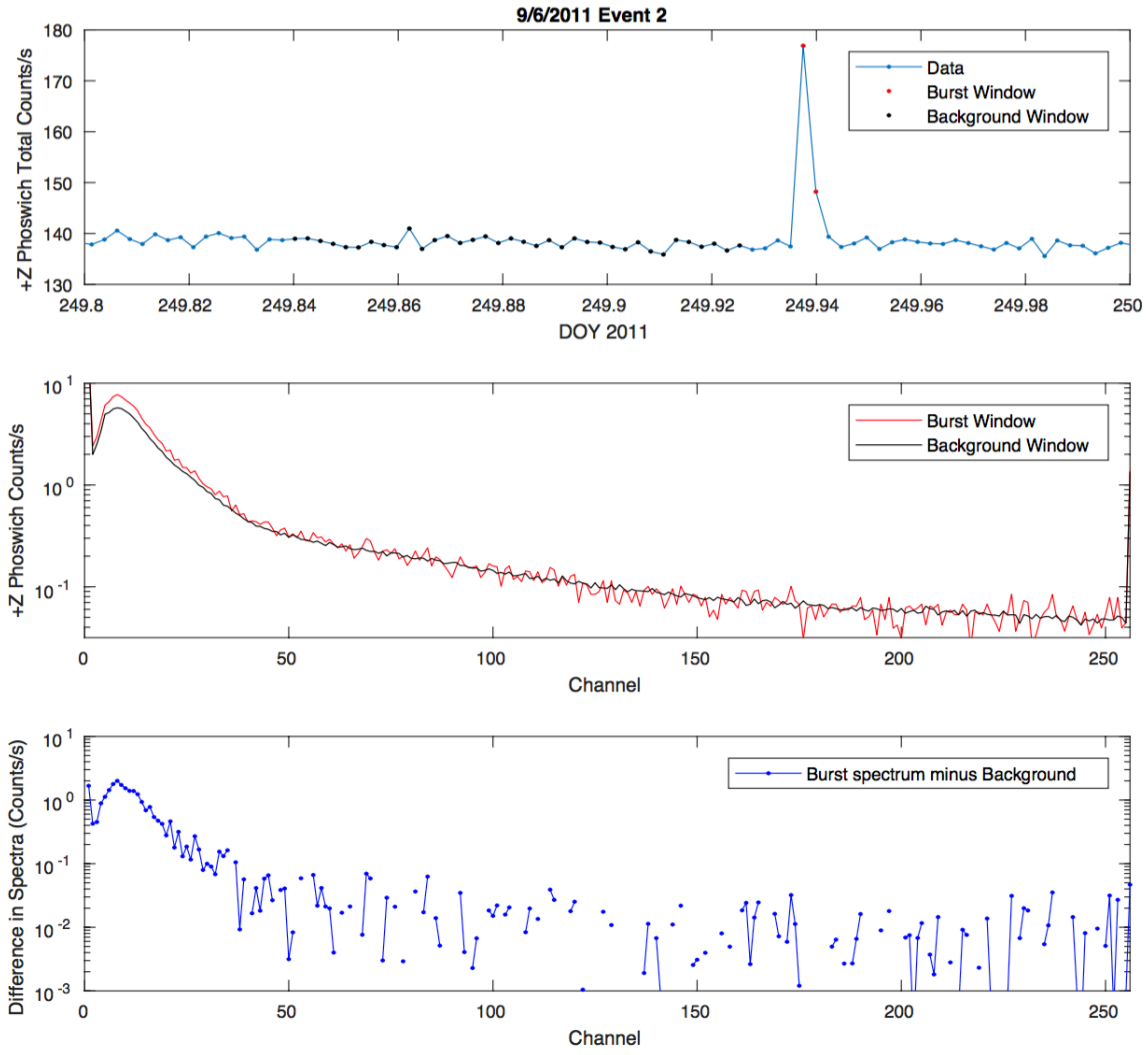

Figure 3.2 *Analysis of the bursts at Vesta. Top panel: the spike window (red) and the background window (black) are defined. Middle panel: Each window is averaged to produce a spectrum for the spike window (red) and background (black). Bottom: the background spectrum is subtracted from the spike spectrum to show which channels the enhancements in counts reside. The increased counts of the bursts are concentrated in channels 50 and below, showing a distribution intermediate between that of energetic electrons and gamma ray bursts.*

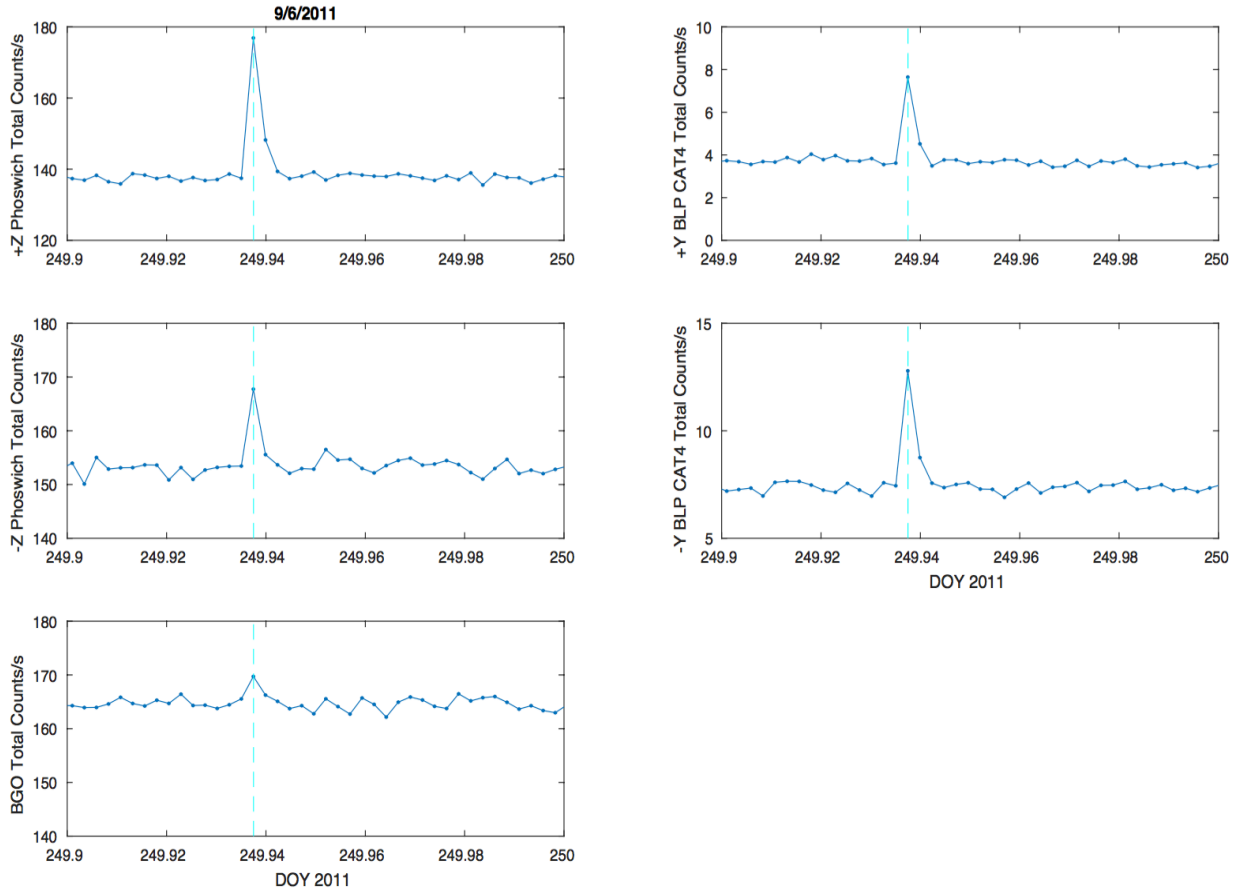

Figure 3.3 *Response of each GRaND scintillator during the 9/6/2011 event. The dashed cyan line shows simultaneous enhancements in each detector, including the BGO. This is inconsistent with energetic electrons as they require unrealistic energies cause a response in the BGO.*

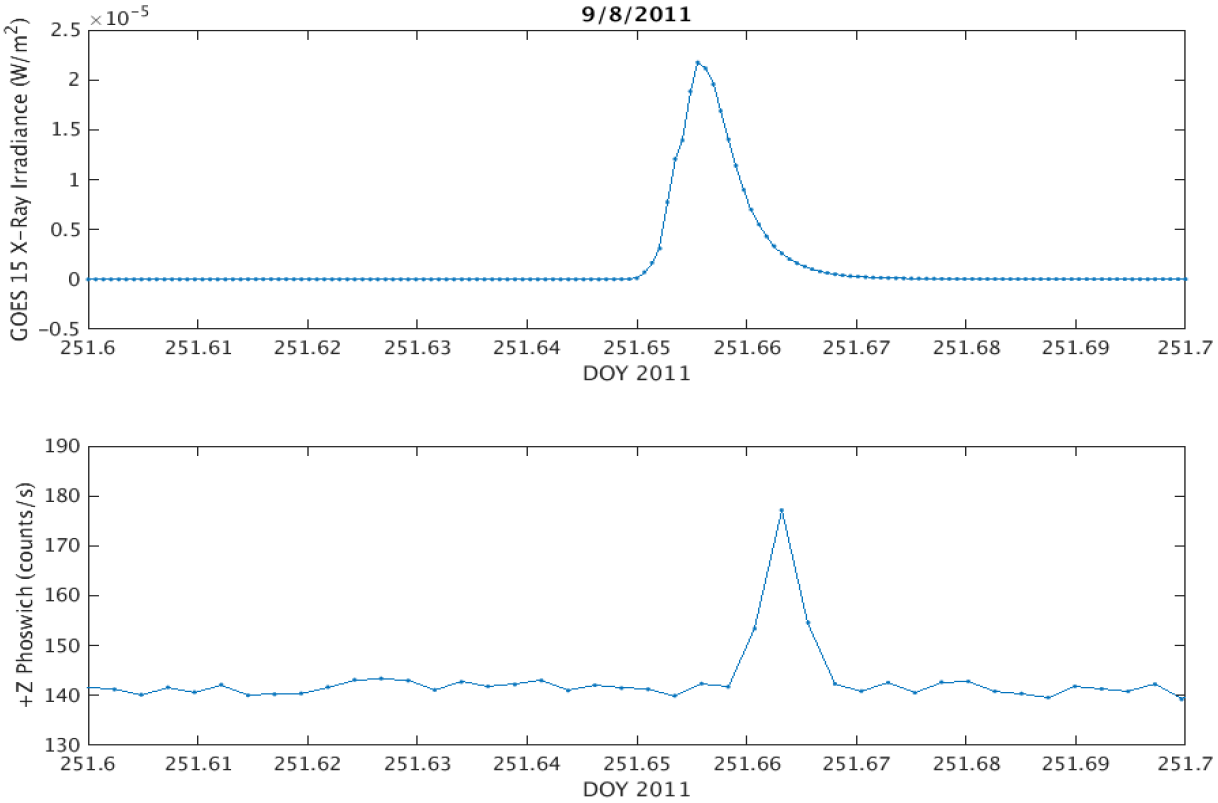

Figure 3.4 *Comparisons of a solar flare observed by GOES 15 in the 0.05-0.4 nm bin (top panel) and a detected burst at Vesta (bottom panel). The peaks of the events are offset by 10 minutes, consistent with the travel time of the speed of light from Earth's distance to the Vesta.*

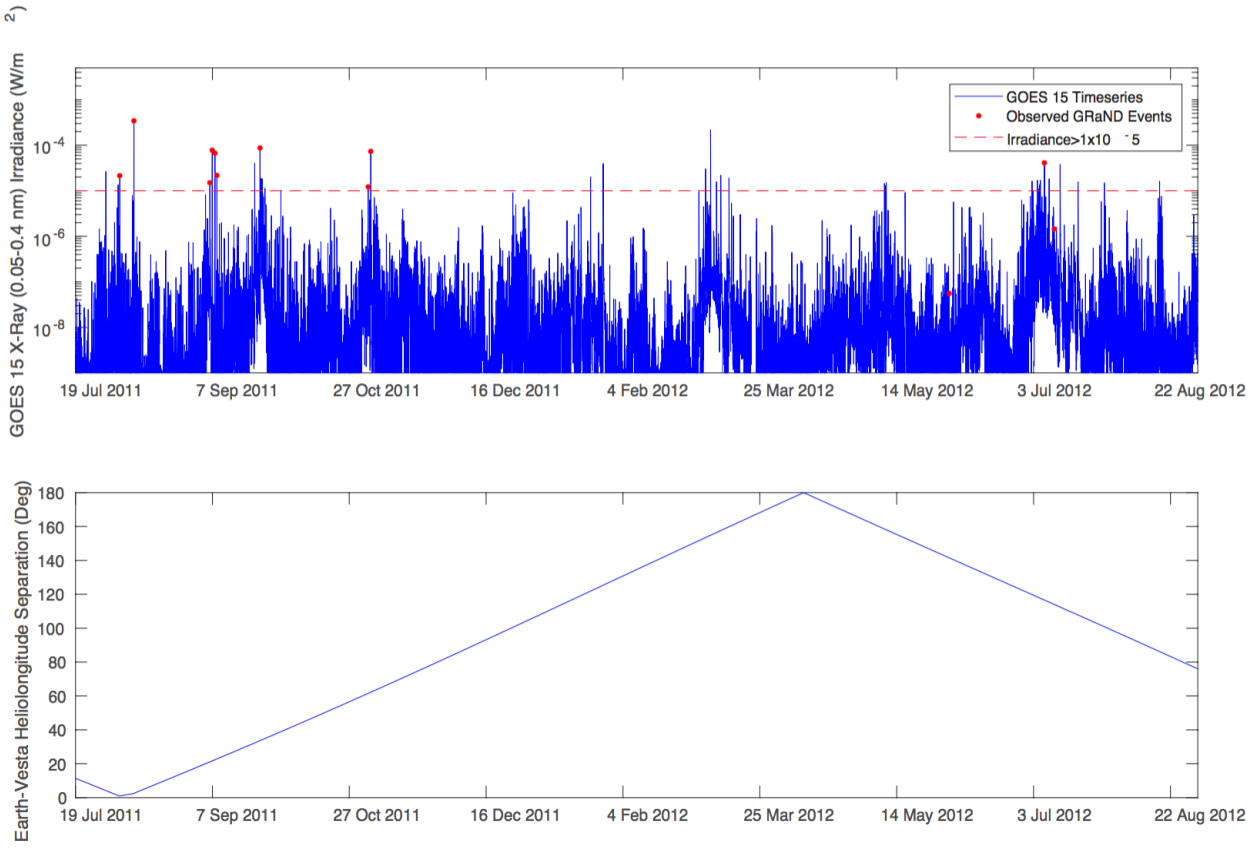

Figure 3.5 *Top panel: Time series of GOES 15 0.05-0.4 nm X-Rays (blue line) while Dawn was in orbit about Vesta. Red dots highlight the instances that Vesta bursts were detected. The bursts appear to be detected when solar flares reach classes M and X flares. Bottom panel: Difference in heliolongitude between Earth and Vesta.*

Figure 3.6 plots the delay between the respective peaks of the GOES solar flare X-rays and the Vesta bursts during 2011 when their separation in heliolongitude was small. The expected time delay is shown as a solid blue line. The theoretical delay neglects separation in heliolongitude and calculates the delay purely based on the radial distances of the bodies to the sun: $\Delta t = (3x10^8 \text{ m/s})*(A_V-A_E)$, where A_V and A_E are the heliocentric distances of Vesta and Earth, respectively. The error bars of the delay are dominantly dictated by the time resolution of the GRaND data. Overall, the data agree very well with the expected time delay between the peaks when the planets are near radial alignment. It is important to note that comparisons between the two GOES 15 wavelength bins themselves show up to a few minutes difference in the arrival time of their peak magnitudes for the same events. As this cannot be due to a difference in the travel speeds, the solar flare is likely emitting a range of wavelengths over time causing the timing of the peak magnitude to be wavelength dependent. As previously mentioned, the GOES wavelength bin used in this analysis overlaps only partially with the lower end of the detectable energy range of the +Z Phoswich. This explains why not all points in Figure 3.6 reside directly on the theoretical delay line, despite knowing the precise travel time of light.

We also investigated the discrepancy in event duration between the Vesta bursts and the GOES X-Rays events. From Figure 3.5 we learned there is a minimum intensity for X-rays to be detectable by GRaND. Hence, we calculated the length of each GOES event using only the portion of the solar flare that exceeded the threshold irradiance of $1x10^{-5}$ W/m^2. Comparisons of the Vesta event lengths to their corresponding GOES event can be seen in Figure 3.7. The figure shows that the solar flare intensities last above the threshold limit between 5-15 minutes, similar to the event lengths observed at Vesta, though the event durations do not have a 1:1 ratio. Similar to the previous paragraph, the exact duration of the event likely varies with wavelength.

Therefore, we should not entirely expect the GOES and Vesta data to have a 1:1 duration profile since the wavelengths that nominally affect GRaND may differ from those contained in the 0.05-0.4 nm bin.

When we first started our study, we noted that there was a notable absence of bursts during the Low Altitude Mapping Orbit (LAMO). There are two factors contributing to the absence of bursts during the LAMO phase: the first is that there were likely not many solar flares directed toward Vesta that exceeded the threshold irradiance limit to be detectable by the GRaND instrument. Figure 3.5 displays that many of the Earth-directed flares were below the GRaND threshold during the LAMO phase (December 2011 to May 2012), indicating the sun to be only mildly active at that time. The second is the change in sensitivity of the GRaND instrument to solar flares during LAMO. The average background levels of GRaND increase from 135 counts/s during Survey orbit to 180 counts/s during LAMO due to a closer proximity of the spacecraft to Vesta. This change in background levels is larger than the average increase in counts provided by bursts (~40 counts/s). Additionally, there is also a cyclical variation in the LAMO background levels which cause the background to vary by another 20 counts/s. This large cyclical variation in counts is due to the oblateness and topography of the body that are amplified in the low altitude mapping orbit. The higher background levels and the cyclical variation would impose an even larger intensity threshold to properly identify bursts due to solar flares. Therefore, the apparent preference for the orbit location described in Section 2.1 can be explained by the observing bias due to both the lower detection sensitivity during the LAMO phase and the decrease in frequency of M- and X-Class flares during this period.

Though these bursts initially appeared to show the signature of electrons, this analysis has shown that intense solar x-rays can affect the GRaND instrument and produce a similar

signature. Prior to this study, it was not known that solar x-rays affected GRaND. All enhancements in counts at Vesta can now be explained as an artifact, gamma ray burst, or solar x-ray. Therefore, we conclude that there is no evidence for energetic electrons reflected by either crustal fields or a bow shock.

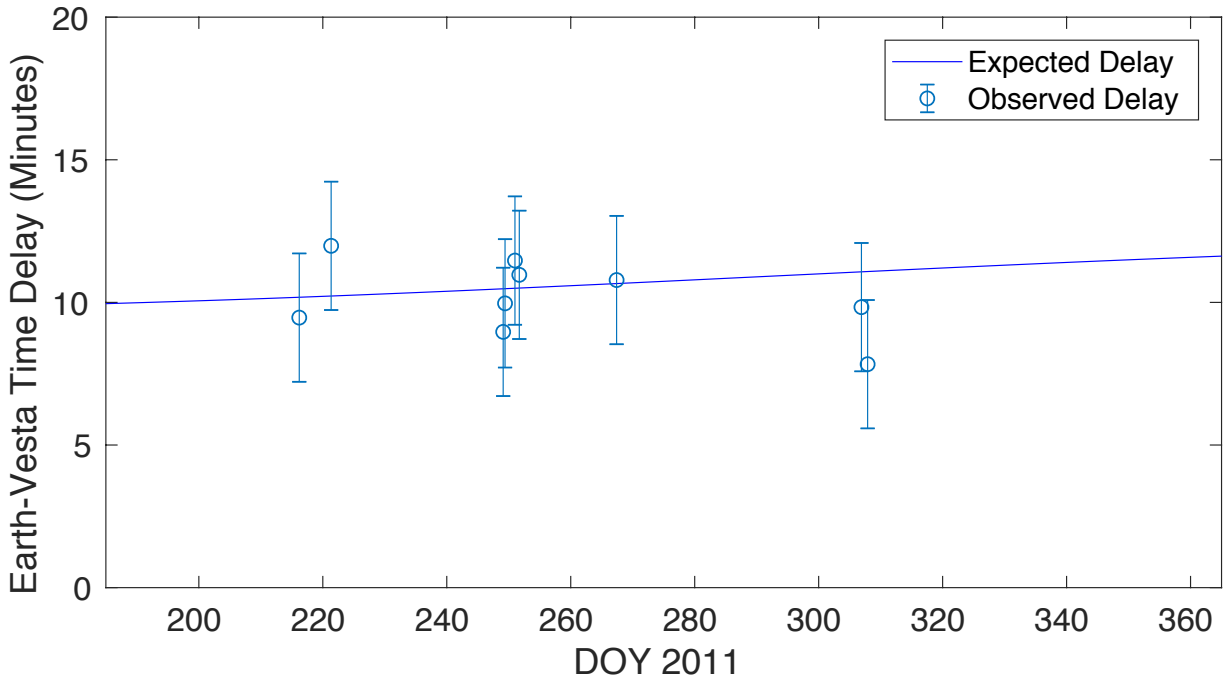

Figure 3.6 *Time delays between the peak magnitude of X-rays at GOES and the peak magnitude of bursts at Vesta. The delays are consistent with the expected delay in the speed of light (solid blue line).*

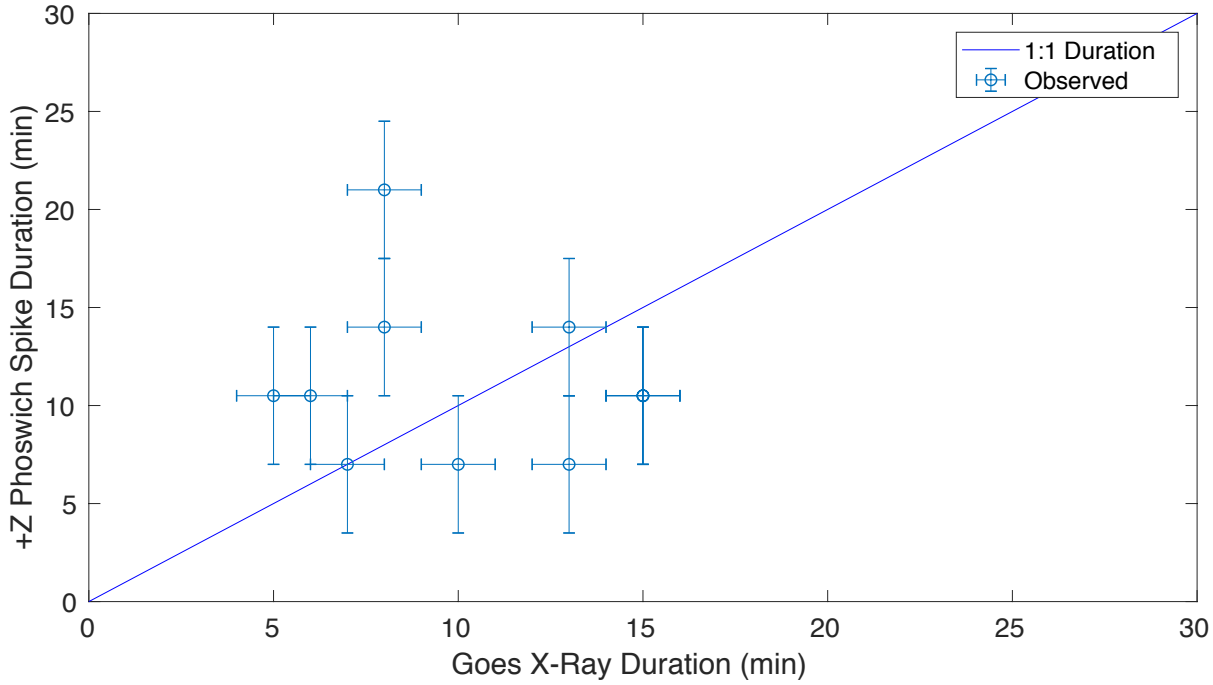

Figure 3.7 *Duration of the bursts observed by the +Z Phoswich and duration of the GOES X-Ray duration for magnitudes greater than the GRaND threshold of* $1x10^{-5}$ W/m^2.

3.3 Using GRaND's Photomultiplier Tube to Detect Crustal Fields

Chapter 2 covered how the photomultiplier tube associated with the Bismuth Germanate (BGO) scintillator of the GRaND instrument can be affected by strong magnetic fields. These fields can cause the electrons to deflect within the photomultiplier tube. For magnetic field strengths less than 100 μT, the photomultiplier tube is only affected when the field is parallel or antiparallel to the spacecraft's Y-axis. If the field strength is large enough, it can create measurable differences in the locations of the elemental peaks of the BGO spectrum. Here we attempt to use the variation in the gain of the photomultiplier tube as Dawn orbits Vesta as a proxy for any crustal fields that may be present.

The remanent magnetic field must be on the order of microteslas at the distance of the

low altitude mapping orbit (~200 km altitude) to cause measurable shifts in the elemental peaks of the spectrum. Though this seems unlikely, the magnitude of the surface field at Vesta is unknown. Only a handful of HED meteorites have provided estimates for the surface field and it is possible strong coherent regions of remanent magnetization exist. This experiment provides the opportunity to detect an unexpectedly large field, or at the very least, provide an upper bound for the surface field.

One particular drawback of this method is that we are only able to measure the magnetic field along the sensitive Y-axis. Since the sensitive axis of the photomultiplier tube is always parallel to the surface, it can only detect components in the parallel plane and cannot provide information on the radial component. Still, if a measurable shift is detected, it provides a constraint on the minimum field required.

3.3.1 Data Selection

Planetary magnetic fields are most readily identified by the fall-off in magnitude with radial distance. Since the spacecraft is emplaced in discrete circular orbits, a decay in the shifts of the elemental peaks back to their average position with increasing distance cannot be easily identified. Instead, we first approach this analysis by comparing instances when the sensitive axis of the photomultiplier tube is parallel and antiparallel to geographical locations on the surface during LAMO orbit. We focus on the LAMO orbit because this is when the spacecraft is closest to the body, thereby providing maximum sensitivity and allowing us to observe the strongest shifts in the BGO spectrum. Parallel alignment of the sensitive axis with a strong magnetic field will shift the elemental peaks to lower energy bins while antiparallel alignment will shift the elemental peaks to higher energy bins. If this trend is observed, the analysis can be

repeated for the HAMO orbit to try to identify a reduction in the signal due to an increase in distance. To guarantee the sensitive axis of the photomultiplier tube resides in a plane parallel to the planetary surface, we only use data where the +Z spacecraft axis is pointing within 10 degrees of nadir. This requirement inherently excludes periods where the spacecraft maneuvered to relay data to Earth.

The solar wind magnetic field is too weak (~few nanoteslas) to substantially deflect the electrons in the photomultiplier tube and can be ignored. However, the settings used for the spacecraft can vary, which can affect the strength of the magnetic fields originating from the instruments. Hence, data is selected for instances where the spacecraft operated at its nominal settings to ensure the background magnetic fields originating from instruments are constant during data acquisition and will result in no net shift of the data. Corrupt data and data containing outliers in external settings (i.e. temperature, triples counts, livetime, etc) have also been removed to not significantly skew the data.

The highest level L1B data products for GRaND are gain-corrected. Therefore, this study uses the L1A data products since we would expect a magnetic field to affect the gain outputted by the photomultiplier tube. The Analog to Digital converter (ADC) suffers from differential non-linearity (DNL), where the differences in channel width sizes of the ADC causes the channels to have different probabilities of detecting events (Yamashita and Prettyman, 2015). This effect is not corrected in the L1A data. The DNL of the ADC displays a systematic pattern that repeats every 32 channels for its variability in counts, which has been identified by Yamashita and Prettyman (2015). We apply their correction to the L1A data.

3.3.2 Identifying Locations of the Annihilation Peak

In this study, we use the intense electron-positron annihilation peak at 511 keV as our reference for the gain of the instrument since it has the highest counting statistics. Gamma ray data are normally averaged over 250 spectra adjacent in time to fully resolve the elemental peaks at higher energies. This corresponds to one complete LAMO orbit. This is not adequate for this project since we expect the remanent field to vary with geographical location and averaging over an orbit will wash away any signal. The 511 keV annihilation peak only requires a minimum of 5 spectra to resolve (Yamashita and Prettyman, 2015). To obtain an optimum trade between statistical accuracy and spatial resolution, we average over 33 spectra, which is about one tenth of Dawn's orbit. The product is an average spectrum centered on the subspacecraft location. This allows us to resolve local regions of remanent magnetization while still maintaining a sufficient signal to noise ratio to properly identify the annihilation peak.

The gamma ray peaks in the BGO spectrum are superimposed on a power-law background continuum. We must first subtract this power-law background to isolate the annihilation peak and determine its centroid position. To do this, we convert the data to a log-log scale and determine the background function using a line of best fit. In the L1A data, the annihilation peak is generally located at channel 36 during the LAMO orbit phase (Yamshita and Prettyman, 2015). We use channels 44-57 adjacent to the annihilation peak to fit the background function (except channels 47-51, which when globally averaged resolve a small elemental peak). The slope and intercept for the line of best fit are calculated and used to determine a fit for the power-law background:

$$m = \frac{\sum_{i=1}^{n}(X_i - \bar{X})(Y_i - \bar{Y})}{\sum_{i=1}^{n}(X_i - \bar{X})^2}$$

$$b = \bar{Y} - m\bar{X}$$

$$fit = 10^{b} Channel^{m}$$

where X=$\log_{10}$(Channel), Y=$\log_{10}$(Counts/s), $\bar{X}$ is the mean of X, and $\bar{Y}$ is the mean of Y. The left panel of Figure 3.8 shows an example of a fit to one of the spectra; the data used to determine the background fit are shown as cyan dots while the calculated background fit is shown as a solid green line.

Next, we subtracted the power-law function from the spectrum to isolate the annihilation peak (Left panel of Figure 3.8, open red circles). We fit the peak (Figure 3.8, right) to a single Gaussian probability density function to locate the peak position. The Gaussian fit uses a weighted least squares method developed by Guo et al. (2012). The gaussian function is solved by taking the natural log of the data and solving a linear set of equations for the resulting parabola. This fitting process alters the classic Caruana algorithm by multiplying the error function used in the system of equations by the dependent variable y to reduce the effects of noise far from the gaussian peak. The fitting process does not require iteration and can be solved using the following sets of equations:

$$y = Ae^{\frac{-(x-\mu)^2}{2\sigma^2}}$$

$$\hat{y} = y + \eta$$

$$\begin{bmatrix} \sum \hat{y}^2 & \sum x\hat{y}^2 & \sum x^2\hat{y}^2 \\ \sum x\hat{y}^2 & \sum x^2\hat{y}^2 & \sum x^3\hat{y}^2 \\ \sum x^2\hat{y}^2 & \sum x^3\hat{y}^2 & \sum x^4\hat{y}^2 \end{bmatrix} \begin{bmatrix} a \\ b \\ c \end{bmatrix} = \begin{bmatrix} \sum \hat{y}^2 ln\hat{y} \\ \sum x\hat{y}^2 ln\hat{y} \\ \sum x^2\hat{y}^2 ln\hat{y} \end{bmatrix}$$

$$\mu = \frac{-b}{2c}$$

$$\sigma = \sqrt{\frac{-1}{2c}}$$

$$A = e^{a - \frac{b^2}{4c}}$$

where A is the amplitude of the Gaussian function, μ is the peak position, σ is the standard deviation of the Gaussian function, η represents the contribution from noise, and a, b, and c are the coefficients to parabola $\ln(y) = a+bx+cx^2$, and x is the channel number. The variable $\hat{y}$ represents the BGO data, where it assumed the data can be described as a Gaussian function, y, plus the effects from noise, η. The linear set of equations solves for a, b, and c which can then be used to calculate A, μ, and σ for the data. The right panel of Figure 3.8 shows an example of the Gaussian fit to the 511 keV annihilation peak after subtraction of the power-law background.

Variables such as temperature, galactic cosmic ray count, live time, and solid angle can all affect the location of the elemental peaks in the gamma ray spectrum. We account for this by calculating the correlation of the annihilation centroid position with each of these factors to determine any dependence. No dependence of peak position with these factors was found except for the galactic cosmic ray counts, where the triples count rate (Chapter 2) is used as a proxy for the flux of cosmic rays (Figure 3.9, left panel). This is because the production of gamma rays emitted from the planetary surface will vary with the amount of cosmic rays interacting with the surface. We determined the line of best fit for the cosmic ray dependence and subtracted it to detrend the data. The right panel of Figure 3.9 shows the data after the correction has been applied.

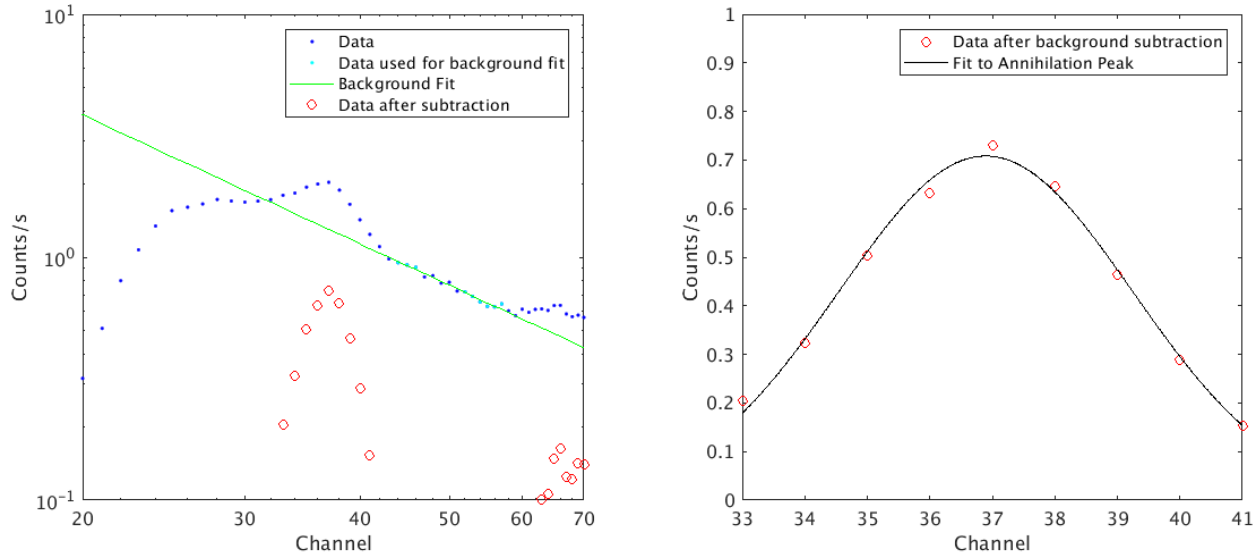

Figure 3.8 *Left: Blue circles are the BGO gamma ray data plotted, with a fit to the background continuum in green. The red circles show isolation of the annihilation peak by subtracting the background continuum from the data. Right: A Gaussian function is used to fit the annihilation peak and determine the peak position.*

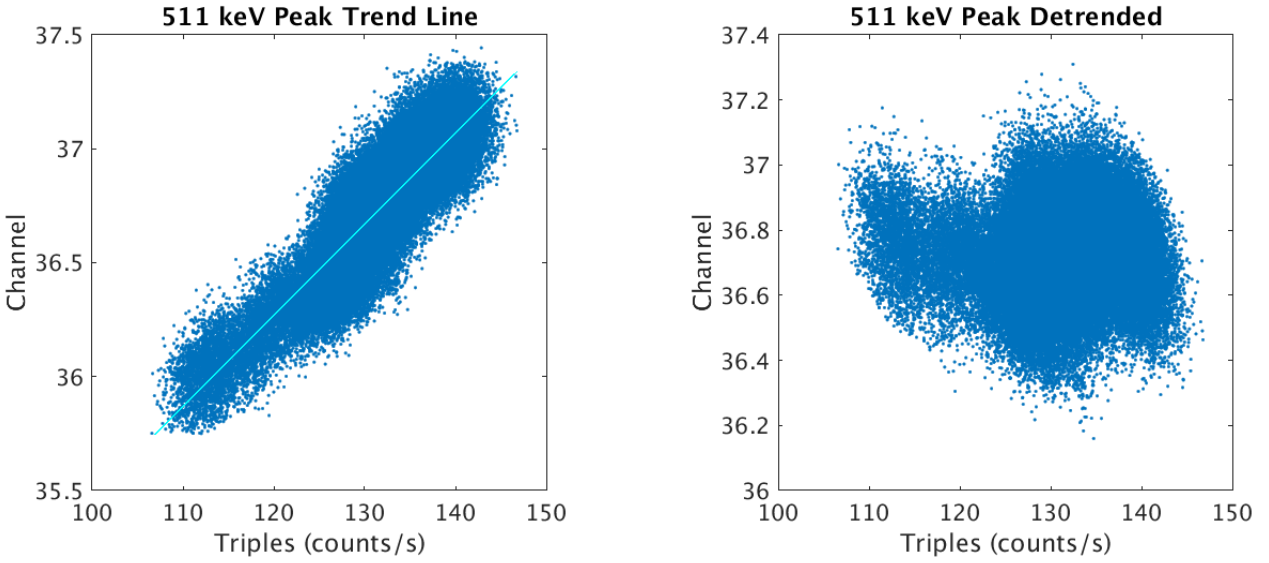

Figure 3.9 *Detrending the gamma ray data of external factors. Left: Correlation of the annihilation peak position with the presence of galactic cosmic rays (triples counts used as a proxy). Right: Dependence on galactic cosmic rays has been removed using the line of best fit.*

3.3.3 Global Maps of Shifts in the Annihilation Peak

The success of this experiment directly depends on knowing the direction of the sensitive axis of the tube relative to the body. Fortunately, the defined axes of the photomultiplier tube are well aligned with the spacecraft coordinate system, which is recorded and sent back to Earth with the ephemeris data. Lab measurements performed by the manufacturer orienting a known magnetic field along the different photomultiplier tube axes showed it is most sensitive when the external magnetic field lies along the $+Y_{spacecraft}$ axis (Chapter 2). The Z-axis of the spacecraft is always pointed toward the body center during data acquisition. This means the sensitive axis of the photomultiplier tube always rotates in a plane parallel to the surface as the spacecraft adjusts itself to catch the optimum amount of light on its solar panels. Therefore, it is most beneficial to orient ourselves in the radial, east, north (R, E, N) coordinate system since the Y-axis of the tube will always be contained in the East-North plane (Figure 3.10).

The data were sorted relative to the angle the $+Y_{spacecraft}$ made with the North vector, which we refer to as Θ_Y (Figure 3.10). Figure 3.11 shows a histogram of the Θ_Y distribution during the LAMO orbit. Data were dominantly acquired with Θ_Y between 0-50 degrees, 130-220 degrees, and 320-360 degrees, with little to no coverage between 50-130 degrees and 220-320 degrees. We divided the data into 60 degree-wide bins, 30 degrees on each side centered on the angle of interest. Bins were created for both parallel and antiparallel directions to Θ_Y= 10°, 25°, 40°, 145°, 160°, and 175°.

The sorted data were then used to create global maps of the relative shift of the 511 keV annihilation peak. Θ_Y orientations with the largest relative shift will provide us with the direction of the magnetic field. The maps were divided into longitude bins of 36 degrees each, while the latitude bins vary in width to create equal-area bins with an area of ~17,000 km^2, about 2% of

Vesta's total surface area. The value in each bin is an average of all the annihilation peak positions at that location for a specified Θ_Y. The color bar is centered on channel 36.72, the mean centroid position of the full LAMO data set, with the bounds defined on each side by the standard deviation of 0.1361. A 2D Gaussian filter was applied to smooth the maps.

Figure 3.12 shows a global map that contains all the LAMO data where the data has not been sorted by Θ_Y. As one would expect, averaging over all the data causes the bins to display a value close to the mean with no strong signal originating at any particular location. This tells us that if a strong trend is observed in the Θ_Y maps, with a corresponding reverse pattern in its antiparallel direction, it is likely due to the presence of a magnetic field.

Global maps for parallel and antiparallel Θ_Y=25°, 40°, 145°, and 175° showed little to no variation in the channel position of the 511 keV peak relative to the mean. Figures 3.13 and 3.14 show the parallel and antiparallel global maps for Θ_Y=10° and Θ_Y=160°, respectively. These correspond to the maps that showed the largest variation in peak position. The antiparallel maps have limited coverage, but we can still draw comparisons in the areas where the maps do overlap.

In Figure 3.13 (top panel), the global map for the direction parallel to Θ_Y=10° shows a dichotomous structure: the northern hemisphere displays a shift to higher channels while the southern hemisphere shows an overall shift to lower channels. If this trend was due to the effects of a magnetic field, we would expect that the antiparallel maps to be inverted to this, with a shift to lower channels in the north and higher channels in the south. However, the corresponding antiparallel map (Figure 3.13, bottom) does not show a systematic shift to higher channels in the overlapping southern hemisphere.

In Figure 3.14 (top), the global map for the sensitive axis parallel to 160° shows a shift to higher channels for areas with a longitude less than 220° that gradually decreases towards the equator. The antiparallel map (Figure 3.14, left) does not have coverage in the southern hemisphere, but does show a corresponding shift to lower channels at the equator. Analysis showed that bins where the maps in Figures 3.13 and 3.14 displayed the largest shift in peak position were also the bins with the lowest counts. Therefore, we conclude that the variation in the maps is due to low statistics and not to the presence of strong magnetic fields.

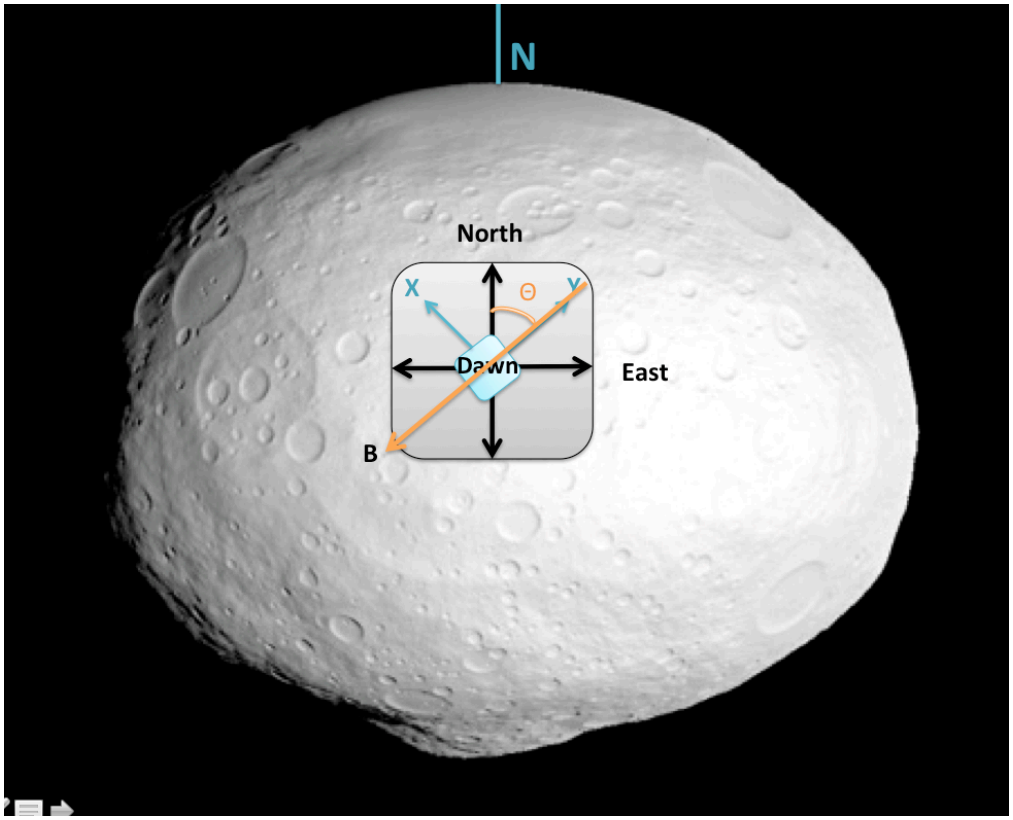

Figure 3.10 *Spacecraft geometry. The +Z spacecraft axis always points toward the body center (into the page) during data acquisition. Therefore, the +X and +Y spacecraft axes (cyan vectors) rotate in the North-East plane. When the (sensitive) Y-axis of the spacecraft is parallel/antiparallel with a magnetic field vector (hypothetical field shown in orange), the electrons in the BGO will experience a deflection. Data are placed into theta bins (angle the Y-axis makes with the North vector) to discern the orientation of the magnetic field.*

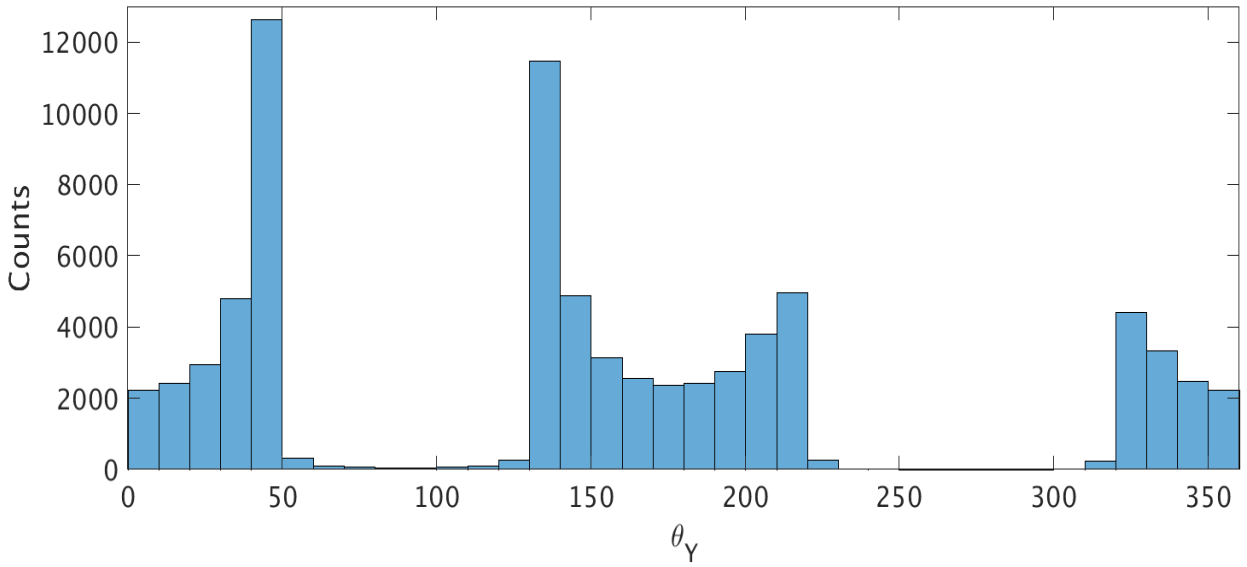

Figure 3.11 *Histogram of the location of the sensitive Y-axis of the photomultiplier tube relative to the north vector. Since the solar panels must remain in an orientation to receive light, the Y-axis pivots back and forth in the R, E, N plane. This Figure shows occurrence with which the Y-axis remains at an angle Θ_Y, defined between the Y-spacecraft axis and the North vector. The Y-axis typically resides at angles between 320-50 degrees and 130-220 degrees.*

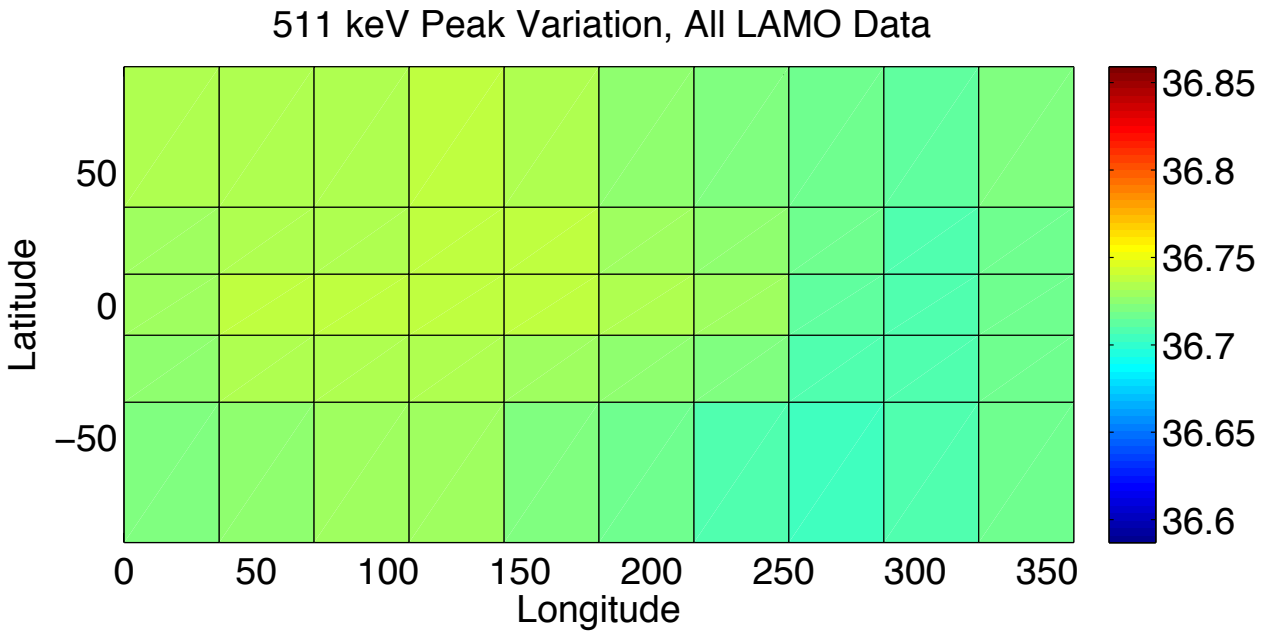

Figure 3.12 *Global map of the relative shift in the 511 keV which includes all LAMO data. Each bin shows an average peak location similar to the mean of all the data at 36.72.*

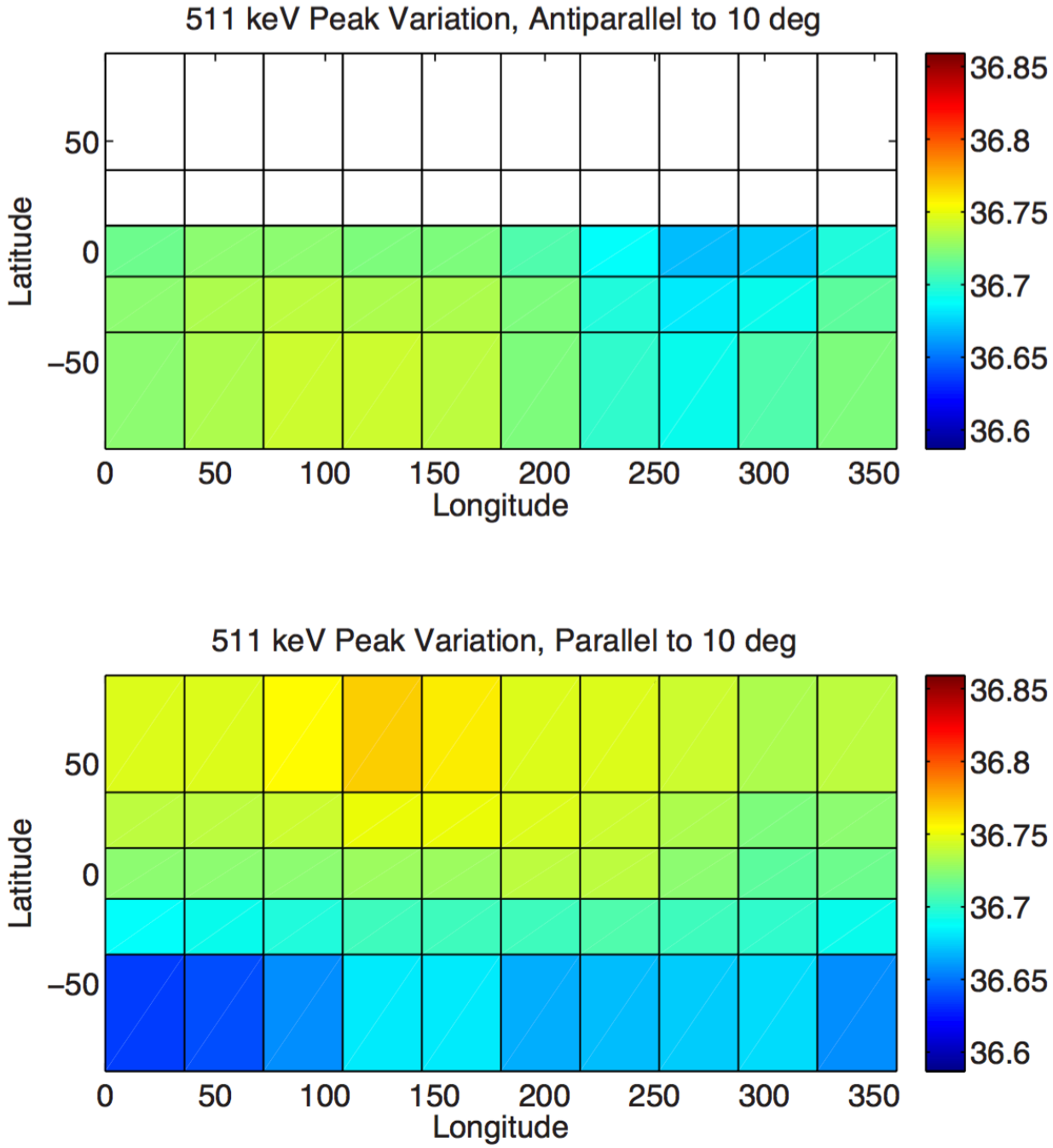

Figure 3.13 *Global map of the relative shift in the 511 keV annihilation peak for Θ_Y parallel and antiparallel to 10 degrees (Right: Θ_Y=190 deg; Left: Θ_Y=10 deg).*

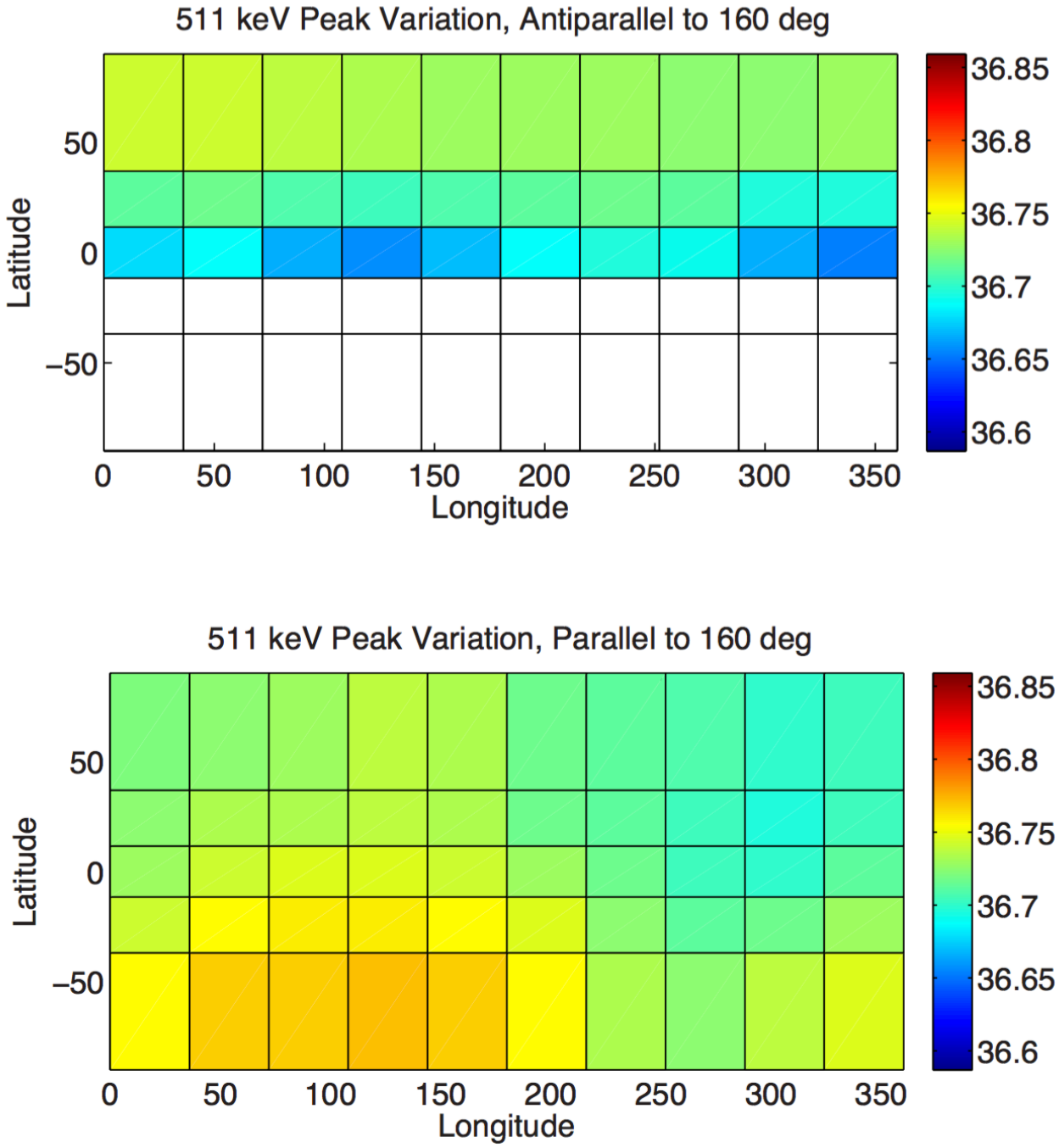

Figure 3.14 *Global map of the relative shift in the 511 keV annihilation peak for Θ_Y parallel and antiparallel to 160 degrees (Right: Θ_Y=340 deg; Left: Θ_Y=160 deg).*

3.4 Constraints on Remanent Magnetic Fields at Vesta and Implications for a Past Dynamo

In this chapter, we have investigated the presence of a vestan magnetic field through two methods: the first, by searching for evidence of a bow shock through an electron foreshock and the second, by searching for effects a magnetic field would cause to the photomultiplier tube of GRaND's BGO scintillator. In both studies, we did not find evidence for the presence of a strong magnetic field. However, despite the absence of these effects we are still able to place an upper bound on the magnitude of the planetary dipole moment.

The standard deviation of the LAMO data corresponds to a difference in 0.37% in the gain relative to the average position. The effects caused by the magnetic field cannot be more than this since the largest shifts shown in Figures 13 and 14 are less than a standard deviation. From Chapter 2 Section 4, the relative output of the photomultiplier tube appears to vary linearly for magnetic field strengths on the order of a microtesla or less when along the sensitive axis of the tube. Using the photomultiplier tube lab data with the five lowest magnetic field magnitudes (Chapter 2, Figure 2.7) and assuming a linear dependence, we arrive at the equation for the change in gain with magnetic field strength as Relative output (%)
= -0.6154B+100, where B represents the magnetic field present in microteslas. Hence, a variation of 0.37% corresponds to a field strength of 0.0060 μT, which is our upper bound field strength at the LAMO orbit. We can then calculate the magnetic dipole moment μ, using $\mu = B_{LAMO} R^3_{LAMO}$, which gives an upper limit for the moment as $\mu = 6.03*10^8$ Tm^3.

The author would like to acknowledge that this is a conservative upper bound. The variation in the peak is most likely caused by noise, and therefore the change in gain caused by a magnetic field is less than this. Secondly, the surface of Vesta is heavily cratered. Impacts that

occurred after the dynamo had ceased would effectively erase the remanent magnetism emplaced: heat from the impact can raise the surface material above the curie point and the electron spins within the surface material would re-solidify in random orientations and lose their magnetization. Due to this, we would not expect the surface to express a dipole-like structure, but would expect local regions where the surface magnetic field has been preserved similar to what has been observed with the crustal fields of the Moon and Mars.

The upper bound magnetic dipole moments of the Moon and Mars have been found to be 1.3×10^3 Tm^3 and 2×10^5 Tm^3, respectively (Russell et al., 1974; Acuña et al., 1999). Though these bodies do not currently possess global magnetic fields, they have been found to possess regions of strong, localized magnetic patches. Results from Lunar Prospector have shown that the moon has regions of strong remanent magnetization with surface fields up to 250 nT (Mitchell et al., 2008). The Mars Global Surveyor detected even stronger crustal fields at Mars, with a magnitude of ~220 nT at the orbital altitude of 400 km (Connerney et al., 2001). The magnetized H. E. D. meteorites reported by Fu et al. (2012) may originate from analogous magnetized regions present at Vesta.

Future missions to Vesta require a magnetometer incorporated into its payload to properly investigate remanent crustal fields within its subsurface. The Veneneia and Rheasilvia craters are the two largest impact craters that are superimposed onto each other in the southern hemisphere. It is likely these large impacts would have wiped out any remanent magnetism in the southern hemisphere if the dynamo had already ceased. Hence, these craters may help reveal the length of the vestan dynamo if crustal fields are found on the body. If the dynamo was no longer active at the time of these impacts, we would predict an asymmetry in the distribution of the

crustal fields where the fields are more preserved in the north and little to no remanent magnetization in the southern hemisphere where the impact basins are located.

Sterenborg & Crowley (2013) used a numerical model for the cooling rate of asteroid-sized bodies to investigate a planetesimal's ability to produce a dynamo. They estimate that a dynamo produced by a Vesta-sized body with a surface field strength of 20 μT can last no longer than 10 million years. Calculations by Weiss et al. (2008) arrive at a longer estimate for the duration of planetesimal dynamos and suggest they can last up to several tens of millions of years if the heat flux out of the core is super-adiabatic. Elkins-Tanton et al. (2011) arrive at a similar estimate arguing that Vesta-sized bodies could sustain a dynamo greater than 10 Myrs if the body accreted within 1.5 Ma following the formation of calcium-aluminum-rich inclusions. Recently, Formisano et al. (2016) performed four thermal evolution models for Vesta composed of different internal structures that are within the gravity constraints reported by Ermakov et al. (2014). Configurations with cores greater than 106 km resulted in the production of a dynamo lasting between 150-500 Myr with surface fields ~2 μT, consistent with the measurements of meteorites reported by Fu et al. (2012).

The ages of the Venenia and Rheasilvia craters are estimated to be 2.1±0.2 billion years ago and 1.0±0.2 billion years ago, respectively (Schenk et al., 2012). If the model predictions are correct, this suggests the dynamo should have terminated before the emplacement of the impacts. Therefore, it is likely that if a follow-up mission to Vesta includes a magnetometer, we will find the north to preserve the remanent crustal fields while the southern hemisphere will be free of magnetism due to these impacts. Confirming remanent magnetization at Vesta would not only provide compelling evidence that a planetesimal could support a dynamo, but would also have substantial implications for internal processes early in planetary evolution.

3.5 References

Acuña M. H. et al., Magnetization Discovered by the Mars Global Surveyor MAG/ER Experiment, Science, Vol 284, 790-793 (1999).

Collinson, D. W. and S. J. Morden, Magnetic Properties of Howardite, Eucrite and Diogenite (HED) Meteorites: Ancient Magnetizing Fields and Meteoritic Evolution, Earth and Planetary Science Letters, 126, 421-434 (1994).

Connerney, J. E. P., et al., The Global Magnetic Field of Mars and Implications for Crustal Evolution, Geophysical Research Letters, Vol 28, No 21, 4015-4018 (2001).

Elkins-Tanton, L. T. et al., Chondrites as Samples of Differentiated Planetesimals, Earth and Planetary Science Letters, Vol 305, Issues 1-2, 1-10 (2011).

Ermakov, A. I. et al., Constraints on Vesta's Interior Structure using Gravity and Shape Models from the Dawn Mission, Icarus, Vol 240, 146-160 (2014).

Formisano, M. et al, A core dynamo in Vesta?, Monthly Notices of the Royal Astronomical Society, Vol 458, 695-707 (2016).

Fu, R. et al., An Ancient Core Dynamo in Asteroid Vesta (2012), Science 338, 238-241 (2012), DOI: 10.1126/science.122564.

Fu, R. et al., Magnetic Fields on 4 Vesta As Recorded in Two Eucrites, 43rd Lunar and Planetary Science Conference abstract, abstract 1946 (2012).

Guo, H., A Simple Algorithm for Fitting a Gaussian Function, in Streamlining Digital Signal Processing: A Tricks of the Trade Guidebook, edited by R. G. Lyons, 297-305 (2012).

Howe, H. C. et al., Energetic Electron Scattering from the Lunar Remanent Magnetic Field, Geophysical Vesearch Letters, Vol 1, No. 3, 101-104 (1974).

Leroy, M. M. and A. Mangeney, A theory of energization of solar-wind electrons by the Earth's

bow shock. *Annales Geophys.* **2**, 449-456 (1984).

Lin, R. P., Constraints on the Origins of Lunar Magnetism From Electron Reflection Measurements of Surface Magnetic Fields.

Mitchell, D. L. et al., Global Mapping of Lunar Crustal Magnetic Fields by Lunar Prospector, Icarus 194, 401-409 (2008).

Nagata, T., Magnetic Properties and Paleointensity of Achondrites in Comparison with those of Lunar Rocks, Lunar and Planetary Science Conference 10ty., P. 2199-2210 (1979).

Rochette, P. et al., Magnetic Classification of Stony Meteorites: 3. Achondrites, Meteoritics & Planetary Science 44, Nr3, 405-427 (2009).

Schenk, P. et al., The Geologically Recent Giant Impact Basins at Vesta's South Pole, Science, Vol 336, 694-697.

Sterenborg, M. G. and J. W. Crowley, Thermal Evolution of Early Solar System Planetesimals and the Possibility of Sustained Dynamos, Physics of the Earth and Planetary Interiors, 214, 53-73 (2013).

Russell, C. T. et al., The Permanent and Induced Magnetic Dipole Moment of the Moon, Proceedings of the Fifth Lunar Conference, Vol 3, 2747-2760 (1974).

Russell, C. T. et al., Dawn arrives at Ceres: Exploration of a small, volatile-rich world, Science, Vol 353, 1008-1010 (2016).

Wu, C. S., A Fast Fermi Process: Energetic Electrons Accelerated by a Nearly Perpendicular Bow Shock, Journal of Geophysical Research, Vol. 89, NO A10, 8857-886 (1984).

Weiss, B. P. et al, Magnetism on the Angrite Parent Body and the Early Differentiation of Planetesimals, Science, Vol 322, 713-716 (2008).

Yamashita, N. and T. H. Prettyman, Dawn's Gamma Ray and Neutron Detector: BGO Data

Processing,

https://sbn.psi.edu/archive/dawn/grand/DWNC4GRD_1A/DOCUMENT/BGO_DATA_PROCESSING/GRD_L1B_BGO_DATA_PROCESSING_V4_1.PDF, (2015).

Chapter 4

Energetic Electron Bursts as Evidence for a Bow Shock at Ceres

4.1 Introduction

Dawn was stationed at Vesta from July 2011-August 2012 and at Ceres from March 2015-present. The period at Vesta corresponded to the portion of the solar cycle just before solar maximum when the sun was very active. This allowed Dawn to record several extreme SEP events, none of which were accompanied by energetic electron bursts (Chapters 3 and 7). Data accumulation at Ceres, on the other hand, was acquired when the sun was heading toward solar minimum and was dominated largely by a quiet sun, with most SEP events having a small to moderate magnitude. Strangely, two SEP events early in the Ceres mission were accompanied by bursts.

During Ceres Science Survey (CSS) orbit in June 2015, Dawn's Gamma Ray and Neutron Detector (GRaND) observed a moderate solar proton event followed by distinctive, short-lived enhancements in its exterior scintillator counts. Despite the solar proton event ceasing, the bursts were seen to reoccur on two additional orbits, lasting for a total of 10 days. After 10 days, the bursts disappeared, despite Dawn remaining in Survey orbit. Prior to this, a similar singular burst was observed during Dawn's approach phase, also following the onset of a SEP event of smaller magnitude but longer duration. GRaND has not seen bursts of this nature since the June 2015 event.

In this chapter, we show our analysis for identification of energetic electrons as the cause of the June 2015 bursts and present a hypothesis that supports a bow shock origin. Given that Ceres does not possess a metallic core (Park et al., 2016), we hypothesize that such a bow shock may be created by either mass loading due to the release of a temporary atmosphere or by an internal layer at depth.

4.2 Short-lived Enhancements in Dawn's Exterior Scintillators While at Ceres

4.2.1 Burst Observed on Approach Phase

As Dawn was in its Approach phase about to insert into orbit around Ceres, it witnessed a small solar energetic particle (SEP) event. Full analysis and identification of all SEP events detected by the Dawn spacecraft are documented in Chapters 2 and 7. The event was relatively small, but lasted several days from March 25th-31st, 2015 (DOY 84-90). Figure 4.1 shows the time series of this event in the +Z Phoswich scintillator. Peculiarly, this SEP event had a sudden burst superimposed on its long-term variation that occurred on March 30th (DOY 89.3), which lasted approximately 55 minutes. The other single point enhancements in Figure 4.1were identified as either Gamma Ray bursts or instrument glitches (Yamashita et al., 2018).

At that time, Ceres was not radially aligned with any spacecraft capable of detecting X-Rays or energetic particles: it was at about a 90 degree angle from Earth and from STEREO A and B (Figure 4.2). Though Ceres was along the Parker spiral field line of STEREO A and B, both were out of commission and not relaying any data. Hence, we could not use these spacecraft as proxies for the energetic particles or X-rays that were encountering Ceres during this event. The Rosetta spacecraft was operational and also along Ceres' parker spiral field line. Rosetta's payload contains the Standard Radiation Environment Monitor (SREM) which measures

energetic protons above 10 MeV and energetic electrons above 0.5 MeV (Mohammadzadeh et al., 2003). Rosetta's SREM shows a small increase in counts during the SEP event but has a data gap on March 30th when the Ceres burst occurred (R. Goldstein, personal communication).

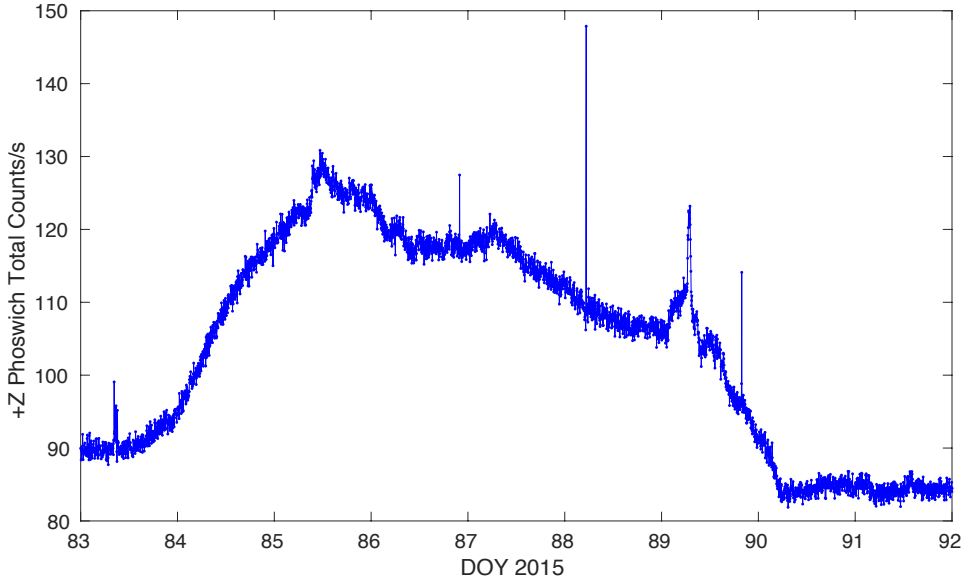

Figure 4.1 *Timeseries of a SEP event seen as Dawn was in its Approach Phase at Ceres. There appears to be a burst superimposed on the SEP event at DOY 89.3.*

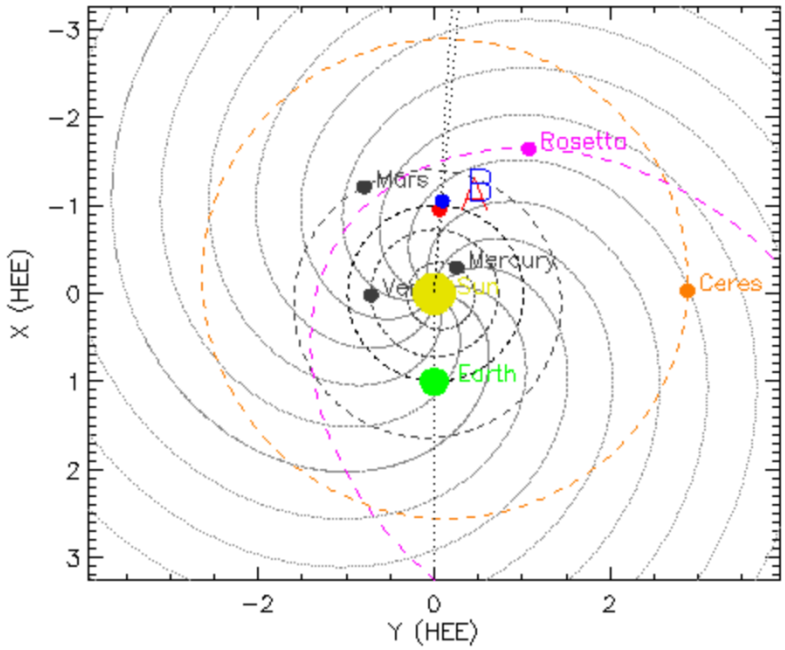

Figure 4.2 *Relative positions of spacecraft on March 30th, 2015. Figure generated at https://stereo-ssc.nascom.nasa.gov/where/.*

Since gradual SEP events do not usually display sudden bursts in their profiles, we investigated whether this burst could be due to electrons. We employed our electron identification method described in Chapter 2. The burst was inconsistent with a glitch and did not occur simultaneously with any known Gamma Ray bursts, and were ruled out. We then defined an enhancement window and compared its average spectrum to a background window comprised of 35 data points immediately preceding the burst. However, the superposition of the burst onto the SEP event complicates the analysis because the background window is during an event itself and is not reflective of ambient conditions. Figure 4.3 shows the steps in the electron identification process. After the subtraction of the background spectrum from the burst spectrum, an increase in counts is observed across all channels. This is likely due to the contributions from the energetic protons, making it difficult to determine which channels the burst source, if different than protons, is contributing to.

Next, we inspected whether any other GRaND scintillators showed a simultaneous response as the +Z Phoswich scintillator. Figure 4.4 shows that the –Z Phoswich and the central BGO scintillator also show an enhancement at the same time as the +Z Phoswich, while the –Y and +Y Boron Loaded Plastic (BLP) scintillators show no change. This behavior immediately rules out energetic electrons as the source of the bursts. As explained in Chapter 2, electrons do not affect the BGO and therefore are not responsible for the presence of the March 2015 burst.

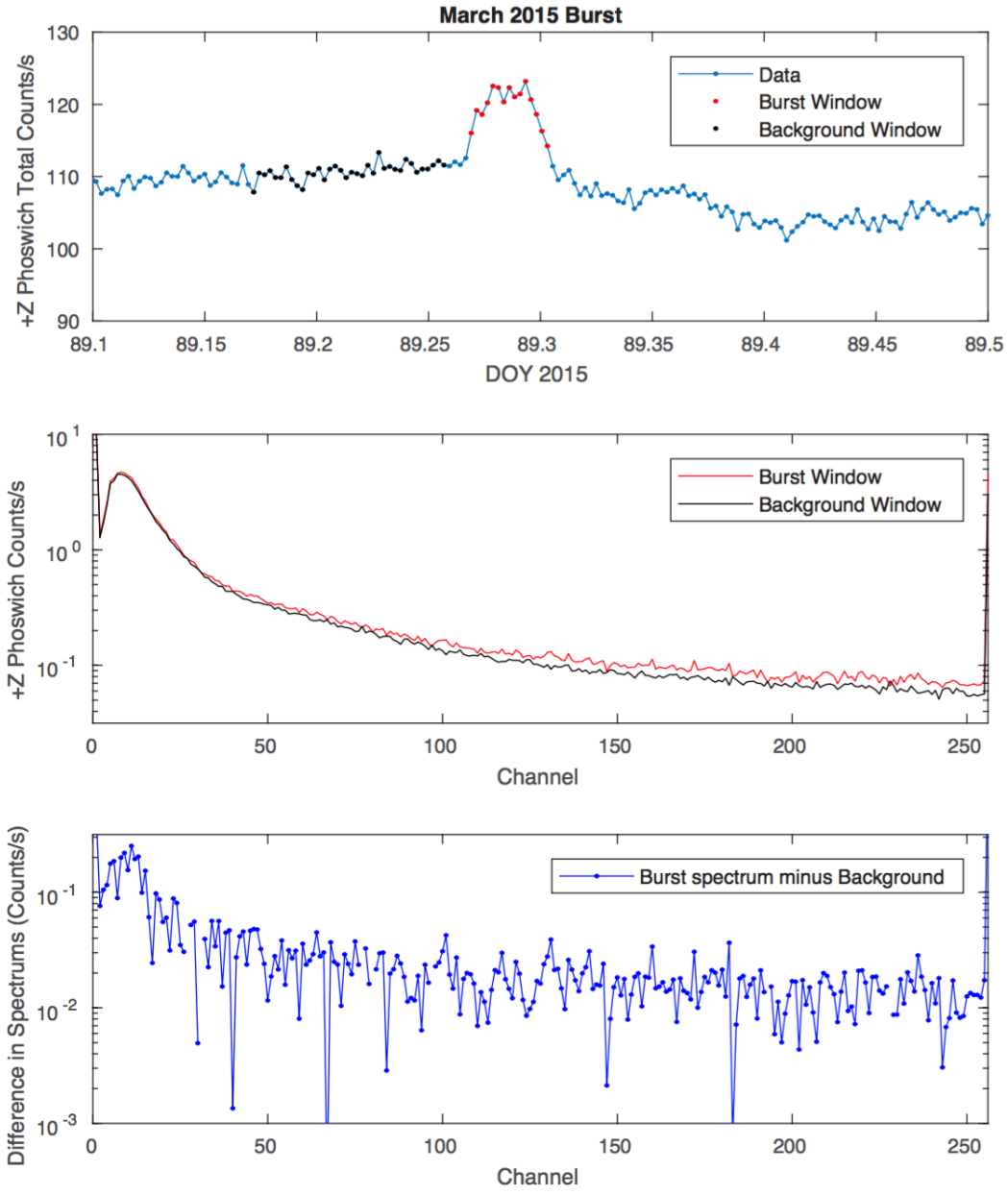

Figure 4.3 *Electron analysis for the March burst. A portion of the SEP event immediately preceding the superimposed burst is used as the background window. An enhancement is observed over all channels, possibly due to the presence of protons, making it hard to identify the contribution from the burst source.*

The properties of the March 30th enhancement—it's burst-like structure, duration, and its effect on the BGO—are qualitatively similar to the solar flare events that affected GRaND at Vesta (Chapter 3). As we learned in Chapter 3, a solar flare must reach at least an M-Class flare intensity to be detected by the GRaND instrument. However, there are no such catalogued flares in the SolarSoft solar flare catalog of this intensity on March 30th and no nearby spacecraft to detect X-Rays in Ceres' direction. Additionally, in comparison to the Chapter 3 solar flare events, this burst appears to last about an hour whereas the bursts due to solar flare typically lasted about 10 minutes.

As a final step in our analysis, we performed an analogous procedure on the BGO data similar to the analysis shown in Figure 4.3 for the +Z Phoswich data (figure not shown). A burst window was identified for the BGO data and compared to a 35 data point window immediately preceding the burst (although this background window contained elevated counts itself since it was during the SEP event). Still, after the subtraction of the relative spectra, the increase in counts during the burst phase resided at the channel corresponding to an energy of 4.4 MeV—a gamma ray that corresponds to inelastic collisions of energetic protons with Carbon. This suggests that the burst present on March 30th was due to a sudden, greater intensity of protons and not due to the presence of energetic electrons nor a solar flare.

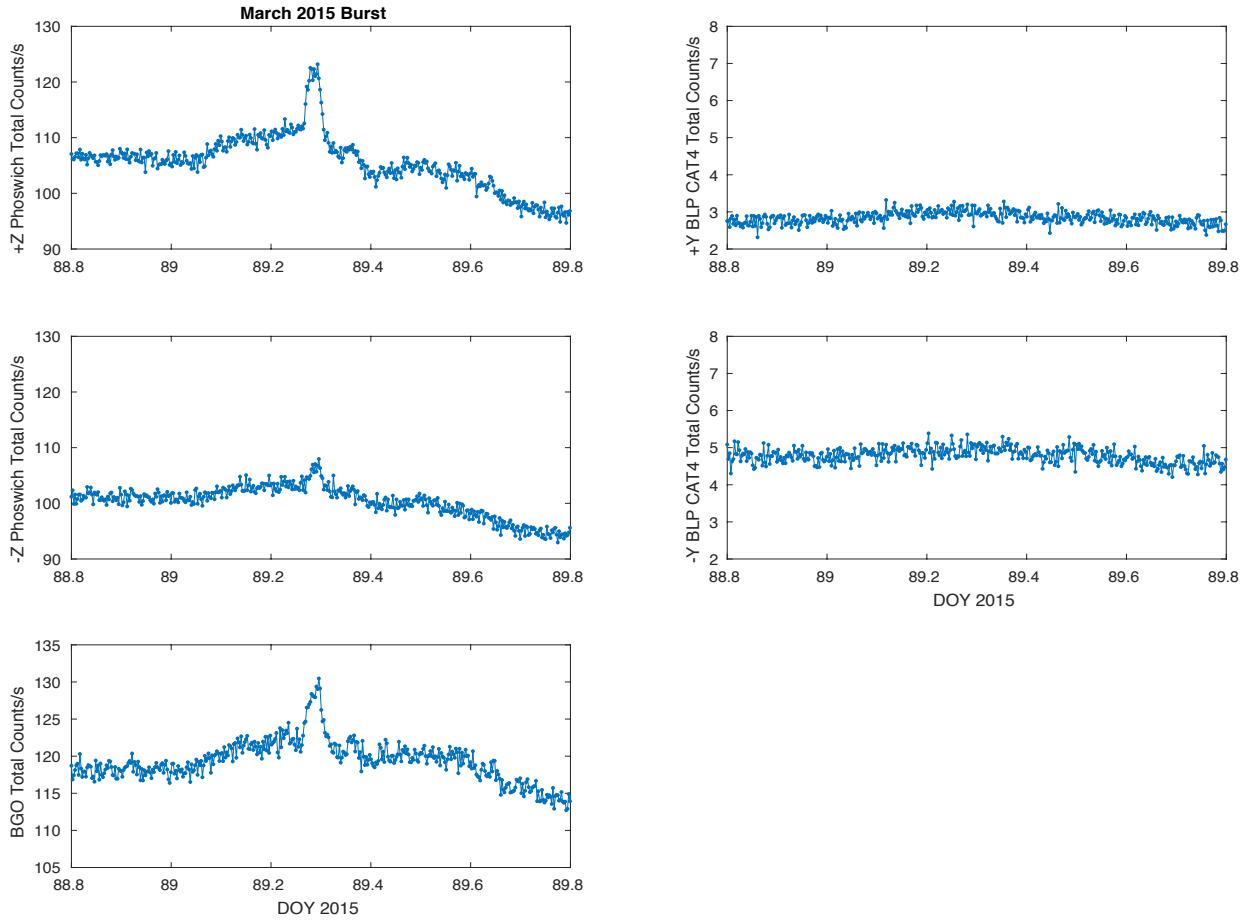

Figure 4.4 *Timeseries of each scintillator for the March burst event. Simultaneous enhancements are seen at DOY 89.3 in the +/-Z Phoswiches and the BGO scintillator. No enhancement is seen in the +/-Y BLP scintillators.*

4.2.2 Bursts Observed during Survey Orbit

GRaND also observed distinctive, short-lived enhancements in its +Z Phoswich scintillator counts during the week of June 18th, 2015 while in its Survey orbit. The bursts occurred repeatedly over a 10 day period: first superimposed on a solar energetic particle (SEP) event then twice after the event had ceased (Figure 4.5). The bursts reappeared with a frequency of three days, which corresponds to one Survey orbit.

Figure 4.6 shows the time series of all the GRaND scintillators during this period. All scintillators show a long-term enhancement in counts between June 18th-21st (DOY 169-172) due to energetic protons during the SEP event. However, burst events only occur in the exterior scintillators with corresponding spikes in counts in the central Bismuth Germanate (BGO) scintillator noticeably absent. This indicates that neither the particles responsible for the spikes in the exterior scintillators nor their progeny reached the BGO. This immediately eliminates energetic protons as the source of the bursts since those particles would induce inelastic collisions which emit gamma rays that increase counts in the BGO spectrum.

We applied an algorithm to systematically identify bursts in each scintillator. Figure 4.7 shows an example of this process for the +Z Phoswich scintillator. First, we identified potential spikes by using a 250 point window centered on each data point. Points greater than two standard deviations than the 250 point array were replaced by the average of the adjacent 10 data points, centered on the data point of interest. We then used a 30 point smoothing function to smooth the data and produce a background spectrum with reduced noise (Figure 4.7, top panel). Next, we subtracted the background spectrum from the original data set to zero the background level and directly compare the magnitude of the bursts. Enhancements that were greater than 2.5 standard deviations in the difference array were categorized as bursts (Figure 4.7, middle panel). It is clear

from Figure 4.7 than once the solar energetic particle event is removed from the data, the bursts reach similar maximum magnitudes on each orbit. The bottom panel of Figure 4.7 shows the locations of the identified bursts in the original data. This scheme was also applied to the –Z Phoswich, +Y BLP, and –Y BLP scintillators to identify corresponding bursts.

The bursts occurred in clusters every 3 days and reached similar maximum magnitudes for the largest spike in each cluster. Count enhancements lasted on the order of 20 minutes on average, with 7 minutes for the shortest burst to an hour for the longest. The time duration of the bursts correlated with their magnitude: the larger the burst, the longer the duration.

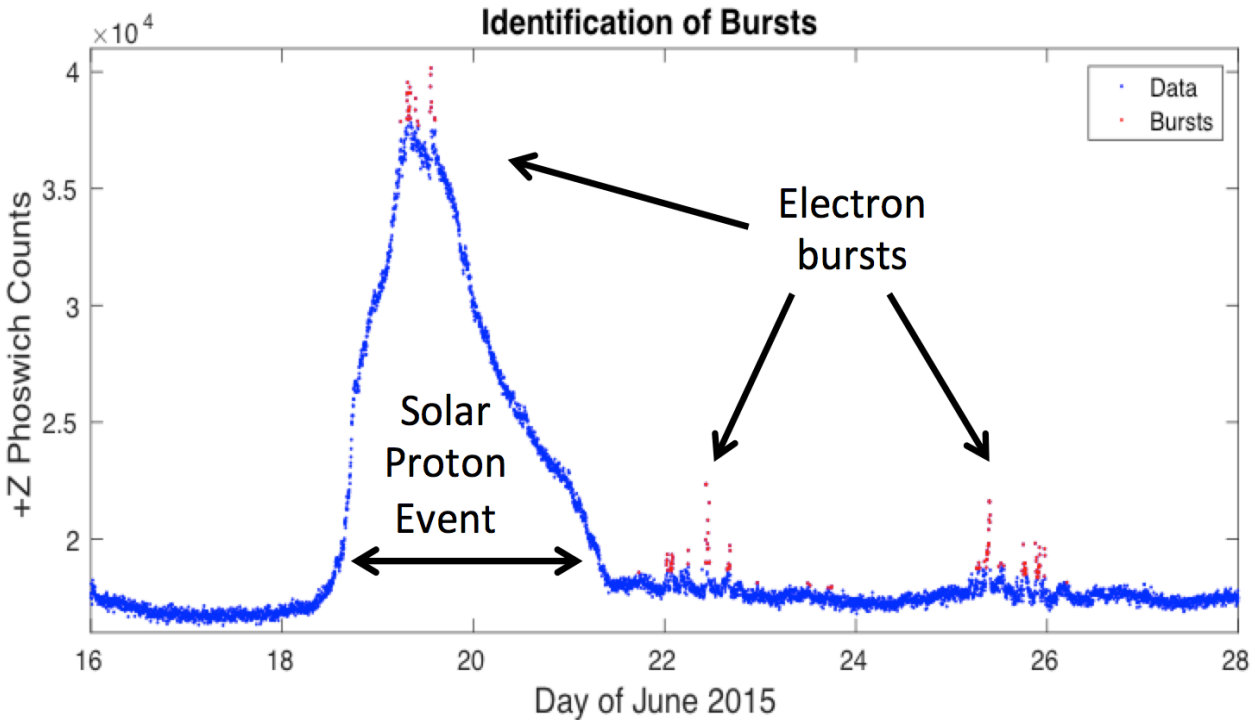

Figure 4.5 *Total counts for the +Z Phoswich from June 16th-June 28th, 2015. There is a large increase in counts from June 19-June 21 due to a solar energetic particle event. Superimposed on the SEP event are electron bursts, which reappear over the next two orbits at the same location.*

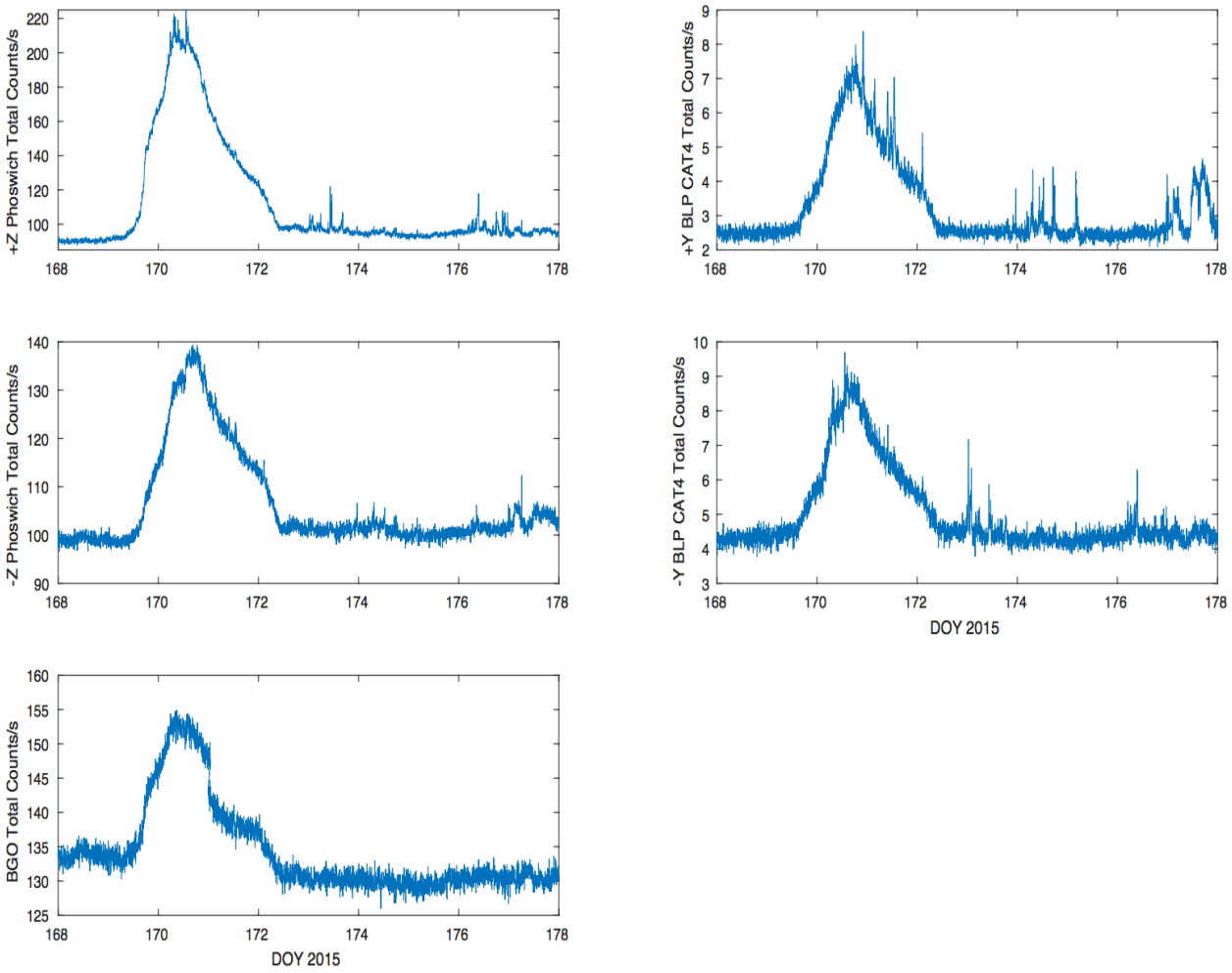

Figure 4.6 *Responses in each GRaND scintillator during the week of June 18th, 2015. All scintillators detect the energetic protons (DOY 169-172). Sudden bursts are observed in the +Z Phoswich, -Z Phoswich, +Y BLP, and –Y BLP scintillators. No bursts are observed in the central BGO scintillator.*

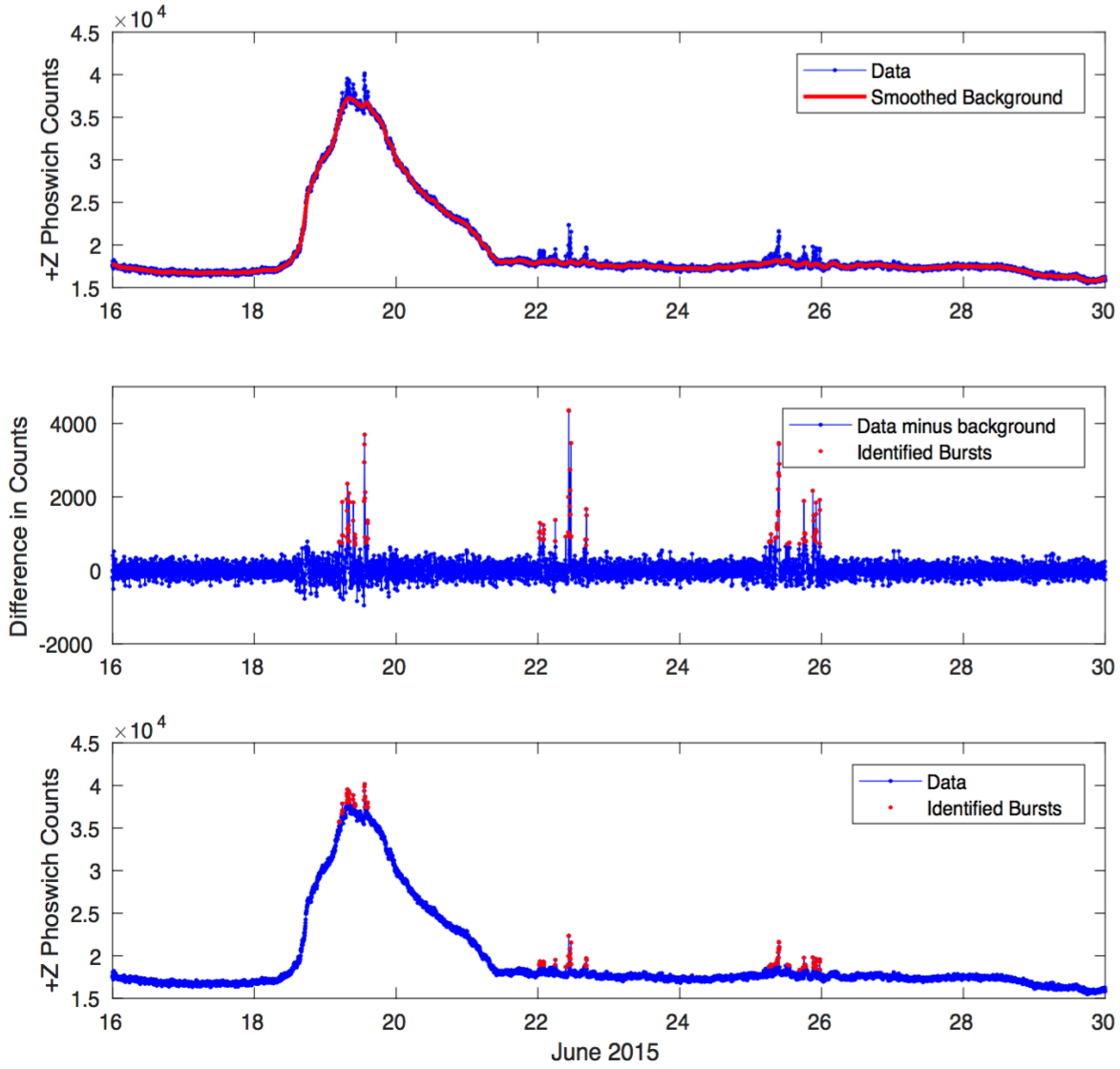

Figure 4.7 *Top panel: The data is removed of spikes and smoothed to create a background spectrum. Middle panel: the background spectrum is subtracted from the data and spikes >2.5 standard deviations are identified as bursts (red dots). Bottom panel: Bursts identified in the +Z Phoswich timeseries.*

As we noted in Chapters 2 and 3, gamma ray bursts and solar flares can cause spikes in the counts of the exterior scintillators. After inspection, no gamma ray bursts or solar x-ray events occurred at the time of these spikes, eliminating them as the source of the bursts. These events also do not exhibit the behavior of gamma rays and x-rays. The Ceres bursts last on the order of 20 minutes and appear in clusters, while gamma ray bursts appear as single point enhancements lasting less than a sampling cycle and the solar x-rays appear as singular bursts typically lasting about 10 minutes. We also probed the instrument health records and found the spikes were not due to a glitch or other instrument failure and were indeed a real signal. Therefore, the source of the enhancements was likely energetic electrons that penetrated directly into the exterior scintillators or interacted with surrounding materials to make bremsstrahlung. To confirm this, we again applied our electron identification method.

Figure 4.8 shows the electron identification process for the June 2015 bursts. The background window is composed of 35 data points and chosen during an ambient period between the spikes in counts. After subtraction of the average background spectrum from the burst spectrum, it is clear that the increase in counts dominantly reside in channels 20 (91 keV) and below. This is a much narrower spread than is typically exhibited by gamma rays and solar x-rays (Chapters 2 and 3). The isolation of counts at lower energy channels with a fall-off towards higher energy is consistent with the distribution we would expect for energetic electrons. The threshold energy of the instrumentation is 20 keV, giving an energy range of the electrons to be between 20-100 keV.

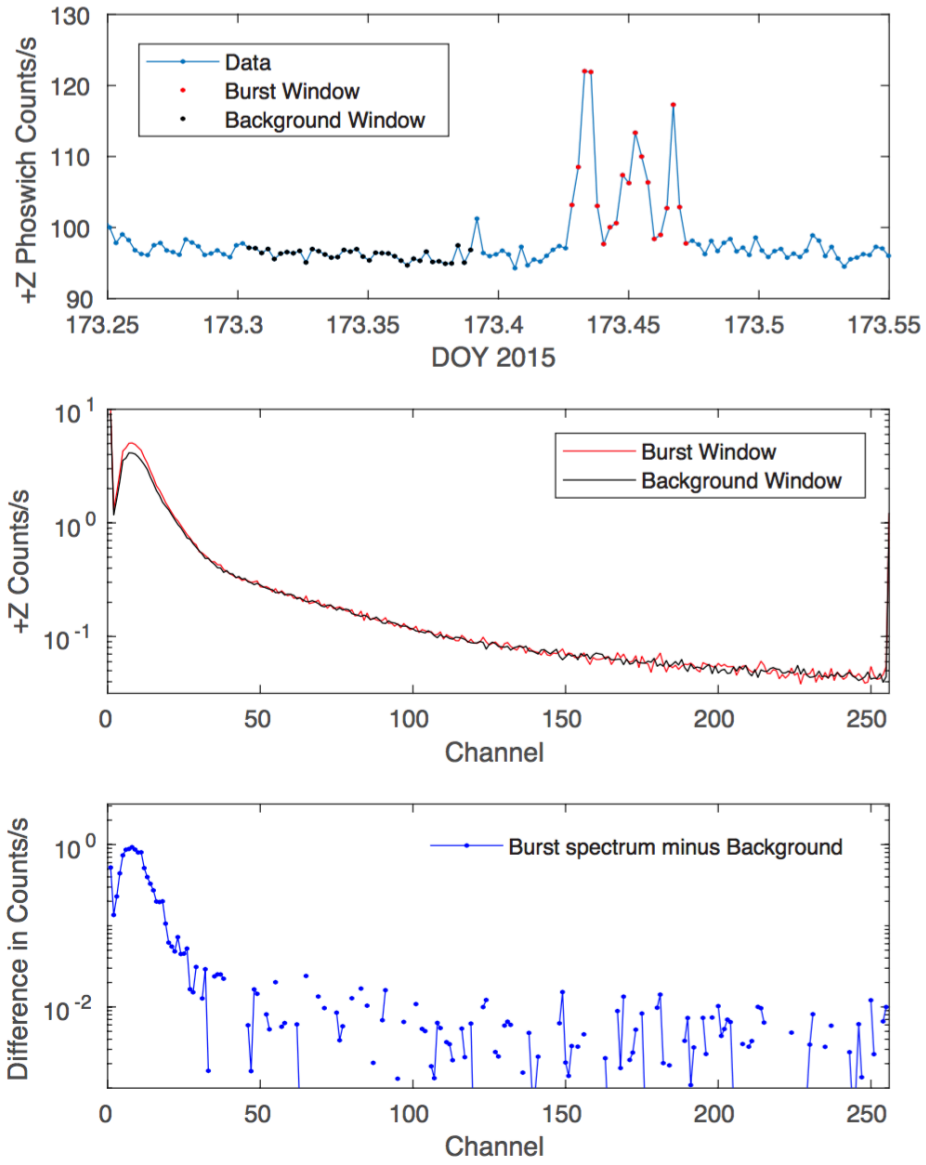

Figure 4.8 *Identification of energetic electrons. The burst window is highlighted by red points while the background window is shown in black. Subtraction of the average background spectrum from the spectrum for the enhancement window shows the increase in counts dominantly resides in channels less than 20, indicating the presence of electrons between 20-100 keV.*

4.3 Solar Wind Electron Data at 1 AU

We first explored whether the energetic electrons present during the June 2015 event could have originated directly from the solar wind. During the week of June 18th, Earth and Ceres were separated by ~30 degrees in heliolongitude, allowing us to use the ACE and Wind spacecraft as proxies for the solar wind environment near Ceres (Figure 4.9). ACE and Wind are spacecraft located at Earth's L1 Lagrangian point outside Earth's bow shock and therefore continuously sample the upstream solar wind.

Figure 4.10 shows comparisons between the arrival of energetic protons ~4 MeV at Wind and at Ceres. It is clear from the figure both spacecraft experience the first SEP event starting on June 18th (DOY 169): both show a similar rise and fall, but with a 10 hour offset, the expected travel time between the Earth distance to Ceres for a 4 MeV proton. However, there is a second SEP event observed at Earth which starts on June 21st, 2015 (DOY 172) while the Ceres data return to their background levels, indicating ambient solar wind conditions rather than a disturbed period. Therefore, the 1 AU energetic electron data between June 18th-June 21st, 2015 (DOY 169-172) will serve as good proxies for Ceres since both locations were connected to the shock while data after June 21st will not be representative because Ceres did not connect to the second CME shock surface.

Figure 4.11 shows flux measurements from the Wind 3DP instrument for electron energies 27 keV-100 keV, similar to the range of electrons detected at Ceres. The time resolution of the data is 12 seconds and is capable of capturing similar burst-like enhancements. The instrument shows a jump in the flux of electrons greater than 20 keV starting June 18th, 2015 (DOY 169) associated with the SEP event. The apparent, obvious spikes in Figure 4.11 are single-point enhancements which primarily occur after June 21st, and are possibly artifacts or gamma ray

bursts. While the flux in energetic electrons remains elevated for the remainder of the week, the variation in the flux is on the order of hours to days and does not exhibit any bursts in the flux of electrons. This is in contrast to Dawn, where the bursts varied on timescales from minutes to an hour.

The June 18th coronal mass ejection (CME) originated on the sun with a heliolongitude between that of Rosetta and Mercury. At the time of the bursts, Rosetta was along the same Parker spiral field line as Ceres (Figure 4.9) and also observed the SEP event with its SREM instrument (R. Goldstein, personal communication). Energetic particles produced by CMEs propagate from the shock surface along the parker spiral field lines connected to the shock. Therefore, we would expect Rosetta and Ceres to sample the same population of energetic electrons and protons during this event. Data from Rosetta's SREM did not exhibit any obvious bursts. However, this instrument is sampling proton energies greater than 10 MeV and electrons greater than 0.5 MeV, while GRaND is sensitive to protons greater than 4 MeV and electrons greater than 20 keV. Interestingly, Rosetta's target body, Comet 67P/Churyumov-Gerasimenko did experience three large outgassing events on June 18th, June 20th, and June 23rd, 2015 (Feldman et al., 2016), within the same time range Ceres experienced its bursts.

The spikes in high-energy electrons cannot be explained simply by the solar wind alone. The typical energy of electrons in the solar wind is 10 eV (Feldman et al., 1975), while the electrons responsible for the bursts were found to be between 20-100 keV. The mechanism producing these electrons must therefore be capable of accelerating them to orders of magnitude higher than what they are normally. Additionally, if the energetic electrons were inherent to the solar wind, they would not show a preference for orbit location. The short-lived nature of these bursts in the spacecraft's trajectory also indicates that the acceleration of the electrons must be a local

process. As was mentioned in Chapter 2, the +Z Phoswich always points nadir during data acquisition. Therefore, when the spacecraft is on the dayside, it is pointing opposite of the solar direction and towards the Ceres surface, implying the source of the electron bursts were coming from the Ceres direction. We explore this more in Section 5.

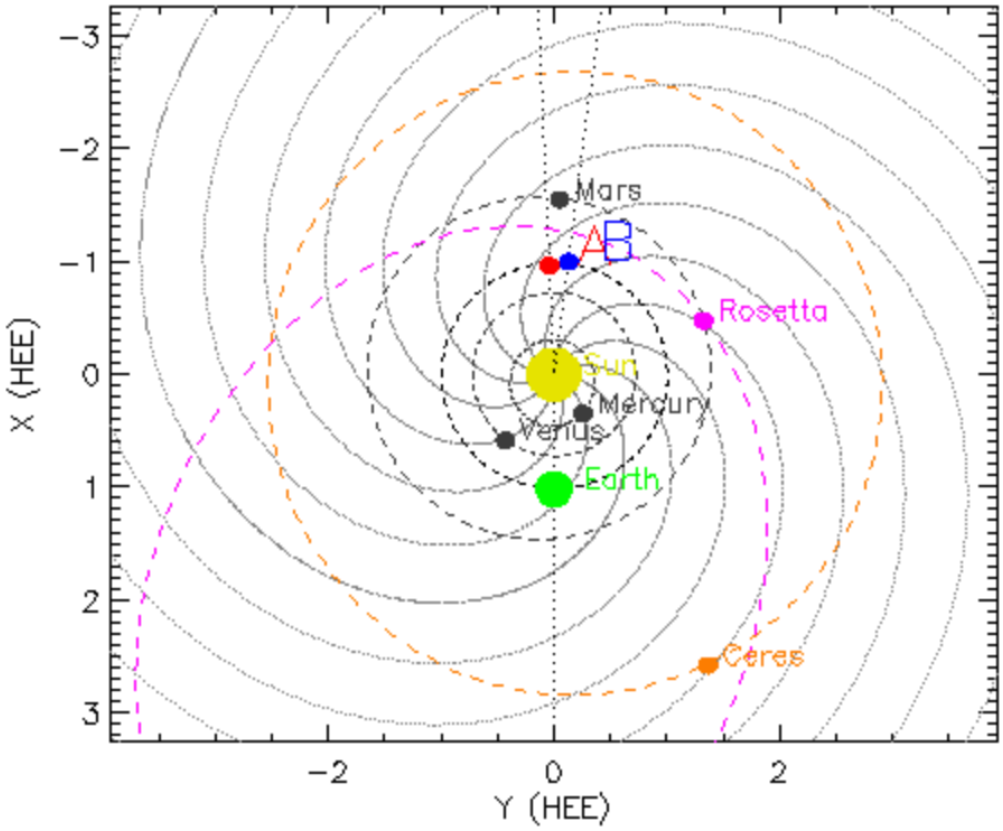

Figure 4.9 *Relative positions of spacecraft on June 18th, 2015. Ceres was near opposition with Earth and was along the same IMF line as the Rosetta spacecraft. Figure generated by https://stereo-ssc.nascom.nasa.gov/where/.*

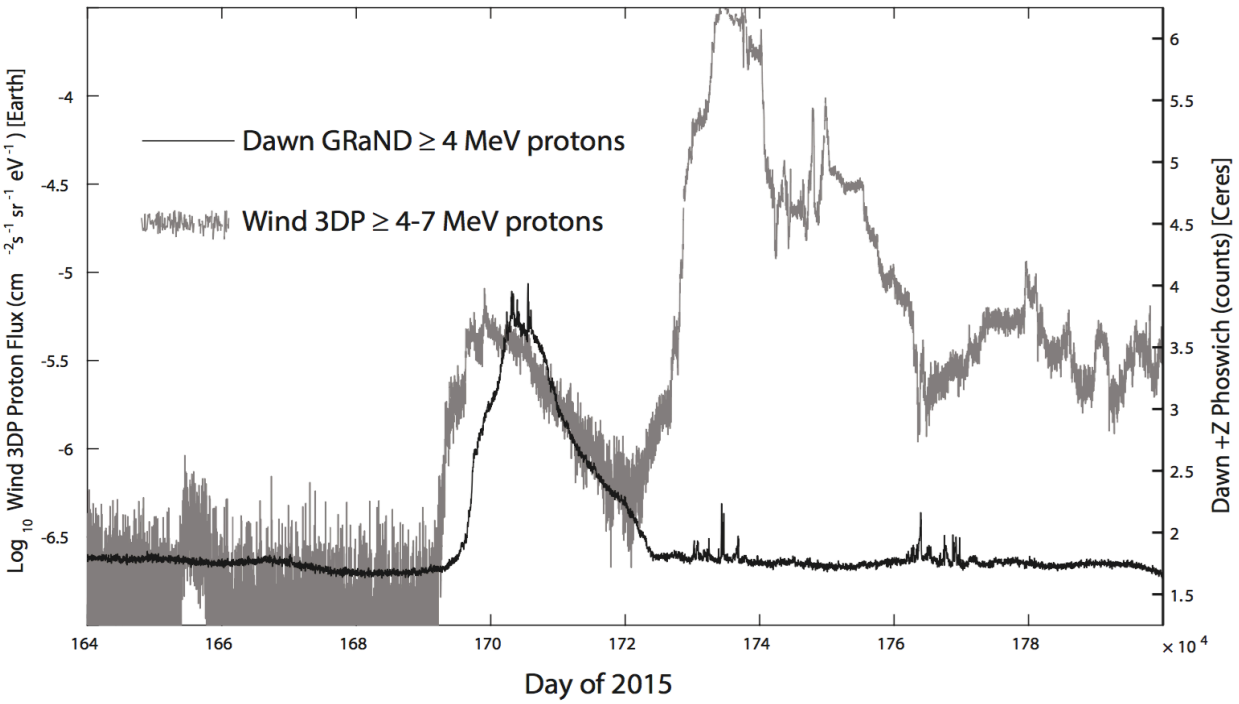

Figure 4.10 *Timeseries of energetic protons arriving at Wind (gray solid line, left axis) and at Dawn (black solid line, right axis). Ceres and Earth both encounter the June 18th, 2015 SEP event while there is a second, larger event that reaches Earth but not Ceres.*

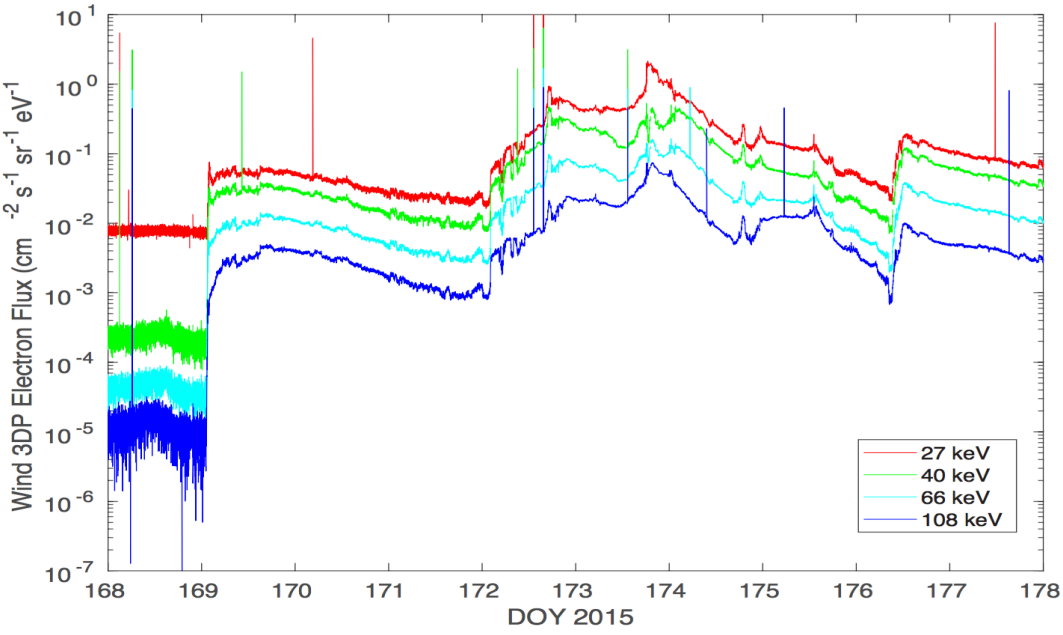

Figure 4.11 *Energetic electron fluxes for energies 27 keV-108 keV from Wind 3DP. Electrons between DOY 169-172 should serve as a good proxy for electrons at Ceres. No electron bursts are observed in the Earth data.*

4.4 Burst Locations in Planetary and Ceres-Solar Orbital Coordinates

The occurrence of the bursts were not random, but appeared at the same portion of the spacecraft's trajectory on three consecutive orbits while Dawn was about 10 R_C away from the planet in its Survey orbit. Though the bursts correlated with orbit location, they did not reoccur over any specific geographical feature and the subspacecraft footprints of the burst locations were randomly scattered over the surface. The bursts became well ordered when transformed into a sun-oriented coordinate system. One such frame is the Ceres Solar Orbital (CSO) coordinate system in which the +X axis points toward the sun along the Ceres-Sun line, the +Y axis is the opposite direction of orbital motion, and the +Z axis completes the right hand set.

Figure 4.12 shows the locations of the electron bursts for each scintillator in the CSO coordinate system over the week long period. A longitude of 0 degrees defines local noon and a longitude of 180 degrees defines local midnight. The size of the plot symbol reflects the magnitude of the respective burst. Since the exterior scintillators detect events differently, we cannot directly compare the increase in total counts caused by bursts from different scintillators. Therefore, we have instead scaled the plot symbols relative to the number of standard deviations above the background mean to compare the bursts' influence on each detector.

The +Z Phoswich and the –Y BLP scintillators dominantly detect energetic electrons as Dawn crosses into the southern hemisphere on the dayside, many times simultaneously. The +Y BLP scintillator typically detects the electron bursts near the equatorial region on the nightside. At that time, the –Y BLP scintillator also sees small magnitude bursts. This is likely due to a contribution from the shared component between the two scintillators on the X-axis of the spacecraft. The –Z Phoswich detects small bursts both on the southern dayside and equatorial nightside. The –Z Phoswich does not exhibit any large bursts. This is likely due to its placement

on the spacecraft: the –Z Phoswich is located on the face of GRaND that is mounted onto to the spacecraft making it difficult for particles to reach that face of the instrument. Still, it is clear that each exterior scintillator is capable of detecting the energetic electrons.

Each scintillator consistently detects electrons in the same regions over the 10 day period, indicating that the electrons are continually present in those locations over the 10 day period. What is noticeable in Figure 4.12 is that the scintillators almost exclusively detect bursts in the southern hemisphere, while bursts are rare in the northern hemisphere. The largest and most frequent bursts occur on the southern dayside by the +Z Phoswich and –Y BLP, while the nightside tends to have more small to moderate sized bursts detected by the +/-Y BLP and –Z Phoswich scintillators.

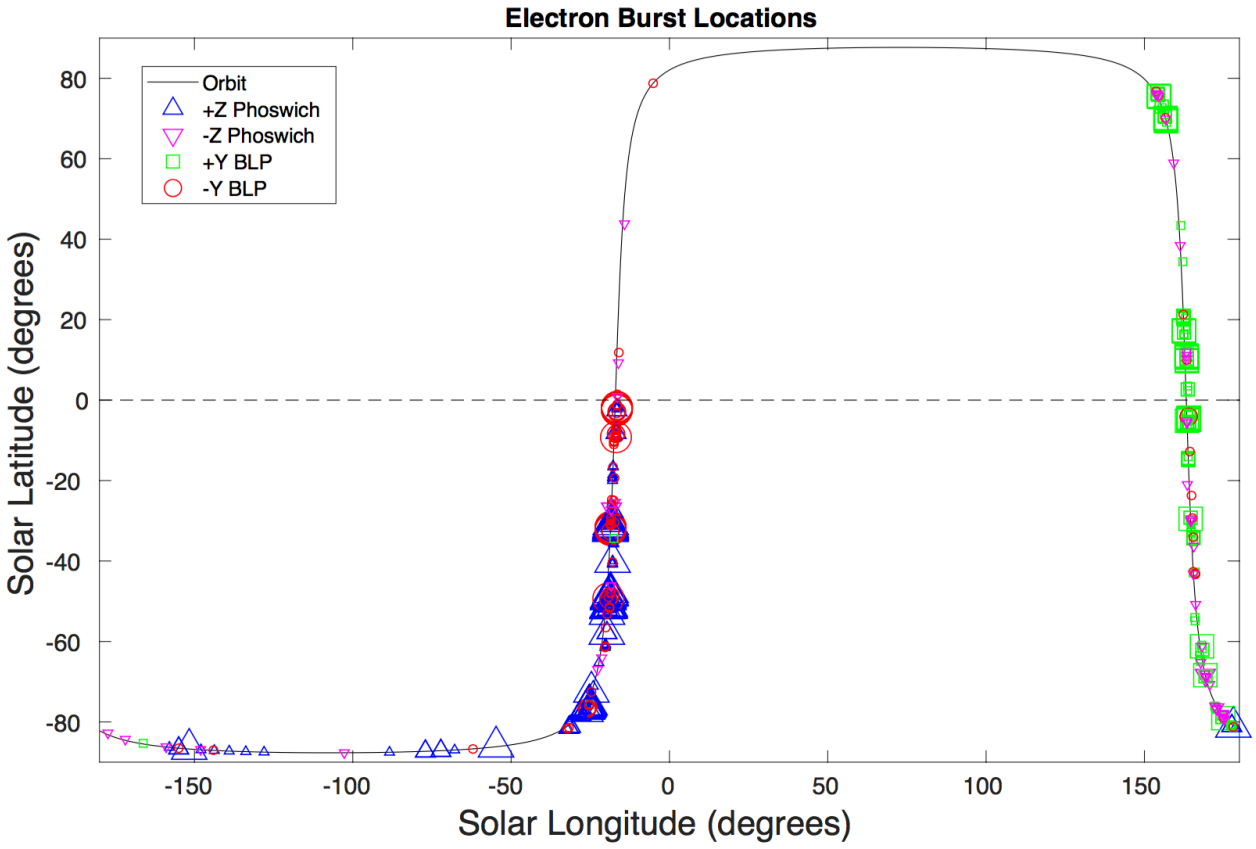

Figure 4.12 *Locations of the electron bursts in Ceres-Solar Orbital coordinates over the period June 16th-June 28th, 2015. Detections by the +Z Phoswich are indicated by blue triangles, the –Y BLP scintillator by red circles, and the +Y BLP scintillator by green squares. The size of the symbols reflect the magnitude of the burst. Each respective scintillator detects bursts at the same locations over three consecutive orbits.*

4.5 Field of View of the Scintillators and the Electron Source Direction

The previous section displayed the locations of the bursts along Dawn's trajectory. Here, we also investigate the pointing directions of each detector to understand the source direction of the bursts. Electrons with 20 keV will be highly magnetized and should travel along interplanetary magnetic field lines until they reach the detectors. Dawn's payload does not include a magnetometer, and therefore information about the direction of the magnetic field at Ceres is not available. However, since GRaND is an omnidirectional instrument, we can narrow the source direction of the electrons by examining where each detector was pointing during the detection of each burst.

In spacecraft coordinates, the $+X_{spacecraft}$ points in the direction of the high gain antenna, $+Z_{spacecraft}$ points in the direction the science instruments are mounted on, and $+Y_{spacecraft}$ points along the solar panel that completes the right hand set (Chapter 2). Each scintillator is named after the spacecraft axis for which is their dominant observing direction. The +/- Z Phoswiches have their full surface area within the spacecraft X-Y plane, giving them zeniths pointing parallel to the +/- Z axis, respectively, with a field of view of ~2π steradians (T. H. Prettyman, personal communication). The +/- Y BLP scintillators are L-Shaped and therefore have an additional (small) contribution from their surface area which points toward the –X axis in addition to their dominant look directions along the $Y_{spacecraft}$ axis (Chapter 2). The portions of the +/-Y BLP scintillators that point parallel to the Y-axis also have a field of view ~2π steradians (T. H. Prettyman, personal communication). In this section, we will ignore the –X portion of the BLP scintillators except for the nightside bursts of the –Y BLP, where we assume the simultaneous detections of bursts with the +Y BLP are due to the shared surface area on the X-axis.

Before we cover the look directions of the detectors at the instances of the bursts, we first

introduce the maneuvers of the spacecraft while in its Survey orbit. Figure 4.13 displays the rotations of the spacecraft axes within the CSO coordinate frame. As previously mentioned, on the dayside of Ceres the spacecraft is oriented so that the +Z spacecraft axis points nadir for data acquisition. During this time, the spacecraft also rotates about the spacecraft's Z-axis so that light shining on the solar panels is maximized. This can be seen in Figure 4.13 on the dayside where a rotation occurs as the spacecraft passes over the equator. The spacecraft then rotates again once it crosses into the nightside (south pole) to transmit data back to Earth. In this orientation, the spacecraft +X axis is quasi-parallel to +X CSO, the spacecraft +Y axis is quasi-parallel to +Z CSO, and the spacecraft +Z axis is quasi-parallel to –Y CSO. The spacecraft stays in this orientation until it crosses over the north pole terminator, at which point it resumes observing.

Figure 4.14 shows the pointing directions of each scintillator at the time they detect their respective bursts for each individual orbit. Panels A, B, and C correspond to the three consecutive orbits between June 18th-28th, 2015 that the bursts were observed. The nominal look directions for each scintillator are indicated by different colored vectors: the +Z Phoswich is represented by blue vectors, -Z Phoswich by magenta vectors, +Y BLP by green vectors, and the –Y BLP by red vectors. Similarly to Figure 4.12, the size of the vectors reflect the magnitude of the burst and are scaled by the amount of standard deviations above the background mean.

The +Z Phoswich bursts only occur on the southern dayside between the equator and the south pole when the spacecraft is pointing toward the body center, at which point the spacecraft rotates the +Z spacecraft axis away from the planetary body. It can be seen from Figure 14 that the +Z Phoswich has the most frequent and largest magnitude bursts in comparison to the other scintillators. The dayside bursts experienced by the –Y BLP scintillator were generally simultaneous with the +Z Phoswich bursts. During this time, the –Y BLP was pointed roughly

toward the –Y CSO direction. However, given a field of view of 2π sr, the body center would be located just on the horizon within the field of view of the detector during the dayside bursts. The –Z Phoswich and the +Y BLP occasionally observed small bursts on the dayside when the –Z Phoswich was pointed antiparallel to the body-center direction and the +Y BLP roughly pointed toward the +Y CSO direction.

The majority of the +Y BLP bursts occur on the near the nightside equatorial region. While the spacecraft is on the nightside, the +Y BLP detector is continuously pointed quasi-parallel to the +Z CSO direction. The –Y BLP detects some small, simultaneous bursts on the nightside, which if due to the –X shared face, is oriented toward the –X direction away from the planet. It is worth mentioning that when the spacecraft is located on the nightside of the planet, the +X spacecraft axis is relatively pointed toward the body direction, which is also the only face of GRaND which is not covered by a scintillator. The –Z Phoswich also observes some small bursts on the nightside, sometimes simultaneous with the +Y BLP.

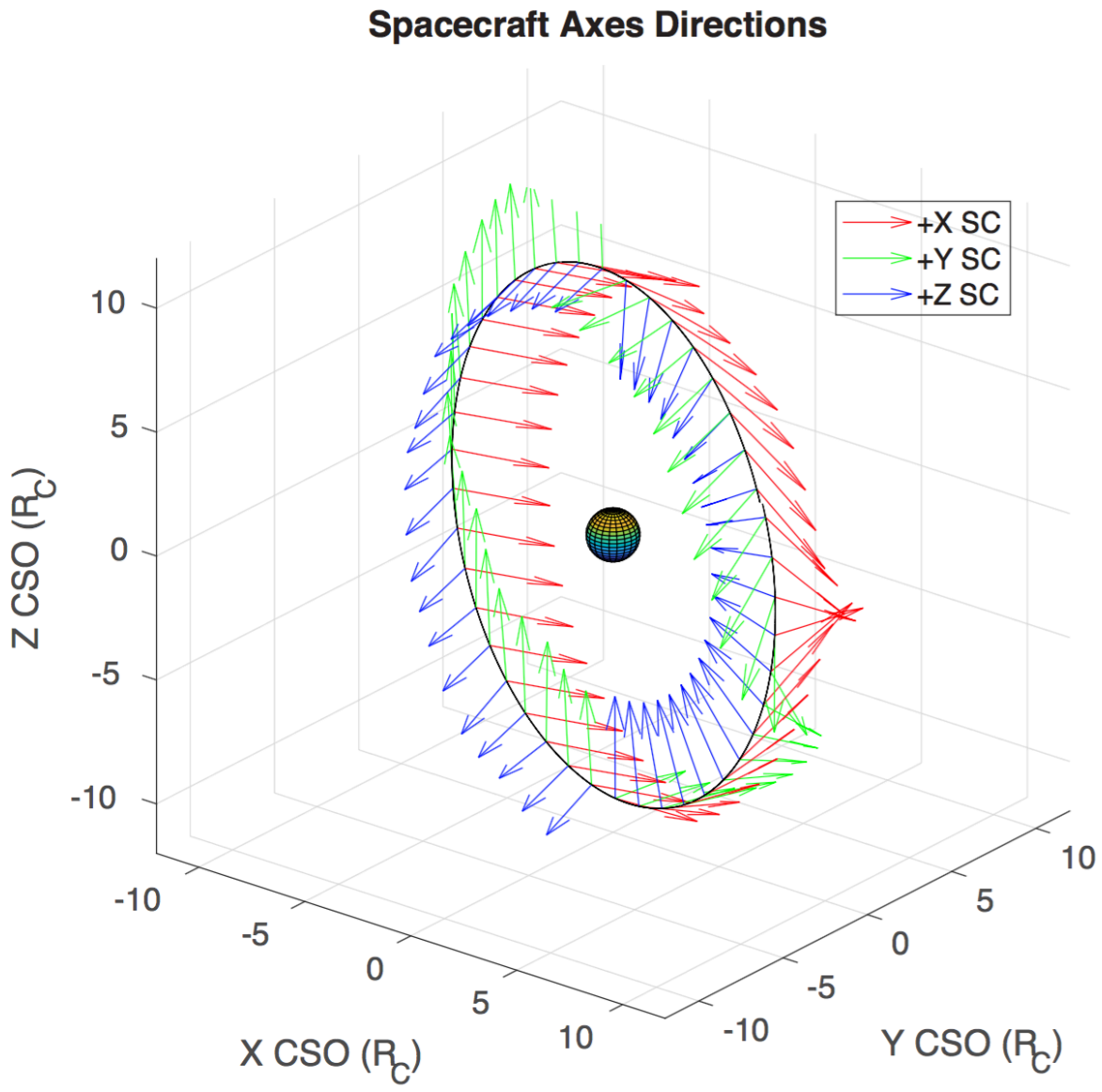

Figure 4.13 *Spacecraft axes in CSO coordinates. The X-axis of the spacecraft is designated by red vectors, the Y-axis by green vectors, and the Z-axis by blue vectors. The Z-axis points toward the body center during data acquisition. After transition into the nightside, the spacecraft maneuvers to point towards earth to relay the data.*

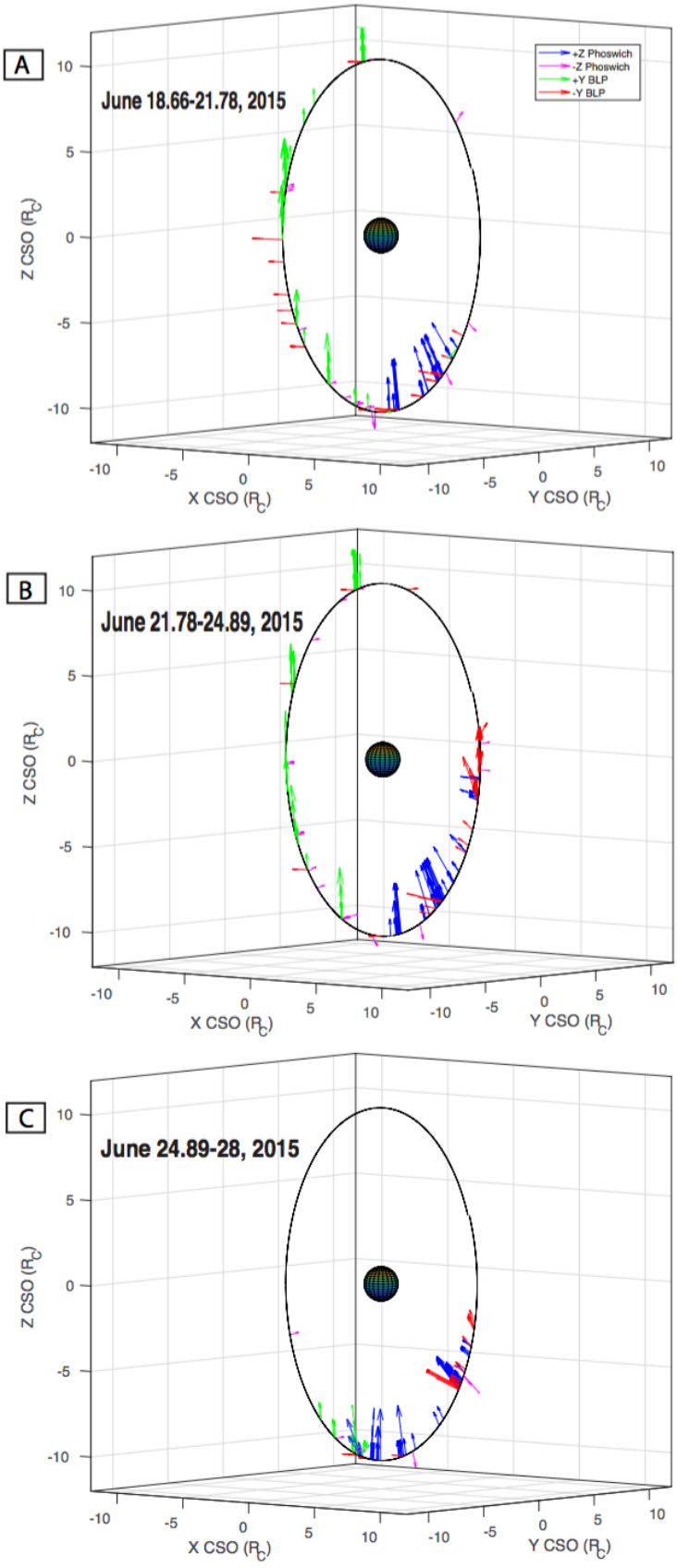

Figure 4.14 *Locations and relative magnitudes of all bursts seen by each scintillator on individual orbits. The panels A, B, and C correspond to the three consecutive orbits which observed the bursts. The +Z Phoswich bursts are represented by blue vectors, -Z Phoswich bursts by magenta vectors, +Y BLP by green vectors, and –Y BLP bursts by red vectors. The lengths of the vectors reflect the relative magnitude of the respective burst. The vectors point in the nominal look direction of each scintillator.*

4.6 Evidence for an Electron Foreshock

Dawn did not observe any electron bursts similar to the June 2015 Ceres bursts while it was present at Vesta (Chapter 3). The Vesta portion of the Dawn mission also corresponded to a much more active solar period, when Dawn saw some of its largest solar energetic particle events (Chapter 7). The SEP event that preceded the June 2015 electron bursts was a relatively mild event, where the flux of both energetic protons and electrons coming from the shock surface would be low in comparison to the large SEP events observed at Vesta. This suggests that if these bursts were directly sourced from the SEP event, we would have expected them to have also been present during events at Vesta. Additionally, these bursts were observed to reoccur after the SEP event had passed Ceres, implying a separate, local phenomenon was occurring.

The duration of the average spike is about 20 minutes, which corresponds to a distance of 137 km travelled by the spacecraft. This is small relative to solar wind spatial scales, indicating the electrons are restricted to localized regions, akin to an electron beam. In addition, the electrons do not come from the solar direction, but are dominantly present when Ceres is contained in the field of view of the detectors, implying the electrons are streaming away from the planetary direction. Furthermore, the event pattern appears to be controlled by Dawn's location in the Ceres Solar Orbital coordinate system, providing strong evidence that the origin of the high-energy electrons were due to the solar wind interaction with the body.

The qualitative characteristics of the electron bursts at Ceres bear many similarities to the electron bursts observed by other planetary spacecraft as they cross a planet's electron foreshock. Electron bursts observed at planetary foreshocks have been characterized as lasting on the order of seconds to minutes, having electron energies on the order of tens of keV, and have been observed as far as tens of planetary radii from their respective planet (Anderson et al., 1979;

Trotignon et al., 1992; Chaizy et al., 1993; Sergis and Moussas, 2003). Langmuir plasma waves generated by the electron beam have also been identified as indirect evidence for an electron foreshock at Venus (Strangeway et al., 1995). The energetic electrons at these planets have been attributed to fast-Fermi acceleration at their planetary bow shocks. As solar wind electrons encounter a planetary bow shock, they enter a region where the magnetic field strength has increased. Electrons with high pitch angles get reflected and accelerated to conserve their magnetic moment (Wu, 1984; Leroy and Mangeney, 1984). Those electrons then gyrate along the Interplanetary Magnetic Field (IMF) field line tangent to the bow shock, creating a narrow beam called the electron foreshock. When a spacecraft happens to encounter the beam, it detects the electrons as short bursts in the timeseries. It is conceivable that this same mechanism is producing the electron bursts at Ceres and we postulate that they are the result of a temporary bow shock formed by either a transient atmosphere or an electrically conducting Ceres interior. This process allows the electrons to travel to the spacecraft from large distances and can provide explanations for why they occur at a particular location, how the bursts are seen 10 Ceres radii away from the body, and how the electrons are able to get to such high energies.

If fast-Fermi acceleration by a bow shock is responsible for these high-energy electrons, the location where the spacecraft detects the electron bursts should strongly depend on the direction of the IMF. Since the bursts were detected at similar locations, this would require similar IMF directions at the time of the detections. Dawn lacks the instrumentation traditionally used to detect electron bursts, plasma waves, and the magnetic field direction needed to confirm the geometry when an electron foreshock is present. We turn to models to determine the possible IMF arrangements that can be tangential to a hypothetical bow shock. In Chapter 6 we will use

models to infer the IMF direction and bow shock geometry that would be necessary for Dawn to encounter an electron beam at the location of the bursts.

Since the assumptions used to derive fast-Fermi theory are generally oversimplified, it would also be beneficial to use in-situ measurements to aid our study. The electron foreshock at Earth has been well studied and we can use various spacecraft to calculate the flux and energies of the reflected electrons with increasing distance from the point of tangency. Since the underlying physics for the Earth and Ceres cases should be the same, we can scale down the Earth results to the Ceres scale. Based on the Earth case, we can use the observations by GRaND to understand if the flux and energies of the electrons are consistent with what we would expect at the calculated travel distances to Dawn from our model. We explore this in the next chapter. The combined results of the model and in-situ data will allow us to discount or credit fast-Fermi acceleration as a likely process for these electrons.

4.7 Discussion

Ceres is not believed to be a magnetized body, so the genesis of the bow shock would have significant implications for its surface and/or internal processes. A transient atmosphere or a conducting layer are the best candidates to act as an obstacle to the solar wind. Recently, Küppers et al. (2014) reported intermittent observations of water vapor at the surface of Ceres using the Herschel Space Observatory. Models suggest that a transient atmosphere on Ceres could last approximately ten days, which is the same timescale over which the electron bursts occured (Formisano et al., 2016). Alternatively, if the planet has an electrically conducting layer, a bow shock can be generated as the layer prevents the penetration of the interplanetary magnetic field. An enhancement in the IMF due to a solar event could trigger such a response. There is

evidence for a partially molten or even perhaps liquid layer tens of kilometers beneath the surface abundant in salt (Castillo-Rogez et al., 2016), which could potentially act as a conductive layer. While this work alone cannot differentiate between an atmospheric or interior origin, the ability to confirm the presence of a bow shock lays the groundwork and provides constraints for future missions and studies.

Further investigation needs to be performed to better interpret the electron bursts. Empirical studies of Earth's electron foreshock will help understand how the electron foreshock varies with distance from the tangent point and connection location on the bow shock surface. Comparisons can help us understand whether the observations at Ceres are consistent with an electron foreshock. Further, magnetohydrodynamic (MHD) models would be useful in discerning what size exosphere would be needed to produce a bow shock, or if alternatively, a bow shock could be produced by an internal conductive layer similar to that proposed for Europa (Khurana et al., 1998). If confirmed, the observations could have significant implications for the composition and activity of the body.

4.8 References

Anderson, K. A. et al., Thin sheets of energetic electrons upstream from the Earth's bow shock, Geophysical Research Letters, Vol. 6, No. 5, 401-404 (1979).

Castillo-Rogez, J. et al., Where is Ceres' Ice Shell?, 47th Lunar and Planetary Science Conference abstract (2016).

Chaizy, P., K. A. Anderson, J. Sommers, and R. P. Lin, Evidence for accelerated electrons upstream from Jupiter's bow shock: Ulysses results, Planet. Space Sci., Vol. 41, No. 11/12, pp.833-838 (1993).

Feldman, W. C. et al., Solar Wind Electrons, Journal of Geophysical Research, Vol. 80, No. 31, 4181-4196 (1975).

Feldman, P. D. et al., The Nature and Frequency of the Gas Outbursts in Comet 67P/Churyumov-Gerasimenko Observed by the Alice Far Ultraviolet Spectrograph on Rosetta, The Astrophysical Journal Letters, 825, L8 (2016).

Formisano, M. et al., Ceres Water Regime: Surface Temperature, Water Sublimation, and Transient Exo(atmo)sphere, MNRAS 455, 1892-1904 (2016).

Khurana, K. K. et al., Induced magnetic fields as evidence for subsurface oceans in Europa and Callisto, Nature, 395, 777-780 (1998).

Küppers, M. et al., Localized Sources of Water Vapor on the Dwarf Planet Ceres, Nature 505, 525-527 (2014).

Leroy, M. M. and A. Mangeney, A theory of energization of solar-wind electrons by the Earth's bow shock. *Annales Geophys.* **2**, 449-456 (1984).

Mohammadzadeh, A. et al., The ESA Standard Radiation Environment Monitor Program First Results from PROBA-I and INTEGRAL, IEEE Transactions on Nuclear Sciences, Vol. 50, No. 6, 2272-2277 (2013).

Park, R. S. et al., A Partially differentiated interior for (1) Ceres deduced from its gravity field and shape, Nature, 537, 515-517 (2016).

Sergis, N. and X. Moussas, The Martian Electron Foreshock Based on Mars Global Surveyor's Measurements, Solar Physics, Volume 218, Issue 1, pp. 281-294 (2003).

Strangeway, R. J. and G. K. Crawford, Comparison of upstream phenomena at Venus and Earth, Adv. Space Res., Vol. 16, No. 4, pp. (4)125-(4)136 (1995).

Trotignon, J. G. et al., Electron Density in the Martian Foreshock as a By-Product of the Electron

Plasma Oscillation Observations, Journal of Geophysical Research, Vol. 97, No. A7, 10831-10840 (1992).

Wu, C. S., A Fast Fermi Process: Energetic Electrons Accelerated by a Nearly Perpendicular Bow Shock, Journal of Geophysical Research, Vol. 89, NO A10, 8857-886 (1984).

Yamashita, N. et al., Catalog of Transient Radiation Events Detected by GRaND at Vesta and Ceres, 49th Lunar and Planetary Science Conference, Abstract 1152 (2018).

Chapter 5

Analyzing STEREO A Data as an Analog to Characterize the Evolution of Electron Foreshocks with Distance

5.1 Introduction

The electron bursts from the previous chapter could not be explained solely by solar wind activity. Instead, the appearance of the bursts were well correlated with the location of the Dawn spacecraft in Ceres-Solar Orbital Coordinates. The bursts lasted on the order of 10 days and reoccurred in the same locations before suddenly disappearing. The nature of the electron bursts resembled electron bursts observed by spacecraft as they transited electron foreshocks. In this chapter, we investigate fast-Fermi acceleration as a possible mechanism to explain the Dawn bursts. We explore the characteristics of the electron foreshock at Earth and compare it to the electron bursts observed at Dawn.

5.2 Electron Foreshocks and Fast-Fermi Acceleration Overview

To begin, we provide an overview of the literature relating to electron foreshocks and the fast-Fermi acceleration process that yield them. The most well-documented electron foreshock is that of the Earth's. Earth's electron foreshock was first discovered by near-Earth spacecraft when the spacecraft were along interplanetary magnetic field (IMF) lines which connected them to the bow shock surface and observed sudden bursts in flux of energetic electrons traveling opposite to the solar wind flow direction (Fan et al., 1964). Subsequent observations provided details on the

characteristics of the electron foreshock: solar wind electrons can become accelerated up to 100 keV after being reflected by the bow shock, the highest energetic electrons were associated with magnetic field lines near tangency, bursts typically lasted on the order of seconds to minutes, bursts were observed tens of R_E upstream from Earth, and the bump-on-tail distribution gave rise to Langmuir waves (Anderson, 1979; Anderson, 1981; Fitzenreiter, 1995). Electron foreshocks and/or their related plasma waves have also been detected at Venus, Mars, Jupiter, Saturn, Uranus, and Neptune.

Fast-Fermi acceleration as a method to produce the electron foreshock was first proposed contemporaneously by Wu (1984) and by Leroy and Mangeney (1984). The theory for energization of electrons at the bow shock surface is similar in concept to that proposed by Fermi (1954) regarding the origin of cosmic rays: particles can get reflected and accelerated when encountering a magnetic mirror. Wu (1984) and Leroy and Mangeney (1984) took similar approaches to derive the net energization of the electrons. They first assume a one dimensional, planar stationary shock relative to the upstream bulk solar wind velocity, V_0 and the upstream interplanetary magnetic field, B_0. They transform into the deHoffman-Teller reference frame where V_0 becomes parallel to B_0 so that the convection electric field, $E' = -V_0' \times B_0 = 0$ (primed values represent the corresponding values in the deHoffman-Teller reference frame). In this reference frame the energy of the particle is constant. This requires a velocity V_{HT} along the shock plane such that $V_{HT} = \frac{\hat{n} \times (\vec{V}_0 \times \hat{b})}{\hat{n} \cdot \hat{b}}$. The restriction $E' = 0$ results in the condition of $E'(x) \times \hat{n} = 0$ everywhere within the shock, where x=0 refers to the start of the shock upstream and x=L is the width of the shock transition region. Therefore, $E'(x)$ can also be written as an electric potential $\phi'(x)$. The energy of the electron across the shock can then be expressed by:

$$\frac{1}{2} m v_{\parallel}^2(x) + \frac{1}{2} m v_{\perp}^2(x) - e\phi'(x) = \frac{1}{2} m v_{\parallel}^2(x) + \mu B(x) - e\phi'(x) = constant$$

where the particle's velocity components are relative to the magnetic field B(x) within the shock, μ is the electron's magnetic moment, and e is the charge of the electron. Since the electron will conserve its magnetic moment, it follows that a particle cannot successfully cross the shock if its magnetic moment exceeds

$$\mu \geq \frac{1}{B(L) - B_0}\left(e\phi'(L) + \frac{1}{2}mv_{\parallel}^2(0)\right)$$

in which case it will get reflected at the shock. It can be shown transforming back into the stationary bow shock frame, the reflected particle has increased its energy by $E_{r\parallel} \sim 4\frac{cos^2\theta_{Vn}}{cos^2\theta_{Bn}}\frac{1}{2}mV_0^2$, where θ_{Vn} is the angle between V_0 and the shock normal and θ_{Bn} is the angle between B_0 and the shock normal. The equation for the reflected electron energy shows that the energy of the particle rapidly increases with increasing θ_{Bn}. However, it can also be shown the flux of particles drastically falls off as θ_{Bn} approaches 90 degrees. This is illustrated in Figure 5.1. Leroy and Mangeney (1984) note that the equation for the predicted flux overestimates the flux at low energies ($\leq 500\ eV$) and underestimates the flux at high energies ($\geq 5\ keV$) when compared to observations.

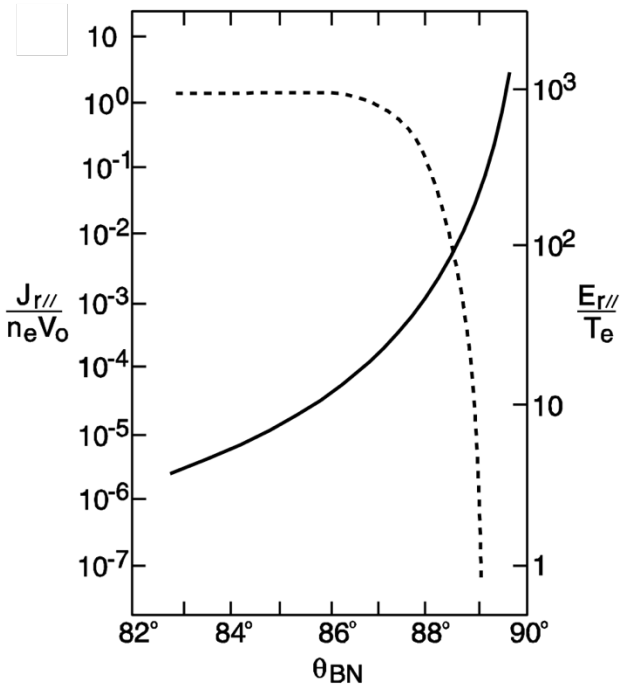

Figure 5.1 *Electron Flux (left y-axis, dashed line) and its corresponding energization (right y-axis, solid black line) as a function of θ_{Bn}. As the energization approaches infinity, the flux goes to zero. Figure from Leroy and Mangeney (1984).*

5.3 STEREO A Electron Bursts

Since the assumptions used to derive fast-Fermi theory are generally simplified, it will also be beneficial to use in-situ measurements to aid our understanding. In this study, we are most interested in understanding how the statistics of flux and connection rates vary with distance from the planet. Many of the previous studies of Earth's bow shock have been performed using spacecraft close to the bow shock, which limited the distance for which the electron foreshock has been observed. Therefore, we have opted to study the early mission STEREO A (STA) Solar Electron Proton Telescope (SEPT) 1 minute data (Müller-Mellin et al., 2008) to evaluate the electron foreshock. STEREO A is advantageous because it provides information about the electron foreshock as the spacecraft continuously increased its distance from Earth. The SEPT instrument consists of four telescopes: two in the ecliptic which are aligned along the Parker Spiral with one

telescope looking sunward and the other looking antisunward and two others that point North-South perpendicular to the ecliptic plane. Its electron detector measures electrons from 30-400 keV.

The energetic electrons detected by Dawn were determined to have an energy range between 20-100 keV (Chapter 4). Hence, in this case study we focus on the SEPT electrons within that range, from 50-95 keV with the energy bins having a $\Delta E \sim 10$ keV. We use the SEPT telescopes pointing sunward/antisunward since foreshock electrons should be observed coming from the antisunward direction, with the sunward-looking telescope allowing us to differentiate the incoming electron direction. Figure 5.2 shows an example of electron bursts at 60 keV seen in the antisunward direction but absent in the sunward telescope. Health records reported normal activity, indicating these bursts were not due to changes in instrument settings. We assume multi-point electron bursts observed in the anti-sunward direction and not present in the sunward telescope to be sourced from the electron foreshock.

We implement a similar process used to identify the electron bursts at Dawn to systematically identify electron bursts in the SEPT data. We categorize potential electron bursts by using a 300 point window centered on each data point to identify if they are two standard deviations above the mean within this time window. Data points marked as potential bursts are then replaced by the average of the twenty adjacent data points, centered on the burst. We then create a background spectrum by using a 100-point smoothing scheme. We subtract the smoothed background from the original data set. This removes the background variation caused by changes in solar conditions and allows us to directly compare the magnitude of the bursts. Enhancements greater than 2.5 standard deviations above the mean of the full length of the array are categorized

as electron bursts. We ignore any single-point enhancements as these may be glitches or gamma ray bursts. The steps of the identification process are shown in Figure 5.3.

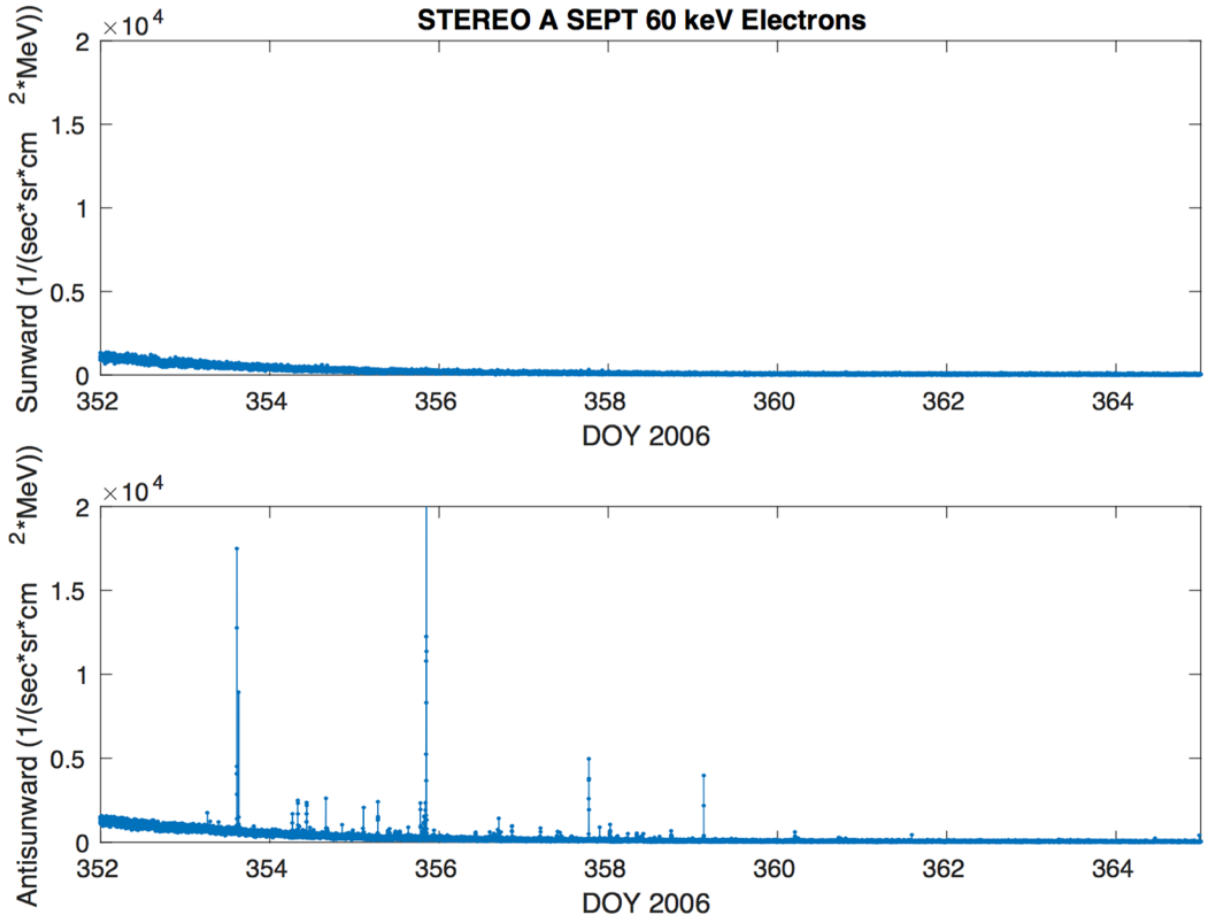

Figure 5.2 *STEREO A SEPT 60 keV electrons. The top panel shows the flux in the sunward direction while the bottom panel shows the flux in the antisunward direction. Electron bursts are present in the antisunward detector but are absent in the sunward detector.*

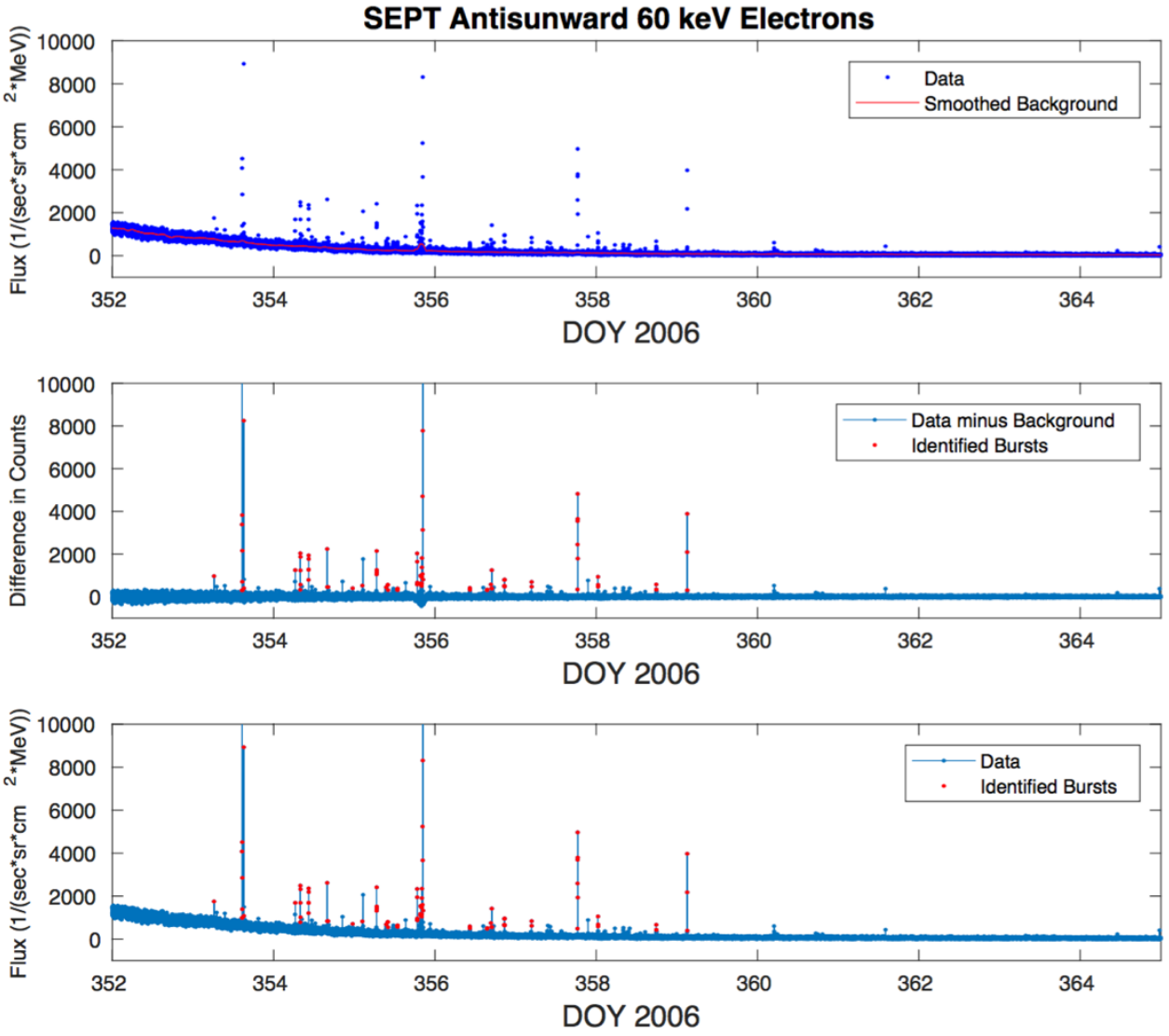

Figure 5.3 *Identification of electron bursts in the STA SEPT data. Top panel: The data is removed of sudden enhancements and smoothed to create a background spectrum. Middle panel: the background spectrum is subtracted from the data and enhancements >2.5 standard deviations are identified as bursts (red dots). Bottom panel: Electron bursts identified shown in the original timeseries of the SEPT data.*

We applied this algorithm to each SEPT energy bin between 50-100 keV to scan the data for electron bursts from December 18th, 2006-May 31st, 2007. The 70 keV bin had technical issues and is not used. We begin our search after December 18th, 2006 (DOY 352) as this is after the lunar gravity assists had been performed, allowing STEREO A to be on a direct trajectory into orbital insertion around the Sun and also after the large CME event seen on December 14th, 2006 (the tail-end of which can be seen at the beginning of Figure 5.2). Though this is the beginning of the mission, the pointing of the spacecraft is close to nominal during this time period, allowing us to be confident in the look directions of the anti-sunward/sunward telescopes.

Figure 5.4 shows all the electron bursts classified by our algorithm, with each energy bin having ~30 bursts identified in their time series. The figure shows the electron bursts in each channel typically occur simultaneously, which is consistent with the presence of electron foreshocks: >2 keV electrons are believed to be sourced from a narrow region on the bow shock when the IMF connecting the spacecraft to the shock is near tangency. Additionally, the lower energy electrons have larger fluxes than the higher energy bins, as would be expected of foreshock electrons since we would expect the flux to drop off with increased energization. Only the two largest magnitude bursts were seen in the 115 keV energy bin (the adjacent energy bin to 95 keV), implying a cutoff in energy at ~100 keV, consistent with previous observations of the foreshock. The average duration of the bursts were 5 minutes, with all energy channels showing similar time lengths. The bursts occurred frequently in clusters between DOY 352-360 when STEREO A was closer to Earth (~100 R_E) and became less frequent and appeared as singular bursts when the spacecraft drifted further away. No bursts are seen after DOY 384, when the spacecraft was ~300 R_E from the Earth. To fully understand the context of the identified bursts, re-creation of their geometry relative to the bow shock source is needed. We examine this in the next section.

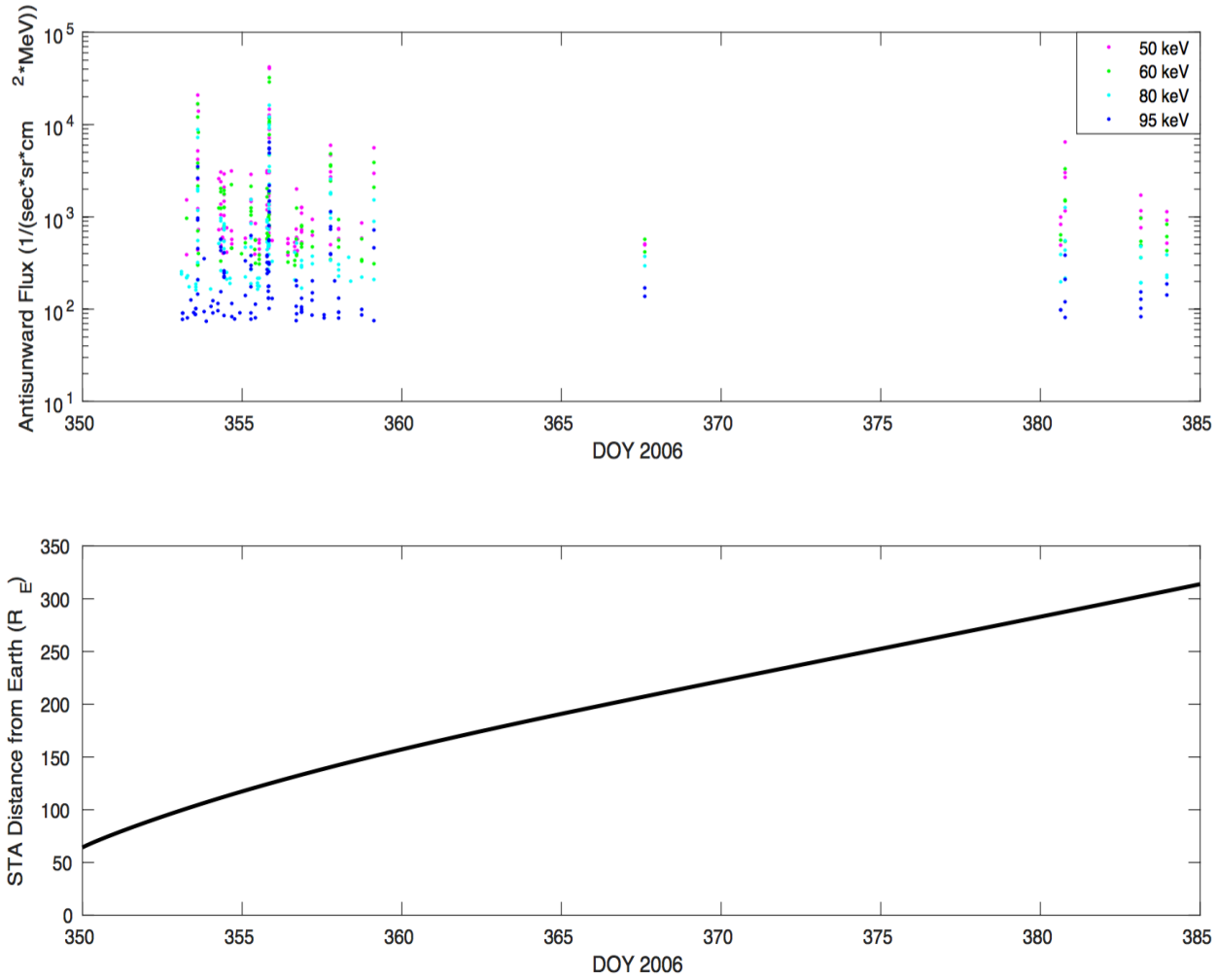

Figure 5.4 *Top panel: Timeseries of the electron bursts identified in each SEPT energy bin. Red dots indicate 50 keV electrons, magenta dots 60 keV electrons, cyan dots 80 keV electrons, and blue dots 100 keV electrons. The electrons bursts in each channel typically occur simultaneously. Bottom panel: Timeseries showing the increasing distance of STEREO A from Earth.*

5.4 Bow Shock Surface Model

We begin our analysis by constructing a bow shock surface model to analyze the geometry at the instance of every electron burst identified in each SEPT energy bin. We orient ourselves in the Geocentric-Solar Ecliptic (GSE) Coordinate system, where $+X_{GSE}$ points from the Earth to the Sun, $+Y_{GSE}$ is the direction opposite of orbital motion, and $+Z_{GSE}$ points perpendicular to the ecliptic plane in the North direction. The surface of Earth's bow shock can be approximated as an axisymmetric paraboloid, defined by $x=A_s-B_s(y^2+z^2)$, where A_s and B_s are the bow shock nose location and the flaring parameter of the paraboloid, respectively. The parameters A_s and B_s vary with the solar wind conditions and are calculated by

$$A_s = A_{MP}\left[1 + 1.1\frac{(\gamma-1)M_1^2+2}{(\gamma+1)(M_1^2-1)}\right] R_E$$

$$B_s = 0.0233\left(\frac{P_{sw}}{1.8\ nPa}\right)^{\frac{1}{6}} R_E^{-1}$$

$$A_{MP} = \left[11.4 + (K * B_z)\right]P_{sw}^{\frac{-1}{6.6}}$$

where A_{MP} is the distance from the Earth to the magnetopause, gamma is the ratio of specific heats and is set to γ=5/3, M_1 is the upstream Magnetosonic Mach number, P_{SW} is the solar wind dynamic pressure, B_z is the Z component of the IMF, and K=0.013 for $B_z > 0$ and K=0.140 for $B_z < 0$ (Farris and Russell, 1994; Chapman and Cairns, 2003; Shue et al., 1997). We take into account aberration due to the incoming solar wind by defining the axis of revolution to be antiparallel to the solar wind direction so that $\hat{x} = -\frac{\overrightarrow{V_{sw}}}{|V_{sw}|}$. All variables thus mentioned are calculated using the solar wind OMNI 1 minute data (https://omniweb.gsfc.nasa.gov/ow_min.html). In instances where the OMNI data was unavailable for a specified electron burst, an average bow shock surface was used, with A_s=13.4 R_E and B_s=0.022 R_E^{-1}, and the axis of revolution antiparallel to the average direction of

the solar wind. We use a grid size of 0.3 R_E to create the bow shock surface and allow the bow shock to extend to -200 R_E along the X_{GSE} axis.

The STEREO A ephemeris data was used to establish its location in GSE coordinates. We also use the STEREO A 1 minute magnetometer data and use the instantaneous vector direction to extrapolate the spacecraft's connection to the bow shock by approximating the IMF as a straight line. We use the extrapolated IMF line and the modeled bow shock surface to determine if and where the IMF line touches the bow shock surface. Since the energization of the particles should be dependent on θ_{Bn}, we calculate the angle between the instantaneous IMF and the bow shock normal at the point of closest approach. The bow shock normal at a location (X_{GSE}, Y_{GSE}, Z_{GSE}) can be calculated by taking the gradient of the paraboloid:

$$\hat{n} = \frac{\langle -1, -2B_s y, -2B_s z \rangle}{\sqrt{1 + 4B_s^2 y^2 + 4B_s^2 z^2}}$$

Figure 5.5 shows an example of the geometry for an arbitrary burst identified in the 50 keV energy bin. The location of STEREO A is indicated by the red square, the IMF line is represented by the black solid line, the bow shock surface is plotted using blue dots, and the bow shock normal at the connection point is shown by the cyan vector. We evaluate the changes in shock connectivity in the next section.

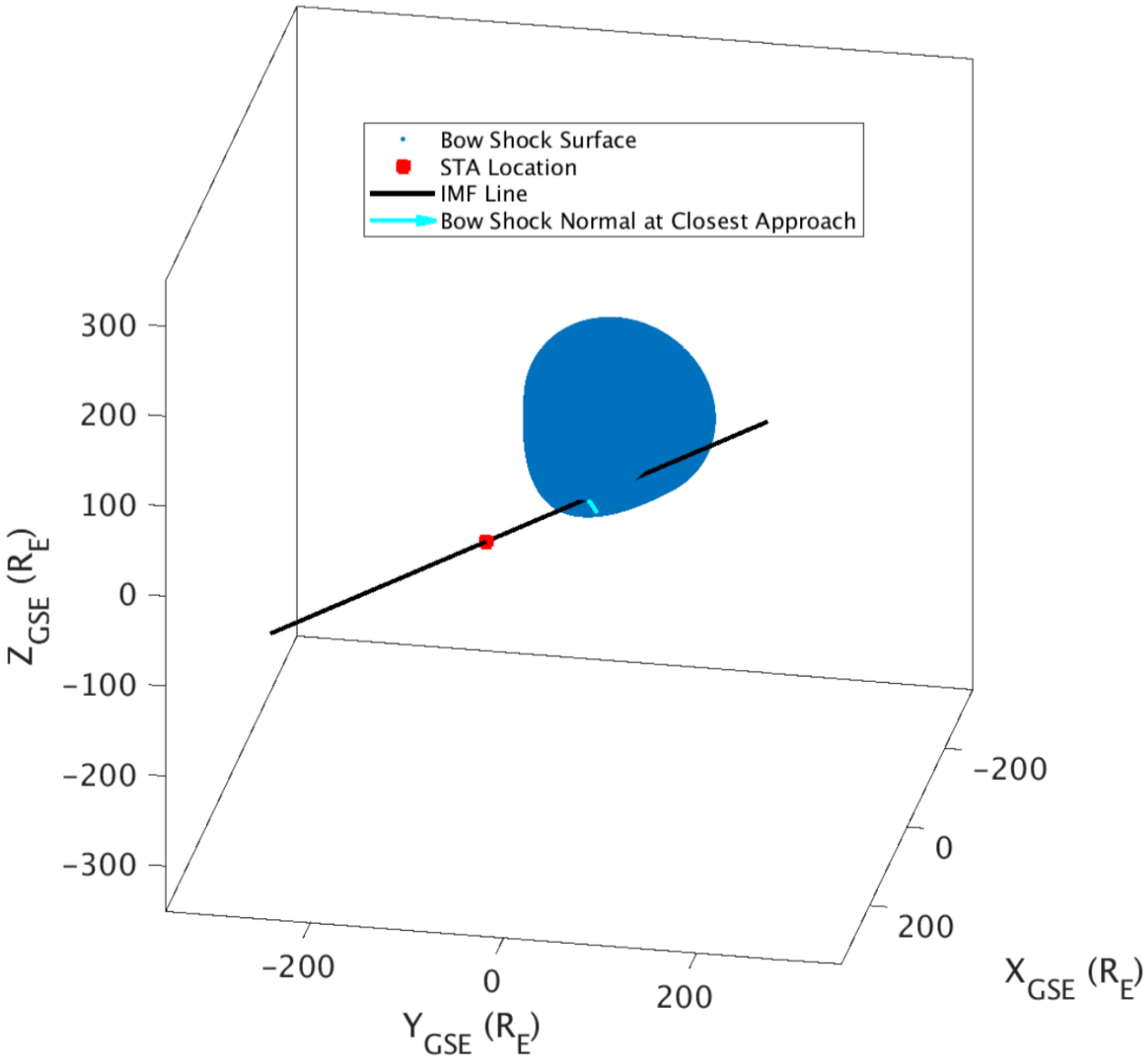

Figure 5.5 *Example of re-created geometry at the instant each electron burst is detected. Ephemeris data is use to establish the location of STA (red square) in GSE coordinates. The STA magnetometer data is used to extrapolate the magnetic field (solid black line) to Earth's distance and analyze how it connects to Earth's bow shock (blue dots), which includes its aberration from the solar wind. We also calculate the normal vector at the connection point, shown in cyan.*

5.5 Results

We analyzed how the electron burst flux varies with several parameters using the geometry from our model. The first value we computed was the X_{GSE} location of the shock at the point of connection between the IMF and the bow shock surface, which we refer to as X_{shock}. This will tell us whether the spacecraft is connecting more toward the nose of the shock, where the shock is strongest, or more tailward, where the shock is weaker. We also considered the distance between the IMF line and its closest approach to the bow shock surface (ie. whether it is magnetically connected to the shock), which we call R_{min}. R_{STA} refers to the distance of STEREO A to the point of closest approach between the IMF line and the shock. Lastly, we also outputed θ_{Bn}, the angle between the IMF line and the normal of the bow shock at closest approach. We normalized all the above distances by the distance from the Earth's center to its bow shock nose, A_s, since we are interested in how these values will scale to the Ceres environment.

Figure 5.6 shows the dependence of the electron flux with each of the above values calculated from our model. Panel A and Panel C show the strongest trends in electron flux with their corresponding variables. Panel A suggests the electron flux drops off with the connection point on the surface: the bursts are larger in magnitude closer to the bow shock nose and decrease when connected further down the tail. However, Panel C also shows a similar general fall-off in electron flux. The flux of the electrons drop with the increasing distance the electrons must travel along the IMF to get to STEREO A. It is unclear whether the fall-off in flux is due to the location on the shock the IMF is connected or to the increased distance of the spacecraft along the IMF, or both.

In Panel B, a value of R_{min}=0 designates the extrapolated IMF line is intersecting the bow shock. While our model predicts many of the bursts were directly connected to the shock, not all

of them show connection. This could possibly be due to our approximation of the IMF as a straight line. This approximation is best when closest to the bow shock but becomes more crude the further STEREO A drifts from the Earth.

From fast-Fermi theory, we should expect the source region of such energetic electrons to be restricted to θ_{BN}~90 degrees. While Figure 5.6 Panel D does display a small cluster in this range, a majority of the bursts appear to have a θ_{BN}<80 degrees. From Panel A we know that a majority of the bursts are being sourced from near the nose of the shock, where the surface normal of the shock is rapidly changing. Deviations of the actual bow shock surface from our model in combination with our simplified approximation of the IMF as a straight line can easily lead to errors in the calculation of θ_{BN}.

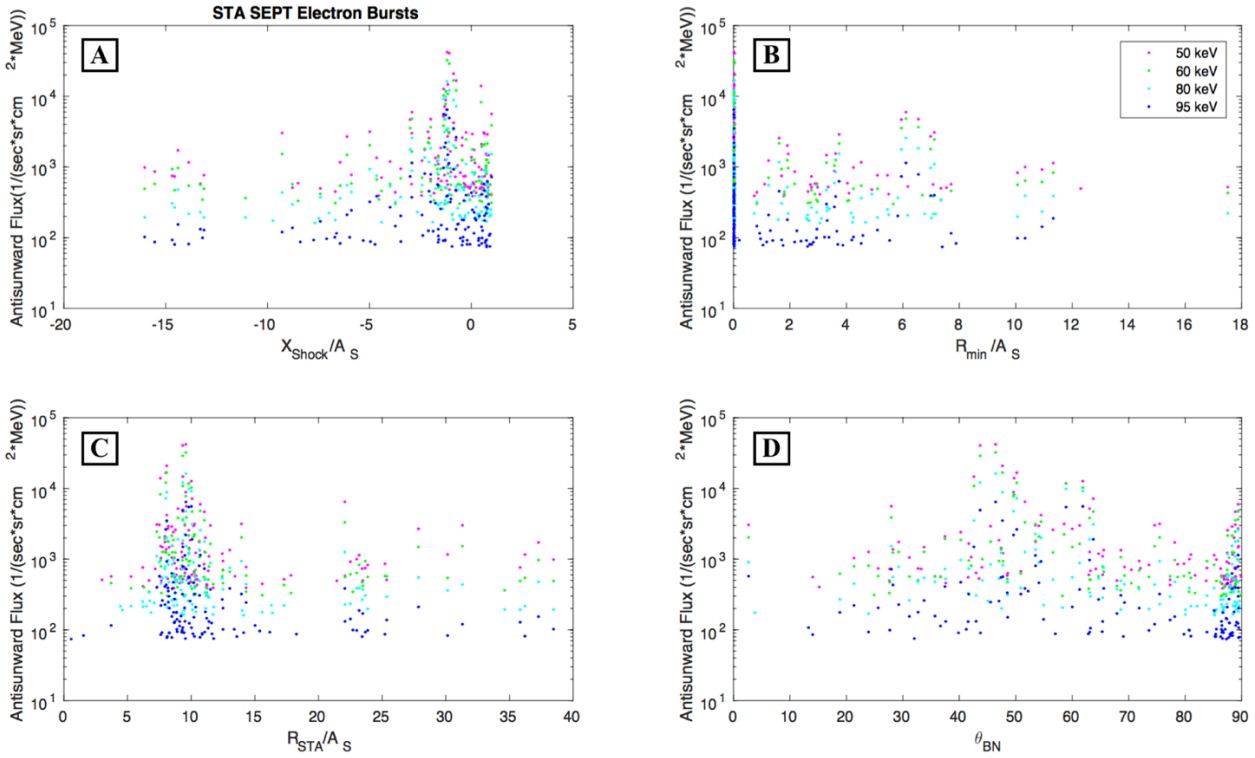

Figure 5.6 *Variation in the flux of electron bursts with variables outputted from the bow shock model. Panel A: Dependence of the flux with the connection location on the shock. Panel B: Dependence of the flux with the distance of the IMF line from the bow shock. Panel C: Dependence of the flux with the distance of STEREO A along the IMF line. Panel D: The dependence of the flux with* θ_{BN}*. All distance values are normalized by the distance to the bow shock nose,* A_s*.*

5.6 Comparisons of Dawn's Electron Bursts with STEREO Data

In Chapter 4, we reported that Dawn's Gamma Ray and Neutron Detector (GRaND) detected energetic electron bursts with energies 20-100 keV. Figures 5.7 and 5.8 show the resemblance between the electron bursts seen by Dawn and by STEREO A on six day and five hour timescales, respectively. The SEPT data have a resolution of 1 minute while the GRaND data is lower resolution at 3.5 minutes. Still, it is clear to see that both timeseries look strikingly similar qualitatively. In both cases, the electron bursts are on the order of tens of keV and manifest as sudden enhancements relative to the background. STEREO A detects the bursts with a steady frequency while Dawn does not due to its orbit, resulting in days-long gaps in bursts when it is not located in a favorable position to detect the bursts. As can be seen in Figure 5.8, STEREO A detects bursts in clusters similar to that as Dawn until it is ~150 R_E from Earth, after which the bursts become singular (Figure 5.4). In the SEPT case, the average duration of a burst is ~5 minutes while the average length of a GRaND burst is four times longer ~20 minutes. However, in five minutes STEREO A travels a distance of ~5,400 km, while Dawn only travels ~140 km in twenty minutes. Hence, though the electron bursts at Earth are shorter in time, the width of the electron foreshock is much larger than that at Ceres.

In Chapter 6, we will use magnetohydrodynamic models to show that a bow shock size produced by vapor production rates reported for the cerean exosphere suggest a bow shock nose ~1.5 R_C. From Figure 5.6 panel C, it is clear that STEREO A frequently detects the shock when R_{STA}/A_s <15. For distances larger than this, the connectivity is sparse and the flux begins to drop off. Assuming a foreshock with these same properties at Ceres and with an assumed cerean A_s~1.5 R_C, this indicates that the bursts are capable of being frequently detected out to ~22 R_C, given a

detector with similar sensitivity. The June 2015 electron bursts were observed when Dawn was at a distance of 10 R_C, well within this range.

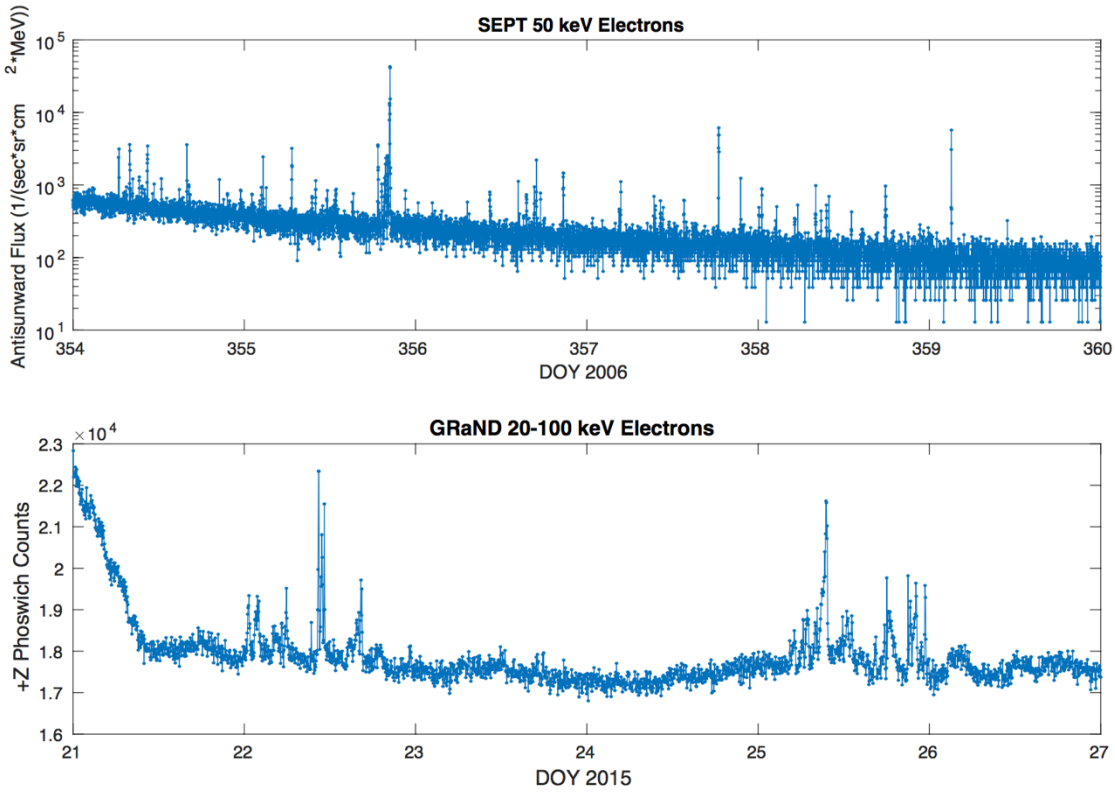

Figure 5.7 *Comparisons of the SEPT 50 keV bursts and the electron bursts detected by GRaND over a six day period.*

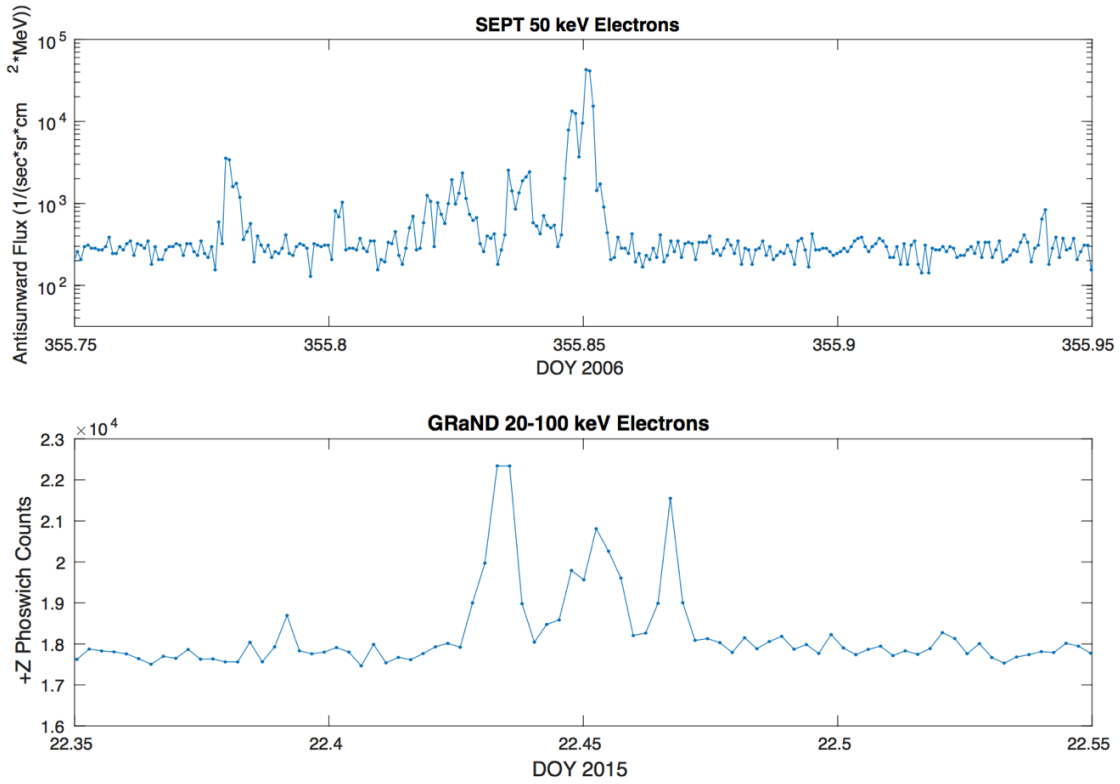

Figure 5.8 *Comparison of the SEPT 50 keV electron bursts and the electron bursts detected by GRaND over a ~5 hr period. Bursts in both cases typically occur in clusters.*

5.7 Summary

Fast-Fermi acceleration provides a reasonable explanation for the energization of electrons up to 100 keV detected at Ceres. It is also consistent with the presence of the electrons restricted to localized regions in the orbit. Dawn does not carry a magnetometer and therefore no information on shock crossings or the in-situ magnetic field direction can be obtained. Despite this, the Ceres-Solar Orbital location dependence and the physical characteristics of the Dawn bursts provide strong support for the presence of an electron foreshock at Ceres.

5.8 References

Anderson, K. A., A Review of Upstream and Bow Shock Energetic-Particle Measurements, Il Nuovo Cimento, Vol. 2C, N. 6, 747-771 (1979).

Chapman, J. F. and I. H. Cairns, Three-Dimensional Modeling of Earth's Bow Shock: Shock Shape as a Function of Alvén Mach Number, Journal of Geophysical Research, Vol. 108, No. A5, 1174 (2003).

Fan et al., Evidence for >30 keV electrons accelerated in the shock transition region beyond the Earth's magnetospheric boundary, Phys. Rev. Lett., 13, 149 (1964).

Farris, M. H. and C. T. Russell, Determining the Standoff Distance of the Bow Shock: Mach Number Dependence and Use of Models, Journal of Geophysical Research, Vol. 99, No. A9, 17,681-17689 (1994).

Fermi, E., Galactic Magnetic Fields and the Origin of Cosmic Radiation, The Astrophysical Journal, Vol. 119, No. 1, 1-6 (1954).

Fitzenreiter, R. J., The Electron Foreshock, Adv. Space Res. Vol. 15, No. 8/9, (8/9)9-(8/9)27 (1995).

Leroy, M. M. and A. Mangeney, A theory of energization of solar-wind electrons by the Earth's bow shock. Annales Geophys. 2, 449-456 (1984).

Müller-Mellin, R. et al., The Solar Electron and Proton Telescope for the STEREO Mission, Space Science Reviews, 136, 363-389 (2008).

Shue, J. H. et al., A New Functional Form to Study the Solar Wind Control of the Magnetopause Size and Shape, Journal of Geophysical Research, 102, 9497-9511 (1997).

Wu, C. S., A Fast Fermi Process: Energetic Electrons Accelerated by a Nearly Perpendicular Bow Shock, Journal of Geophysical Research, Vol. 89, NO A10, 8857-886 (1984).

Chapter 6

Magnetohydrodynamic Models for a Cerean Bow Shock

6.1 Introduction

In Chapter 4 we proposed that the energetic electron bursts observed in the exterior scintillators of the Gamma Ray and Neutron Detector (GRaND) could be produced by fast-Fermi acceleration of solar wind electrons as they were reflected by a bow shock surface and created an electron foreshock. However, since Ceres' internal structure does not include a metallic core (Park et al., 2016), a bow shock cannot be produced by an intrinsic magnetic field. In this chapter, we explore alternative mechanisms that can produce a bow shock at Ceres.

There are two possible mechanisms that can act as an obstacle to the solar wind: an exosphere or a conductive layer at depth. Over the past three decades Ceres has been observed to have a transient exosphere; this exosphere could potentially mass-load the solar wind and slow it down to create a bow shock. Alternatively, geochemical models suggest a muddy, saline layer may persist today (Castillo-Rogez et al., 2016). This could produce an induced dipole through magnetic induction which can oppose sudden changes in the interplanetary magnetic field and potentially result in a bow shock. In this chapter, we employ magnetohydrodynamic (MHD) models for both an exospheric and internal source to produce a bow shock. We investigate what internal and surface conditions are necessary to recreate the bow shock geometry and timescales needed to be consistent with the GRaND burst observations. We further analyze the likelihood these conditions are present at Ceres.

6.2 Magnetohydrodynamic Model Description

In this study, we use a single-fluid magnetohydrodynamic (MHD) simulation to model the conditions necessary to generate a bow shock. This model has previously been applied to Saturn's moons by Jia et al. (2010) to replicate the moons' interactions with the magnetospheric plasma. The simulation uses a Cartesian grid set in Ceres Solar Orbital (CSO) coordinates, where $+X_{CSO}$ points from the sun toward Ceres' center, $+Y_{CSO}$ is the direction of orbital motion, and $+Z_{CSO}$ completes the right hand set. The domain size of the model is a rectangle with lengths of 80 x 40 x 40 R_c (R_c~500 km) centered on Ceres and varies its grid size from 0.6 R_C (~300 km) at the edge of the domain to 1/12 R_c (~40 km) near Ceres' surface. An exception is our Case 1, where a higher resolution grid size of 1/24 R_C is used due to the low vapor production rate. The standard MHD model that we used for the first five cases assumes an ion gyroradius smaller than the grid size, while the actual ion gyroradius is larger than Ceres. Thus, the MHD result is useful in estimating the shock distance and the size of the atmosphere while not necessarily replicating downstream conditions.

Our MHD model investigates the effects of both an exosphere and internal conductor and therefore we vary the inner boundary conditions to differentiate between the two scenarios. In both cases, the cerean surface is set as the inner boundary. For the exospheric case, the solar wind plasma is absorbed onto the surface and water neutrals are released from the surface, with the flux rate set to a specified value and location for each case. In all exospheric cases, the temperature of the water neutrals is set to 170 K, the same as the surface temperature with zero velocity at the surface. We allow the magnetic field to convect through Ceres unperturbed. In contrast, to replicate the effects of an internal conductor at depth, we set the cerean surface to be

a perfect conductor. This requires the radial component of the magnetic field to be zero at the cerean surface.

The model applies the conservation of mass, conservation of momentum, and conservation of energy equations:

$$\frac{\partial \rho}{\partial t} + \boldsymbol{\nabla} \cdot (\rho \boldsymbol{u}) = Q_\rho$$

$$\frac{\partial (\rho \boldsymbol{u})}{\partial t} + \boldsymbol{\nabla} \cdot (\rho \boldsymbol{u}\boldsymbol{u}) = \rho \boldsymbol{g} - \nabla p + \boldsymbol{J} \times \boldsymbol{B} + \boldsymbol{Q}_M$$

$$\frac{\partial p}{\partial t} + \boldsymbol{\nabla} \cdot (\rho \boldsymbol{u}) = -(\gamma - 1) p (\boldsymbol{\nabla} \cdot \boldsymbol{u}) + Q_p$$

where ρ is the plasma mass density, u is the velocity of the plasma, p is the thermal pressure, g is gravity, J is the current density, B is the magnetic field, Q are the source terms, and γ=5/3. The plasma density is calculated by ρ=nm, where n denotes the ion number density and m the ion mass. The pressure is calculated by p=nkT, where the k is the Boltzmann constant and T is the temperature of the plasma. In this model, we assume the thermal pressures of the ions and electrons are equal. The magnetic field is frozen-in to the plasma and can be described by $\frac{\partial \boldsymbol{B}}{\partial t} = \boldsymbol{\nabla} \times \boldsymbol{u} \times \boldsymbol{B}$. We solve Ampere's law to calculate the current density, $\boldsymbol{J} = \boldsymbol{\nabla} \times \mathbf{B} / \mu_0$.

The model takes into account photoionization, impact ionization, and charge exchange. We denote impact ionization by IN, and calculate it by $IN = m n_n f_i$, where m is the ion mass, n_n is the neutral density, and f_i is the combined rate of photoionization and impact ionizations. Likewise, we denote charge exchange by CX and calculate it by $CX = m n_n n k_{in}$, where k_{in} is the ion-neutral charge exchange rate. The source terms used in the governing equations are calculated by:

$$Q_\rho = IN$$

$$\boldsymbol{Q_M} = (IN + CX)\boldsymbol{u_n} - CX\boldsymbol{u}$$

$$Q_p = \frac{\gamma - 1}{2}(IN + CX)(\boldsymbol{u_n} - \boldsymbol{u})^2 + \frac{k}{m}(2INT_n + CX(T_n - T_i))$$

where u_n is the velocity of the neutrals and T_n is the temperature of the neutrals. The combined photoionization and impact ionization rate for both hydrogen and water group neutrals is $f_i=10^{-7}$ s^{-1} (Huebner et al., 1992), while the charge exchange rate is $k_{in}=2x10^{-15}$ m^3/s (Häberli et al., 1997). The average surface temperature of Ceres is ~170 K. Therefore, we set the neutral speed to u_n=360 m/s and let the neutral particles flow radially outward.

At the time of the electron burst event, Ceres was approaching opposition, with less than 30° separation between Earth and Ceres. Therefore, we use solar wind measurements from the Advanced Composition Explorer (ACE) and Wind, both solar wind monitors located at the L1 Lagrange point of Earth, to extrapolate the solar wind conditions to Ceres' location at 2.8 AU. Since the travel time for the solar wind from Earth to Ceres is about 6 days (assuming ~500 km/s velocity), we averaged the solar wind conditions at 1 AU between June 13-19, 2015 to extrapolate conditions to Ceres' distance for June 19-25, 2015 and assume these conditions are steady during the duration of the simulation. The extrapolated solar wind values are shown in Table 1. These are the solar wind conditions used in each MHD simulation unless otherwise noted. Using these parameters, the solar wind plasma is allowed to flow from the –X direction until steady state is reached.

In the simulations presented in this paper, we investigate what combinations of gas production rates and source locations are capable of producing a bow shock. A bow shock is identified by instances where the obstacle mechanism is sufficient enough to convert the supersonic solar wind to subsonic, allowing the solar wind flow to divert around Ceres. We then assess whether each simulation is capable of producing the geometry needed for the magnetic field to connect the bow shock to the location of the Dawn spacecraft at the time of the electron

bursts detected by GRaND's +Z Phoswich (Chapter 4). We chose to focus on these bursts because they correspond to the largest magnitude and most frequent bursts detected by Dawn.

Parameters	Value Used
Solar wind density, n_{sw}	1.3 cm^{-3}
Velocity, u_{sw}	500 km s^{-1}
IMF $(B_x, B_y, B_z)_{sw}$	(-1.2, 0.88, -0.45) nT
Solar wind temperature, T_{sw}	10^5 K
Alfvenic speed, V_A	30 km s^{-1}
Sonic speed	37 km s^{-1}
Mach number	12
Plasma β	2

Table 6.1 *Solar wind conditions used for the MHD simulations. Solar wind values are extrapolated from the ACE and Wind Spacecraft located at 1 AU during June 19-25, 2015.*

6.3 Case Studies

6.3.1 Single-fluid MHD Models for a Global Exosphere

6.3.1.1 Lower Limit to Produce a Shock

We begin by evaluating the lower limit production rate necessary to create a bow shock at Ceres. In this simulation, the water vapor is released globally at a rate of 1.8 kg/s ($6x10^{25}$ H_2O/s). The heavy water molecules become ionized and picked-up by the solar wind, thereby mass-loading the solar wind and causing it to slow down. These conditions reflect a scenario that could be produced by the release of water molecules from the global water-ice table reservoir, which is within 1 m of the surface for latitudes greater than 40 degrees (Prettyman et al., 2017). Figure 6.1 shows X-Z and X-Y plane slices of the mass density of the lower limit global model in CSO coordinates. The blue circle traces the Survey orbit and the black squares indicate the locations of the strongest bursts seen by the +Z Phoswich. Our analysis shows a weak but

identifiable shock develops just above the cerean surface at 1.1 R_C. The global exosphere gives rise to a bow shock that is rotationally symmetric about the X-axis. A follow-up run using a global release rate of 0.9 kg/s ($3x10^{25}$ H_2O/s) did not show the formation of a bow shock upstream, indicating it was below the threshold. Therefore, we conclude that for a globally-released exosphere a minimum gas flux rate of $6x10^{25}$ H_2O/s must be present to form a bow shock.

The minimum 1.8 kg/s ($6x10^{25}$ H_2O/s) flux rate is considerably lower than the vapor production rates reported by telescopic observations, which report ~$2x10^{26}$ H_2O/s on positive detections. This implies that a bow shock should have been present during each positive telescopic detection.

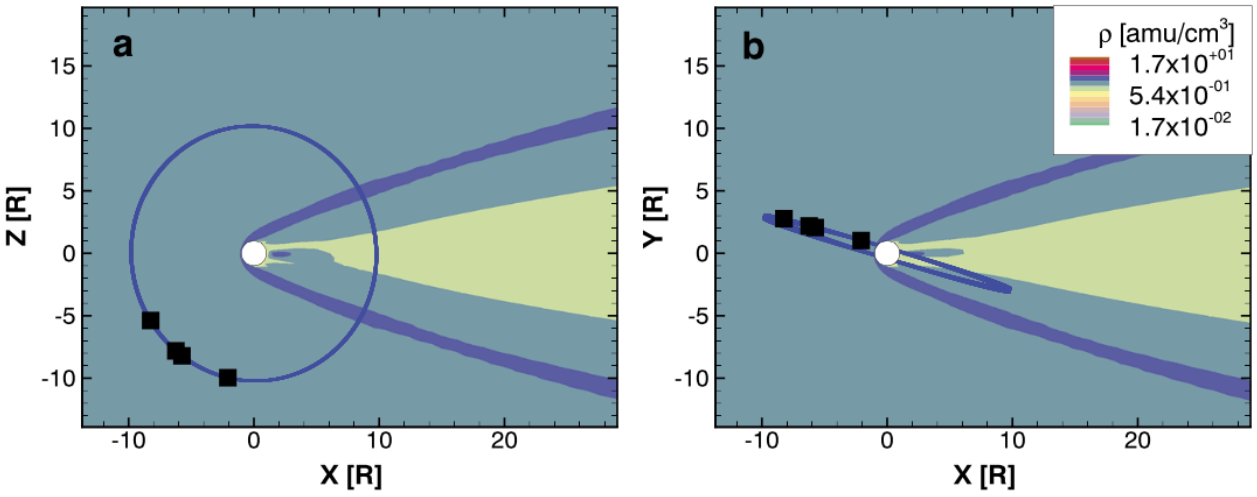

Figure 6.1 *MHD simulation for a global exosphere with an outgassing rate 1.8 kg/s. Panels a and b show cuts through the X-Z and X-Y planes in CSO coordinates. The bow shock is relatively axially symmetric with the shock nose residing near the cerean surface at 1.1 R_C.*

6.3.1.2 Gas Flux Rates Comparable to Telescopic Observations

Next, we evaluate the bow shock geometry that would be produced by a global exosphere using a gas flux rate similar to those reported by telescopic observations. In this run, we use a flux rate of 9 kg/s ($3x10^{26}$ H_2O/s), intermediate between the largest vapor production rate reported by Küppers et al. (2014) of $4x10^{26}$ H_2O/s and their follow up positive detections of $2x10^{26}$ H_2O/s. Figure 6.2 shows the mass density contours for the simulation in cuts through the X-Z and X-Y planes in CSO coordinates. Again, the blue trace indicates Dawn's Survey orbit and the black squares represent the locations of the strongest +Z Phoswich detections. From Figure 6.2, it is clear a symmetric shock develops, with the nose of the bow shock residing at 1.3 R_C.

The black lines shown in Figure 6.2 are the extrapolated IMF field lines that pass through the Dawn burst locations and are tangent to the bow shock surface. The hollow squares signify the locations on the bow shock surface to which Dawn is connected. This geometry allows for the incoming solar wind electrons reflected and accelerated at the bow shock surface to travel along the IMF field lines to the various Dawn locations. Therefore, the dayside +Z Phoswich and –Y BLP bursts (Chapter 4) are consistent with the geometry created by the bow shock formed for the expected gas flux rates of a transient exosphere. However, this magnetic field orientation does not intersect the survey orbit on the nightside and lacks an explanation for the appearance of the electron bursts observed by the +Y BLP scintillator on the nightside (Chapter 4).

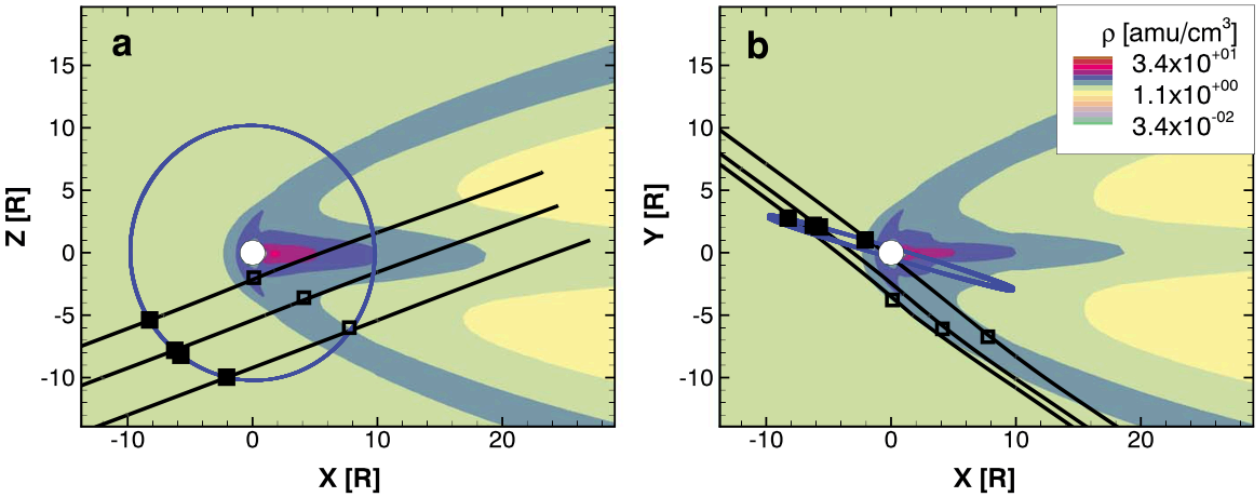

Figure 6.2 *MHD simulation for a global exosphere with outgassing rate 9 kg/s. Panels a and b show cuts through the X-Z and X-Y planes in CSO coordinates. The bow shock is relatively axially symmetric with the shock nose residing at 1.3 R_C. The extrapolated IMF (black) lines show the shock produced in this simulation produces a geometry that allows for reflected electrons from the bow shock surface to travel to the Dawn's locations at the time of the observed bursts.*

6.3.2 Single-fluid MHD Models for a Localized Source

It is still not known what water reservoir(s) on Ceres supply the exosphere. In the last section, we explored an exosphere supplied by the global water-ice table just beneath the subsurface. However, there are also localized water-ice reservoirs observed on the surface of Ceres which could also provide a source for the exosphere, such as those found in Oxo and Juling craters (Combe et al., 2016; Combe et al., 2018). Küppers et al. (2014) suggested their positive water absorption detections corresponded to localized regions on the surface, which they proposed were cryovolcanic plumes. Whether locally released by surface ice patches or cryovolcanism, the release of water molecules will be similar in nature and therefore would have similar exospheric shapes.

In this section, we investigate the bow shock geometries produced by different gas flux rates originating from a localized region on the surface. We place the localized source at an arbitrary location in the x-z plane, 60° from the –Z axis. The water molecules are released in a cone, with a cone angle of 20°. It takes about twenty minutes for a newly released water molecule to travel 1 R_C, which is farther than the subsolar stand-off distance of the bow shock from our second global exosphere case. In twenty minutes, the source will only move 10° at the 9.1 hour rotation period of Ceres. Hence, we neglect rotation and use a steady state source in a fixed arbitrary location to demonstrate the effect of an asymmetric source. Since our simulation does not incorporate a rotating Ceres, we produce two end members for each gas flux rate simulation: one where the source is directed sunward and one directed antisunward. The average bow shock geometry should be intermediate between the two extreme cases.

6.3.2.1 Localized source with a Gas Flux of 4.5 kg/s

We begin by using a gas flux of 4.5 kg/s ($1.5x10^{26}$ H_2O/s), about half the magnitude observed by telescopic observations and that used in our second global exosphere case. Figure 6.3 panels a and b show the simulation for the source facing sunward and panels c and d show the simulation with the source facing antisunward. In both instances, an asymmetric bow shock is produced due to the water molecules originating from only one hemisphere.

For the sunward simulation, the shock location is much further from the body than previous cases with a stand-off distance ~4 R_C in the X-Y plane (Figure 3b; the deep magenta contour outlines the surface of the shock). The shock is also not centered at the subsolar point, but is shifted toward the south. The asymmetric shock is stronger in the southern hemisphere and gradually weakens towards the north. In addition, the southern portion of the shock is

stronger and farther from the body than the shock produced for the 9 kg/s global exosphere case, though it does not extend globally. This highlights that a localized source could produce a shock strength similar to that produced by a global exosphere with a fraction of the outgassing rate. For a southern localized source with an outgassing rate ~9 kg/s, we would expect the burst locations during Survey orbit to be fully contained within the bow shock. Therefore, for fast-Fermi acceleration to be consistent with this type of source, the gas flux rate must be below 9 kg/s.

Figure 6.3 panels c and d show the simulation when the localized source is pointed antisunward. Like the sunward case, the shock is again highly asymmetric with a larger spatial extent in the X-Z plane containing the plume than the plane perpendicular to it. However, the shock has now become much narrower than previous cases. The shock nose does not reside in front of the dayside of Ceres, but exists solely in the southern hemisphere where it has a maximum standoff distance ~4 R_C similar to the sunward plume. Again, the concentration of the gas flux from a small-area source location produces a shock that is stronger than the 9 kg/s global exosphere case.

The actual bow shock surface produced by a localized source with a 4.5 kg/s outgassing rate should be somewhere between these two extremes. Therefore, the shock surface should dominantly reside in the hemisphere for which the source is located. Both cases displayed stronger local shocks than the global exosphere, indicating an outgassing rate of less than 4.5 kg/s can produce a shock strength similar to a global exosphere with a 9 kg/s outgassing rate.

6.3.2.2 Lower Limit Outgassing Rate for a Localized Source

The previous simulation illustrated that a lower outgassing rate for a localized source can produce a stronger shock than a global exosphere. Hence, we again examine what the minimum outgassing rate is necessary to generate a bow shock if the water is concentrated at a local source. We use the same cone and location conditions as the previous run, except we lower the gas flux rate by an order of magnitude to 0.9 kg/s (1.5 x 10^{25} H_2O/s). Figure 6.3 panels e and f show this run for the case where the source is pointed in the sunward direction. The stand-off distance of the shock is now reduced to 2 R_C and resides only to the south of the planet. Similar to the antisunward simulation in the previous section, the shock surface does not extend to lie in front of the dayside surface.

Though the vapor production rate is quite low, when concentrated in a localized source, it is still sufficient to create a shock. This production rate is half the magnitude of the lower limit derived for the global exosphere of 1.8 kg/s. Comparing Figure 6.1 to Figure 6.3 (panels e and f) we expect the lower limit for the localized source case to be a few times smaller than this value.

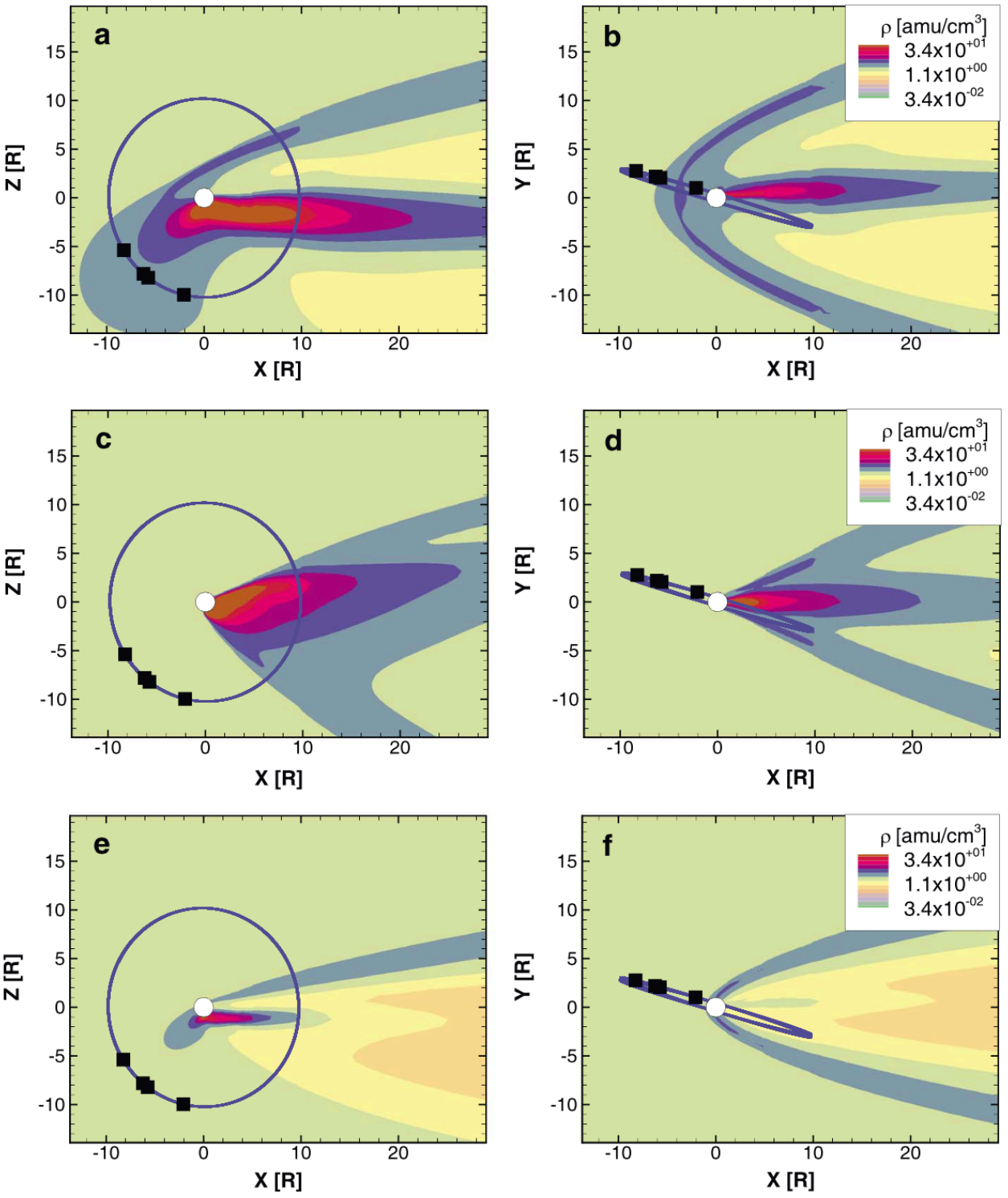

Figure 6.3 *MHD simulation for an exosphere produced by a localized source with outgassing rates 4.5 kg/s (sunward, panels a and b; antisunward panels c and d) and 0.9 kg/s (sunward, panels e and f). In all cases, an asymmtric shock is produced where the shock is stronger in the southern hemisphere and weakens towards the north.*

6.3.3 Single-Fluid MHD Models with Varying Solar Wind Conditions

The models thus far have used average solar wind conditions extrapolated from 1 AU corresponding to the week the electron bursts were observed. The ACE data show a small change in velocity, but significant changes in density and the magnetic field vector during this period. Additionally, we would expect the solar wind conditions to be quite variable during the different telescopic observations of the exosphere. Therefore, in this section we simulate a globally-released exosphere with an outgassing rate of 9 kg/s ($3x10^{26}$ H_2O/s), similar to section 3.1.2, but we have adjusted the solar wind density to be twice that of the average conditions, thereby increasing the solar wind dynamic pressure by a factor of 2. Figure 6.4 shows the results of the simulation. The shock retains its axially symmetric shape, but the stronger dynamic pressure of the solar wind compresses the envelope of the bow shock to just above the surface at 1.1 R_C, despite the 9 kg/s outgassing rate. Hence, during periods with larger solar wind velocities and/or solar wind densities, the minimum outgassing rate would need to be larger than 1.8 kg/s derived previously to sufficiently stand off the solar wind. Conversely, occasions when a weaker solar wind dynamic pressure is present, a limit less than 1.8 kg/s should stand-off the solar wind.

We also ran a case where the solar wind velocity and density are set to the week-long average conditions but have adjusted the IMF magnitude to be twice the average condition. This results in a stronger pile-up region in front of Ceres as the magnetic field that is carried with the solar wind slows down as the solar wind becomes mass-loaded. The enhanced magnetic pressure aids the exosphere in holding off the solar wind and pushes the bow shock nose to a subsolar distance of 1.5 R_C (simulation not shown), further than case 2. Therefore, the lower-limit for a bow shock-producing exosphere will also vary with the magnetic field strength.

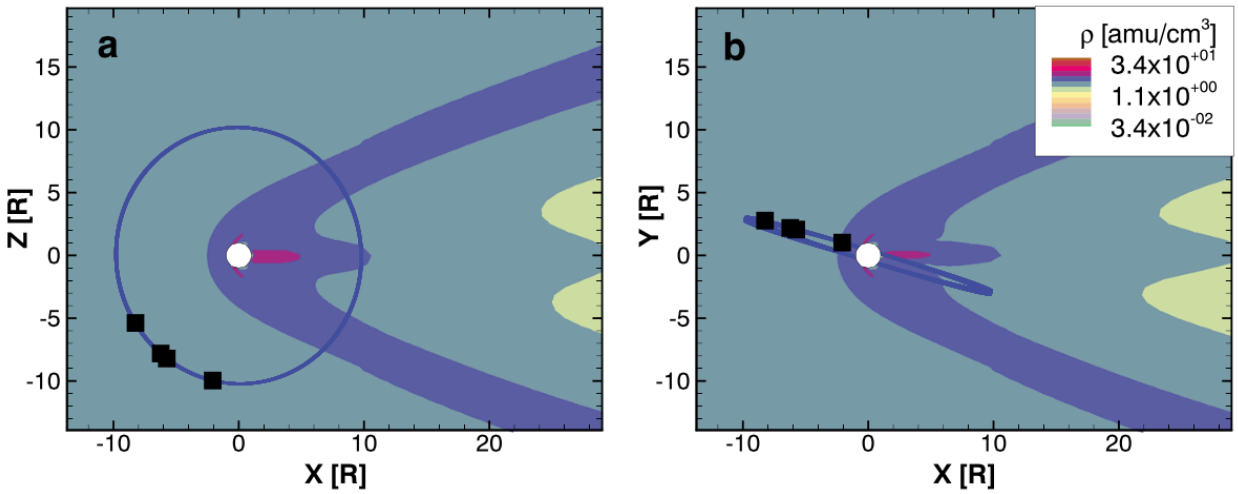

Figure 6.4 *MHD simulation for a global exosphere with outgassing rate 9 kg/s, similar to the case in 3.2.1, but with twice the solar wind dynamic pressure.*

6.3.4 Single-fluid MHD Model for a Conductive Interior

In this section we explore the possibility that the bow shock at Ceres was not produced by an exosphere, but could have been generated via an internal muddy ocean at depth. A conductive ocean could oppose strong changes in the interplanetary magnetic field, such as those that accompany coronal mass ejections, through magnetic induction. In this simulation, we set the outgassing rate of the dwarf planet to zero and treat the cerean surface as a perfect conductor while using the same solar wind conditions as our previous cases. Figure 6.5 shows the bow shock produced under these conditions.

Though this simplified, ideal scenario is able to produce a bow shock, the shock nose resides near the cerean surface at 1.1 R_C and the shock shape is quite narrow in comparison to the 9 kg/s global exosphere case. Figure 6.5 also shows the extrapolated IMF field lines that pass through the Dawn locations during the electron bursts. Due to the narrow shape of the shock, the field lines passing through the Dawn locations do not touch the shock surface at any point

indicating this production mechanism cannot produce a geometry that would allow its electron foreshock to intersect the Dawn locations. An IMF orientation with a large Bx component would be necessary to create such a geometry.

Setting Ceres to be a perfect conductor gives rise to the maximum bow shock that could be produced by a conducting Ceres. The muddy ocean will be less conductive than this and will be displaced some depth beneath the surface, indicating a bow shock will not form for the more realistic case. Furthermore, the appearance of the electron bursts lasted on the order of a week. Russell et al. (2016) showed this would require a conductivity at least 25 S/m to last on that timescale. This means Ceres' muddy layer would need to be five times more conductive than Earth's ocean which is ~5 S/m.

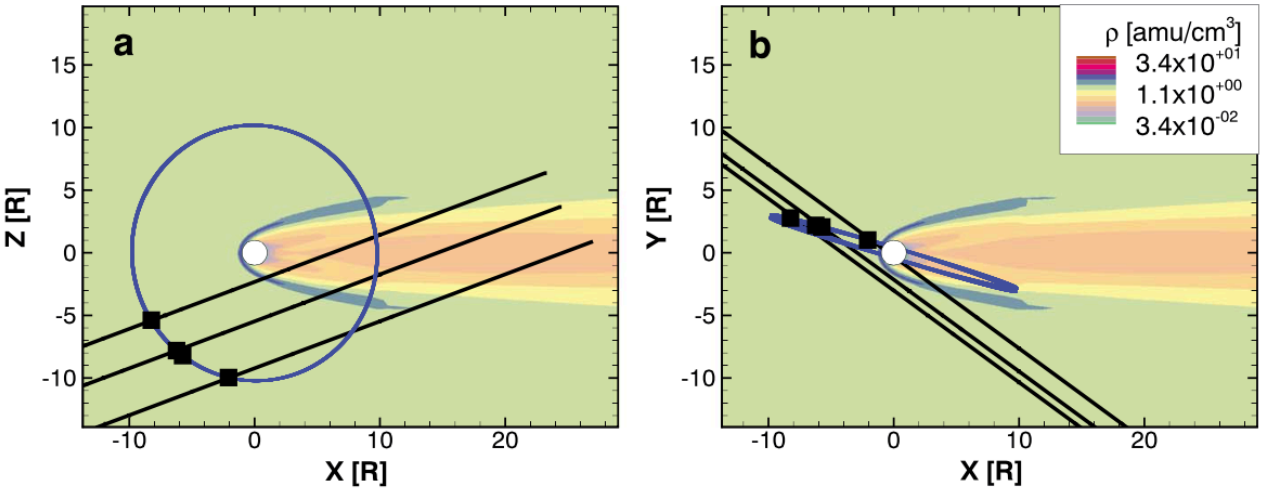

Figure 6.5 *MHD simulation where Ceres' surface is treated as a perfect conductor and the gas flux rate is set to zero. In this ideal scenario, the bow shock nose resides just above the cerean surface. The shock shape is much narrower in comparison to that produced by a global exosphere with 9 kg/s gas flux rate (Case 2).*

6.4 Multi-fluid MHD Model for a Global Exosphere

Our previous cases use a single-fluid approach, which neglects the convection electric field of the solar wind and leads to a symmetric bow shock structure for a globally-released exosphere. Though the single-fluid simulations do not fully replicate the bow shock shape, they are still useful because they provide information on the development and location of a bow shock. To more realistically capture the dynamics of the interaction, a more computationally expensive multi-fluid approach is needed.

We treat the solar wind H^+ ions and the pick-up water group ions (grouping O^+, OH^+, H_2O^+, and H_3O^+) as decoupled fluids, which allows the model to capture asymmetries in the plasma distribution that do not arise when using a single-fluid approach. In the multifluid approach, the magnetic field is convected with the flow of the electrons—assumed to be a massless fluid. Hence, the force felt by the ions can be described as: $\mathbf{F}=q(\mathbf{V_s}-\mathbf{V_e})\mathbf{xB}$, where q is the charge of the ion, V_s is the velocity of the ion species, V_e is the bulk velocity of the electrons, and B is the magnetic field. Hence, H+ solar wind protons traveling faster than the electron bulk velocity will be accelerated antiparallel to the convection electric field, while water group pick-up ions starting at rest are deflected along the convection electric field direction.

The multi-fluid simulation uses modified versions of the equations for the conservation of mass, momentum, and energy which solve the equations by ion species (indicated by subscript s; electrons are indicated by subscript e) and includes the effects from the convection electric field:

$$\frac{\partial \rho_s}{\partial t} + \boldsymbol{\nabla} \cdot (\rho_s \boldsymbol{u_s}) = Q_{\rho s}$$

$$\frac{\partial (\rho_s \boldsymbol{u_s})}{\partial t} + \boldsymbol{\nabla} \cdot (\rho_s \boldsymbol{u_s u_s}) = \rho_s \boldsymbol{g} - \nabla p_s - \frac{n_s}{n_e} Z_s \nabla p_e + n_s Z_s e(\boldsymbol{u_s} - \boldsymbol{u_e}) \times \boldsymbol{B} + \boldsymbol{Q}_M$$

$$\frac{\partial p_s}{\partial t} + \boldsymbol{\nabla} \cdot (p_s \boldsymbol{u_s}) = -(\gamma - 1) p_s (\boldsymbol{\nabla} \cdot \boldsymbol{u_s}) + Q_{ps}$$

where the terms are defined similarly as the single fluid equations. Quasi-neutrality is assumed, therefore the electron density can be calculated by $n_e = \sum_s n_s Z_s$, where n_s is the number density of ion species s and Z_s is its corresponding charge. The temperature of the electrons is set to be equal to the average temperature of all the ion species, $T_e = \frac{\sum_s n_s Z_s T_s}{n_e}$. We calculate the electron velocity using the definition of the electric current, $\boldsymbol{u_e} = \frac{\sum_s n_s Z_s \boldsymbol{u_s}}{n_e} - \frac{\boldsymbol{J}}{e n_e}$. Since the magnetic field is frozen into the flow of the electrons, the magnetic field can be described by $\frac{\partial \boldsymbol{B}}{\partial t} = \boldsymbol{\nabla} \times (\boldsymbol{u_e} \times \boldsymbol{B})$. The source terms also become modified:

$$Q_{\rho s} = S_s - L_s$$

$$Q_{Ms} = S_s \boldsymbol{u_n} - L_s \boldsymbol{u_s}$$

$$Q_{ps} = \frac{\gamma - 1}{2} S_s (u_n - u_s)^2 + \frac{k}{m_s} (S_s T_n - L_s T_s)$$

The subscript n denotes neutrals. The addition of the pick-up ions through photoionization, impact ionization, and charge exchange is contained within term $S_s = \sum_{s'=neutrals} m_s n_{s'} (f_{ss'} + \sum_{t=ions} k_{s't-st'} n_t)$, where $f_{ss'}$ is the combined photoionization and impact ionization rate and its subscripts indicate a neutral species s' converting into ion species s. Similarly, $k_{s't-st'}$ is the charge exchange rate where the interaction between neutral species s' and ion species t results in ion species s and neutral species t'. The corresponding loss of ions through the charge exchange process is described by $L_s = \sum_{t'=neutrals,t=ions} m_s n_{t'} n_s k_{t's-ts'}$. Solar wind conditions used are the same as Table 1 and held constant. The simulation runs until steady state is reached.

In this multi-fluid run, we use a global exosphere with a gas flux of 9 kg/s to be comparable to our case 2 single-fluid simulation. Figure 6.6 (panels a and b) shows the results of the multifluid simulation for the same solar wind conditions as Table 1 where the convection electric field is dominantly in the -Z CSO direction and for another case (panels c and d) where

the magnetic field direction has been reversed, causing the convection electric field to be in the opposite direction. The multi-fluid simulation varies from the single-fluid equivalent in two major ways (Case 2; Figure 6.2): the extent of the mass distribution of the water molecules is much broader due to gyroradii effects the shock is now very asymmetric as a result of the pick-up ions getting accelerated in the direction of the convection electric field.

The density contours in Figure 6.6 show the mass density increases in a much broader region than its single-fluid counterpart, as represented by the outermost blue contour level ranging from -7 to 14 R_C on the upstream side of Ceres. This is because the water ions are no longer averaged into the protons as in the single-fluid MHD result. We find that the proton density did not increase in this region, while the water group number density is about 3% that of the proton number density (not plotted). This region is the local pick-up region. The flow is not significantly slowed, as indicated by the proton density. Thus, the flow did not form a shock at large distances from Ceres.

In Figure 6.6 (panels a and b) the blue contour line extends more on the –Z CSO (southern hemisphere) than on the +Z CSO (northern hemisphere) because the convection electric field is pointing in the –Z direction, accelerating the ions in the southern hemisphere away from the body. Accordingly, the density gradient to the south of Ceres is smaller than the gradient to the north, making it hard to form a well-defined shock surface to the south of Ceres. The shock surface is only seen to the north of Ceres, represented by the innermost contour line (red color) in Figure 6.6. Upstream of the shock, about 24% of the total ions are water ions.

Even though the IMF cone angle is constrained by the shock surface, the field can be either positive or negative. Reversing the IMF by 180° reverses the direction of the convection electric field and thus the direction the pick-up ions will get accelerated. This will flip which

hemisphere the water molecules are pushed outward. This case is shown in Figure 6.6 (panels c and d) where the solar wind conditions are the same as panels a and b, except the magnetic field is now antiparallel. As expected, both cases are the same, just flipped by 180º about the x-axis.

Figure 6.7 displays contours of the bulk velocity of the electrons for the case where the magnetic field has been reversed and shows that significant slowing of the solar wind only occurs close to the planet, with an asymmetric bow shock located at 1.5 R_C. This is similar to the stand-off distance of Case 2, where the shock was located at 1.3 R_C. Although the subsolar distance of the shock is at 1.5 R_C, which is slightly farther out than the equivalent 9 kg/s single fluid case, the flaring angle of the shock is smaller than the single-fluid case.

Comparing both cases in Figure 6.6 we conclude that to create a well-defined shock surface that accelerates electrons back toward Dawn, the magnetic field vector must point toward $+X_{CSO}$ (from the Sun toward Ceres) and $-Y_{CSO}$. In the 7 day period, reversals in the polarity of the IMF are seen in the ACE data, indicating heliospheric current sheet crossings. Such an IMF direction will not change the conclusions drawn from the previous cases because the single-fluid runs are not affected by the limited gyroradius effect. A weaker compression gradient indicates that the minimum outgassing rate of a global atmosphere should be larger than the single-fluid derived lower limit of 1.8 kg/s. Our parameter study has found 3 kg/s ($1x10^{26}$ H_2O/s) to be an appropriate lower limit for such assumptions. However, if the outgassing is restricted to a localized region, the outgassing rate can be lower than 3 kg/s and still sustain a shock.

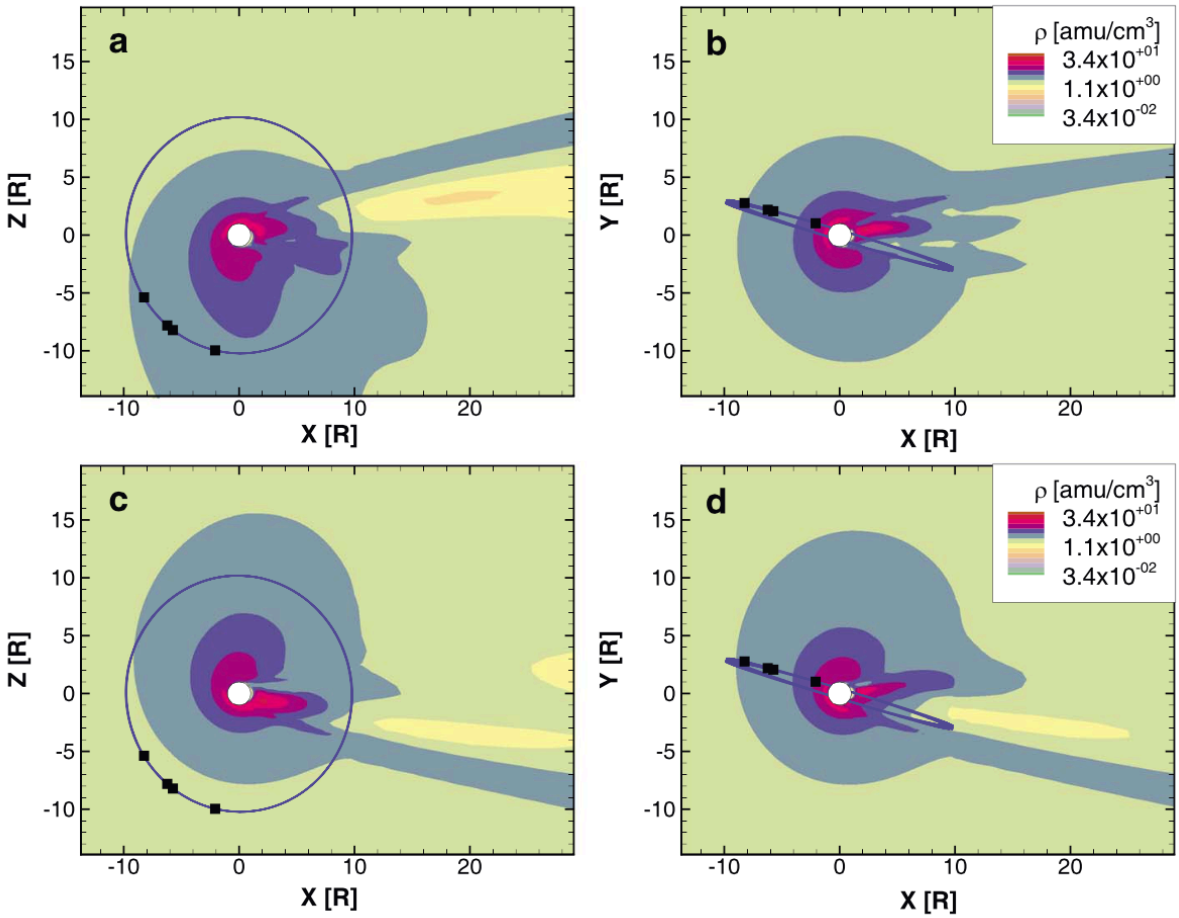

Figure 6.6 *Multi-fluid MHD simulation for a global exosphere with outgassing rate 9 kg/s showing mass density. The presence of the convection electric field leads to an asymmetric shock, dominantly in the X-Z plane. Panels a and b use the extrapolated magnetic field in Table 1, while c and d reverse the magnetic field direction.*

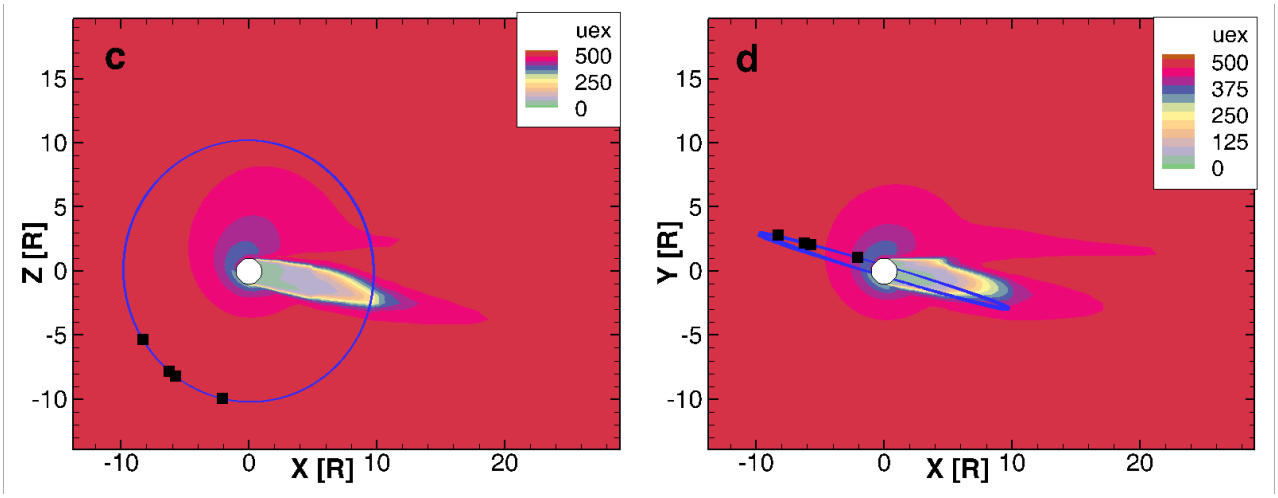

Figure 6.7 *Corresponding velocity plot for Figure 6.6 panels c and d. Though the gyroradii cause the pick-up water group ions to extend far from the planet, the shock still remains relatively close to the planet at 1.5 R_C, but is now asymmetric and more flared.*

Case Number	Fluids	Inner BC	Gas Flux *Q*	Condition difference	Subsolar distance
Case 1	Single	Exosphere	1.8 kg	Avg solar wind	1.1
Case 2	Single	Exosphere	9 kg	Avg solar wind	1.3
Case 3s	Single	Sunward plume	4.5 kg	Avg solar wind	4
Case 3t	Single	Tailward plume	4.5 kg	Avg solar wind	<1
Case 3l	Single	Sunward plume	0.9 kg	Avg solar wind	<1
Case 4n	Single	Exosphere	9 kg	Double density	1.1
Case 4u	Single	Exosphere	9 kg	Double IMF	1.5
Case 5	Single	Induction	0 kg	Avg solar wind	1.1
Case 6p	4	Exosphere	9 kg	Avg solar wind	1.5
Case 6n	4	Exosphere	9 kg	Negative IMF	1.5

Table 6.2 *Summary of the MHD simulations performed in this study.*

6.5 Implications for the Source of the Bow Shock at Ceres

In this study, we treat the shock surface as a thin discontinuity, while in reality, the shock thickness may be more than tens of kilometers (Schwartz et al., 2011). Using the Case 2 parameters, the proton and electron gyroradii are 2 R_C and 0.002 R_C, respectively. The proton and electron inertial lengths are 0.4 R_C and 0.01 R_C, respectively. Measured by these critical lengths, if the Ceres shock thickness is comparable to that of the Earth, our assumption is still applicable. Nevertheless, a hybrid model on the magnetic induction case (Lindkvist et al., 2015) and on thin air interaction at Ceres (Lindkvist et al., 2017) may improve the accuracy of such thickness estimations.

We examined the density ratio between pick-up ions and solar wind protons at the shock for our multi-fluid simulation. A density increase upstream of a shock is typical for cometary pick-up shocks. Biermann et al. (1967) calculated a critical limit for mass loading. The flow has to become shocked after the number density ratio of picked-up CO^+ ions to protons exceeds 2%. This was later found to be consistent with in-situ observation at comets (Wilken et al., 1987). Koenders et al. (2013) examined this number with MHD and hybrid models but found other factors like the IMF cone angle and the IMF strength to affect the shock distance as well. Shou et al. (2015) used a single-fluid, multispecies MHD model to find that the shock distance varies widely for comets at heliocentric distances 0.17 to 1.75 AU, in contrast to the Biermann model. In our single-fluid 9 kg/s global exosphere case, the shock formed along the comet-Sun line when the number density ratio between the pick-up ions and total ions was about 10%, while the equivalent multi-fluid case increased to 24%. We believe this is due to significant decoupling interactions: the gas production ratio is 3 orders of magnitude smaller than that of comet 1P/Halley.

These models also have applications to comet-solar wind interaction and active asteroids. The transition between shock formation and a kinetic pick-up wake has been studied extensively recently, using both modeling (Rubin et al., 2015) and Rosetta observations, when comet 67P/Churyumov-Gerasimenko was at 3.4 AU with an outgassing rate of about $5x10^{25}$ s^{-1} (Broiles et al., 2015). This Ceres study may add more knowledge to this transition problem.

This work has shown that vapor production rates similar to those reported by telescopic observations are sufficient to produce a bow shock at Ceres. All our simulation cases are summarized in Table 2. The shock distances are also listed for comparison. The subsurface subsolar distance of the shock listed for Cases 3t and 3l are projections from shock surface below Ceres. The stand-off distance extends over 2 R_C to the south, where the plume is pointed. For the same outgassing rates, a localized source was able to produce further stand-off distances, although the shock only present in one hemisphere, as opposed to globally for the global exosphere single-fluid cases.

The minimum outgassing rate necessary to produce a bow shock is ~3 kg/s ($1x10^{26}$ H_2O/s) for a globally-released exosphere and even lower when localized to a small region on the surface. Our models show that a globally released exosphere or an exosphere released from a small area on the surface can produce geometries allowing for the connection of the spacecraft to the bow shock surface. For the localized source case, a source located in the southern hemisphere would be needed since the location of the shock is highly dependent on the source's location on the surface. The direction of the of the convection electric field is also important in both situations, as it will affect the density gradient of the water molecules which will in turn affect the location of the shock. A saline layer at depth is not sufficient to produce a bow shock since it cannot provide a large enough obstacle to the solar wind nor last on the timescales observed by

Dawn. While the genesis of the bow shock is likely not due to a conductive layer at depth, it is still possible that a saline layer at depth may still exist.

This chapter has focused on the release of water vapor due to its positive detection by telescopic observations and the current surface-ice detections by Dawn. However, the authors would like to note that similar solar-wind interaction would occur for an exosphere that consisted of different a composition if the molecules had a molecular mass comparable to water. If the method of exospheric release is due to sputtering during solar energetic particle events, it is possible that these energetic protons are sputtering more from the surface than just water ice. Therefore, it is also possible that some portion of the exosphere could be due to an additional source, which would lower the amount of water vapor required to produce the exosphere.

6.6 References

Biermann, L. et al., The interactions of the solar wind with a comet, Sol. Phys., 1, 254-284 (1967).

Broiles, T. W. et al., Rosetta observations of solar wind interaction with the comet 67P/Churyumov-Gerasimenko, Astron. Astrophys., 583, A21(2015).

Castillo-Rogez, J. et al., Where is Ceres' Ice Shell?, 47th Lunar and Planetary Science Conference abstract (2016).

Combe, J. P. et al., Detection of local H_2O exposed at the surface of Ceres, Science, Vol 353, Issue 6303 (2016).

Combe, J. P. et al., Exposed H_2O-rich areas detected on Ceres with the Dawn Visible and Infrared Mapping Spectrometer, Icarus 000, 1-20 (2018).

Häberli, R. M. et al., Quantitative Analysis of H_2O+ Coma Images Using a Mutliscale MHD Model with Detailed Ion Chemistry, Icarus 130, 373-386 (1997).

Huebner, W. F. et al., Solar Photo Rates for Planetary Atmospheres and Atmospheric Pollutants, Astrophysics and Space Sciences 195, 1-294 (1992).

Jia, Y.D. et al., Interaction of Saturn's magnetosphere and its moons: 1. Interaction between corotation plasma and standard obstacles, J. Geophys. Res., 115, A04214 (2010).

Koenders, C. et al., Revisting cometary bow shock positions, Planet. Space Sci., 87, 85-95 (2013).

Küppers, M. et al., Localized sources of water vapour on the dwarf planet (1) Ceres, Nature, 505, 525-527 (2014).

Lindkvist, J. et al., Callisto plasma interactions: Hybrid modeling including induction by a subsurface ocean, J. Geophys. Res. Space Physics, 120, 4877-4889 (2015).

Lindkvist, J. et al., Ceres interaction with the solar wind, Geophys. Res. Lett., 44, 2070-2077 (2017).

Park, R. S. et al., A Partially differentiated interior for (1) Ceres deduced from its gravity field and shape, Nature, 537, 515-517 (2016).

Prettyman, T. H. et al., Extensive water ice within Ceres' aqueously altered regolith: Evidence from nuclear spectroscopy, Science, Vol 355, Issue 6320, 55-59 (2017).

Rubin, M. et al., Modeled interaction of comet 67P/Churyumov-Gerasimenko with the solar wind inside 2 AU, Earth Moon Planets, 116, 141-157 (2015).

Schwartz, S. J. et al, Electron temperature gradient scale at collisionless shocks, Phys. Rev. Lett., 107 (21), 215002 (2011).

Shou, Y. et al., The plasma environment in comets over a wide range of heliocentric distances: Application to comet C/2006 P1(McNaught), Astrophys. J., 809, 156 (2015).

Wilken, B. et al., Pick-up ions at Comet P/Halley's bow shock—Observations with the IIS spectrometer on Giotto, Astron. Astrophys., 187, 153-159 (1987).

Chapter 7

Dependence of the Cerean Exosphere on Solar Energetic Particle Events

7.1 Introduction

Earth-based telescopes have been monitoring the cerean exosphere for the past three decades. Fanale and Salvail (1989) first proposed the existence of a water exosphere since ice should not be stable at the surface of the ice-rich body given its surface temperature. Many have argued that the variation in the gas production rate should be dependent on the solar illumination of the body and therefore the dwarf planet should have a denser exosphere closer to perihelion when sublimation is strongest (A'Hearn and Feldman, 1992; Küppers et al., 2014). Telescopic observations since 1990 have detected water vapor and its by-products. However, rather than displaying a gradual increase in the gas rate with decreasing heliocentric distance, the exosphere has proven to be transient: out of the nine attempts to detect an atmosphere, only four observations resulted in positive detections of water vapor or its by-products. In addition, the strongest magnitude water exosphere observed did not occur when Ceres was closest to perihelion.

The first observations of the exosphere were conducted by A'Hearn and Feldman (1992). They observed the dwarf planet for OH emission on two attempts using the International Ultraviolet Explorer (IUE) telescope in 1990 and 1991. Only the second attempt resulted in the detection of OH emission, despite the observations being equidistant on either side of perihelion, when Ceres was at a distance about 2.65 AU. They attributed the contrasting measurements to an

asymmetry in the distribution of water ice near the surface since the two observations were centered on different hemispheres. Rousselot et al. (2011) attempted to repeat this study with the Very Large Telescope (VLT) in 2007 when Ceres was further away from perihelion at almost 2.85 AU. That observation resulted in a non-detection of OH emission despite the telescope having a similar sensitivity to the previous study.

The launch of the Herschel Space Observatory (HSO) in 2009 provided a new instrument sensitive to atmospheric water. Küppers et al. (2014) used HSO to observe the exosphere four times as the body increasingly approached perihelion. The study resulted in no detection of H_2O absorption when Ceres was furthest from the Sun, but was followed by three positive detections later. Though this set of detections appears to be in agreement with the sublimation hypothesis, its important to note that the strongest magnitude exosphere was observed on the second attempt, while both the third and fourth attempts that were closer to perihelion had vapor production rates approximately half the magnitude as that detected on the second attempt. Recently, Roth et al. (2016) and Roth (2018) have attempted to observe the cerean exosphere with the Cosmic Origin Spectrograph (COS) onboard the Hubble Space Telescope in 2015 and 2016 when Ceres had heliocentric distances of 2.96 AU and 2.88 AU, respectively. Those attempts did not detect the presence of Oxygen nor Hydrogen emission.

Figure 7.1 plots the vapor production rates calculated from the above observations with their heliocentric distance. Symbols with a down arrow indicate the derived upper limits for non-detections. Positive detections indicate a magnitude of ~$2x10^{26}$ H_2O/s when the exosphere is present. While the positive detections tend to cluster near perihelion, the magnitude of these detections do not increase with decreasing heliocentric distance as would be expected due to sublimation. Though sublimation may be occurring at Ceres, it does not capture well the trend in

vapor production rates reported by telescopic observations.

This discrepancy lead Küppers et al. (2014) to propose localized plumes as the source of volatiles to the Cerean exosphere. This scenario is problematic as it would require a heat source to persist till today. There have also been no geologic units identified consistent with current-day cryovolcanism. Dawn attempted to test the plume hypothesis while in its rotational characterization orbit (RC3) at an altitude of 13,520 km. Forward scattering observations of Ceres' limb were conducted in an attempt to detect lofted dust particles, which produced a null result (Russell et al., 2016). However, the spacecraft was not designed for this type of experiment and would have required a substantial amount of dust to be detected by the spacecraft.

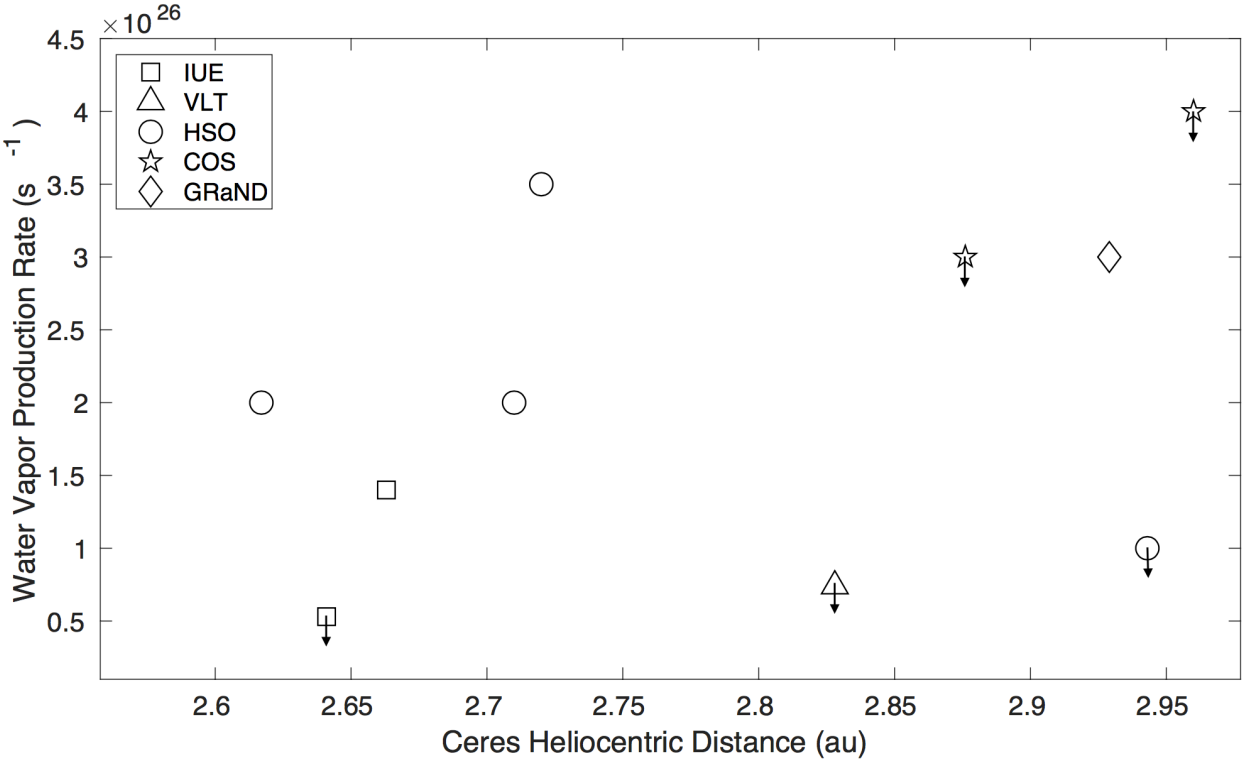

Figure 7.1 *Vapor production rates reported for the cerean exosphere with heliocentric distance. Upper limits are plotted for non-detections, indicated by down arrows. While the positive detections cluster near perihelion, the magnitudes do not steadily increase with shorter heliodistances.*

Evidence for the exospheric production process was provided by Dawn's Gamma Ray and Neutron Detector (GRaND) (Prettyman et al., 2011), which pointed to an exogenic solar source triggering the appearance of an atmosphere. While Dawn was in Ceres' Survey orbit at 4,400 km altitude, energetic electrons were inferred to be arriving at the Dawn spacecraft from the direction of Ceres over a period of a week (Russell et al., 2016; Chapter 4). The strength and temporal behavior of these electron bursts were similar to electron bursts seen at Earth when spacecraft are connected by the interplanetary magnetic field to the Earth's bow shock (Chapter 5). The Earth's bow shock electrons are accelerated by fast-Fermi acceleration when the interplanetary field is compressed as it crosses the shock at near tangency and the electrons experience a moving magnetic mirror that accelerates them away from the point of intersection with the shock (Wu, 1984; Leroy & Mangeney, 1984). One way of producing a transient, standing bow shock at Ceres is a comet-like interaction of the solar wind with a cerean atmosphere which can mass load the solar wind and cause it to deflect. Once the temporary atmosphere dissipates, there will no longer be a significant obstacle to the solar wind to form a bow shock and the electron acceleration will cease. The longevity of a transient atmosphere produced by sudden release of particles is expected to be about a week at Ceres from the time of the production of the atmosphere (Formisano et al., 2016). The electron event seen by Dawn began shortly after a large jump in the flux of solar energetic protons, which have a different signature in the GRaND instrument than the electron bursts (Russell et al., 2016, Supplementary Text; Chapter 4).

The observation of the bow shock raised the question as to whether solar energetic particle (SEP) events could explain the appearance of a transient cerean atmosphere on this, as well as other occasions. Ceres does not appear to have a metallic core (Park et al., 2016) and

therefore has likely never possessed a dynamo. Without a magnetosphere or a substantial atmosphere to provide an induced magnetosphere, Ceres is unshielded from the solar wind and its surface is directly exposed to energetic particles coming from the sun. This is significant because exospheres of icy moons are known to be created via a sputtering process from the bombardment of energetic particles on their surfaces (Lanzerotti et al., 1983; Johnson et al., 1984; Eviatar, 1984). In this chapter we investigate how SEPs could induce an exosphere at Ceres. Section 7.2 examines the solar energetic proton flux during the various telescopic attempts and discusses the correlation between the SEP flux at 1 AU and the magnitude of the vapor production rates observed at Ceres. Section 7.3 addresses methods than can be used to test the SEP hypothesis using spacecraft at 1 AU during a telescopic reactive campaign. Section 7.4 provides calculations for the expected amount of water released due to the bombardment of SEPs onto an icy surface with Ceres-like conditions. Section 5 addresses additional SEP events observed by Dawn while at Ceres.

7.2 Solar Energetic Particle Events as a Production Mechanism for the Cerean Exosphere

7.2.1 SEP Sources and the Effect of Energetic Particles on Icy Surfaces

Due to its low binding energy, water ice is prone to sputtering by energetic particles. Creating a tenuous atmosphere via sputtering requires ions with energies between ~1 keV-1 MeV, with the sputtering rate peaking at ~100 keV (Shi et al., 1995; Brown et al., 1980). The atmospheres of Europa and Ganymede are thought to be created by this process as the energetic particles trapped in Jupiter's magnetosphere impact the surface and eject water molecules (Cheng & Johnson, 1989). In Ceres' case, solar energetic particle (SEP) events provide energetic

ions with the required energies to induce sputtering. Protons with energies higher than 100 keV are capable of penetrating the planet's surface. These protons can scatter and slow down as they penetrate the crust and may release the water molecules from exposed ice at the surface (Combe et al., 2016; Combe et al., 2018) or from Ceres' near-surface global ice table (Prettyman et al., 2017). Water will be sputtered over a range of depths and can diffuse to the surface on time scales similar to that of the transient atmosphere.

Figure 7.2 shows typical spectra of solar protons detected at 1 AU from 10 eV solar wind ions to 10 GeV galactic cosmic rays. While at low energies the flux is relatively stable, the flux of protons ~100 keV and above jump by orders of magnitude between quiet times and the disturbed times of SEP events. The variable fluxes of these particles are capable of causing a temporary enhancement in the sputtering rate at the dwarf planet. The much less variable interstellar pickup ions and the corotating interaction region do not have sufficient energy to cause this variation. SEP induced water release could explain the irregular observations of the cerean exosphere since the occurrence of SEP events are sporadic. A planet will only experience a SEP event if the IMF lines at its location are connected to the SEP source.

Solar Energetic Particles (SEPs) are known to be produced by two mechanisms: at the reconnection point during a solar flare and at the shock surface of a coronal mass ejection (Reames et al., 2017). These production mechanisms give rise to two distinct types of events. SEP events originating at solar flares are known as impulsive events as they are relatively short, only lasting several hours to a day (Reames et al., 2017). Since the acceleration point is localized on the Sun's surface, the energetic particles streaming away along interplanetary magnetic field (IMF) lines will only affect the limited region of the heliosphere that is magnetically connected to the flare source. However, SEPs can have a broader impact when produced by a coronoal

mass ejection. Interplanetary shocks associated with solar coronal mass ejections are the source of the strongest SEP events which last on the order of several days. As the shock expands into interplanetary space, it becomes connected to more field lines, allowing the energetic particles to reach heliolongitudes far from the eruption point (Reames 2017). During both types of SEP events, the flux of solar energetic particles above 100 keV jump by orders of magnitude.

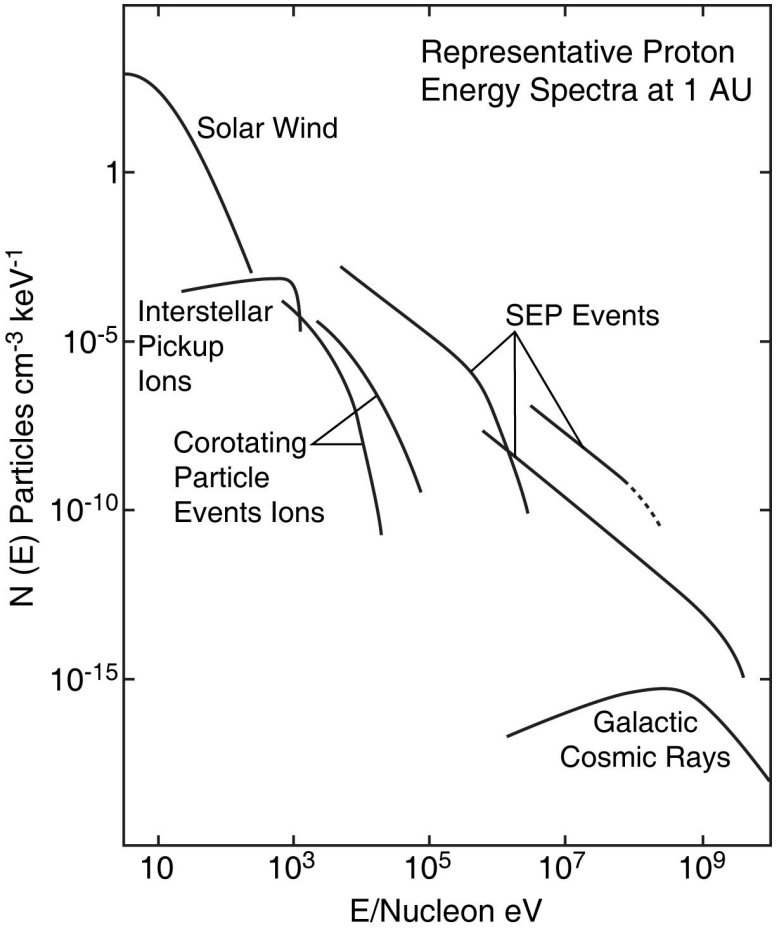

Figure 7.2 *Proton energies and densities provided by different sources. SEP events produce high densities of energetic protons. Figure reproduced from Russell et al. (2016b) with permission.*

7.2.2 Correlation Between SEP Fluxes at 1 AU and Telescopic Observations

In this section we examine the hypothesis that SEPs were responsible for creating the previous transient atmospheric detections. We begin by analyzing the SEP event associated with the electron bursts in June 2015. This event was recorded by both Dawn and Earth spacecraft when the planets were 28° apart. Figure 7.3 shows the comparison between protons ~4-7 MeV measured by Wind 3DP (Lin et al., 1995) with the counts from GRaND's +Z Phoswich, which is sensitive to protons greater than 4 MeV (Prettyman et al., 2011). The SEP event recorded by Wind on Day 169 strongly resembles that seen at Ceres ~10 hrs later, indicating that Earth is a good proxy for the response at Ceres. Following that SEP event, a second larger event on Day 173 is seen at Earth but not at Ceres. Though the Earth and Ceres are in similar regions of the heliosphere, they are not on the same IMF line and therefore are not always magnetically connected to the same events. Still, the typical broad extent of SEP events in heliospheric longitude make it likely that both bodies will experience the same event when they have a small angular separation in the footprints of their IMF lines. In these cases, the Earth data can provide a useful estimate of the SEP fluxes at Ceres, but we should not expect the fluxes to be identical.

Attempts to detect water in Ceres' atmosphere are ideally made when Ceres and Earth are near opposition since the observations are more sensitive with a smaller distance. The IUE and VLT observations were 20°±10° from opposition and the HSO observations were 55°±5° as shown in Figure 7.4. In the following analysis, we assume the 1 AU measurements to be a good proxy for the passage of SEP events at the Ceres' location given the small angular separation during telescopic observations.

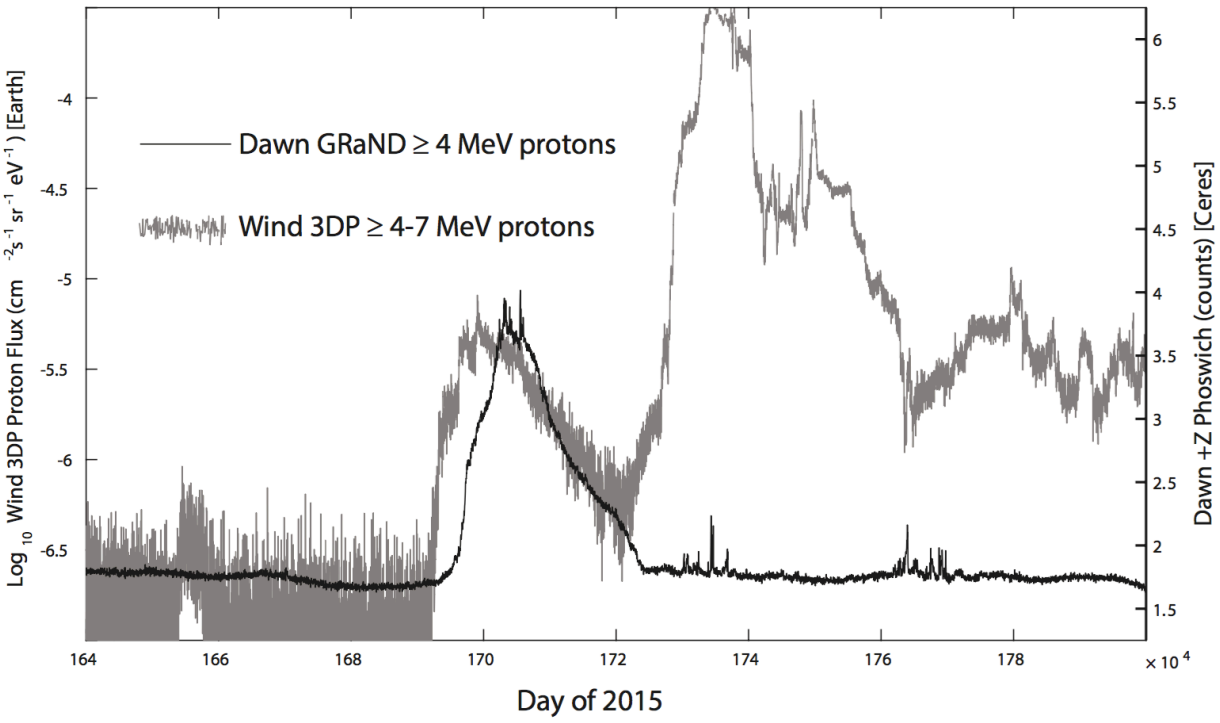

Figure 7.3 *Comparison of Earth's Wind 3DP 4–7 MeV proton data with GRaND's +Z Phoswich counts for the 2015 June event. Protons with energies greater than 4 MeV contaminate the Phoswich scintillator. The same SEP event seen at Earth on Day 169 is also seen by Dawn 10 hr later.*

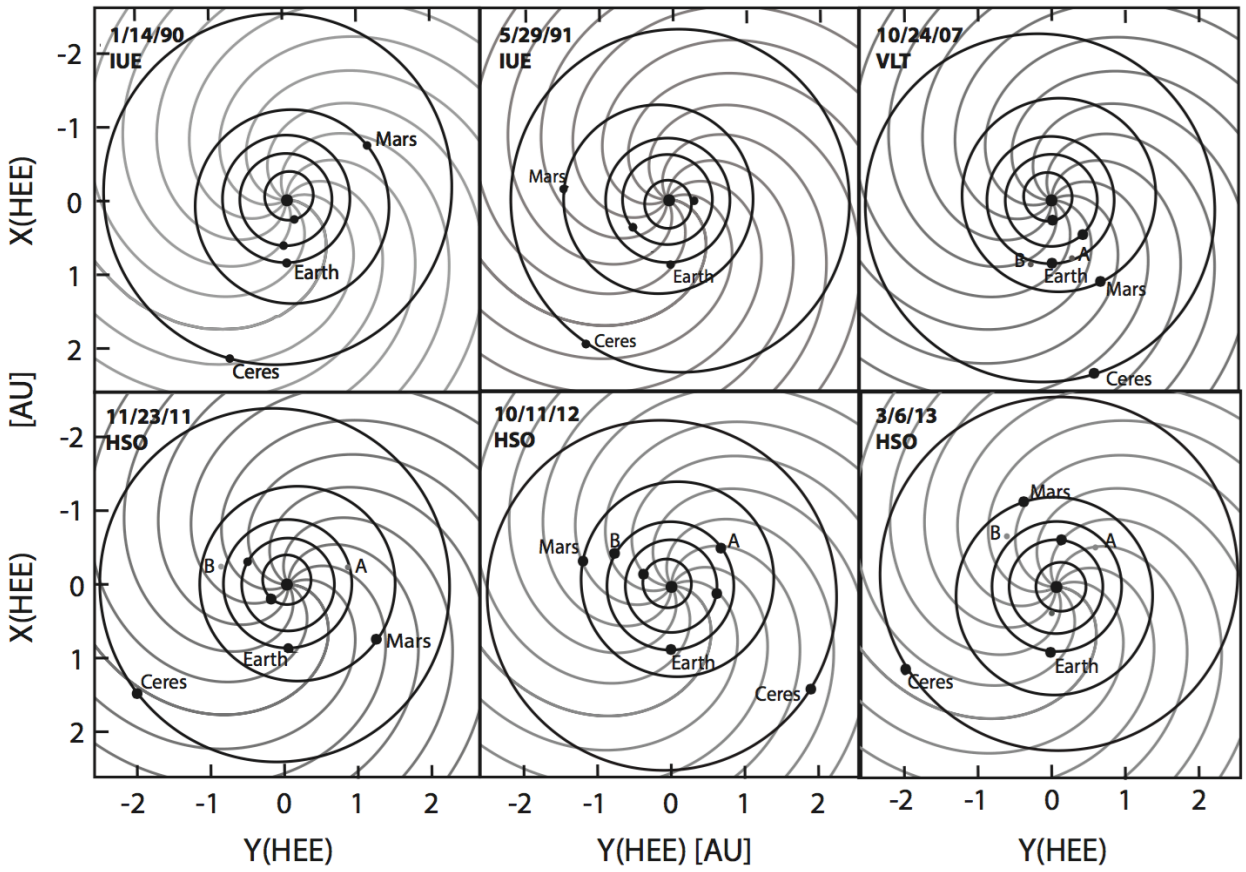

Figure 7.4 *Relative geometries of Ceres, Earth, STEREO A/B, at the time of each exospheric detection attempt. The spiral lines show the nominal interplanetary magnetic field that must connect the shock sources of the solar protons to the various observation sites.*

We used solar energetic proton data from the Advanced Composition Explorer (ACE) Electron, Proton, and Alpha Monitor (EPAM) (Gold et al., 1998), Wind 3DP (Lin et al., 1995), and the OMNI data provided by the Space Physics Data Facility (http://omniweb.gsfc.nasa.gov). We inspected the proton fluxes for energies of ~100 keV-7 MeV for a ten day period prior to each observation, the estimated timescale for which an exosphere is expected to last at Ceres (Formisano et al., 2016). The IUE observations occurred before the respective 1994 and 1997 launches of Wind and ACE. Hence, only OMNI data greater than 1 MeV are available for the IUE cases. The relative delay in arrival times of the particles at Ceres from Earth will depend on how each is magnetically connected to the source. However, the travel time between Earth and Ceres for a 2 MeV particle should be on the order of a few hours. Thus, the 1 AU data roughly reflect the real-time arrival of particles at Ceres.

There have been a total of nine observational attempts to detect H_2O or OH in the Ceres exosphere. Figure 7.5 shows examples of the proton fluxes present at 1 AU during each Ceres observation. The IUE 1990 and 1991 cases are plotted using the OMNI data for energies of 2-4 MeV, while all other cases are taken from the ACE EPAM instrument for energies 1.91-4 .75 MeV. The energetic proton flux during the 1991 IUE observation, when OH emission was detected, is about three orders of magnitude larger than the 1990 observation, which did not detect exospheric OH. Similarly, during the VLT 2007 non-detection the proton flux is continually steady at background levels, which is consistent with a low sputtering rate. These are the three observations made closest to opposition. The strongest absorption feature seen by HSO on October 11th, 2012 (Küppers et al., 2014) corresponds to the period with the highest ion flux bombardment. After the ion flux returns to its normal value, the water signal observed on October 24th, 2012 becomes significantly weaker. This may reflect the decay of the exosphere

due to the end of the solar event. Likewise, the water absorption feature was weaker during the March 6th, 2013 detection (Küppers et al., 2014), when the proton flux was smaller in comparison to October 11th, 2012, but still above the background value. The 10-day period before the November 23rd, 2011 non-detection observation is slightly above the average background, but the ion flux may not have been high enough to produce an exosphere above the observable limit. In the case of the June 2015 GRaND event, the ion flux is large and comparable to that of the October 11th, 2012 case. The August 26th, 2015 and the October 26th, 2016 COS observations are the only telescopic attempts conducted while Dawn has been in orbit about Ceres and can therefore confirm the presence of SEP events during their observing period. These measurements occurred as the sun was headed toward solar minimum and thus no solar events at Dawn were seen on those occasions (Table 7.1), consistent with the non-detection results for both attempts.

For all telescopic-related SEP events detected while it has been in operation, the Wind 3DP instrument shows protons with energies greater than 200 keV to have similar variations in their fluxes as the 2-4 MeV protons. Protons below 200 keV energy are fairly constant during the solar proton events and thus should not significantly enhance the sputtering rate. Figure 7.6 shows the correlation between the ion flux averaged over the 10-day period leading up to the time of observation with the reported water vapor production rates. For cases where water vapor or its components were not detected, the upper limits are used.

The water vapor production rate was estimated by A'Hearn and Feldman (1992) to be 1.4×10^{26} s^{-1}. However, in that calculation, the OH is assumed to be escaping at the thermal speed of 0.5 km/s. If we quadratically add the excess dissociation velocity (1.1 km/s, isotropic) we obtain a production rate for this measurement of $\sim 3 \times 10^{26}$ s^{-1}. For the HSO observations, only the

March 6th, 2013 attempt observed Ceres for a full rotation, providing a production rate of $2x10^{26}$ s^{-1} (Küppers et al., 2014). However, we can estimate the global vapor production rates for the remaining attempts with a larger uncertainty. The strength of the water signal on October 24th, 2012 was similar to that of March 6th, 2013, providing a similar estimate of 2×10^{26} s^{-1} for that observation. The strongest signal from HSO on October 11th, 2012 gives an estimated production rate between $3\text{-}4x10^{26}$ s^{-1}; this measurement has the highest amount of noise present and the largest uncertainty in its estimation. For the HSO non-detection on November 23rd, 2011, the estimated upper bound on the vapor production rate is $1x10^{26}$ s^{-1}. The vapor production rate for the Dawn event is based on a magnetohydrodynamic model that calculates the vapor production rate necessary to produce a bow shock (Jia et al., 2017; Chapter 6). This model is similar to the code used by Jia et al. (2014) to study comets in the solar wind.

Figure 7.6 shows a positive correlation between the calculated water production rates and the measured flux of solar energetic particles at 1 AU. In instances where the observations were preceded by an above-average flux of energetic ions, water vapor was detected. The non-detections appear to reside below an average ion flux of ~0.1 $cm^{-2}s^{-1}sr^{-1}MeV^{-1}$ and the positive detections above this, when 2-4 MeV protons are used as a proxy. In interpreting the correlation one should note that a factor of two variation in the HSO observations is significant but a factor of two difference between HSO and IUE may not be significant since the two techniques have not been intercalibrated.

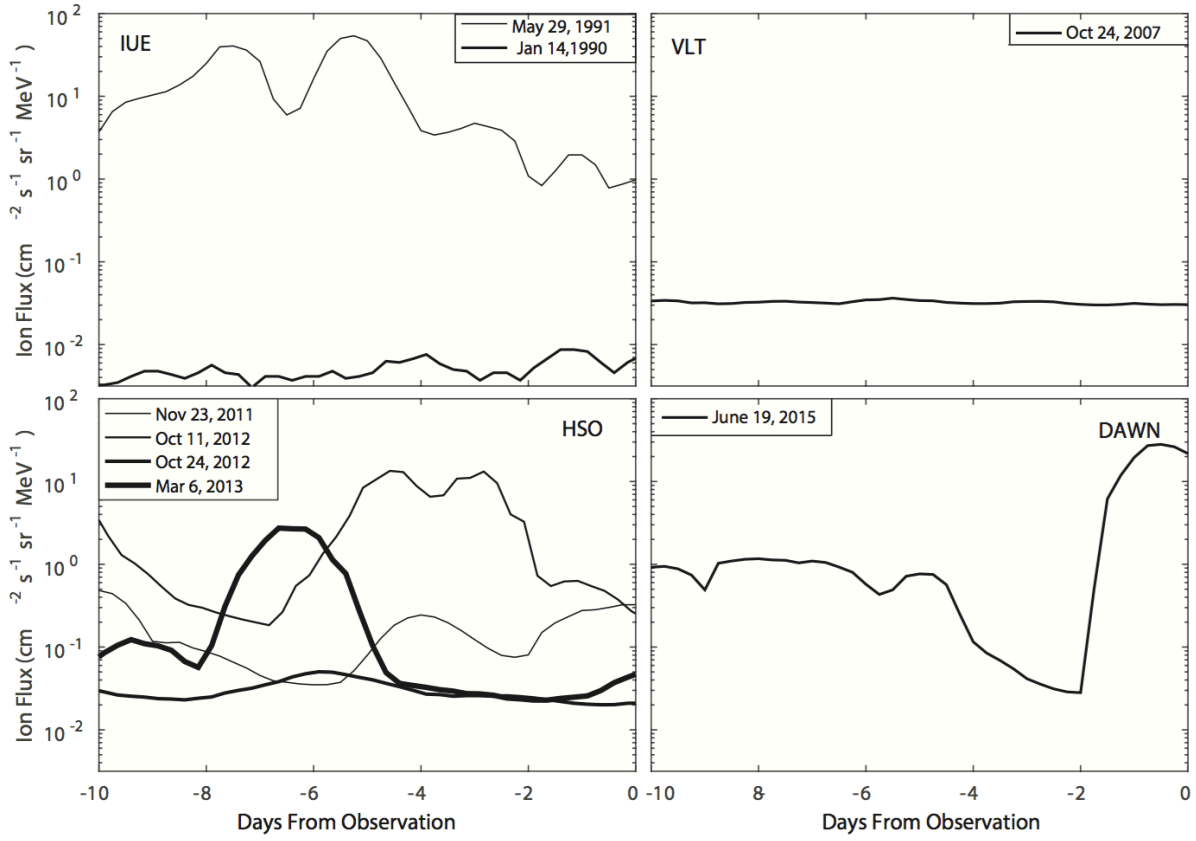

Figure 7.5 *Daily averages of the ion fluxes prior to each observation. The data for the IUE cases are provided by the OMNI data (2–4 MeV), while all other cases are taken from the ACE EPAM instrument (1.91–4.75 MeV).*

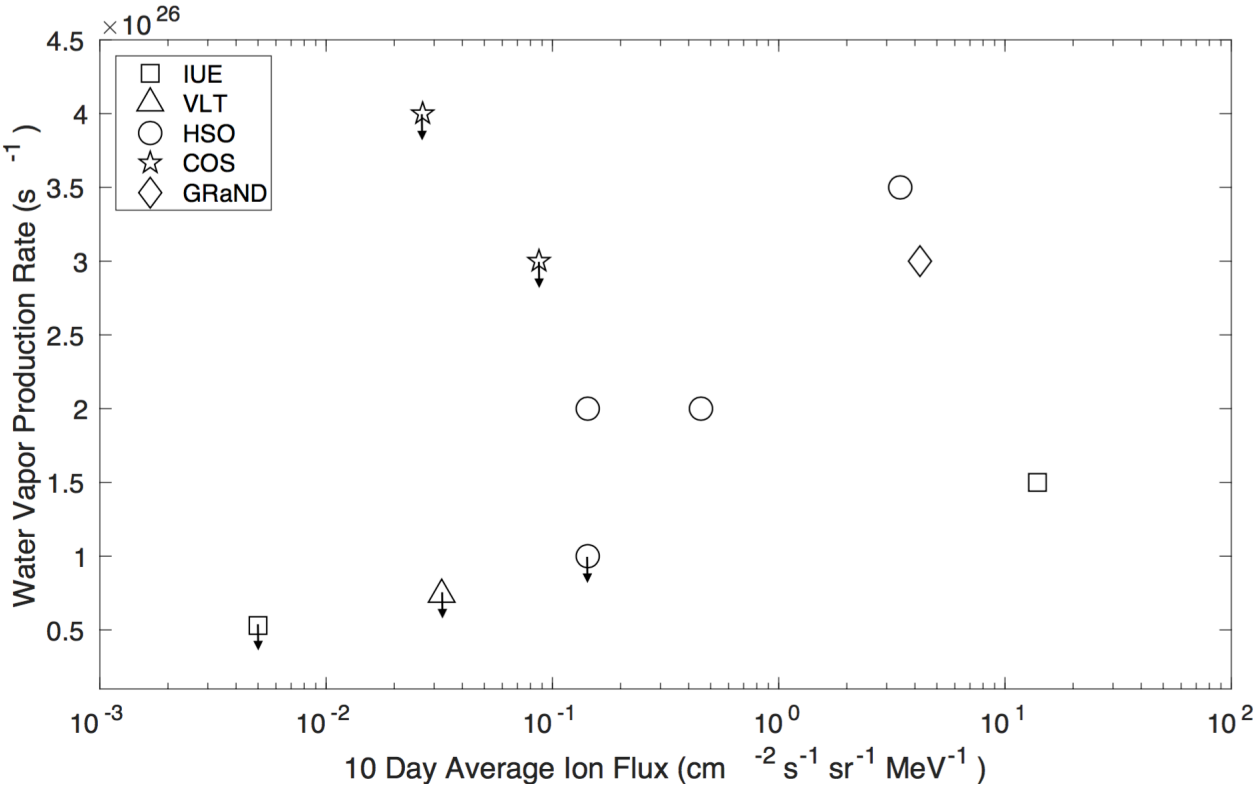

Figure 7.6 *Energetic ion flux at 1 au averaged over 10 days prior to observation vs. the water vapor production rate detected. Upper limits are used for cases where water was not detected.*

Previously proposed methods for the production of the cerean atmosphere do not provide satisfactory explanations for its occurrence. Dawn has seen no evidence for active plumes, optically or thermally. A sublimation-driven exosphere is inconsistent with the orbital locations of Ceres during the positive and negative water detections. The IUE observations were taken at similar heliocentric distances near perihelion, yet have contrasting detection results. HSO saw the strongest water signal when it was midway between aphelion and perihelion, followed by detections that were about half the magnitude as it approached the sun. While sublimation may be the original source of the water stored on the surface of Ceres, the correlation with the solar proton flux indicates that solar particle sputtering is the proximate agent for the temporary enhancements in the vapor production rate, allowing the exosphere to be detected telescopically.

The observed variability in solar energetic protons is consistent with the transient behavior of Ceres' water exosphere. The differing solar energetic proton conditions provide a plausible explanation for the difference in exospheric detection during the two IUE measurements. The positive OH detection directly followed a large proton event, while the negative detection occurred when the proton flux was at background levels. The magnitudes of the water signals detected by HSO also varied with the particle flux observed at 1 AU.

Continuous GRaND observations during the event shown in Figure 7.3 indicate the transient exosphere can last on the order of a week once produced. Solar protons may generate the exosphere by sputtering water ice from exposed ice patches on the surface (Combe et al., 2016), water ice in polar cold traps (Platz et al., 2016; Schorghofer et al., 2016), the global ice table (Prettyman et al., 2017), or water molecules adfixed to the Ceres soil. We conclude that the time variability of solar proton sputtering from one or more of these possible sources is the most likely cause of the transient nature of Ceres' exosphere. A reactive telescopic program observing

the cerean exosphere immediately following large solar events is necessary to test the SEP-sputtering hypothesis. This could be instituted during alignments with MAVEN, Earth, or the STEREO spacecraft, all of which are properly instrumented to observe solar energetic particles.

7.3 Testing the SEP-Induced Exosphere Hypothesis

In order to test the sputtering hypothesis, how SEP events arrive at Ceres and their impact on the surface need to be better understood. Care will need to be taken with the reactive campaign as not every SEP event is expected to be capable of inducing an observable exosphere. If methods are not in place to determine whether Ceres is connected to the SEP source, one may trigger the reactive campaign after a SEP event though no SEPs may actually arrive at the body. Alternatively, if the SEP event is connected to the body but is small in magnitude, it may not kick up enough exosphere to be above the detectable limit of telescopes.

In this section, we analyze the magnitude of SEP events at the Ceres' distance as observed by Dawn and compare with 1 AU measurements. This will allow us to analyze real-time delays, how the event changes along the same IMF line, and how different IMF lines experience the same event. We then use the empirical Dawn SEP measurements and compare to potential real-time SEP prediction models to evaluate how well these models replicate events at 1 AU and Ceres. This work will lay the foundation for a reactive telescopic campaign to observe the cerean exosphere with earth-based telescopes immediately following a large SEP event.

7.3.1 Comparison of SEP Events at 1 AU and Ceres' Location

Determining how the flux of a SEP event will vary from 1 AU to ~3 AU at Ceres is not straightforward since the shock surface is continually expanding and accelerating particles.

Therefore, one cannot simply extrapolate from the 1 AU data using a fall-off relation. Previous studies have tried to quantify how the flux during solar events changes with heliolongitude and radial distance (Lario et al., 2006), but have been limited in analysis given the narrow longitudinal and radial ranges of Earth-based spacecraft. Hence, this analysis is also of interest to the heliophysics community as it provides observations for solar events much further in the heliosphere.

Though Dawn has only been stationed at Ceres since early 2015, SEP events that occurred during its previous stay at Vesta are useful in this study. Vesta and Ceres are located in similar regions of the asteroid belt with Vesta at ~2.4 AU and Ceres at ~2.8 AU, providing more data points for how SEP events arrive in this region of the solar system. In addition, the Vesta portion of the Dawn mission was conducted during solar maximum when SEP events were more energetic and occured more frequently while observations at Ceres occurred as the sun was headed toward solar minimum.

Dawn's payload does not include traditional instrumentation used for studying the properties of the solar wind. Despite this, Dawn is still capable of sensing its local space environment by detecting energetic protons and electrons with its Gamma Ray and Neutron Detector (GRaND). Inelastic collisions of the energetic protons with spacecraft material leave nuclei in an excited state. The nuclei then emit gamma rays which are detected by the exterior scintillators and the center Bismuth Germanate (BGO) scintillator. For example, energetic protons will cause an increase in counts at 4.4 and 6.1 MeV (C and O peaks) in the BGO spectrum due to the composition of the detector housing. Here, we have applied the technique described in Chapter 2 for identifying energetic protons to catalogue solar events observed by Dawn.

We identified 13 SEP events from 2011-2018 observed by Dawn's Gamma Ray and Neutron Detector (GRaND). To accomplish this, we first scanned the +Z Phoswich data for abrupt, large enhancements in counts lasting days to flag events with behavior typical of SEPs. We then confirmed the events by analyzing the corresponding enhancments in the gamma ray spectrum at energies 4.4 and 6.1 MeV. These SEP events are listed in Table 7.1. The table lists the relative magnitude and duration of each event. The magnitudes listed have had the background levels subtracted and therefore reflect the increase in counts caused solely by the protons. There is a gap in SEP events between August 2012-March 2015 because GRaND was turned off while the spacecraft was in its cruise phase between planets. The SEP events vary in intensity, with the enhancement in counts of the +Z Phoswich varying over an order of magnitude. SEP enhancements lasted an average ~6.5 days, with some events exhibiting consecutive shocks.

The recorded SEP events were then compared to measurements by space weather monitoring spacecraft: Wind 3DP (Lin et al., 1995), STEREO A LET (Mewaldt et al., 2008), and STEREO B LET (Mewaldt et al., 2008), all located at different heliolongitudes near 1 AU. Protons need a minimum energy of 4.4 MeV to be detected by GRaND. We therefore compared the GRaND measurements to equivalent energy bins from the Wind (4.6 MeV) and STEREO (5 MeV) spacecraft.

Figure 7.7 shows an example of a solar energetic particle event arriving at the Earth-based Wind spacecraft (black line) in comparison to the response at Vesta (cyan line), while Figure 7.8 shows the same event for STEREO A and Vesta. At that time, Earth and Vesta were radially aligned, while Vesta's magnetic footprint was closest to STEREO A. Considering that energetic particles travel along field lines until they arrive at a specified location, one might

naively expect Vesta to experience the event similarly to STEREO A. However, the ability to identify a good proxy based on the proximity of magnetic footprints is complicated because the field lines typically do not source energetic particles directly from the Sun's surface, but rather from the surface of a CME which can intersect a monitor's field line at any radial distance as the CME expands through the heliosphere. In Figures 7 and 8, all three monitors observe the arrival of 2 consecutive shocks. However, in this case, Earth serves as a better proxy for the arrival of SEPs at Vesta than STEREO A, despite Vesta's Parker field line having a closer proximity to STEREO A. The SEP event at Vesta has similar slopes in its rise and fall to that measured by Wind, along with similar arrival times of the peaks. Meanwhile, the event at STEREO A is more gradual and experienced both its peaks two days after their arrival at Vesta. The CME originated in the direction of Earth, expanding and connecting to Earth's and Vesta's field lines allowing SEPs to travel, while it needed more time to expand to STEREO A field line, causing a delay. This example exhibits how the best spacecraft to use as a proxy for SEP encounters may not always be the one closest in proximity to its IMF field line. The location and expansion of the shock must be carefully considered.

We repeated this analysis for all the events listed in Table 7.1 by comparing Dawn's responses to those of Wind, STEREO A, and STEREO B. In instances when Dawn was along or very near the same field line as 1 AU spacecraft and the origin of the CME had a similar heliolongitude to that of the 1 AU spacecraft, measurements by that monitor served as an ideal proxy for the arrival of SEPs at Ceres with both spacecraft recording similar responses. In that scenario, the Dawn data often showed an onset ~10 hrs after the onset recorded by the 1 AU satellite (the expected travel time for a 4 MeV particle from 1 AU to ~3 AU). However, if the CME had an origin with a heliolongitude similar to Ceres, spacecraft whose magnetic footprints

were located close to Ceres' magnetic footprint did not provide a good proxy. In those cases, spacecraft near radial alignment with Ceres, though not on the same field line, gernerally served as a good substitute for a proxy. For those cases, the events at Ceres' location had a similar variation to 1 AU events, but were more 'compressed' thatn their counterparts (i.e. they had shorter durations than their 1 AU counterparts but still displayed the same main features of the events; Figure 7.7). It is important to note that the interplanetary magnetic field lines can become highly distorted during a CME event and relying on the ideal Parker spiral to infer a planet's ability to serve as a good proxy can be misleading. We explore the importance of this distortion using models in the next section.

Start Date	Peak Magnitude (Δcounts/s)	Length (Days)	Enlil Simulation?
6/5/2011	2020	8.3	No
8/5/2011	102	4.2	Yes
8/9/2011	38	3.4	Yes
11/4/2011	77	8.1	No
1/28/2012	203	3.8	Yes
3/7/2012	1941	13.7	No
7/24/2012	2358	10.7	Yes
3/25/2015	43	6.2	No
5/2/2015	17	2.6	No
6/18/2015	115	2.5	Yes
10/29/2015	23	4.4	No
7/24/2017	604	4.1	Yes
9/11/2017	1487	13.9	Yes

Table 7.1 *List of SEP events observed by Dawn. Dawn was stationed at Vesta from 2011-2012 and permanently at Ceres after 2015. Background levels have been subtracted to calculate the relative peak magnitudes.*

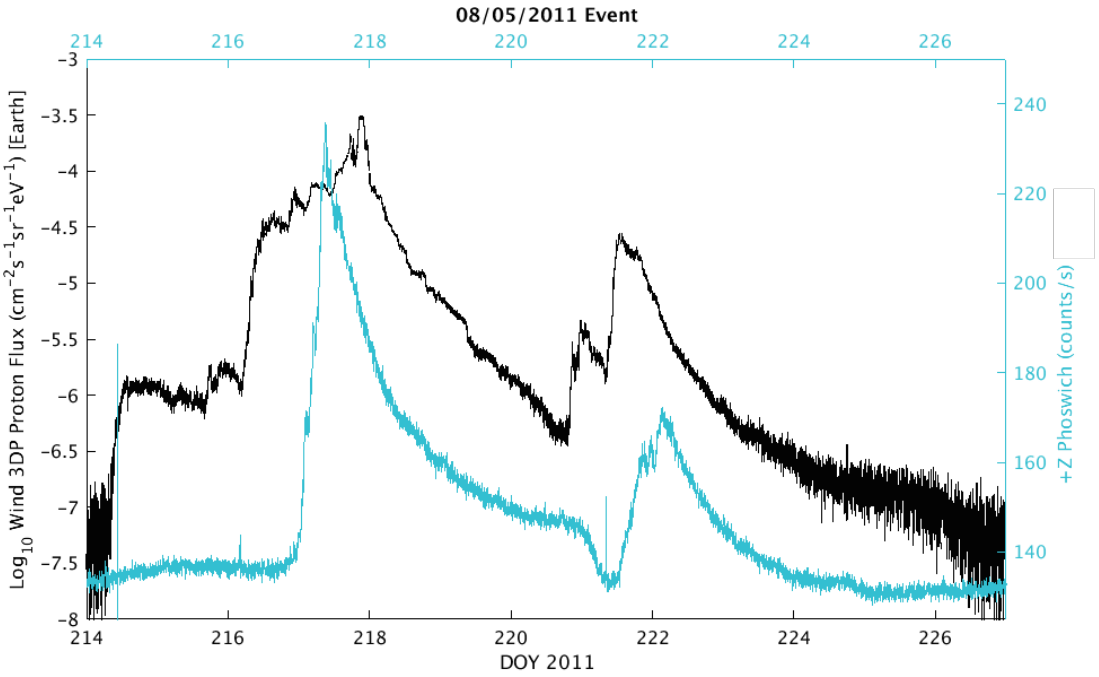

Figure 7.7 *Comparisons of a solar energetic particle event observed by Wind at 1 AU (black line/left axis; 4.6 MeV protons) and by Dawn's Gamma Ray and Neutron Detector at Vesta (cyan line/right axis). Vesta and Earth were radially alligned.*

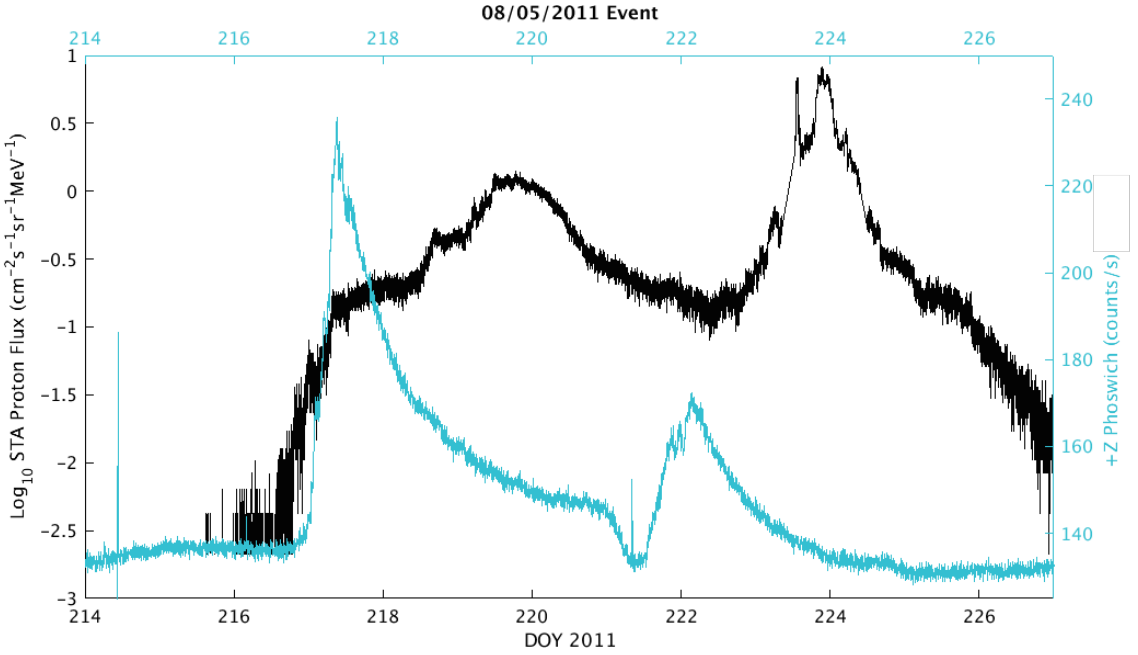

Figure 7.8 *Comparisons of a solar energetic particle event observed by STEREO A at 1 AU (black line/left axis; 5 MeV protons) and by Dawn's Gamma Ray and Neutron Detector at Vesta (cyan line/right axis). STEREO A and Vesta had similar magnetic footprints.*

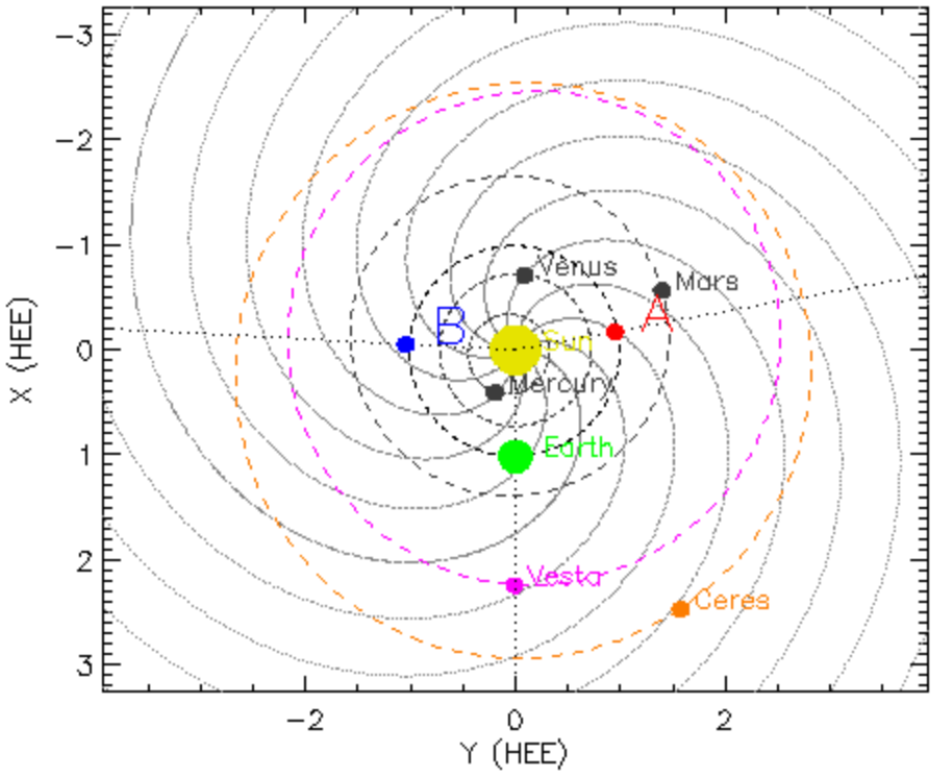

Figure 7.9 *Relative geometries of spacecraft on 08/05/2011 when Dawn was stationed at Vesta. Figure produced by https://stereo-ssc.nascom.nasa.gov/where/.*

7.3.2 Enlil and SEPMOD Simulations of Empirial SEP Events

In practice, real-time prediction models will be needed to anticipate whether a SEP event will encounter Ceres. If a SEP event were to occur during an opportunity to observe the exosphere, a system needs to be in place to forecast if Ceres will be connected by interplanetary magnetic field lines to the shock surface, allowing for the propagation of SEPs to the body. In this section, we discuss how Enlil (Arge et al., 2004), a magnetohydrodynamic model that predicts how solar disturbances will propgate in the solar wind, in conjunction with SEPMOD (Luhmann et al., 2007) , an energetic flux predictor for the arrival of SEP events, can be used to predict the arrival of SEP events at Ceres. We further compare the empirical Dawn events to the

Enlil and SEPMOD model results to assess how well the models replicate the response at Dawn's location.

Enlil is a magnetohydrodynamic model that predicts how coronal mass ejections will propagate into the heliosphere. The ambient solar wind is calculculated by a potential field source surface constructed from daily magnetograms. Solar coronograph images are used to estimate properties of solar events such as angular width, location, and velocity which become parameters into a cone model for the CME. It then tracks how the event propagates through the ambient solar wind and outputs the changes in solar wind conditions (ie velocity, density, magnetic field) at specified observer locations.

Enlil modeled events are used by SEPMOD to understand how an observer is connected to the shock surface and predict the flux of SEP particles at the observer's location. At each timestep, SEPMOD updates the shock location and magnetic field connectivity using inputs from Enlil. SEPMOD then uses an emprically derived power law by Lario et al. (1998) to determine the amount of protons to inject at the connectivity site; this power law is dependent on parameters such as the shock compression ratio and shock normal angle. The protons travel from the connection site to the observer location to produce the estimated SEP event profile for proton energies between 1.2-26 MeV. To validate these predictions, we can retrospectively compare the model outputs to the in-situ observations analyzed in the previous section to understand the accuracy of the model and its usefulness for the reactive campaign. We inspected Enlil and SEPMOD simulations for six of the SEP events identified in Table 7.1.

Figures 7.10 shows the relative locations of the spacecraft during the January 28th, 2012 event when Dawn was stationed at Vesta. Though Vesta and STEREO B are near radial alignment, the timeseries of their proton fluxes show no resemblance (figure not shown).

However, the event detected at Earth has almost an identical response, with a ~10 hr shift expected for these energies (Figure 7.11), despite a heliolongitude separation ~120 degrees between the two planets. A fair amount of separation also exists between their magnetic footprints. Figure 7.11 shows the tail end of another event before January 27th, which both planets observe similarly. Only data after January 26th is available for Dawn due to a data gap, so it did not fully observe the first event.

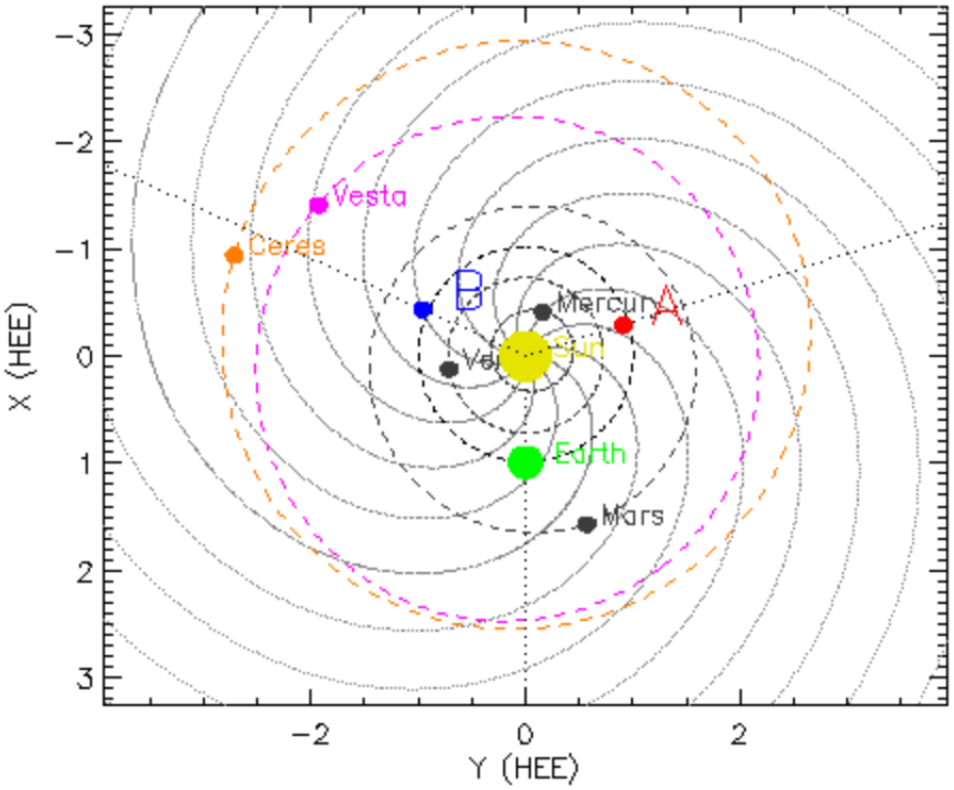

Figure 7.10 *Relative positions of the spacecraft on January 28, 2012 when Dawn was stationed at Vesta.*

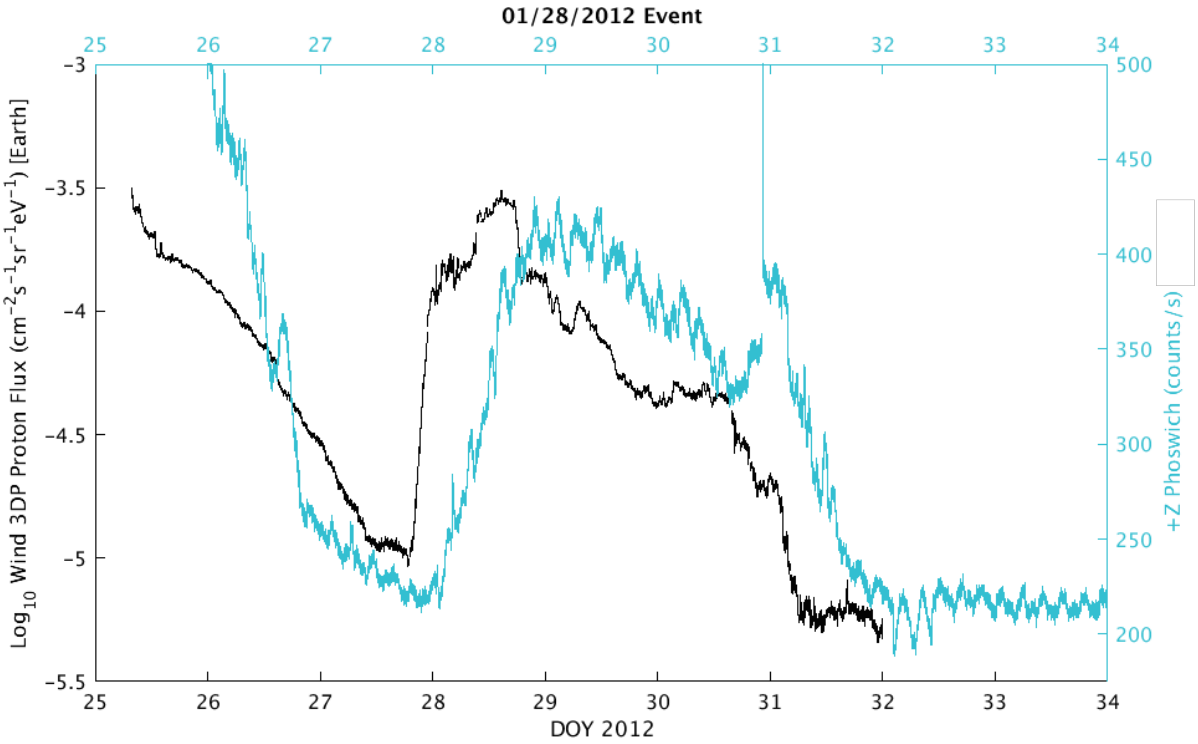

Figure 7.11 *The responses to the 1/28/2012 SEP event at Earth (black line, left axis) and at Vesta (cyan line, right axis). The timeseries' are remarkably similar, with the Dawn data shifted about 10 hrs (the expected travel time).*

Figure 7.12 shows a snapshot of the Enlil simulation produced for this event, with the simulation starting on Junary 22nd, 2012. The CME events originate with a heliolongitude similar to Mars, roughly on the opposite side of the sun from Vesta. The propagation of the first cornoal mass ejection causes a distortion of Earth's interplanetary magnetic field line to where its IMF line moves back and forth over Dawn's location. This means that Dawn and Earth are essentially sampling the same population of protons therefore giving rise to nearly identical (but time shifted) responses. This explains why Dawn and Earth were observed to have similar time series (Figure 7.11) even though they had a large separation in their locations.

Figure 7.13 and 7.14 show the SEPMOD prediction of the proton flux at each monitor for the August 2011 and January 2012 events, respectively. The start times for the SEPMOD simulations are August 2nd, 2011 and January 22nd, 2012 (time zero in each case). In comparison

to the Earth and Dawn data (Figures 7.7 and 7.11), SEPMOD accurately predicts the onset of the SEP events at each observer location. For the August 2011 event, it predicts the onset at Earth to be on August 2nd, 2011 and at Vesta on August 5th, 2011. These are the same onset times that we observe in the data (Figure 7.7). Similarly, SEPMOD predicts an onset of the second January 2012 event at Earth starting at the end of January 27th, and predicts Dawn's profile to rapidly increase starting January 28th, the same as the data. However, for the Dawn cases, it does not fully capture the fluctuations of the SEP events and predicts the events to last many days longer than the events were observed by Dawn.

These issues were common in the additional Dawn SEP event runs we inspected. The simulations usually produced satisfactory predictions of the SEP fluxes at 1 AU in terms of their onset, rise and fall, and duration. For the Dawn distance, the models did a good job at estimating the onset of the SEP events, but generally did not reproduce well the variation in the SEP event and predicted the events to last much longer than observed. SEPMOD typically outputted events for Dawn exceeding ten days in length while the average event length for the modeled events was ~6.5 days. Why these problems occur remains to be investiaged. Still, these models are useful tools for predicting how and when the Ceres location becomes connected to a CME event.

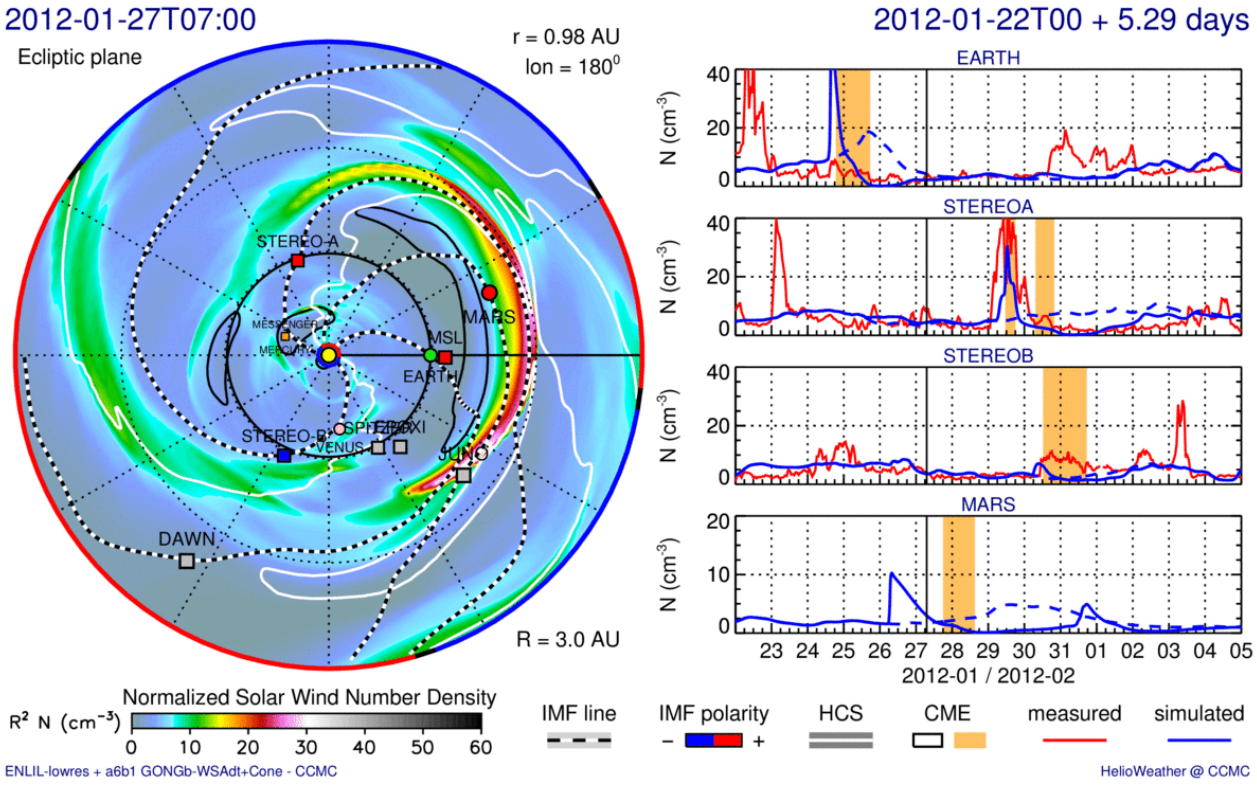

Figure 7.12 *Snapshot of the Enlil simulation produced for the January 2012 SEP event in the ecliptic plane. The simulation shows the interplanetary lines become so distorted that the Earth and Dawn are now along the same IMF line.*

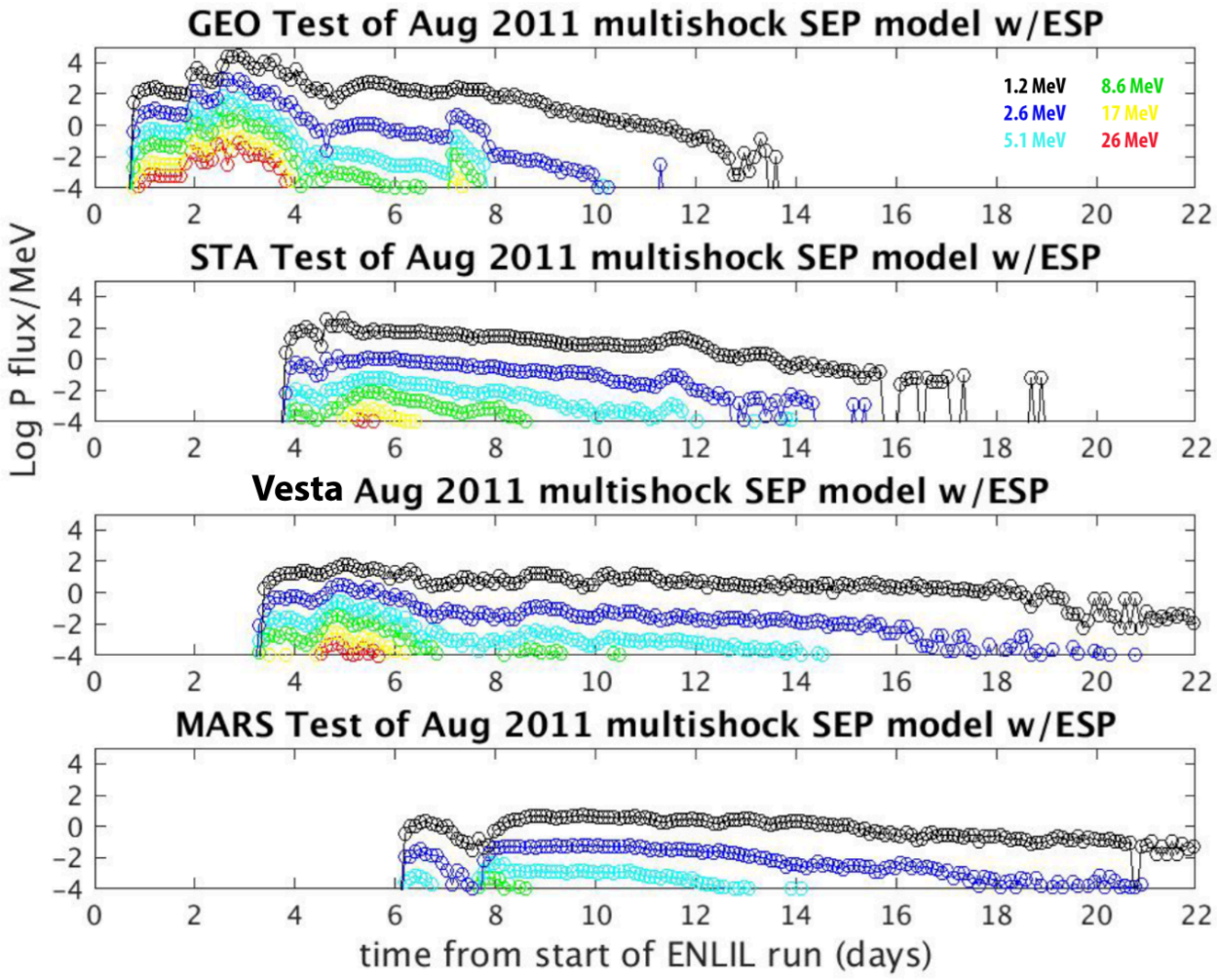

Figure 7.13 *SEPMOD predicted fluxes at different observer locations for the August 2011 SEP event (shown in Figures 7.11). Time zero corresponds to August 2nd, 2011.*

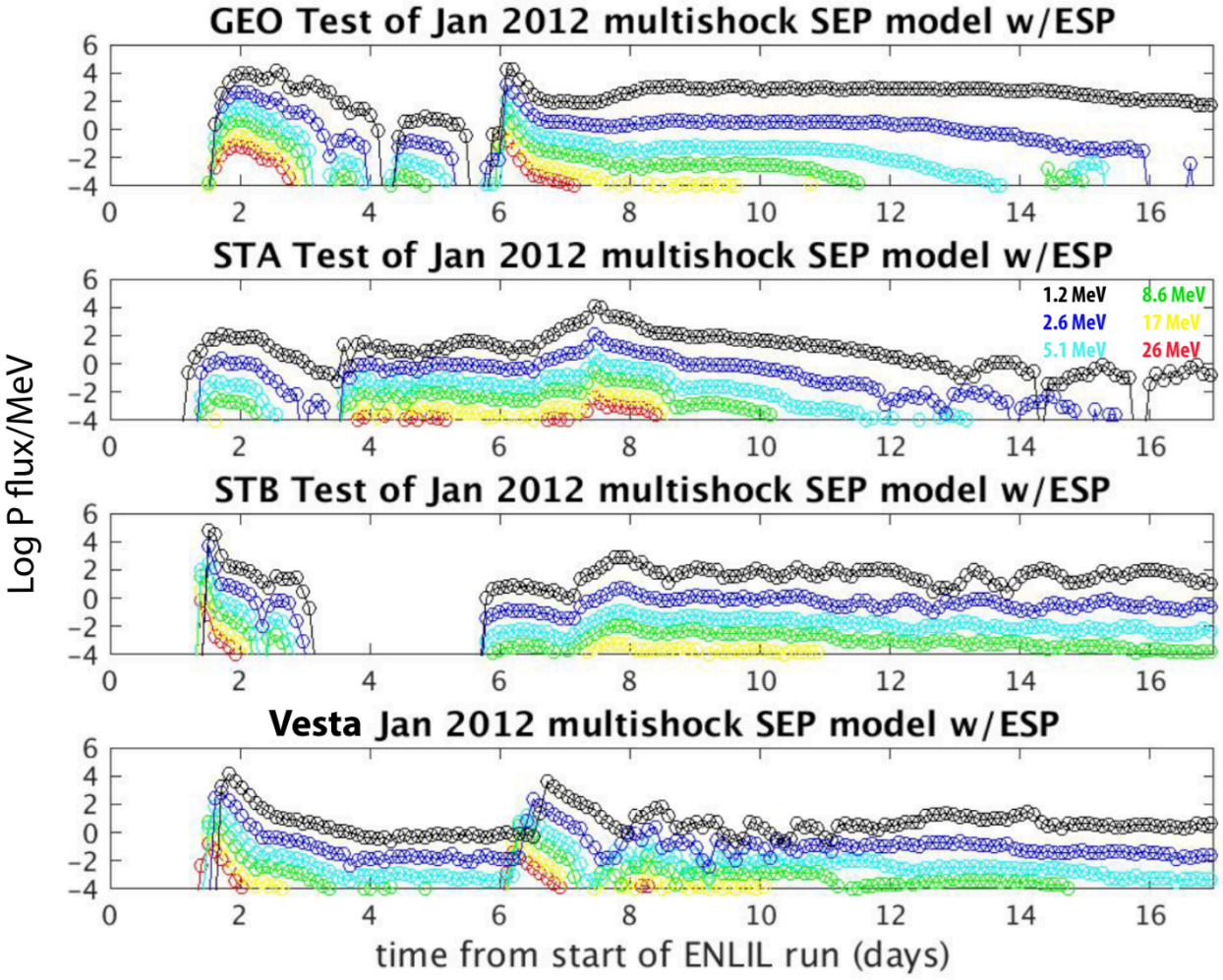

Figure 7.14 *SEPMOD predicted fluxes at different observer locations for the January 2012 SEP event (shown in Figures 7.7 and 7.8). Time zero corresponds to January 22nd, 2012.*

7.4 Calculations for the Liberation of Water Molecules by SEPs

In this section, we perform an order of magnitude calculation to understand what flux of energetic protons is needed to reproduce vapor production rates similar to those reported by telescopic observations. We approximate Ceres to be a sphere of pure water-ice and assume the protons to be coming from the hemisphere containing the sun (ie. 2π steradians). We calculate the average proton flux for energies 74 keV-1 MeV at 1 AU from the Wind 3DP instrument over the ten days prior to the October 11th, 2012 telescopic observation. We extrapolate the flux to Ceres distance by assuming a R^{-2} fall-off and calculate the expected rate of protons/s impacting the Ceres' surface for each H^+ energy bin.

Shi et al. (1995) performed lab measurements which showed that the sputtering yield of water ice by 30 keV H^+ ions rapidly increased with temperature for temperatures greater than 60 K. Similarly, Brown et al. (1982) also found that the sputtering yield of H_2O by 1.5 MeV He^+ ions rapidly increased at temperatures greater than ~110 K. The sputtering yields measured for H^+ ions with energies between 10 keV to 1 MeV bombarding a water ice surface were measured for a temperature of 77 K (Shi et al., 1995; Brown et al., 1982). However, the average surface temperature of Ceres is about 80 degrees warmer than this, at ~155 K (Shorghofer, 2016; Hayne and Aharonson, 2015). Therefore, the lab measurements need to be adjusted to reflect the increased yield at these higher temperatures.

Shi et al. (1995) derived the yield dependence for 30 keV bombarding H^+ ions from lab measurements as $Y(T) = 2.76 + 880e^{-0.052\,eV/kT}$, where 0.052 eV is the binding energy of H_2O, k is the Boltzmann constant, and T is the temperature. Using this equation, it is simple to show that the yield at 155 K is ~6.5 times more efficient than the yield at 77 K. In this order of magnitude calculation, we assume that this increase factor in the yield production is the same

across all energies. We then multiply the lab measurements reported in Shi et al. (1995) for the number of water molecules sputtered per H^+ ion for energies 10 keV-1 MeV by a factor of 6.5 to adjust the measurements from 77 K to 155 K. We multiply our calculated proton flux rates by the adjusted H_2O per proton energy and integrate over all energies to estimate the expected vapor production rate. We arrive at a ten-day average value of ~$1x10^{21}$ H_2O/s. This is about five orders of magnitude lower than the observed vapor production rate for this event, ~$3x10^{26}$ H_2O/s. Though this number is much lower than expected, there are many assumptions in this calculation that need to be better understood. For example, in this calculation we have used the average surface temperature of Ceres at 155 K. However, the protons should be more efficient at releasing water from the dayside, where the subsolar temperature can reach up to 237 K (Shorghofer, 2016). Lab measurements for Ceres-like temperatures need to be performed in addition to in-situ observations of the actual proton flux arriving at Ceres during these SEP events.

This order of magnitude calculation is solely for the ejection of H_2O molecules from the surface. However, lab measurements have found that sputtering by ions can also form and release H_2 and O_2 from the surface, where these yields also drastically increase with temperature (Brown et al., 1982; Pirronello et al., 1983). Therefore, there may also be a contribution of these sputtered species to the exosphere as well.

In this section we have specifically focused on the liberation of H_2O molecules from a pure-ice surface. In reality, most of Ceres' surface ice is expected to be located in the subsurface a few mm (near the poles) to greater than a meter (at the equator) depth (Prettyman et al., 2017) covered by regolith. There are a few exceptions where surface water ice has been detected by Dawn within the shadowed walls of craters and polar ice traps (Combe et al., 2016; Combe et al.,

2018; Platz et al., 2016). How the regolith affects the sputtering yield is not known; however, exospheric contributions from the subsurface water table will dominantly be sourced at higher lattitudes where the ice is very near the surface and not near the equator where water is likely too deep to access. Up to this point, we have not considered the general surface composition of Ceres. Ammannito et al. (2016) found that the surface of Ceres is ubiquitously covered by hydrated minerals. Thus far, no lab measurements for the sputtering yield of these minerals are available. However, it is possible that solar protons could release OH and/or H_2O from interactions with the phyllosilicates in addition to sputtering of the known water sources.

7.5 The Large September 2017 Event at Ceres

As the Sun was headed toward solar minimum at the end of 2017, it released one last large coronal mass ejection event which encountered Ceres. This event was larger in both magnitude and length than the June 2015 SEP event which spurred the detection of electron bursts (Table 7.1). We would expect this event to produce a transient atmosphere of equal or greater magnitude as the June 2015 event, thereby producing a transient bow shock. However, unlike the June 2015 event, no electron bursts were seen during the September SEP event, nor the week following the end of its passage. This could be due to several factors. The first, is the larger distance of the orbit. Figure 7.15 shows comparisons of Dawn's orbit during the June 2015 (blue line) and September 2017 (red line) events. The Survey orbit in 2015 was a three day, circular orbit located at a distance of 10 R_C. In contrast, the September 2017 orbit is a ~30 day orbit which has a periapsis at 12 R_C and an apoapsis at 82 R_C, thereby larger than the Survey orbit at each point. From Chapter 5, our STEREO A electron foreshock analysis suggested we could observe the Ceres electron bursts to a distance ~20 R_C. Figure 7.15 highlights in black the

portion of the September orbit when Dawn was within this observable range. Therefore, the September 2017 orbit is outside the observable range for most of its orbit, except for a 2-day period. However, 1.3 days of this segment were spent over the northern hemisphere. This is the region of the Survey orbit where electron bursts were noticeably absent. This means Dawn spent only 0.7 days in the area where we would expect it to observe September burst events. Finally, it is possible the direction of the interplanetary magnetic field did not connect the bow shock surface to Dawn's orbit. Hence, though there was an absence of bursts in the GRaND data for the large September event, this does not disprove its presence since the spacecraft was, for most of its orbit, not in a position to observe the bursts. Dawn remained in this orbit for all of 2017 and the same arguments can be made for the absence of bursts during the smaller July 2017 SEP event.

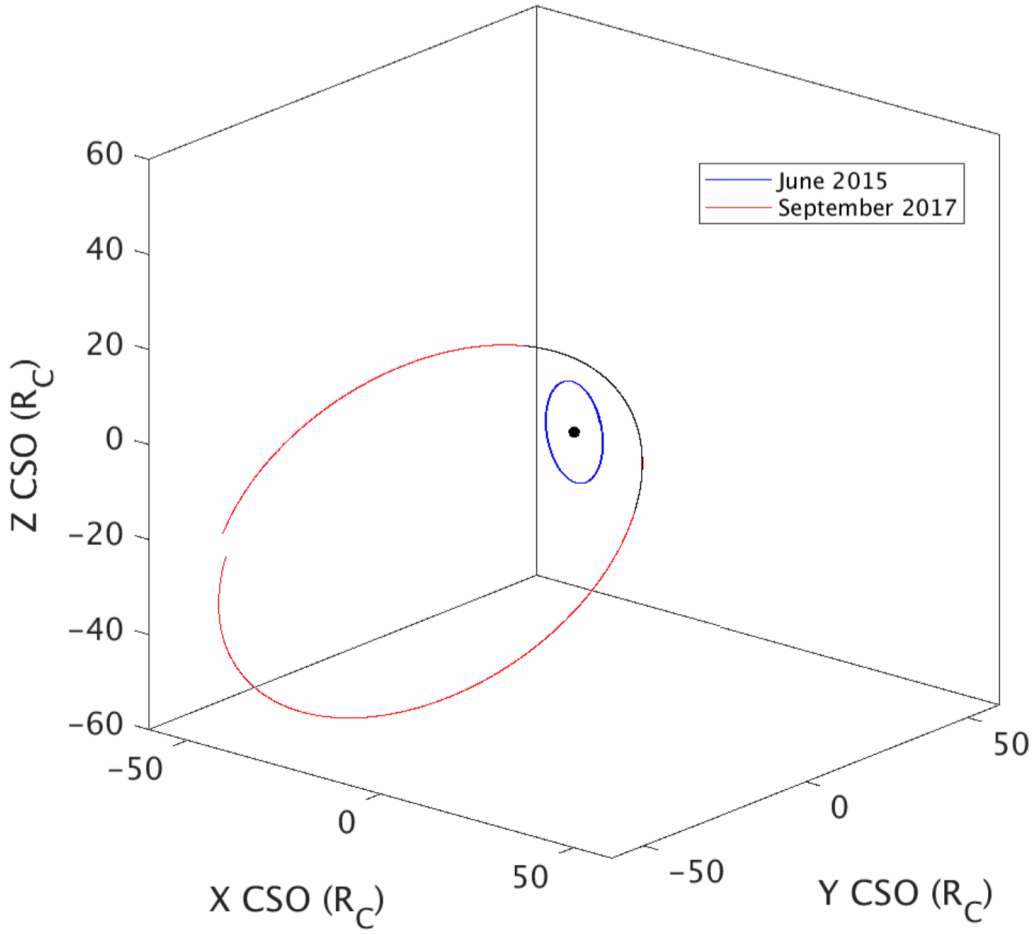

Figure 7.15 *Comparisons between the survey orbit (blue) and the orbit during the September CME event (red). The black portion of the 2017 orbit highlights when Dawn was within 20 R_C of Ceres.*

7.6 Summary

Previous telescopic observations have suggested a cometary-like sublimation process for the production of the cerean exosphere. However, the magnitude of the observations are not consistent with this hypothesis. We have presented an alternative theory, which hypothesizes the transient exosphere is produced by solar energetic particle events bombarding the surface and sputtering water. Review of the solar wind conditions during previous telescopic observations show that each positive detection was preceded by a SEP event and each negative detection

occurred when observations were taken during times of quiet solar activity. We also showed a correlation between the magnitude of the exosphere detected and the measured flux of energetic protons at 1 AU. This work is also relevant to cometary studies as this process could release water from a nucleus' subsurface before solar heating is strong enough to induce sublimation. Lab measurements for a Ceres-like temperature is needed to better understand this sputtering process.

Comparisons of the Enlil and SEPMOD models have shown that they can serve as good indicators for if and when a SEP event will encounter Ceres. However, the models still need to be refined as they do not always capture the the shape and duration of the event well. In the meantime, measurements at 1 AU can serve as good proxies for the arrival of SEPs at Ceres, given they meet the criteria we have previously mentioned.

7.7 References

A'Hearn, M. F. and P.D. Feldman, Water Vaporization on Ceres, Icarus 98, 54-60 (1992).

Arge, C. N., Stream structure and coronal sources of the solar wind during May 12th, 1997 CME, Journal of Atmospheric and Solar-Terrestrial Physics 66, 1295-1309 (2004).

Brown, W. L. et al., Linear and Nonlinear Processes in the Erosion of H_2O Ice by Fast Light Ions, Phys. Rev. Lett., 45, 1632-1635 (1980).

Brown, W. L. et al., Erosion and Molecule Formation in Condensed Gas Films by Electronic Energy Loss of Fast Ions, Nuclear Instruments and Methods, 198, 1-8 (1982).

Cheng, A.F. & Johnson, R. E., Effects of Magnetosphere Interactions on Origin and Evolution of Atmospheres, Univ. of Arizona Press, Tucson, 682-722 (1989).

Combe, J. P., et al., Detection of local H_2O exposed at the surface of Ceres, Science, Vol 353, Issue 6303 (2016).

Combe, J. P. et al., Exposed H_2O-rich areas detected on Ceres with the Dawn Visible and Infrared Mapping Spectrometer, Icarus 000, 1-20 (2018).

Eviatar, A., Plasma in Saturn's Magnetosphere, J. Geophys. Res., 89, 3821-3828 (1984).

Fanale, F. P. and J. R. Salvail, The Water Regime of Asteroid (1) Ceres, Icarus 82, 97-110 (1989).

Formisano, M. et al., Ceres Water Regime: Surface Temperature, Water Sublimation and Transient Exo(atmo)sphere, 2016, MNRAS 455, 1892-1904 (2016).

Gold, R. E. et al., Electron, Proton, and Alpha Monitor on the Advanced Composition Explorer Spacecraft, Space Science Reviews, 86, 541-562 (1998).

Hayne, P. O. and O. Aharonson, Thermal Stability of Ice on Ceres with Rough Topography, Journal of Geophysical Research: Planets, 120 (2015).

Jia, Y.D., M.N. Villarreal, C. T. Russell, Possible Ceres Bow Shock Surfaces Based on Fluid Models, J. Geophys. Res. Space Physics, 122, 4976-4987 (2017).

Johnson, R. E. et al., Sputtering process: Erosion and chemical change, Adv. Spac Res., 4, 41-51 (1984).

Küppers, M. et al., Localized sources of water vapour on the dwarf planet (1) Ceres, Nature, 505, 525-527 (2014).

Lario, D. et al., Energetic Particle Events: Efficiency of Interplanetary Shock as 50 keV<E<100 MeV proton accelerators, Astrophysical Journal, 509, 415-434 (1998).

Lario, D. et al., Radial and Longitudinal Dependence of Solar 4-13 MeV and 27-37 MeV Proton Peak Intensities and Fluences: HELIOS and IMP 8 Observations, The Astrophysical Journal, Vol. 653, 1531-1544 (2006).

Lanzerotti, L. J. et al., Implications of Voyager data from energetic ion erosion of the icy

satellites of Saturn, J. Geophys. Res., 88, 8765-8770 (1983).

Leroy, M. M. and A. Mangeney, A theory of energization of solar-wind electrons by the Earth's bow shock. *Annales Geophys.* **2**, 449-456 (1984).

Lin, R. P. et al. (1995), A Three-Dimensional Plasma and Energetic Particle Investigation for the Wind Spacecraft, Space Sci. Rev. **71**, 125-153.

Luhmann, J. G. et al. (2007), A heliospheric simulation-based approach to SEP source and transport modeling, Adv. Space Res., 40 (3), 295-303.

Mewaldt, R. A. et al. (2008), The Low-Energy Telescope (LET) and SEP Central Electronics for the STEREO Mission, Space Sci. Rev. 136, 285-362.

Park, R. S. et al., A Partially differentiated interior for (1) Ceres deduced from its gravity field and shape, Nature, 537, 515-517 (2016).

Pirronello, V., G. Strazzulla, and G. Foti, H_2 Production in Comets, Astron. Astrophys. 118, 341-344 (1983).

Platz, T. et al., Surface water-ice deposits in the northern shadowed regions of Ceres, Nature Astronomy, Vol 1, 7 (2016).

Prettyman, T.H. et al. (2011), Dawn's gamma ray and neutron detector, *Space Sci. Rev.* **163**, 371-459, doi: 10.1007/s11214-011-9862-0.

Prettyman, T. H. et al., Extensive water ice within Ceres' aqueously altered regolith: Evidence from nuclear spectroscopy, Science, Vol 355, Issue 6320, 55-59 (2017).

Reames, D. V., Solar Energetic Particles: A Modern Primer on Understanding Sources, Acceleration, and Propagation, Springer International Publishing (2017).

Roth, L. et al., Constraints on an Exosphere at Ceres from Hubble Space Telescope Observations, Geophysical Research Letters, 43, 2465-2472 (2016).

Roth, L., Constraints on Water Vapor and Sulfur Dioxide at Ceres: Exploiting the Sensitivity of the Hubble Space Telescope, Icarus, 305, 149-159 (2018)

Rousselot, P. et al., A Search for Water Vaporization on Ceres, The Astronomical Journal, Vol 142, 125 (2011).

Russell, C. T. et al., Dawn arrives at Ceres: Exploration of a small, volatile-rich world, Science, Vol 353, 1008-1010 (2016a).

Russell, C. T., Luhmann, J.G., Strangeway, and R. J., In Space Physics, 145 (2016b).

Schmidt, B. et al., Geomorphological evidence for ground ice on dwarf planet Ceres, Nature Geoscience, 10, 338-343 (2016).

Schorghofer, N. et al., The permanently shadowed regions of dwarf planet Ceres, Geophysical Research Letters, Vol 43, 6783-6789 (2016).

Schorghofer, N., Predictions of Depth-To-Ice on Asteroids Based on an Asynchronous Model of Temperature, Impact Stirring, and Ice Loss, Icarus, 276, 88-95 (2016).

Shi, M. et al., Journal of Geophysical Research Letters, Vol. 100, NO. E12, 26387-26395 (1995).

Wu, C. S., A Fast Fermi Process: Energetic Electrons Accelerated by a Nearly Perpendicular Bow Shock, Journal of Geophysical Research, Vol. 89, NO A10, 8857-886 (1984).

Chapter 8

Telescopic Observations of Ceres Following a SEP Event

8.1 Introduction

Following the completion of the prime mission, the Dawn spacecraft was inserted into a highly elliptical orbit to continuously collect background GRaND data. This also allowed for the monitoring of SEP events that could encounter Ceres. However, the Sun became very inactive after the large September 2017 coronal mass ejection (CME) event. On February 12th, 2018 the sun released a moderately-sized CME that appeared to be headed toward both Earth and Ceres. Figure 8.1 shows the relative locations of the planets. Since Ceres was near opposition, this allowed for telescopic observations of OH emission using the Very Large Telescope (VLT) located in the Atacama Desert, Chile. Since the Sun was entering solar minimum and was expected to continue to have limited activity in addition to the expectation that the Dawn spacecraft would run out of fuel by October 2018, this provided perhaps the only opportunity to conduct telescopic observations of Ceres' exosphere during a SEP event while an in-situ spacecraft was present.

8.2 Solar Conditions and 1 AU Observations

On February 12th, 2018, a coronal mass ejection emerged from sunspot AR 2699 directed towards the Earth. At that time, Ceres was near radial alignment with the Earth (Figure 8.1), likely to also be impacted by the CME. The February 12th CME was only moderately-sized and

much weaker than the burst of CME events in September 2017. However, the SEP proton fluxes that arrived at 1 AU for this event were similar to that recorded to the June 2015 SEP event which preceded the electron bursts observed by Dawn (Chapter 4).

Figure 8.2 shows a comparison between the February 12th, 2018 event and the June 2015 event at 1 AU for proton energies 550 keV-7 MeV detected by the Wind instrument, which is located in the solar wind at Earth's L1 Lagrange point. In both cases, the 550 keV-2 MeV protons jump about two orders of magnitude and roughly reach the same peak flux. Protons in the hundreds of keV energy range are the most efficient at sputtering water from an icy surface (Shi et al, 1995). However, protons above 4 MeV do not significantly increase for the February event while they did for the June event. This is important because protons greater than 4.4 MeV are needed to induce nuclear reactions in GRaND to register the SEP event. Though their magnetic footprints were separated about 45 degrees, the SEP flux at Earth indicated that the event produced protons with sufficient energy capable of sputtering an exosphere at Ceres.

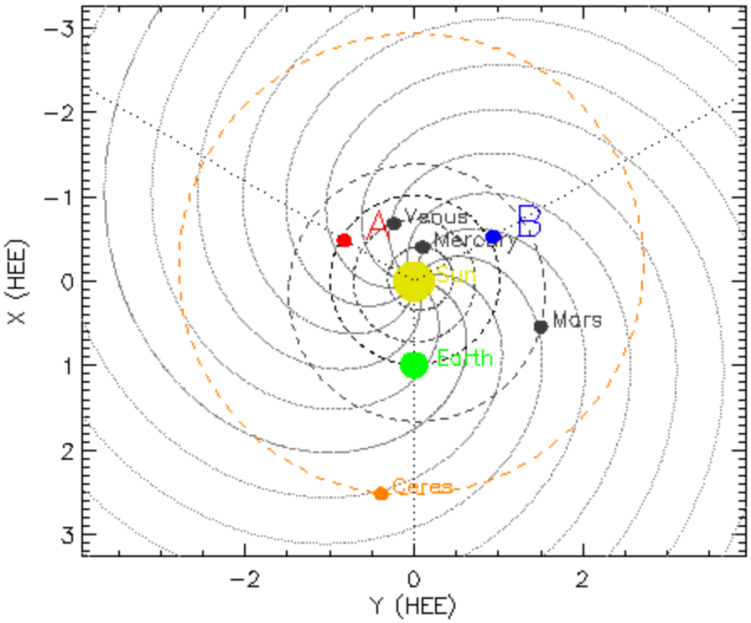

Figure 8.1 *Relative positions of the planets on February 12th, 2018. Ceres was near opposition with Earth. Figure generated by the STEREO orbit tool https://stereo-ssc.nascom.nasa.gov/where/.*

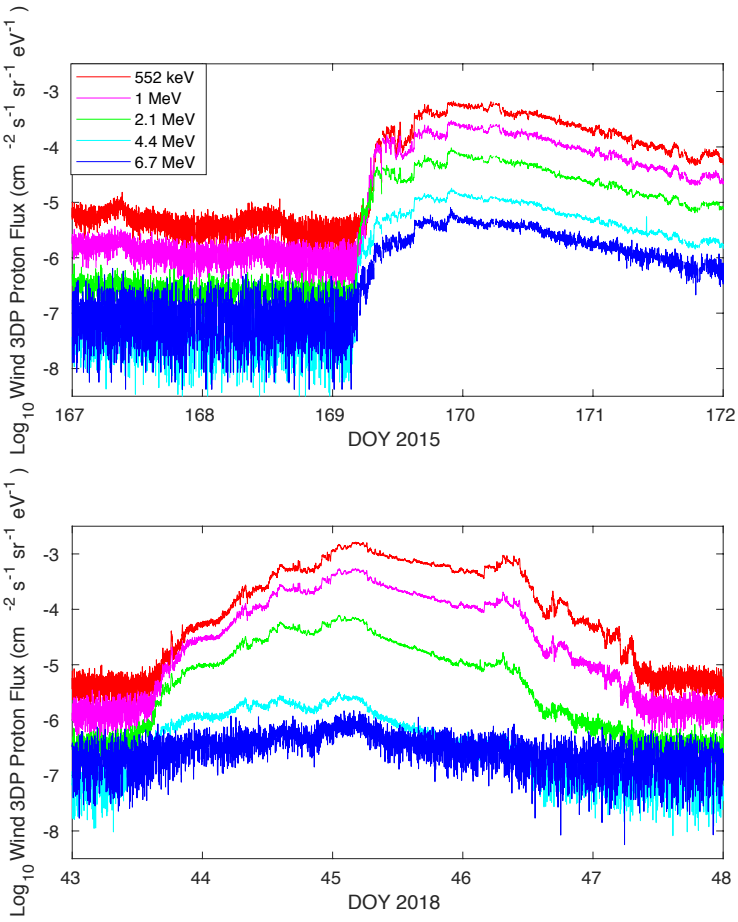

Figure 8.2 *Comparisons of SEP fluxes at Earth's location during the June 2015 event (top panel) and February 2018 event (bottom panel). SEP fluxes are similar for the 500 keV-2 MeV range, but are about an order of magnitude lower for energies above 4 MeV.*

8.3 Concurrent Observations by Dawn's Gamma Ray and Neutron Detector

Dawn provided in-situ measurements of the February 12th, 2018 event at Ceres. Figure 8.3 shows the total counts recorded by the +Z Phoswich of GRaND. The expected duration of the event is bounded by the red and blue dashed lines. These lines are the start and end time of the event at Earth shifted by 10 hrs, the approximate travel time for 4 MeV protons from the Earth to Ceres' distance. As can be seen in Figure 8.3, there is some increase in the total counts of the +Z Phoswich, but it does not appear to be related to the SEP event as the rise in counts began before the event and continue to increase after the expected end of the event.

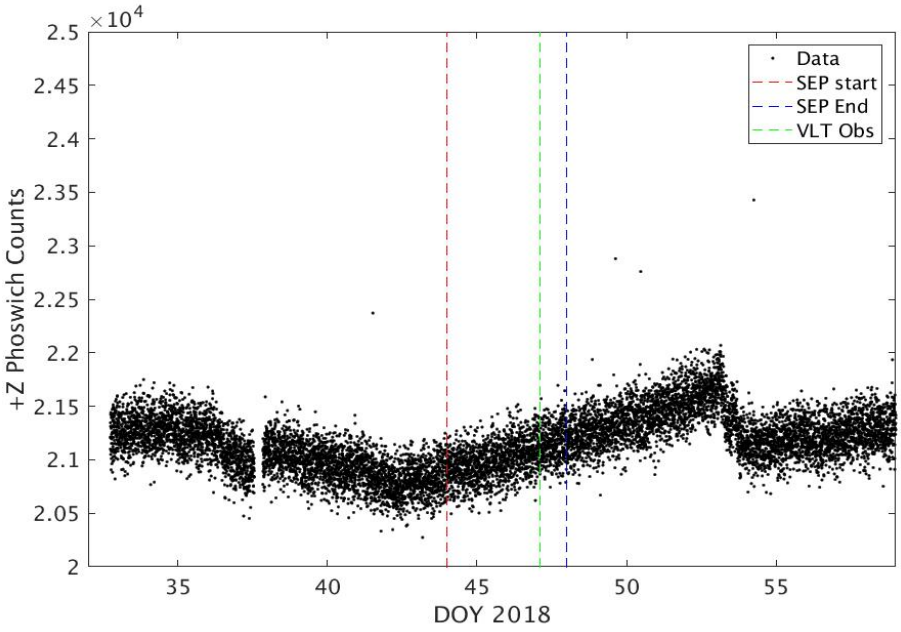

Figure 8.3 *Total counts in the +Z Phoswich. The red and blue dashed lines indicate the anticipated start and end of the SEP event, respectively. The timing of the VLT observation is indicated by the green dashed line. No obvious SEP event is observed to have impacted Ceres.*

For completeness, we employed our technique to identify any increase in counts due to the presence of energetic protons (Chapter 2). Figure 8.4 shows this analysis, where we have again defined the window of the event as 10-hr shifted from the Earth measurements. We have defined the background as a 100-pt window immediately preceding the beginning of the SEP event window (Figure 8.4, top panel). The bottom panel shows the subtraction of the averaged spectrum of the background window from the averaged spectrum of the SEP window. If protons were present, we would expect to see increases in counts in the spectrum located at 4.4 MeV (~channel 500) and 6.1 MeV (~channel 700) due to the interactions of the protons with Carbon and Oxygen, respectively. The bottom panel of Figure 8.4 shows there are no identifiable enhancements of these elemental peaks, suggesting energetic protons greater than 4 MeV were not present during the expected arrival of the SEP event.

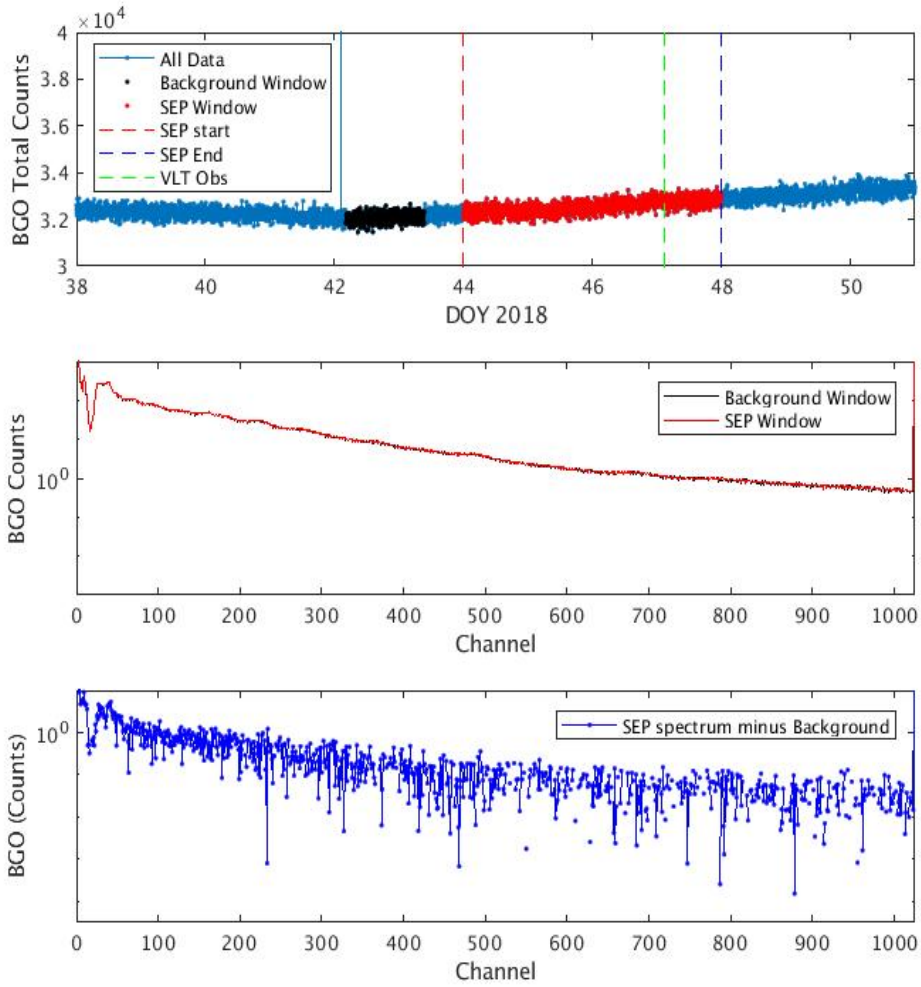

Figure 8.4 *Procedure to identify energetic protons. Comparisons of the background window and the SEP event window do not show any enhancements in the excited energy levels of carbon or oxygen, indicating no energetic protons were present.*

The previous section showed a sharp drop in the flux of the energetic protons above 2 MeV for the same event observed at Earth. This suggests that it is possible the SEP event could have encountered Ceres, but the flux of greater than 4 MeV protons may have not exceeded the threshold to be detected by GRaND. To investigate whether this is may be the case, we employ the Enlil and SEPMOD models to explore whether Ceres may have been connected to the CME shock.

8.4 Enlil and SEPMOD Models for the February 12th CME Event

We employ the Enlil and SEPMOD models described in Chapter 7. Figure 8.5 shows a snapshot of the Enlil simulation as the CME was traveling through the heliosphere. The black and white dashed lines show the IMF field lines to which each spacecraft is connected. In the simulation, Ceres becomes connected to the shock starting February 13th. This connection would allow for the travel of solar energetic particles to the Ceres' location.

SEPMOD predicts the solar energetic particle flux at a given location based on how a spacecraft is connected to the shock surface (Chapter 7). Figure 8.6 shows the outputs of the SEP arrivals at Earth, STEREO A, Ceres, and Mars where the onset of the simulation is defined as February 12th, 2018 (time zero). The lowest energy modeled by SEPMOD is 1 MeV. At the Ceres location, the flux of the 1 MeV (black circles) protons jumps by orders or magnitudes while all protons energies greater than that show weak enhancement. The increase in energetic particles for this event is much weaker in comparison to the SEP events explored in Chapter 7. The model also predicts the event at Ceres to last longer than ten days. From the previous chapter, we noted that the model often grossly overestimated the SEP duration at the Ceres distance.

The SEPMOD model output also predicts the protons above 4 MeV jump orders of magnitude above their background levels at the Earth location, which we know is not in agreement with the 1 AU in-situ data. Similar to examples shown in Chapter 7, it is likely that Enlil is correct in predicting when a location is connected to the shock, but the SEPMOD output is not accurately estimating the fluxes and the variation arriving at that location. Therefore, we conclude that though it is probable that Ceres was connected to the shock surface, the proton fluxes would have been too low to induce a detectable exosphere.

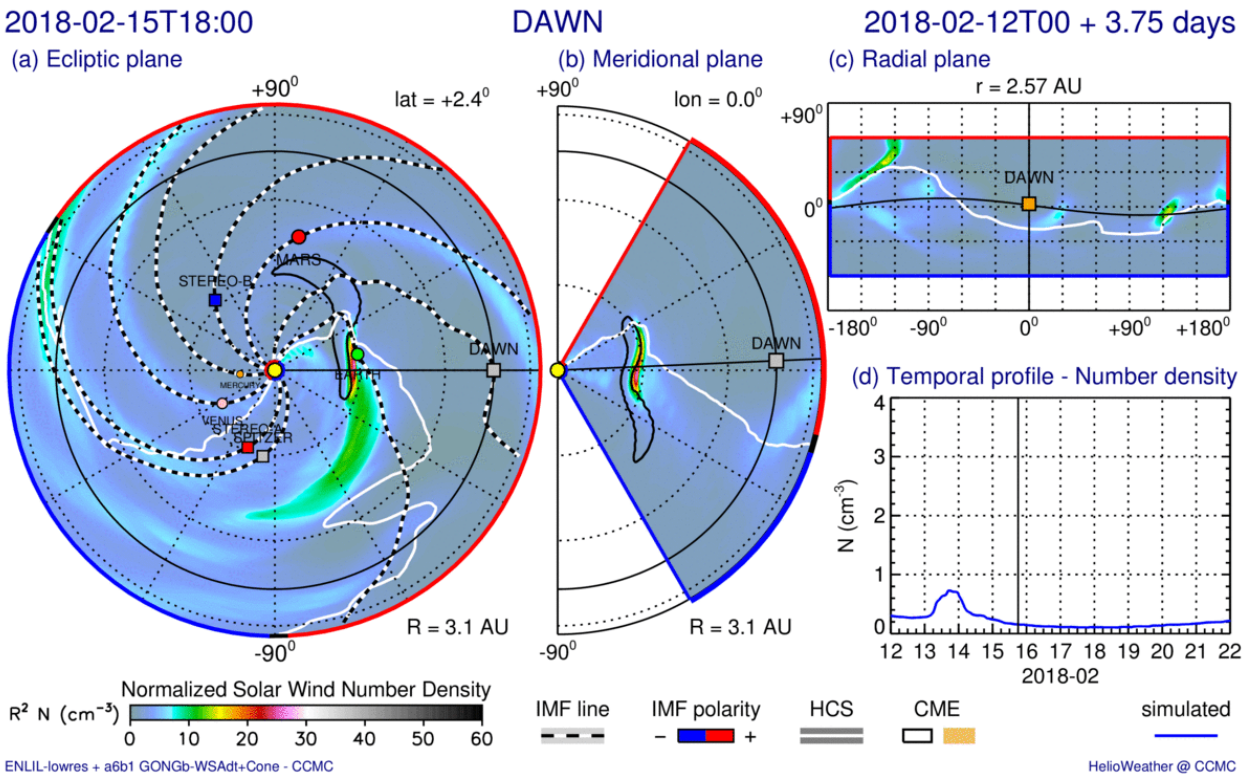

Figure 8.5 *Snapshot of the Enlil simulation for the February 12, 2018 event. The simulation suggests that Ceres was connected to the CME shock surface by its IMF line.*

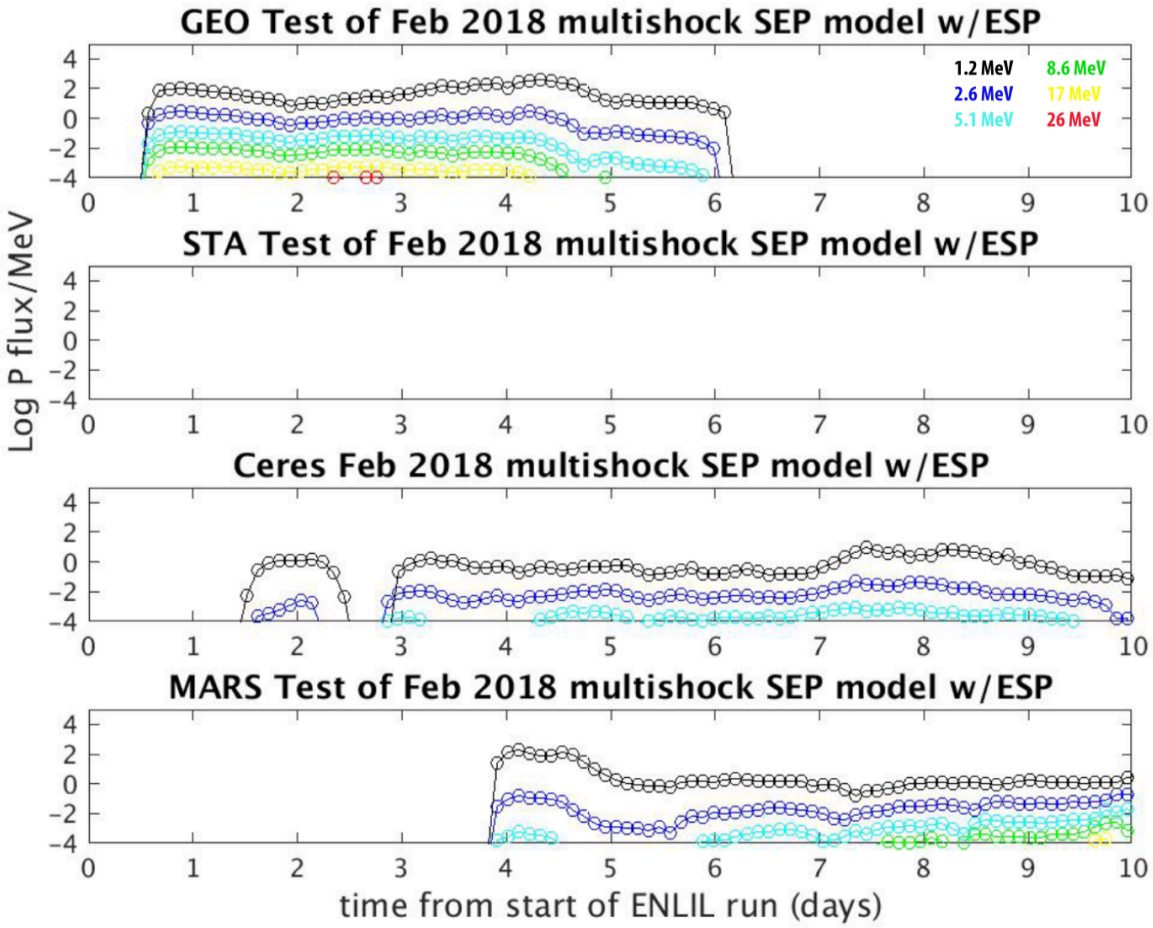

Figure 8.6 *SEPMOD predicted proton fluxes at various spacecraft locations. The top panel is the flux at Earth, second panel is the flux at STEREO A, the third panel is the flux at Ceres, and the bottom panel is the flux at Mars. Time zero corresponds to February 12, 2018.*

8.5 Very Large Telescope (VLT) Observations of OH Emission at Ceres

Given the limited number of observations of the cerean exosphere, more data points are needed to test the SEP-induced exosphere hypothesis (Chapter 1; Chapter 7). To observe Ceres with earth-based telescopes, several conditions need to be met to successfully observe. The first condition relies on the separation between Earth and Ceres: the dwarf planet needs to be near opposition to be within the telescopes' pointing range. The second, is the phase of the moon. If the moon is near its full moon phase, the reflected light from the moon will interfere with the

measurements. Therefore, it is best to observe when the Earth's moon is near its new moon phase. Lastly, to observe the exosphere following a SEP event, a CME will need to be headed in such a direction that the IMF line along Ceres will connect it to the shock and provide a sufficient amount of energetic protons to sputter the surface.

The only present-day operational telescope capable of observing water products for an outgassing rate ~10^{26} H_2O molecules/s is the Very Large Telescope (VLT), a ground-based telescope located in Chile which is sensitive enough to detect OH emission in the cerean exosphere. The sensitivity of the telescope will vary with observing conditions, but a previous non-detection observed Ceres with a sensitivity of ~10^{25} H_2O/s (Rousselot et al., 2007), similar to the magnitudes reported for the positive OH (A'Hearn and Feldman, 1992) and H_2O (Küppers et al., 2014) detections.

The CME event on February 12th, 2018 presented itself to be the only opportunity to observe Ceres exosphere following a SEP event while Dawn was still acquiring in-situ measurements. Fortunately, at that time, all the required observing conditions were met: Ceres was near opposition, the moon reached its new moon phase on February 15th, and the CME was headed in the direction of both Earth and Ceres, also allowing for Earth data to serve as a proxy for the expected proton flux at Ceres.

On February 16th, 2018, Ceres was observed by Rousselot et al. (2018) for OH emission using the Ultraviolet and Visual Spectrograph (UVES) instrument that is part of the Very Large Telescope (VLT). The slit was positioned above Ceres' north pole, a region where ice traps have previously been reported (Platz et al., 2016; Schorghofer et al., 2016). Analysis showed no evidence for OH emission detected, and Rousselot et al. (2018) placed an upper limit for the vapor production rate ~10^{26} molecules/s.

8.6 Implications for the Production of an Exosphere

The February 2018 telescopic observation occurred at an interesting time: though there was a moderate SEP event, Ceres was also located near perihelion at 2.566 AU. This is closer to the sun than any of the previous telescopic observations. If the previously proposed sublimation hypothesis was correct, we would expect the February 2018 observation to display the largest magnitude exosphere observed due to the small heliocentric distance. No such exosphere was detected. The non-detection by the VLT is more consistent with the SEP-induced exosphere hypothesis. GRaND did not observe the presence of energetic protons in any of its detectors, suggesting the fluxes of energetic protons would be too low to release a sufficient amount water molecules. This non-detection in conjunction with the previous telesocopic observations provides strong support for a transient atmosphere at Ceres triggered by solar energetic particle events.

8.7 References

A'Hearn, M. F. and P.D. Feldman, Water Vaporization on Ceres, Icarus 98, 54-60 (1992).
Küppers, M. et al., Localized sources of water vapour on the dwarf planet (1) Ceres, Nature, 505, 525-527 (2014).

Platz, T. et al., Surface water-ice deposits in the northern shadowed regions of Ceres, Nature Astronomy, Vol 1, 7 (2016).

Rousselot, P. et al., A Search for Water Vaporization on Ceres, The Astronomical Journal, Vol 142, 125 (2011).

Rousselot et al., Search for water outgassing of (1) Ceres near its perihelion, EPSC Abstracts Vol 12, EPSC2018-484 (2018).

Schorghofer, N. et al., The permanently shadowed regions of dwarf planet Ceres, Geophysical Research Letters, Vol 43, 6783-6789 (2016).

Shi, M. et al., Journal of Geophysical Research Letters, Vol. 100, NO. E12, 26387-26395 (1995).

Chapter 9

Conclusions

9.1 Introduction

The Dawn mission was the first to explore the two largest asteroids in the asteroid belt, Vesta and Ceres. The mission began on September 27, 2007, with arrival at Vesta in 2011 and at Ceres in 2015. Finally, on October 31st, 2018, the Dawn spacecraft expelled all its hydrazine fuel, ending the mission. Dawn was placed into an orbit around Ceres which is expected to be stable over the next fifty years. The mission shed light on many aspects of these dwarf bodies and revealed that their surfaces are still quite active. It was found that several regions on Vesta appear to be much younger than their age derived by crater counting, suggesting a process is occurring capable or overturning the surface in the top millimeters. Though Dawn found Vesta to be a relatively dry body, evidence for past transient water flow was identified in the Marcia, Calpurnia, and Minucia craters implying small, localized pockets of ice may exist in the subsurface of Vesta. In contrast, Dawn saw an abundance of evidence for past and current water ice in the near-surface and subsurface of Ceres. Despite this, it was still unclear which water sources were contributing its transient exosphere and by what mechanism the exosphere was being released.

This dissertation aimed to better understand the surface processes of Vesta and Ceres by analyzing each planet's interaction with the solar wind. Though Dawn did not have a magnetometer or a plasma suite, we recognized we could still accomplish this by utilizing the sensitivity of the Gamma Ray and Neutron Detector's (GRaND) to energetic protons, electrons, and magnetic fields.

9.2 Insights into Vesta's Past Dynamo

We used Dawn's Gamma Ray and Neutron Detector to investigate the presence of magnetic fields at Vesta. We scanned the data for the presence of electron bursts, which could arise by being reflected from remanent magnetic patches on the surface (i.e. electron reflectometry similar to the Moon), or by an electron foreshock if the magnetic field was strong enough to produce a bow shock. While our inspection found several spikes in the data during Vesta orbit, it was found that these bursts were not the result of energetic electrons but were by-products of the interaction of solar flare radiation with the instrument. Spikes not produced by solar flares could be explained by instrument glitches or cosmic rays. Therefore, Dawn did not observe any energetic electrons associated with the magnetism of Vesta.

We also attempted to use GRaND to detect shifts in the BGO spectrum due to deflections of the electrons in the photomultiplier tube caused by strong magnetic fields. This did not result in the detection of a planetary dipole, leading us to place an upper limit on its magnetic moment of $\mu=6.03*10^8$ Tm^3 based on the sensitivity of the instrument. This is not surprising since Vesta should have expelled most of its internal heat early in the age of the solar system, given its small size. However, this study does not exclude the possibility of localized, remanent fields on Vesta similar to the Moon and Mars and as suggested by some magnetized H. E. D. meteorites. Several dynamo models indicate the Vestan dynamo could last at most 500 million years after its formation. Given that the large Venenia and Rheasilvia impacts occurred 2.1 and 1 Gyr ago, this means that the heat of the impact should have erased the remanent magnetism in the southern hemisphere. Therefore, we predict an asymmetry in the distribution of remanent magnetism across Vesta: remanent magnetic patches should be preserved in the northern hemisphere while the southern hemisphere should contain little to no remanent magnetism.

9.3 Discovery of Electron Bursts at Ceres Suggest a Transient Bow Shock

The GRaND data showed evidence of sudden bursts of energetic electrons 20-100 keV during its Survey orbit when Dawn was ~10 R_C from Ceres. Though the onset of the bursts occurred alongside the passage of a Solar Energetic Particle (SEP) event, the bursts continued after the event ceased, indicating it source was not the event itself. Further, the absence of electron bursts during larger solar events at Vesta and the directionality of the bursts inferred from the exterior scintillators imply that the bursts are not naturally occurring in the solar wind. Analysis showed the characteristics of these bursts to be most qualitatively similar to that observed during the transit of electron foreshocks. We performed analog studies of the Earth's electron foreshock using STEREO A. This work suggested we should expect to detect a potential Ceres' foreshock to a distance ~20 R_C, indicating Dawn was within this detectability range. To further probe the bow shock possibility, we conducted single-fluid magnetohydrodynamic (MHD) simulations for a bow shock produced by either a water exosphere or by an internally conducting interior. We found that a conductive layer at depth would be insufficient to produce a bow shock based on the internal geochemical conditions expected for Ceres. However, vapor production rates similar to those reported by past telescopic observations of the exosphere were capable of producing a bow shock by mass loading the solar wind. We found that a minimum vapor production rate ~3 kg/s is necessary to produce a bow shock, though this varies slightly depending on how localized the source is. We ran several MHD cases which varied the magnitude and localization of the water vapor from the surface. The shape of the shock was highly dependent on the degree of localization for which the water was released. Exospheres produced by localized regions on the surface produced highly asymmetric, stronger shocks than that produced by a globally released exosphere. However, both cases had similar bow shock distances ~1.5 R_C.

Though this work does not definitively prove the presence of a bow shock at Ceres, it does supply strong evidence for its existence. The onset of the bursts with a solar energetic particle event in combination with water vapor as the likely source to produce a bow shock hinted that the energetic solar protons may be releasing the transient exosphere through a sputtering process. It is important to note that the solar protons may be sputtering surface material other than water ice, which could release other species of heavy molecules that contribute to the mass loading of the solar wind.

9.4 New Hypothesis for the Generation of Ceres' Exosphere

Prior to Dawn, the leading hypothesis for the formation of the exosphere was sublimation driven by decreasing heliocentric distance as Ceres revolved around the Sun. However, the sporadic nature of its presence did not correlate well with this hypothesis, leading some to speculate a cryovolcanic source. In this dissertation we presented a new theory: the transient exosphere is produced during solar energetic particle events when solar protons have sufficient energy to sputter water from the surface. This work is also relevant to cometary studies as it may release water from a nucleus' subsurface before solar heating is strong enough to induce sublimation.

One way of testing this hypothesis is to examine the solar conditions present during past telescopic observations. We found that positive detections of the exosphere occurred when there was a SEP event within ten days of observation (the expected lifetime of the exosphere) and negative detections were preceded by solar wind conditions at background levels. We also showed that the magnitude of the exosphere positively correlated with the energetic proton flux measured at 1 AU as a proxy. Earlier this year we conducted another telescopic observation using the Very

Large Telescope (VLT) to observe Ceres for OH emission. At that time, a SEP event was directed towards Ceres with Ceres closer to perihelion than any other previous telescopic campaign. No energetic protons were detected by GRaND, indicating the SEP event missed Ceres. Interestingly, the telescopic results showed no detection of an exosphere despite the short heliocentric distance. This observation lends more support to the sputtering hypothesis and contradicts the sublimation theory. Though some degree of sublimation may be occurring at Ceres, it is likely the release of water molecules by SEP events is needed to allow the magnitude to reach the detectable limit ~10^{26} s^{-1} of most telescopes.

To aid future telescopic campaigns, we retrospectively used the solar events observed by Dawn while at both Vesta and Ceres to understand the propagation of SEP events and when 1 AU spacecraft can be used as a proxy for the arrival of a SEP event at Ceres. Generally, a spacecraft upstream along the same interplanetary magnetic field line serves as a good proxy for the SEP arrival at the Ceres distance. However, if the emergence of the CME has a heliolongitude radially downstream that of Ceres this does not usually hold. In these instances, a spacecraft with a heliolongitude between Ceres and the origin of the CME usually provides a good substitute despite not being located on the same IMF line.

Since SEP events are sporadic, rapid turnaround time is needed to perform telescopic campaigns following an event. Therefore, we also explored the accuracy of Enlil in conjunction with SEPMOD in predicting whether a given SEP event will encounter Ceres using the above empirical events. This established the models were good at predicting if and when Ceres would be connected to the shock, but its prediction of the magnitude and variation of the fluxes need to be improved.

9.5 Future Studies

We recommend the payloads of future missions to Vesta and Ceres carry both a magnetometer and a plasma suite. This would allow spacecraft to probe remanent magnetism on Vesta (and its possible hemispheric dichotomy), observe the solar conditions present during exospheric production, and allows the identification of bow shock crossings. We also suggest conducting Ceres exospheric observations during solar maximum when the sun is likely to produce many SEP events. Lab studies involving electron and proton beams aimed at the duplicate GRaND instrument would help understand the flux necessary to increase the count rate and the directionality of the bursts. Similarly, lab measurements for Ceres' surface conditions using energy ranges similar to those present during SEP events would inform the expected sputtering rate of water during these events.